Cosmic applications of Gravitational Lens Assisted Spectroscopy (GLAS)

by

Karunananth G. Thanjavur
B.E., University of Madras, India, 1979
M.E., University of Madras, India, 1988
M.A.Sc., Concordia University, Montreal, 1997

A Thesis submitted in Partial Fulfillment of the
Requirements for the Degree of

Doctor of Philosophy

in the

Department of Physics and Astronomy

Supervisory Committee

Cosmic applications of Gravitational Lens Assisted Spectroscopy (GLAS)

by

Karunananth G. Thanjavur

Supervisory Committee

Dr. David Crampton, (NRC Herzberg Institute of Astrophysics)

Co-Supervisor

Dr. Jon Willis, (Department of Physics and Astronomy)

Co-Supervisor

Dr. Chris J. Pritchet, (Department of Physics and Astronomy)

Departmental Member

Dr. Florin Diacu, (Department of Mathematics)

Outside Member

Supervisory Committee:

Dr. David Cramption, Co-Supervisor (NRC Herzberg Institute of Astrophysics)

Dr. Jon Willis, Co-Supervisor (Department of Physics and Astronomy)

Dr. Chris J. Pritchet, Departmental Member (Department of Physics and Astronomy)

Dr. Florin Diacu, Outside Member (Department of Mathematics)

Abstract

The principal observational contribution of this thesis is an innovative technique, using spatially resolved spectroscopy of highly magnified, gravitationally lensed galaxies, to study their internal structure and kinematics at redshift, $z \geq 1$ on *sub-galactic scales*. The scientific objective is to measure the important, but poorly understood, role of star formation and associated feedback on galaxy evolution. With Gemini GMOS-IFU observations of CFRS03+1077, a lensed galaxy at z=2.94, we determined surface brightness and integration time requirements for spatially resolved kinematics with spectra in the visible region (< 1 micron). For reasonable exposure times the presence of a strong emission line is key, limiting the redshift range to < 1.5 for [OII]3727Å. To tackle the lack of suitable lenses for such studies, we designed a lens search algorithm suitable for multi-color photometric data (with a minimum of 2 colors). Our method uses a two-step approach, first automatically identifying galaxy clusters and groups as high likelihood lensing regions, followed by a dedicated visual search for lensed arcs in pseudo-color images of sub-regions centered on these candidates. By using the color-position clustering of elliptical galaxies in high density environments, the algorithm efficiently isolates candidates

with a completeness $\geq 80\%$ for $z \leq 0.6$ in Monte-Carlo simulations. Implemented on the CFHT Legacy Survey-Wide fields with available g, r and i photometry, the present yield is 9 lenses (8 new and 1 previously known) from 104 deg^2. With Gemini GMOS, we confirmed two lensed galaxies with strong [OII]3727Å emission suitable for IFU spectroscopy. The follow-up of both systems, the confirmation of remaining lenses and the application of the lens detector to the remaining 91 deg^2 of CFHTLS-Wide are ongoing.

In a complementary project, we aim to understand non-linear structure formation within the Λ-CDM framework by characterizing the mass distributions and mass/light ratios of galaxy groups; these structures (where 60% of all galaxies reside), have masses representative of the critical break between cluster and field galaxy mass scales. We use strong gravitational lensing to constrain the mass in the inner core, with velocity dispersion measurements from MOS spectroscopy to map the mass distribution up to the scale of the virial radius. The formalism supporting this approach as well as the tools for analysis (including an efficient B-spline based method for flat fielding and sky subtraction of sky limited spectra) are presented in this thesis. The deflectors of 6 lenses in our catalog resemble galaxy groups suitable for this study. One group, for which the observations are complete, is compatible with either NFW or Hernquist profile; these results will be corroborated with observations of other candidates in forthcoming observing programs. The objective is to amalgamate our results with mass measurements from weak lensing and X-ray observations from our Strong Lensing Legacy Survey (SL2S) collaborators to build a comprehensive picture of the dark matter profile and thus constrain theoretical predictions of mass assembly in galaxy groups.

Table of Contents

List of Tables

List of Figures

Acknowledgments

A journey of a thousand miles, said Confucius, begins with a single step. In my present journey of exploration of our universe, that hesitant initial step was the first lecture by Dr. Hartwick in the 'Stellar Atmospheres' course. Since I had no previous background in physics, leave alone astrophysics, I remember being dumbstruck with the jargon and acronyms, and wondering whether I was even hearing English! I continued my journey nonetheless, and if I have reached a small personal milestone today, it is only because of the continued support and guidance, which I received from many benefactors along the way. And amongst the many on whose help and good wishes I have drawn, it is my sincere pleasure to begin with acknowledging the intangible support of five people, to whose spirit of true sharing I dedicate my work.

Dave Balam, co-data junkie and friend, by generously helping me with observational results that you gleaned from long hours of labor, to me you embody the essence of collective research. It would be no exaggeration to say that you offered me that proverbial ray of hope at a point in my journey when all seemed dark and lost.

Dr. Werner Israel, teacher, mentor and friend, I am honored to have this place in your presence, to be able to listen to the wisdom you share freely and to laugh together cheerfully as we strive to understand Nature's fascinating paradoxes.

Russ Robb, astro-guru and friend, it was your patient and cheerful guidance of a newbie in the dome that now has me hooked to the right end of the 'scope, and enjoying it!

Purnima, my dear kid sister, with your care and thoughtfulness, you convey the love of our parents, Amma and Naina, who are always with us in spirit, and of our elders and the extended family living far and near.

Pippa and Penny, with your cheerful and positive attitude toward life's many challenges, you have inspired me to rise above barriers, either real or perceived,

along my way.

The list of people, on whose support and guidance I have freely drawn, continues on well past these five. Of these, I wish to begin by acknowledging my supervisors, who with patient guidance and unwavering support, have belied the adage of not being able to teach an old dog, new tricks. My sincere thanks to my principal supervisor, Dr. David Crampton, who always set aside his many responsibilities and found time to discuss and guide my work. In his position as leader of an international team of engineers, I was his excuse to do science, he said. To Dr. Jon Willis, my co-supervisor, my thanks especially for his critical eye for detail in dealing with the many challenges of observational cosmology and for the time he devoted to my work amongst his teaching, research, many other departmental responsibilities, all these in addition to his growing family.

I gratefully acknowledge the advice and guidance of my committee members. It is a honor to have Dr. Jean Paul Kneib as my external examiner and I thank him sincerely for all the detailed comments and suggestions he has provided to improve my work. To Dr. Chris Pritchet, Dr. Florin Diacu and Dr. Michael Valente, my sincere thanks for their thought provoking and insightful questions and comments regarding the work and its relevance to the broader science goals. As understanding and supportive members of the examining committee, they helped dispel my initial nervousness and helped me benefit from and enjoy the discussions. On the same vein, my special thanks to Dr. Luc Simard, who kindly read my thesis prior to the defense and offered valuable suggestions and advice regarding both the manuscript as well as the oral presentation during the defense.

My sincere thanks to the staff in the departmental office for their cheerful support throughout my graduate program, especially to the graduate secretaries past and present, Geri Blake, Joy Austin, Rosemary Barlow and to Monica Lee. I cannot fully express my gratitude to Dr. Stephenson Yang for his help both with questions regarding astrophysics as well as anything to do with the computing and associated

systems - even on weekends and holidays! And to my co-graduate students in these six years, my thanks for all their support and cheer which always made the good times better and the challenging times manageable.

Having moved to Victoria to live close to my sister just prior to beginning my graduate studies, it has been a pleasure to become part of a growing community of friends over the six years as a graduate student. Since space does not permit me to thank each of them individually, I have to be content with thinking of them all when I express my thanks for their continued support, especially to my friends in the Herzberg Institute of Astrophysics, the Alpine Club of Canada, the Poetry Lovers Circle of Victoria and the UVic Pamwe Gumbooters.

Though I leave this phase of my education behind, my journey of exploration in physics continues, as will all these friendships, I hope, and I look forward to returning in some small measure all the support and cheer I have been fortunate to receive.

The results presented in this thesis are based on observations obtained at the Gemini Observatory, which is operated by the Association of Universities for Research in Astronomy, Inc., under a cooperative agreement with the NSF on behalf of the Gemini partnership: the National Science Foundation (United States), the Science and Technology Facilities Council (United Kingdom), the National Research Council (Canada), CONICYT (Chile), the Australian Research Council (Australia), Ministrio da Cincia e Tecnologia (Brazil) and SECYT (Argentina)

This research used the facilities of the Canadian Astronomy Data Centre operated by the National Research Council of Canada with the support of the Canadian Space Agency.

A substantial part of the data reduction was done using IRAF, which is distributed by the National Optical Astronomy Observatory operated by the Association of Universities for Research in Astronomy (AURA) under cooperative agreement with the National Science Foundation.

To my five zen roshis,
who by their examples taught me the truth
of fully being
in simple sharing.

Chapter 1 | *Introduction*

1.1 Prelude

Recent years have seen rapid - and exciting - progress in *Physical Cosmology*, the study of structure growth in the Universe. Complementary advances on both the observational and theoretical fronts have been the key drivers of these developments. With this growing knowledge, we are piecing together details of how the near perfect isotropy of the early Universe, imprinted in the Cosmic Microwave Background at redshift z$\sim$ 1000 (Figure 1.1, top panel [*]), metamorphosed to the stunning variety of gravitationally bound structures we observe in the Universe today, on mass scales ranging from super clusters (mass $\sim 10^{15}\,\mathrm{M}_{\odot}$), through clusters, groups, individual galaxies like the Milky Way down to that of individual stars and their planetary systems, with mass of $\leq 1\,\mathrm{M}_{\odot}$ - a scale that extends over 15 orders of magnitude. A striking example of gravitationally bound structure in the local universe on the scale of clusters is shown on the bottom panel [†] of Figure 1.1, by galaxy cluster, Abell A2218.

In the current cosmological paradigm, the growth of this large scale structure was driven primarily by gravitational collapse and occurred through a series of hierarchical merging processes, with structure on small mass scales forming first and then merging to form structure at ever increasing scales (Longair, 1998). From observations and extensive theoretical work, supported by numerical simulations

[*] http://map.gsfc.nasa.gov/

[†] http://apod.nasa.gov/apod/ap011007.html

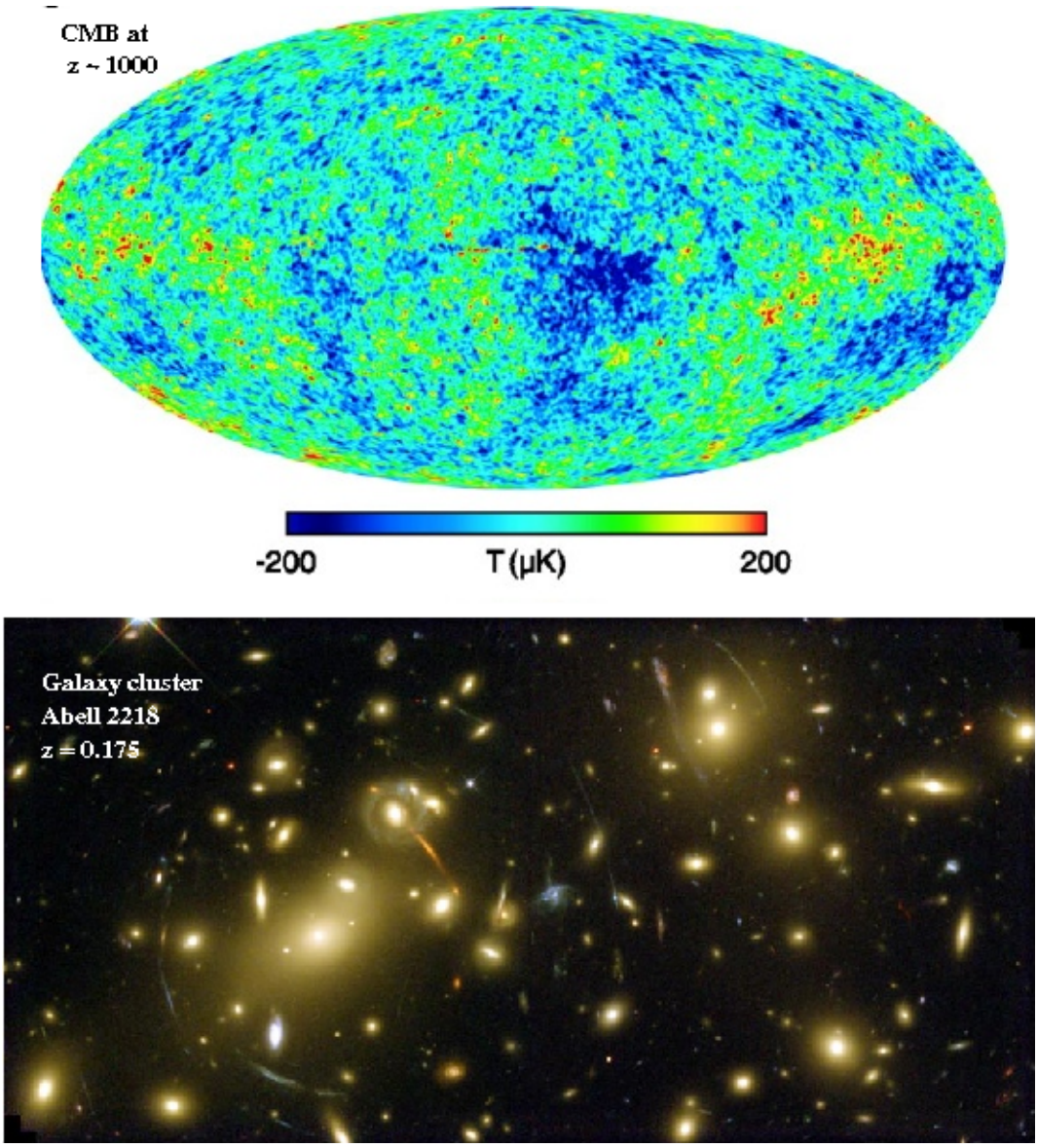

Figure 1.1: Large scale structure in the universe as imprinted on the Cosmic Microwave Background (CMB) at redshift z∼1000 (*top*), compared with gravitationally bound structure in the local universe on the scale of a galaxy cluster, spectacularly illustrated by Abell A2218 at z=0.175. Several gravitationally lensed arc images of galaxies at higher redshifts are clearly visible in the cluster.

and semi-analytic models, our understanding is converging toward a concordance cosmological model - the spatially flat, vacuum energy dominated Λ-CDM [‡] model (Spergel (2005), Springel et al. (2005) and references therein). The general principles of the model have successfully withstood tests from a variety of independent and complementary observations, such as the WMAP CMB observations (Komatsu et al., 2008, Spergel et al., 2003), high redshift supernovae observations (Riess et al., 2007), redshift surveys such as the 2dF (Percival et al., 2002) and by cosmic shear observations (Massey et al., 2005). Finer details, however, such as the inner slope of cluster dark matter profiles, (Sand et al., 2004, Primack, 2004), or the assembly of stellar mass in clusters (Balogh et al., 2008), are yet to be fully resolved.

In this cosmological model, the principal components of the universe are dark energy (Λ), non-relativistic (cold) dark matter (CDM) and baryonic matter; in this context, baryonic matter includes all matter that we detect through their electromagnetic interactions. Recent WMAP-CMB 5-year results, (Komatsu et al., 2008), constrain the energy budget of the universe to 4.4% baryonic matter, 21.4% dark matter with the remaining being dark energy. Dark energy drives the overall dynamics of the Universe at present times, dark matter governs the formation of large scale structure, while it is the physics of baryonic matter, the most visible, which is the principal driver of evolution on the lower end of the mass scale, that of galaxy clusters and smaller structures.

It is to understand the important role of baryonic processes associated with active star formation in galaxies in the early universe (at redshift, $z \geq 1$), that the *principal* focus of the thesis is devoted. Section 1.2 presents a review of the rapidly advancing state of research in this area and the specific questions which motivate this work. The complementary observational approaches of wide field surveys and detailed studies of individual objects, both of which provide the bulk of our

[‡]A list of acronyms and abbreviations used in this thesis, with corresponding expansions, is provided in Appendix B for reference

knowledge on high redshift star formation are reviewed. The relative importance of detailed sub-galactic scale investigations and the enormous observational challenges of carrying out such studies are set forth in Section 1.2.2. These provide the background for the principal observational goal of this thesis, to develop a unique method harnessing the magnification of gravitational strong lensing coupled with spatially resolved IFU spectroscopy - concisely, Gravitational Lens Assisted Spectroscopy, *GLAS* - to successfully overcome the observational hurdles. This review thus sets the stage for the detailed description of the pilot implementation of our observational technique, which forms the bulk of Chapter 2.

In a complementary project, we aim to understand non-linear structure formation within the Λ-CDM framework by characterizing the mass distributions and mass to light ratios of galaxy groups; these structures (where 60% of all galaxies reside, Silk (2004)), have masses representative of the critical break between cluster and field galaxy mass scales. The observational strategy we adopt is to combine mass estimates from gravitational lensing in the inner core of the groups with measurements of the mass distribution up to the virial radius derived from the observed velocity dispersion of the member galaxies. We utilize the catalog of lensing galaxy groups and clusters developed for the IFU work to carry out these investigations. Due to the complementary mass measurements from gravitational lensing and from the kinematics of member galaxies determined by spectroscopy, we include this investigation as a second application of GLAS. Section 1.3 reviews pertinent results from literature, highlighting the issues and outlining the methodology we adopt in Chapter 5 to address these questions.

1.2 High redshift star forming galaxies

The bulk of our knowledge of the nature and evolution of star forming galaxies even at redshifts, $z \sim 3$ and higher comes from large spectro-photometric surveys,

which constrain the statistical properties of the high-redshift populations. From these surveys, it is now clear that even at early times in the history of the universe, galaxies had very high star formation rates (Nesvadba et al., 2007, Pettini et al., 2001), were screened by appreciable amounts of dust (Shapley et al., 2006, Savaglio et al., 2004, Sawicki and Yee, 1998) and were dominated by starburst-driven outflows of material seen both in the kinematics of their gaseous and stellar components (Pettini et al., 2000) and in their effect on the surrounding Lyα forest (Adelberger et al., 2003). A compilation of results from several observational surveys, shown in Figure 1.2, (Reddy et al., 2008), traces the evolution of universal star formation rate density as a function of redshift or equivalently with the age of the universe (usually referred as a *Madau* plot, Madau et al. (1998)); the star formation rates in the plot are derived from UV and Infra-red measurements which have been corrected for extinction. The striking feature is the peak in star formation activity at z$\sim$1 followed by the rapid decline to the present. It is at the period of intense star formation, $1 < z < 1.5$, with consequent rapid stellar mass build up and evolution of the galaxies, that we direct our observational investigations, as discussed in the following Section 1.2.2.

However, while all this evidence indicates that galaxies were undergoing intense episodes of star formation at z = 1 or higher, we do not yet have a clear understanding of the mechanisms that trigger and govern the associated baryonic processes. Theoretical models at present invoke poorly understood feedback mechanisms to match these observational results (e.g. Bertone et al. (2007), Cattaneo et al. (2007)). Detailed observations of such processes at work in individual low mass galaxies - principal star formers at all redshifts (Juneau et al., 2005), are therefore a pressing requirement.

Even with the aperture and resolution of today's 8m telescopes, such studies are very difficult (at $z = 1$, a disk scale of 4kpc is $\leq 0''.5$ on the sky). Our research goal is therefore to test and apply the innovative observational technique of spatially

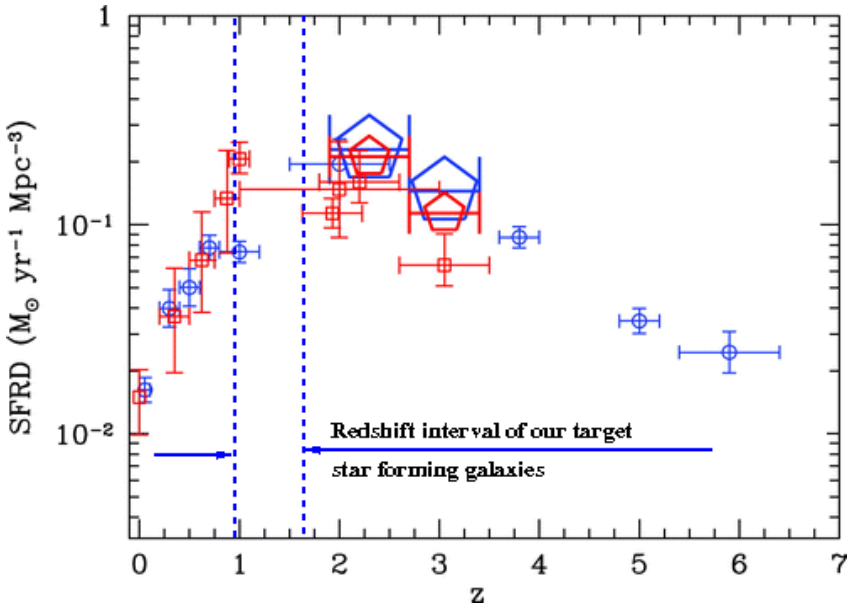

Figure 1.2: In this recent *Madau* plot from Reddy et al. (2008), a compilation of results from several observational surveys in the UV (blue symbols) and Infra-red (red symbols), trace the evolution of the star formation rate density with redshift. The redshift interval at which we focus our IFU spectroscopy is indicated by dashed lines; it coincides with the interval of peak star formation activity in the universe. The lack of points in this region highlights the presence of the 'redshift desert', discussed in §1.2.1. The upper redshift bound is only an observational limitation at present; see concluding paragraph of §2.11 for a discussion

resolved spectroscopy combined with the magnification boost from gravitational lensing to carry out such detailed studies of galaxies at $z \geq 1$. In order to motivate our scientific objectives, the following section provides a summary of pertinent results from published studies of high redshift star forming galaxies, highlighting the outstanding issues which we aim to address with our research.

1.2.1 Results from surveys

Our understanding of the population of high redshift star forming (SF) galaxies received a big boost with the advent of the Lyman Break technique (Steidel et al., 1996). This method uses two colors to effectively isolate the break in the observed flux between the high ultra-violet (UV) continuum (from the O and B stars) and the low flux blueward of the Lyman limit at 912Å due to absorption by the neutral hydrogen in the galaxy itself as well as by intervening absorbers. For $z \sim 3$ galaxies, Steidel et al. (1996) used (U-G) and (G-R) colours; the technique has since been extended to higher redshifts by using the appropriate filter sets, e.g., for galaxies at z ∼7-8 in the HUDF (Hubble Ultra Deep Field), Bouwens et al. (2004) use the optical z- and the infra-red J and H filters.

For the z∼1-2 range, a similar increase in observed numbers was achieved by Gemini Deep Deep Survey, GDDS, (Abraham et al., 2004) using the 'Nod and Shuffle' technique for optical spectroscopy. The z∼1-2 redshift range is aptly named the 'redshift desert' due to the lack of strong emission features in the rest frame UV spectrum, which is redshifted into the (observed) optical band - this lack of spectral features therefore demands high quality data, specifically low sky residuals from the strong atmospheric hydroxyl emission. For their survey, Abraham et al. (2004) combined the Nod and Shuffle technique (Cuillandre et al., 1994) with multi-object spectroscopy (MOS) to achieve the required high signal-to-noise ratio (SNR) in their observations.

Results from these surveys have clearly shown that even at z ∼3-4, these 'Lyman Break Galaxies', LBGs (so named for the technique used by Steidel et al. (1996)), were actively forming stars when the Universe was less than 2 Gyr old in standard cosmology. Their measured UV continuum luminosities - indicative of massive, young stars - are over 60 times those of the brightest SF regions observed in the local universe (Steidel et al., 1999, 1996). With even more intense star formation rates, $\geq 100 \mathrm{M}_{\odot} yr^{-1}$, the dust enshrouded Sub-Millimeter galaxies (SMGs) observed

at $z \geq 2$ fall into a category on their own (Blain et al., 2002). The far-infrared luminosity of these galaxies far exceeds that of their local counterparts, the Ultra Luminous Infrared galaxies (ULIRGs) at $z \leq 0.1$, leading Goldader et al. (2002) to hypothesize some very efficient and as yet unknown mechanism of gas cooling and star formation at high redshifts. However, Erb et al. (2006) argue that intense star formation can equally be induced by 'wet' mergers of gas rich galaxies, which would funnel the molecular gas in them to their core; along with increasing star formation, this would also lead to the observed higher active galactic nucleii (AGN) activity. Recent observations of a SMG at $z = 2.6$ seem to support this merger scenario (Nesvadba et al., 2007). One of *our goals* is to address this uncertainty by constructing spatial maps of the star forming regions in these galaxies - irregular patches of star forming regions will support the merger scenario of Erb et al. (2006), while a stable disc-like structure will lend support to the hypothesis of Goldader et al. (2002).

'Downsizing' in the evolution of star formation rate densities is a related issue which is also being actively investigated. First proposed by Cowie et al. (1996), this refers to the observed anti-correlation between galaxy mass and the evolution of star formation rate density. GDDS results (Juneau et al., 2005) have shown that massive galaxies ($M \geq 10^{10.8}$ $M_{\odot}$) formed their stars early, at $z \geq 2$, while the peak occurred at $z \sim 1.5$ for intermediate mass systems; recent results from the Cosmic Evolution Survey (COSMOS) survey lend support to these findings (Mobasher et al., 2008). In addition, Willmer et al. (2006) find that luminosity function of the red population remains unchanged at least up to $z \sim 1$ indicating that there is a substantial population of massive galaxies with passively evolving stellar populations even at this early time. Further support comes from two other studies - Bell et al. (2004) find that the red sequence is well in place by $z \sim 0.7$ indicating that galaxies at the massive end of the sequence have no ongoing star formation. However, Faber et al. (2007) find that the stellar mass in these massive

galaxies shows a significant rise from $z = 1$ to the present, perhaps due to 'dry' gas poor, galaxy mergers. All these complementary results run counter to the hierarchical mass assembly expected in the Λ-CDM paradigm in which more massive galaxies should be actively forming stars to the present due to continued accretion of gas. The nature of the mechanism which quenches the associated star formation is unclear. Both Bell et al. (2007) and Faber et al. (2007) point out that most of the star formation at z $\geq$ 1.5 happens in massive blue galaxies; if star formation were therefore *somehow* quenched, these massive blue galaxies would migrate to the massive end of the red sequence, where they would continue to accrete mass by 'dry' mergers. Current galaxy evolution models (Bertone et al., 2007, Cattaneo et al., 2007, Bower et al., 2006, Croton et al., 2006) have only been able to reproduce these observational results by invoking poorly understood feedback mechanisms, eg. superwinds and AGN activity, to regulate star-formation. Results from surveys therefore provide only the general trend in the assembly of stellar mass in galaxies; an understanding of the mechanisms driving this evolution will require detailed observations on sub-galactic scales of the associated baryonic processes at work. This unresolved issue of 'downsizing' is a *key motivation* for our research and we aim to verify the various proposed theoretical models with our observations.

Finally, there is no consensus yet on how these rapidly star forming galaxies in the early universe are related to the galaxies in the local universe. The strong clustering of LBGs resembles that expected of massive dark matter halos (Adelberger et al., 1998), suggesting that they may be direct ancestors of present-day massive ellipticals and spirals (Baugh et al., 1998, Steidel et al., 1996). In an alternative scenario, LBGs could be low-mass systems seen undergoing brief bursts of star formation as they orbit their massive dark-matter hosts (Somerville et al., 2001, Sawicki and Yee, 1998). On the basis of a handful of measurements, the LBGs' metallicities appear to be sub-solar (Pettini et al., 2001), and so in agreement with either scenario, while broadband colors cannot rule out the presence

of large numbers of old, faint stars expected in massive systems (Papovich et al., 2001, Sawicki and Yee, 1998). It thus remains unclear if LBGs are the direct precursors of present-day massive galaxies, if they build up mass through repeated, merger-induced star-forming episodes, or if they turn into faded, low-mass objects.

1.2.2 Studies on sub-galactic scale

For a more complete picture, population statistics must be complemented by detailed observations of individual galaxies. Spatially resolved observations (both spectroscopy and multi-color imaging) of the stellar and gaseous components would allow us to construct pixel-by-pixel maps of the internal kinematics, outflows and of the dust and star formation history on sub-galactic scales. Such results will help answer fundamental questions as, "Are star forming regions in these galaxies distributed or centrally condensed?", "Are they rotationally supported?", "Is there evidence for the Tully-Fisher (Tully and Fisher, 1977) relation at high redshift?", and "Are super novae (SNe) driven gas outflows in galaxies common?".

Unfortunately, at redshift ≥ 1, galaxies are too compact with half light radii, HLR $\sim 0''.25$ (Giavalisco et al., 1996) and too faint to allow spatially-resolved studies even with HST. The limited number of published studies of individual $z \geq 1$ SF galaxies have therefore focused upon gravitational lens systems. Lensing magnifies the spatial extent of distant galaxies while conserving the surface brightness, such that even $z \sim 3$ SF galaxies are magnified into giant arcs of extent 10 square arcseconds.

The most detailed study of a high-redshift SF galaxy concerns MS1512-cB58 (referred as cB58), located at $z = 2.73$, which is lensed by a foreground galaxy cluster, MS1512+36 at $z = 0.37$ (Yee et al., 1996); the resulting magnification has been determined to be up to 30 (Seitz et al., 1998). Pettini et al. (2000) used the Low Resolution Imaging Spectrograph (LRIS) and the high resolution Echelle Spectrograph and Imager (ESI) (Pettini et al., 2002) on the 10m Keck

telescope to resolve the stellar and interstellar lines and obtain a variety of kinematic and chemical abundance measurements. It must be mentioned that the lensed image of cB58 is only $< 1''$ in length (Yee et al., 1996), making it unsuitable for IFU observations at present; the development of Adaptive Optics combined with the IFU, will make this interesting target accessible for spatially resolved optical spectroscopy in the near future.

Pettini et al. (2000) find that cB58 is a LBG with a stellar mass $\sim 10^{10}\,M_\odot$ and is undergoing an intense burst of star formation. The stellar spectrum resembles that of a local starburst galaxy and is well reproduced by a synthetic spectrum containing O and B stars with a Salpeter IMF (Salpeter, 1955) extending beyond $50\,M_\odot$. The strength of α-elements such as Mg, O and Si, produced mainly by the higher mass stars, are already enriched to 2/5 solar values while the Fe-peak elements, mainly from the lower mass stars, are smaller by a factor of 3 compared to the solar value. Based on the timescales needed for the α and Fe-peak element enrichment, Pettini et al. (2002) deduce that the start of the burst was within the previous 300Myr and that the intensity of the continuous SF had converted nearly a third of its gas into stars.

In addition, the stellar and interstellar spectral lines show a relative velocity of $\sim 250\,\mathrm{km\,s^{-1}}$, with the gas blue shifted toward the observer indicative of a bulk motion of gas driven by the intense star formation and consequent SNe explosions. Comparing the dynamical mass of the galaxy and the estimated outflow gas speed, Pettini et al. (2000) surmise that only part of this outflowing material is retained by the galaxy, leading to a rapid chemical enrichment of the interstellar medium (ISM), while the rest of the gas is lost to the intergalactic medium (IGM).

A similar large scale outflow of $\sim 300\,\mathrm{km\,s^{-1}}$ has been observed in another lensed galaxy at $z = 4.92$ (Franx et al., 1997). Given that there are only these two observations, it is important to determine if galactic winds are common in high redshift galaxies. If so, they could be the mechanism regulating SF by driving away

the gas while allowing the escape of ionizing photons as well as enriching the IGM with metals (Pettini et al., 2000)

In addition, cB58 may not be representative of the LBG population since both the lack of a Balmer break in its rest frame optical spectrum (Teplitz et al., 2000) and its broadband colors indicate that it is much younger than nearly all LBGs. Therefore, only a detailed spectroscopic study of a larger sample of galaxies will give us a more representative picture of the processes going on inside high-z galaxies.

Swinbank et al. (2003) carried out pioneering work in this direction, albeit at a lower redshift. Using the boost provided by gravitational lensing, they obtained a detailed rotational velocity curve for a galaxy at $z = 1.034$. The galaxy lies behind the rich Abell cluster A2218, (shown in Figure 1.1), one of several multiply imaged sources; the magnification is 4.9, as determined from a detailed mass map of the cluster. Spatially resolved spectroscopy of the strong [OII]3727Å emission line was carried out with the Gemini Multi Object Spectrograph plus the Integral Field Unit (GMOS-IFU).

Using a lens model, the distortion introduced by the lensing was removed in order to compute a rotational velocity of 206 $\mathrm{km\,s^{-1}}$, a remarkable result indicating the presence of a disc at a lookback time of 8.7Gyr. The inferred rotational velocity places this galaxy on the B- and I-band Tully-Fisher relations for local spiral galaxies, assuming passive evolution. These observations provide clear proof that such studies can resolve galaxies at $z \geq 1$ and probe the kinematics and other key properties of the stellar and gaseous components on scales which are otherwise not accessible.

It must however be mentioned that very recently Near Infra Red IFU spectroscopy with Adaptive Optics (AO) has made successful inroads into resolving these high redshift galaxies even without the magnification boost of gravitational lensing. First results using this technique from the ongoing Spectroscopic Imaging survey in the Near Infra-red with SINFONI (SINS, Förster Schreiber et al. (2006))

at the European Southern Observatory, Very Large Telescope (ESO-VLT), indicate that, of the currently observed total of 14 galaxies at $z \sim 2$, nine show lumpy disk-like rotation while two others show clear signs of mergers. The SINS methodology requires a natural guide star for AO correction and is thus restricted to fields close to stars of suitable brightness. However, with the advent of Laser Guide Star Adaptive Optics (LGSAO) this restriction is largely removed, making large areas of the sky available for observation. In an impressive demonstration of this technique, Wright et al. (2007) have obtained a variety of results including bulk rotation and velocity dispersion, metallicity and the dereddened SF rate of a galaxy at $z = 1.5$. Their kinematic model of this galaxy is well fit by an inclined disk combined with the likelihood of an ongoing merger. Since then, Law et al. (2007) have extended this technique to z$\sim$2-3 and have obtained the kinematics of three LBGs with just 4h of integration per target. Therefore, this complementary technique for sub-galactic scale observations of high redshift galaxies may soon provide a viable alternative to GLAS for the study of high redshift galaxies.

Finally, it must be emphasized that though IFU observations of gravitational lenses offers a viable and tested method of observing high redshift galaxies with sub-galactic scale resolution, few suitable lenses for such studies are known, principally due to the lack of dedicated searches. To address this pressing need for *confirmed* gravitational lenses to carry out these investigations, we have developed an automated search algorithm tuned for multi-color imaging (with a minimum of 2 colors). Our method uses a two-step approach, first automatically identifying galaxy clusters and groups as high likelihood lensing regions, followed by a dedicated visual search for lensed arcs in pseudo-color images of sub-regions centered on these candidates. Chapter 3 provides a review of various cluster detection methods in order to motivate our chosen approach as well as to highlight its aptness to the imaging on which it is implemented. Details of the implementation of this method using the photometric catalogs from the Canada France Hawaii Telescope,

Legacy Survey, Wide component, (CFHTLS-W) are also given, as well as details of the cluster and galaxy group catalogs that we have constructed as a useful by-product of this work. Chapter 4 provides details of the 9 candidate lenses we have discovered by the visual inspection and of the observations completed to confirm them. As a continuation of this work, the visual search for lensed images in RGB stamp images has been matched by an automated scheme. To provide the necessary background, a review of available algorithms for the detection of lensed images in wide field imaging is given, along with the test results which support our choice of *Arc_detector*, developed by Lenzen et al. (2004). The fully automated implementation awaits selection and completeness estimations, which are discussed along with plans for future observations in the concluding remarks in Chapter 6.

1.3 Dark matter distribution in galaxy groups

In this complementary project, we turn the focus of Nature's telescope - the gravitational lens - from studying the evolution of high redshift galaxies, to studying the properties of the telescope - the deflector - itself. In strong lensing, the geometry and relative magnifications of the multiple images are a sensitive function of the mass distribution in the deflector (along with the redshfits and relative positions of the source and the deflector). Therefore, the observed positions and magnifications of the lensed images may be inverted to deduce the underlying distribution of gravitating mass - dark matter plus the baryonic components- of the deflector, referred as the lens model. Kneib et al. (2003) have reconstructed the mass distribution of the rich cluster Cl 0024+1654 at z=0.395 as an illustrative application of the principle.

Our objective in this work is to infer the dark matter profile of *galaxy groups* using this technique in order to constrain models of hierarchical assembly of mass, specifically on the scale of $10^{13} \leq M \leq 10^{14}$ $M_{\odot}$. In this section, we provide a

summary of pertinent literature to highlight the critical mass regime galaxy groups occupy as well as the questions which motivate our work. In order to obtain a more comprehensive picture of the dark matter distribution, we complement the mass estimates from strong lensing in the core of the group with the dynamical mass measured using the observed line of sight velocity distribution (LOSVD) of the member galaxies. This extends the mass estimate to the scale of the virial radius. Our catalog of galaxy clusters and groups with strong lensing images (referred hence as *lensing clusters* for brevity) from the CFHTLS-Wide fields provides an adequate observational sample to undertake this work. We wish to point out that our results will be complemented and extended to radii beyond the virial radius by the multi-wavelength observations being undertaken by other members of the Strong Lensing Legacy Survey (SL2S) collaboration, of which we are a part. A list of these complementary observations being pursued by various members of the SL2S is provided at the end of this section.

1.3.1 Structure formation on the scale of galaxy groups

The evolution of large-scale clustering of mass in the Universe is well described by the concordance Λ-CDM model (Springel et al., 2005), salient features of which are described in Section 1.1. In this model, the homogeneous density field of the early universe following Inflation was seeded by minute quantum mechanical perturbations (Longair, 1998). Due to self-gravity, these perturbations grew even as the Universe expanded. Baryonic matter could not follow this density growth at early times since it was coupled with the hot radiation through Thompson scattering; overdensities in the baryonic field existed in an oscillating density field due to interactions with the high energy photons. Dark matter, on the other hand, interacts only through gravity and was thus free to clump and grow into gravitationally bound halos. Therefore, large scale structure (LSS) formation is governed primarily by gravitational interactions of dark matter, the dominant mass component; the

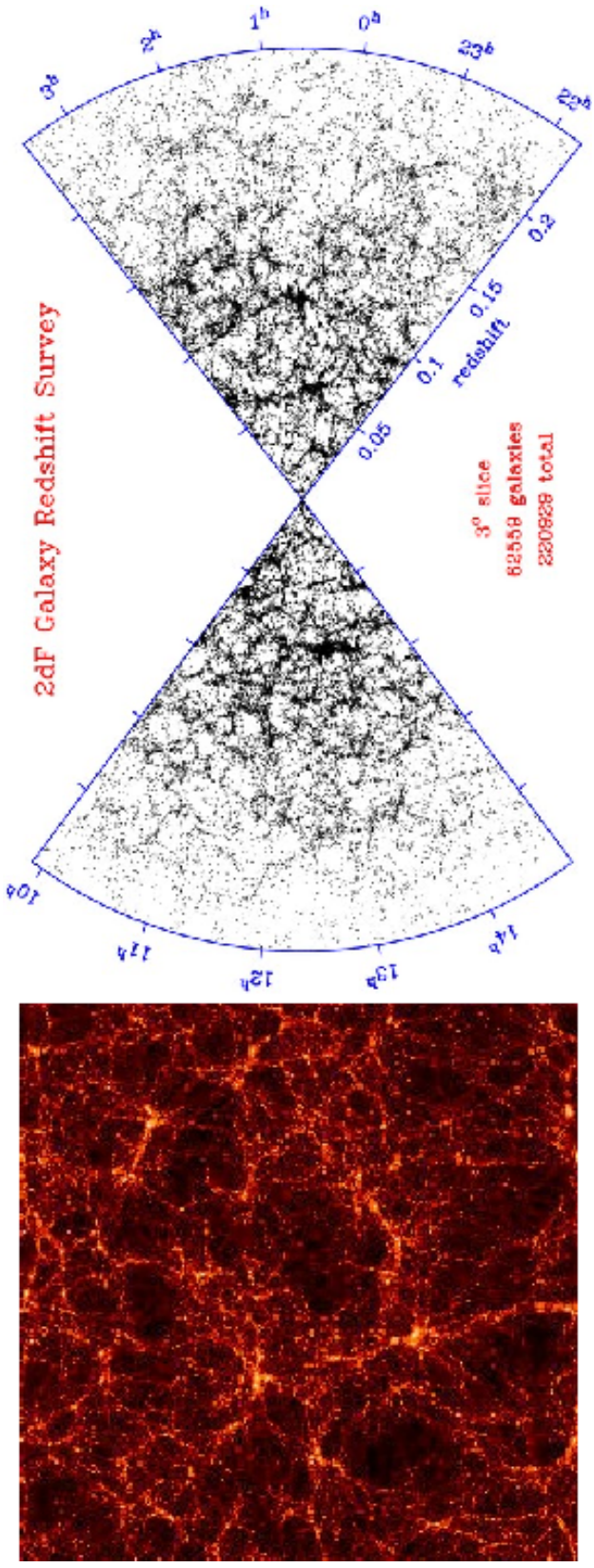

Figure 1.3: A comparison of large scale structure in the universe in the Millennium Simulation (left panel, Springel et al. (2005)) and the observed distribution of bound structure in the 2 degree Field survey (2dF, Colless et al. (2001), right panel) show remarkable similarity, highlighting the success of the hierarchical Λ-CDM model at scales where gravity is the dominant force driving structure evolution.

linear scale referred to in this context is $\gg$ few$\times$Mpc, the scale of clusters, the largest, gravitationally bound structures observed in the Universe today. On this large scale, two views of the structure in the universe (Figure 1.3), one observed by the 2 degree Field Galaxy Redshift Survey (2dFGRS, Colless et al. (2001)) and the other taken from The Millennium Simulation, a large numerical simulation (10^{10} particles in a 500Mpc region, Springel et al. (2005)) show remarkable similarity. The simulated structure (*left panel*, Figure 1.3) and the observed one (*on the right*) not only visually resemble each other remarkably well, but their statistical correlation functions match closely (Primack, 2005), which gives further support to the Λ-CDM model.

As the universe expanded and cooled, the primordial baryonic matter effectively decoupled from the background radiation; it is the imprint of structure at the time of this decoupling that is observed as the temperature fluctuations, (at the level of 10^{-3}K), in the Cosmic Microwave Background, shown in Figure 1.1. Present estimates put this decoupling at redshift, z$\sim$1100. Once decoupled, the baryons, consisting of 75% hydrogen, 24% helium with traces of other light elements from Big Bang nucleosynthesis (Wagoner, 1973), accreted rapidly into the large gravitational potential wells of the dark matter halos. During the ensuing *dark ages*, the gases cooled and grew denser till the threshold for nuclear reactions was reached and the first stars 'turned on'. Present estimates put this epoch of first light in the range $20 > z > 6$, though this remains to be confirmed (e.g. Ellis et al. (2001), Kneib et al. (2004)). The progression from first stars to first star forming galaxies, if such a distinction could be made, was rapid. In the Λ-CDM picture, these proto-galaxies merged and built the stunning variety of visible bound structures we observe, massive elliptical galaxies, galaxy groups up to the scale of galaxy clusters, an example of which, Abell 2218, is seen on the bottom panel of Figure 1.1.

Observations and simulations show that galaxy clusters, residing at the upper end of the mass hierarchy, with mass $\geq 10^{14}$ M$_\odot$, are dominated by dark matter.

In a survey of 72 low redshift clusters as part of the Cluster Infall Regions in the Sloan Digital Sky (CIRS) survey, Rines and Diaferio (2006) found that the mass distribution is well fit by either a NFW (Navarro et al., 1997) or a Hernquist profile (Hernquist, 1990), both of which describe dark matter density distributions. At the other end of the mass scale, the observed mass to light ratio of galaxies, M/L$\sim$ 5 indicates that the visible baryonic matter, gas and stars, contributes a significant fraction of the mass; early type galaxies show a higher ($\sim$ 10) value (Freeman, 2001), indicating a larger dark matter component. The distribution of mass in early type galaxies, determined from lensing analyses, shows that they are well fit by a single power law ellipsoidal profile. Results from a joint strong lensing and stellar dynamics analysis for 15 early type galaxies at z $\leq$ 0.33 from the Stong Lensing in Advanced Camera for Surveys (SLACS, Koopmans et al. (2006)), show that the density profile, $\rho \propto r^{-\gamma}$, with $\gamma = 2$, indicative of an isothermal instead of NFW-like distribution. The mean dark matter mass ellipticity within the Einstein radius is 0.78; more importantly, they find that there is remarkable alignment between the light and mass distribution. Within the Einstein radius, the contribution of dark matter to the total mass is only 25%, indicating that the inner core is baryon rich while the dark matter is dominant only at larger radii. These results are consistent with results for 5 early type field galaxies at higher redshift ($0.5 < z < 1.$) in the Lenses Structure and Dynamics survey (Treu and Koopmans, 2004). In addition, the lens model for the spectacular double Einstein ring, SDSS J0946+1006, where the deflector is an early type galaxy at z=0.22, gives similar values for the power law slope of the density profile as well as ellipticity (Gavazzi et al., 2008), indicating that the distributions of mass at the scale of galaxies are clearly different from the NFW-like distributions observed in clusters. The interaction of baryons are a likely cause of these observed differences.

In the hierarchical Λ-CDM model, galaxy groups are assembled from field galaxies, such as those studied in SLACS. If this were the case, it is unclear if the density

profile of the group would match that of the dominant central galaxy or if it would appear as a smoothed out version of the contributions of all the group members. On the other hand, the CDM model also predicts that the dark matter distribution should be similar over a wide range of virialised mass (Navarro et al., 1997). Under this assumption, galaxy groups should represent the lower mass end of clusters and scaling relations, such as the X-ray luminosity-temperature (L_X - T) relation, should be the same for both classes of objects. For local clusters, the observed relation, expressed as $L \propto T^{\alpha}$, gives $\alpha = 2.64 \pm 0.27$ (Markevitch, 1998). It is interesting to note that this value is much higher than a naive CDM prediction, $\alpha = 2$, which does not take into account radiative cooling of the intracluster gas or heating by super novae and AGN feedback; this highlights the importance of including baryonic contributions toward not only the mass budget but also its distribution as a function of radius in virialised structures. The observed slope of the L_X - T relation for galaxy groups is much steeper, $\alpha = 4.9 \pm 0.8$, estimated from 24 X-ray bright galaxy groups (Helsdon and Ponman, 2000). Mulchaey (2004) cautions however that in this comparison of cluster and group properties, aperture effects have to be accounted for, since the observed properties of groups are obtained from a smaller aperture relative to the virial radius; results from the Group Evolution Multiwavelength Study (GEMS) find that the slope estimated from 60 groups does match the cluster value (Osmond and Ponman, 2004). In addition, a recent compilation of results taken from several surveys for groups and clusters shows a closer agreement in the slopes (Fassnacht et al., 2008). On the other hand, Hartley et al. (2008) find that in their recent large hydrodynamical simulation (matching the Millenium Simulation (Springel et al., 2005) in number of particles and volume), mergers drive clusters both along as well as below the L_X - T plane; though they do not specifically discuss galaxy groups, the higher merger rate in the group environment may be expected to have a similar and stronger effect on their X-ray luminosities as well.

To summarize therefore, galaxy groups fall in an important transition range in

mass between massive field galaxies, governed by baryonic processes, and clusters, which are dark matter dominated. It is still unclear how the mass distribution and M/L ratio of groups fit within the evolution from galaxy to cluster scales. There are several other reasons that call for detailed studies of galaxy groups. More than 60% of the galaxy population reside in groups. Active mergers in the group environment have a strong effect on the star formation rates in the member galaxies (Silk, 2004); ongoing episodes of such merger induced star formation have a strong effect on the M/L ratio of galaxy groups. In a model comparison of the properties of virialised objects of different halo masses in various cosmologies, Marinoni and Hudson (2002) find that, for Λ-CDM, the M/L ratio increases monotonically with X-ray luminosity as $L_X^{0.5}$ for the range of mass from poor groups, M=10^{13} $M_\odot$, to that of rich clusters, 10^{15} $M_\odot$. Interestingly, Marinoni and Hudson (2002) find that the slope of the power law relation between optical and X-ray luminosities shows a clear break at a mass scale corresponding to that of a poor group, (consisting of ≤ 5 L_* galaxies, with Milky way scale mass). Whether this break is observed will be interesting to determine and interpret.

These unresolved issues related to density distribution in galaxy groups and their relation to clusters, which are discussed above, have initiated several large observational surveys, e.g, GEMS (Osmond and Ponman, 2004), X-ray Multi-Mirror Large Scale Structure Survey, XMM-LSS (Willis et al., 2005), XMM/IMACS (XI) Group Project (Rasmussen et al., 2006) as well as studies using galaxy group catalogs detected in public wide field surveys, such as the SDSS DR5 (Tago et al., 2008) and the 2dF (Tago et al., 2006). These reasons are also the prime drivers behind our work and we have initiated observations using our catalog of *lensing* galaxy groups and clusters. Given the strong constraints the SLACS were able to derive on the distributions of visible and total mass in the early type galaxies by combining strong lensing with mass estimates from stellar dynamics (GLAS-II), our proposal is to extend this methodology to observations of the galaxy groups

in our catalog. The dynamical mass we estimate is from the observed LOSVD of the member galaxies. It must be mentioned that our contribution fits with a larger multi-wavelength survey undertaken by our SL2S collaborators. Details of the collaboration as well as a list of observations already underway or planned for the near future are listed in the following section.

1.4 Strong Lensing Legacy Survey (SL2S)

The Strong Lensing Legacy Survey (SL2S) is an international collaboration of researchers interested in the various applications of gravitational lensing, both strong and weak, to address questions in cosmology. The research is directed principally on observational aspects, though there are substantial contributions on the theoretical side as well as on the development of tools for data analysis and lens detection. At present, the observations are exclusively follow-up programs of strong lenses found in the public releases of the Canada France Hawaii Telescope Legacy Survey (CFHT-LS) imaging, from both the Deep and the Wide components. Extension to future space and ground based surveys is a natural evolution. Details of the collaboration as well as the lens catalogs, descriptions of the ongoing observational programs as well as listings of the publications from this work may be found at the SL2S website[§] and are also summarized by Cabanac et al. (2007).

Amongst the several avenues of research being pursued by the members of the collaboration, for the project focussed specifically on building a comprehensive mass map of galaxy groups, using the sample of *lensing* clusters and groups in the SL2S catalogs, we have initiated a multi-wavelength observational campaign consisting of:

- – Deep multicolor imaging available from CFHTLS

[§]http:www-sl2s.iap.fr

- – HST/ACS and WFC2 (following the failure of ACS) imaging for arcs properties/lens modeling (Kneib, J-P (PI), Cycles 15 and 16),
- – X-ray imaging (XMM-LSS covers CFHTLS-W1 and Chandra/COSMOS, the CFHTLS-D2); submitting an XMM proposal for the candidates in the other fields is planned.
- – Near-IR imaging for the stellar mass of the groups.
- – Optical or Near-IR spectroscopy to confirm the redshifts of the lensed galaxies (sources).

With Gemini MOS spectroscopy, our contribution to this suite of observational data is the estimate of the dynamical mass from measured kinematics of select member galaxies ($i \leq 21$ mag). The members are also pre-selected for observation using CFHTLS colors or photometric redshifts, if available. As part of these spectroscopic programs, we also confirm the redshifts of the sources, when possible. Full details of our objectives as well as the observational strategy are given in Chapter 5. With the combined expertise of our collaboration, we are confident of achieving the objectives of the velocity dispersion work as well as all the broader goals of the SL2S campaign.

Chapter 2

Spatially resolved (IFU) spectroscopy of CFRS03+1077, a gravitationally lensed galaxy at $z = 2.94$

2.1 Introduction

Our principal research goal is to understand the role of baryonic processes in the evolution of star forming galaxies in the early universe ($z \geq 1$). The summary of published literature given in Chapter 1 clearly underlines that spatially resolved observations of individual galaxies at high redshift are essential to provide us with this knowledge. Carrying out detailed observations on these high redshift galaxies is extremely challenging at the current state of observational technology. We have addressed this observational challenge by devising an innovative technique, which combines spatially resolved spectroscopy with the magnification boost from gravitational lensing, and thus achieve detailed observations of galaxies even at $z \sim 2 - 3$.

We tested the viability and scope of our technique in a pilot observation of a confirmed, gravitationally lensed, star forming galaxy, $CFRS03 + 1077$, (here-

after CFRS03), at a redshift of 2.94. Spatially resolved spectra of the galaxy were obtained using the Integral Field Unit (IFU) on the Gemini North spectrograph, GMOS-IFU. This chapter focusses on these pilot observations, describing in detail the instrumentation used, the data processing and analysis techniques developed specifically for this work as well as the results and experiences we gathered from this study. Subsequent chapters describe the progress and current results from the survey mode observing strategy we have initiated based on this pilot study.

Finally, we wish to point out that we initiated our pilot study of spatially resolved spectroscopy of lensed high redshift galaxies at the same time as a similar project by Swinbank et al. (2003) (discussed in Chapter 1), but unaware and independent of each other. It is reasonable to assume that the commissioning and availability of the GMOS-IFU during the Gemini Telescope 2002B observing semester, during which both observations were carried out, brought about this coincidence. Our objective was to study galaxies at much higher redshift ($z \sim 3$) than the emission line galaxies at $z \sim 1$ which Swinbank et al. (2003) successfully observed.

The chapter is arranged as follows: in Section 2.2 we describe our target, the gravitational lens, CFRS03, using results from earlier published observations. We include a discussion of the outstanding questions that motivated our GMOS-IFU observations as well as additional objectives we aimed to achieve in Section 2.3. Since the GMOS-IFU is key to our chosen observational method, a pertinent description of its construction and operation are given in Section 2.4. The specific IFU configuration we had chosen to achieve these goals and details of our observing program are provided in Section 2.5. Data reduction results using the Gemini IFU pipeline are set forth in Section 2.6, highlighting the presence of appreciable sky subtraction residuals. The characterization of the IFU we undertook to isolate the cause of these residuals is set forth in Section 2.7, along with a description of the correction method we devise for scattered light, which we find is the principal cause of these residuals. The final data cube incorporating the scattered light correction

is presented in Section 2.7.4 along with the extracted and co-added spectra of the elliptical galaxy and the lensed high redshift star forming galaxy. We turn to our objectives and address the question about the existence of a counter image in Section 2.8. For the measurement of the velocity dispersion of the elliptical galaxy, we devise and implement our own approach using direct fitting based on Singular Value Decomposition. The motivation for our approach and details of implementation, the characterization and calibration against published velocity dispersion results compose the bulk of Section 2.9. We then successfully apply our method to the elliptical galaxy of CFRS03 in Section 2.10. We summarize and discuss the results from all these sections in the concluding Section 2.11, along with planned improvements and proposed direction for future observations.

2.2 The gravitational lens, CFRS03

The chosen target for our pilot GMOS-IFU observations was the confirmed gravitational lens, CFRS03, (α = 03:02:30.9, δ = 00:06:02.1), in which a star forming galaxy at $z = 2.94$ is gravitationally lensed into an arc of length $3''$ by a foreground elliptical galaxy at $z = 0.94$, as seen in the HST image, Figure 2.1, (Schade et al., 1995). CFRS03 and another gravitational lens, $CFRS14.1311$, were discovered serendipitously by Schade et al. (1995) from HST imaging of a set of high redshift field elliptical galaxies selected from the Canada France Redshift Survey (CFRS) (Lilly et al., 1995). With follow up CFHT long slit spectroscopy, Crampton et al. (2002) obtained the redshift of the source and thus confirmed CFRS03 as a bone fide gravitational lens system; the deflector redshift was already known from the earlier CFRS MOS observations (Hammer et al., 1995). Pertinent details of the lens and source gathered from the CFRS MOS spectroscopy, the HST imaging and the CFHT long slit observations (Schade et al., 1995, Crampton et al., 2002) are summarized in Table.2.1 for reference.

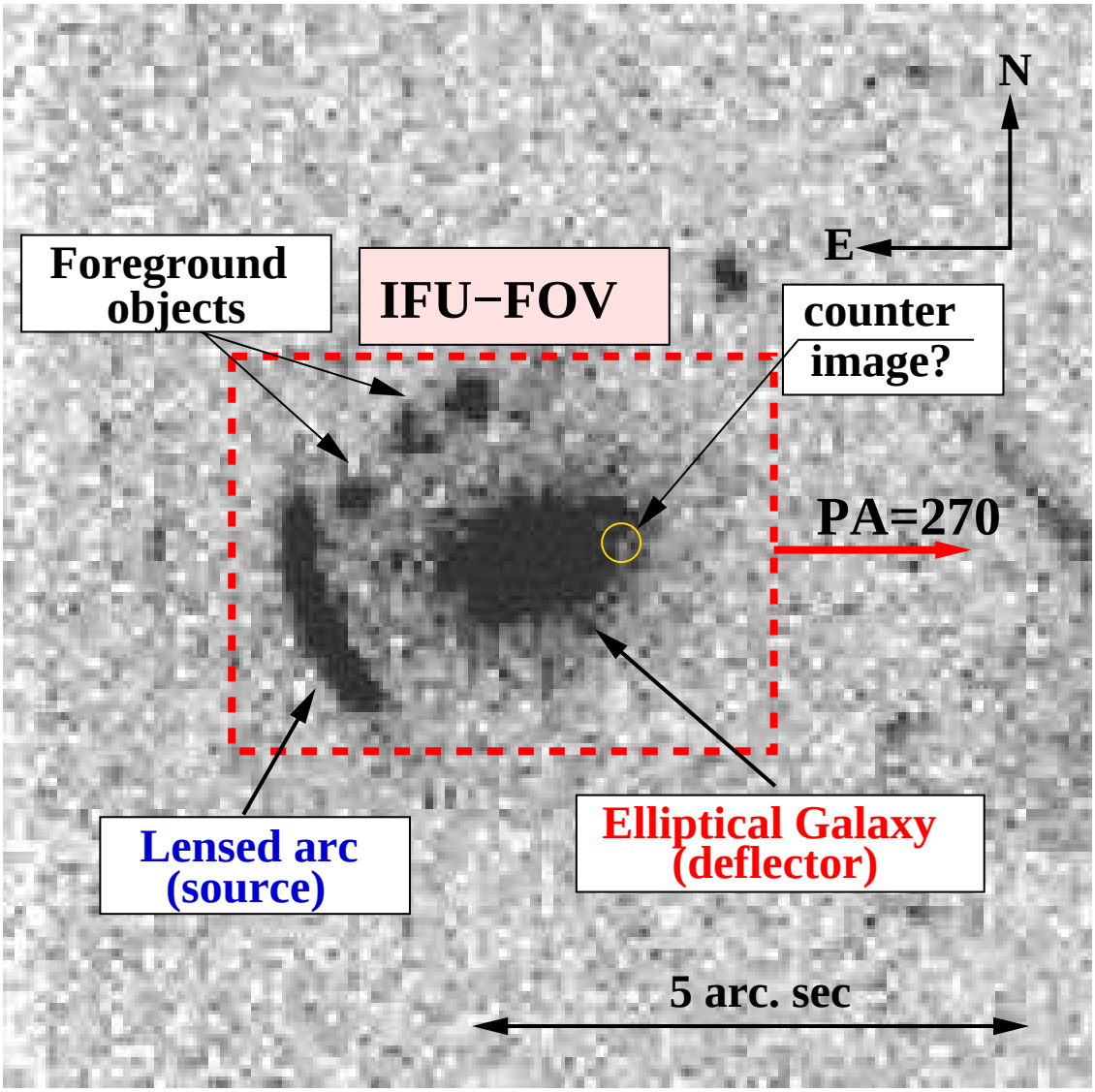

Figure 2.1: HST F814W image of our target, CFRS03+1077, showing the gravitationally *lensed arc* image of a star forming galaxy at $z = 2.94$ and the foreground *elliptical galaxy* at $z = 0.94$ which is the deflector; three unrelated objects in the field are also indicated. The likely location of the counter image, as identified with a lens model by Crampton et al. (2002), is indicated by the yellow circle. The overplotted GMOS-IFU $3''.5 \times 5''$ field of view (red dashed lines) at the chosen orientation (PA=270°) clearly covers both the lensed arc and deflector within one pointing

Table 2.1: Measured properties of CFRS03+1077

Deflector		**Source**	
Elliptical Galaxy		Star forming galaxy	
Redshift	0.938	Redshift	2.941
I_{AB}	20.36mag	μ_i	$21.2\,\mathrm{mag.arc.sec}^{-2}$
$R_{1/2}$	$1.74''$	Radius	$2''.1$
Ellipticity	0.67	Length	$\sim 3''$

Photometric, spectroscopic and geometric properties of deflector and lensed source in CFRS03, summarized from Schade et al. (1995) and Crampton et al. (2002) for reference.

For our pilot IFU observations, we chose CFRS03 based on results from earlier observations (Hammer et al., 1995, Schade et al., 1995, Crampton et al., 2002) which showed that the redshift of the lensed galaxy ($z = 2.94$), its adequate surface brightness ($\mu_i = 21.2\,\mathrm{mag.arc.sec}^{-2}$) and the proximity of the lensed image to the deflector galaxy (arc radius $= 2''.1$) made it an ideal test for our observing technique. In addition, the relative brightness of the elliptical galaxy ($i_{AB} = 20.36\,\mathrm{m}ag$) and the strength of the spectral absorption features were adequate for also measuring its spatially resolved velocity dispersion, which was the main objective of our observing program. These objectives and details of the observations are provided in Sections 2.3 and 2.5 following the description of the target in the following paragraphs.

The CFRS MOS spectrum of the deflector, Figure 2.2 (Hammer et al., 1995), showed an elliptical galaxy at $z = 0.938$ with a strong 4000Å Balmer break and other spectral features typical of an evolved stellar population. The surface brightness in the HST image was well fit by a deVaucouleurs $R^{1/4}$ profile, typical of a relaxed elliptical galaxy (Schade et al., 1995). The CFHT longslit spectrum of the lensed galaxy, Figure 2.3 (Crampton et al., 2002), showed a typical star forming galaxy at redshift $z = 2.94 \pm 0.008$, which was derived by cross correlating against the HST ultra-violet spectra of two local star burst galaxies. The spectrum showed a deep Ly_α absorption trough typical of a star burst galaxy with a flat continuum and

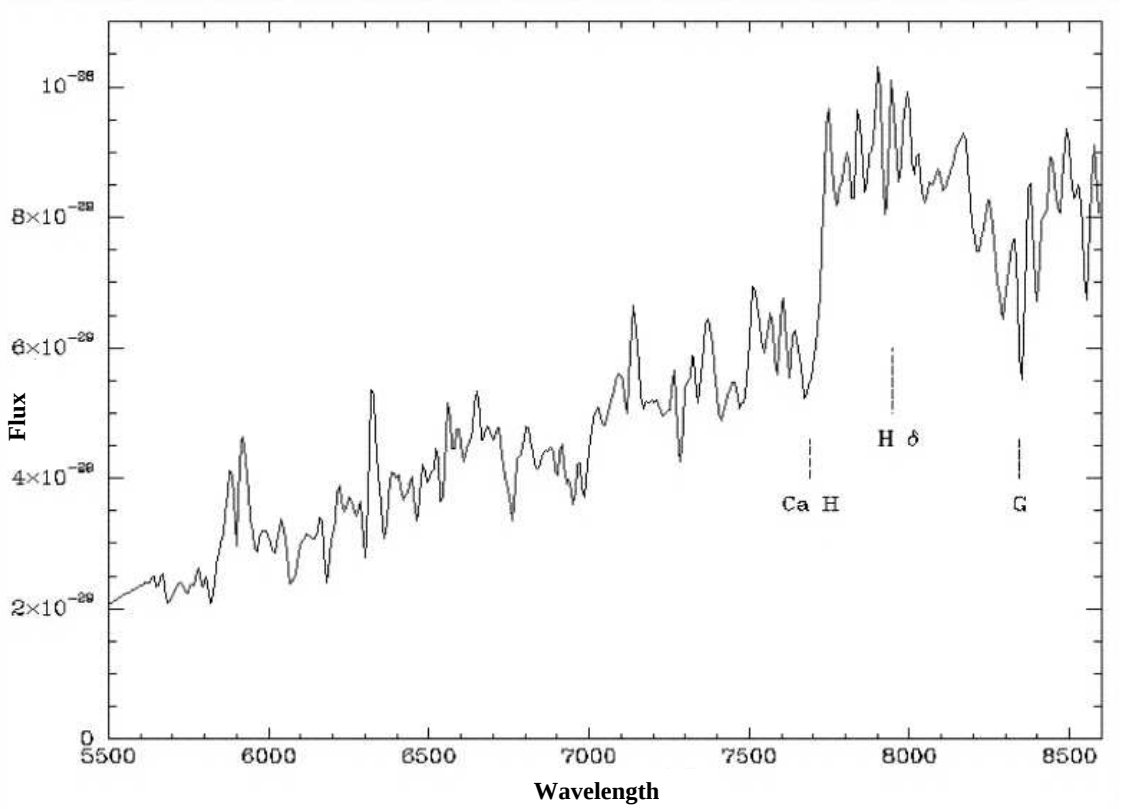

Figure 2.2: CFHT-MOS spectrum (with flux $[ergs/cm^2/s/Hz]$ and wavelength [Å]) of the field elliptical galaxy at $z = 0.94$, which acts as the deflector in the gravitational lens, CFRS03 (reproduced with permission from Crampton et al. (2002)). The spectrum was taken as part of the CFRS. The 4000Å break and other typical spectral features of an early type galaxy are indicated.

several nebular and inter-stellar absorption features, principally Si (1393, 1402), CII (1334), and CIV (1549).

Crampton et al. (2002) used these complementary observations to estimate the mass of the elliptical galaxy from the observed line of sight velocity dispersion (LOSVD), which in turn they derived using two independent methods. First, they used the constraints provided by the positions, orientations and the surface brightness of the lensed arc (along with two *likely* counter-images) in the HST image, to reconstruct the lensing geometry and thus obtain the mass distribution from the

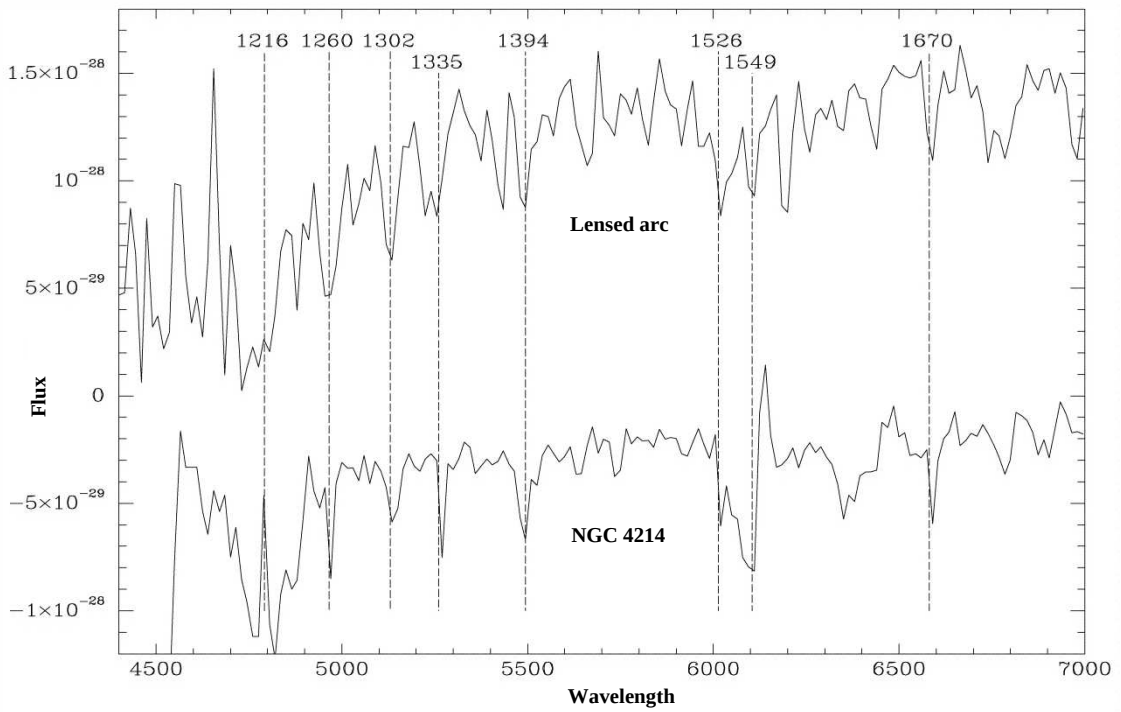

Figure 2.3: CFHT longslit spectrum (with flux $[ergs/cm^2/s/Hz]$ and wavelength [Å]) of the star forming galaxy at $z = 2.94$, which confirmed CFRS03 as a bone fide gravitational lens (reproduced with permission from Crampton et al. (2002)). The star burst galaxy template, NGC4214 is shown to highlight the prominent UV spectral features which confirmed the redshift of the lensed galaxy

best fit lens model. In this, the mass distribution was assumed to be an isothermal sphere, thus described by only two parameters, namely the LOSVD, σ_{los}, and the core radius, r_c; the spherically symmetric mass model was justified in this case because of the simple lens configuration of an isolated field elliptical galaxy acting as the deflector. The best fit values for the mass distribution parameters were $\sigma_{los} = 387 \pm 5\,\mathrm{km\,s^{-1}}$ and $r_c = 2.3$kpc in the rest frame of the galaxy. They compared this mass estimate with the value obtained from the Fundamental Plane (FP) relations for elliptical galaxies in the *local* universe. Using the rest frame central surface brightness, μ_0 and the half light radius, R_e, both measured from the HST image, and the FP relation for field elliptical galaxies in the local universe,

($z \sim 0.02$), from Jorgensen et al. (1996), they obtained the corresponding LOSVD as $380 \pm 60\,\mathrm{km\,s^{-1}}$, which was consistent with their LOSVD estimate from the lens model.

However, they point out that if they also took into account the expected dimming of $\sim$ 1mag in the luminosity of field ellipticals due to passive evolution from $z = 1$ to the present (Schade et al., 1999), the consequent lower μ_0 would correspond to a $\sigma_{los} \sim 214\,\mathrm{km\,s^{-1}}$ in the FP relation. They use this discrepancy in the LOSVD to argue that field elliptical galaxies may have followed very different evolutionary histories. Their hypothesis runs counter to the passive evolutionary scenario, and a uniform FP as a consequence, presented by Kochanek et al. (2000) from their study of 30 lensing galaxies. The principal objective of our GMOS-IFU program, described in the following section, was therefore to obtain the spatially resolved LOSVD of the elliptical galaxy from the IFU spectra, constrain the dynamical mass and thus address this important question related to the evolution of elliptical galaxies.

2.3 Objectives of the IFU observations

The science goals of our pilot GMOS-IFU observations focussed on three areas, -1- Fundamental Plane studies of field elliptical galaxies, -2- evolution of star forming galaxies at high redshift, ($z \sim 3$), from spatially resolved spectroscopy of gravitationally lensed images and -3- identification of the positions of the counter images of the lensed source, which are expected in such a strong lens geometry; the locations would help constrain the lens model and thus the mass distribution of the CFRS03 gravitational lens system.

Of these, the principal objective was to derive the LOSVD of the elliptical galaxy, which was the 'deflector' in CFRS03 and thus test the hypothesis of Crampton et al. (2002) that elliptical galaxies may have followed different evolutionary paths in their

mass assembly than what has been predicted by the Fundamental Plane relation alone, as explained in Section 2.2.

During these observations, the IFU was oriented so that the lensed arc too was well within the field of view, as shown in Figure 2.1. The spectrograph, configured principally for the velocity dispersion measurement of the elliptical galaxy, still permitted us to obtain the rest-frame UV spectrum (1380 - 2100Å) of the lensed galaxy, with which we aimed to achieve the following objectives related to high redshift star forming galaxies:

1. measure velocity offsets in the observed stellar absorption lines in different regions of the lensed image; transform these velocity offsets, indicative of stellar kinematics, to rest frame values with a lens model and thus estimate the mass distribution in this high redshift galaxy ,

2. estimate the speed of starburst-induced outflows by comparing the velocity differences between stellar and interstellar absorption lines and nebular emission lines (if any are observed); the outflow rates would permit us to estimate rates of mass loss to the intergalactic medium (IGM),

3. estimate the star formation rate from the strength of the UV continuum, and

4. identify PCygni profiles, which are indicative of the presence of massive stars (Pettini et al., 2000), and thus constrain the stellar initial mass function, IMF, in this high redshift galaxy.

Finally, we also aimed to constrain the location of the counter image(s) of the lensed source in CFRS03, and thus refine the lens model. Crampton et al. (2002) had identified two objects seen in the HST image as *likely* counter images since they were located within $0''.03$ of the positions predicted by their lens model. Our objective was to confirm this spectroscopically since both candidate counter images fell within the IFU FOV; the IFU observations would also permit us to identify

other lensed images by searching for anomalous spectral lines in the spectrum of the elliptical galaxy but corresponding to the redshift of the source. Identifying the counter images would add strong constraints on the lens model and thus help de-lens the image and reconstruct the intrinsic properties of this $z \sim 3$ galaxy.

2.4 Description of the GMOS-IFU

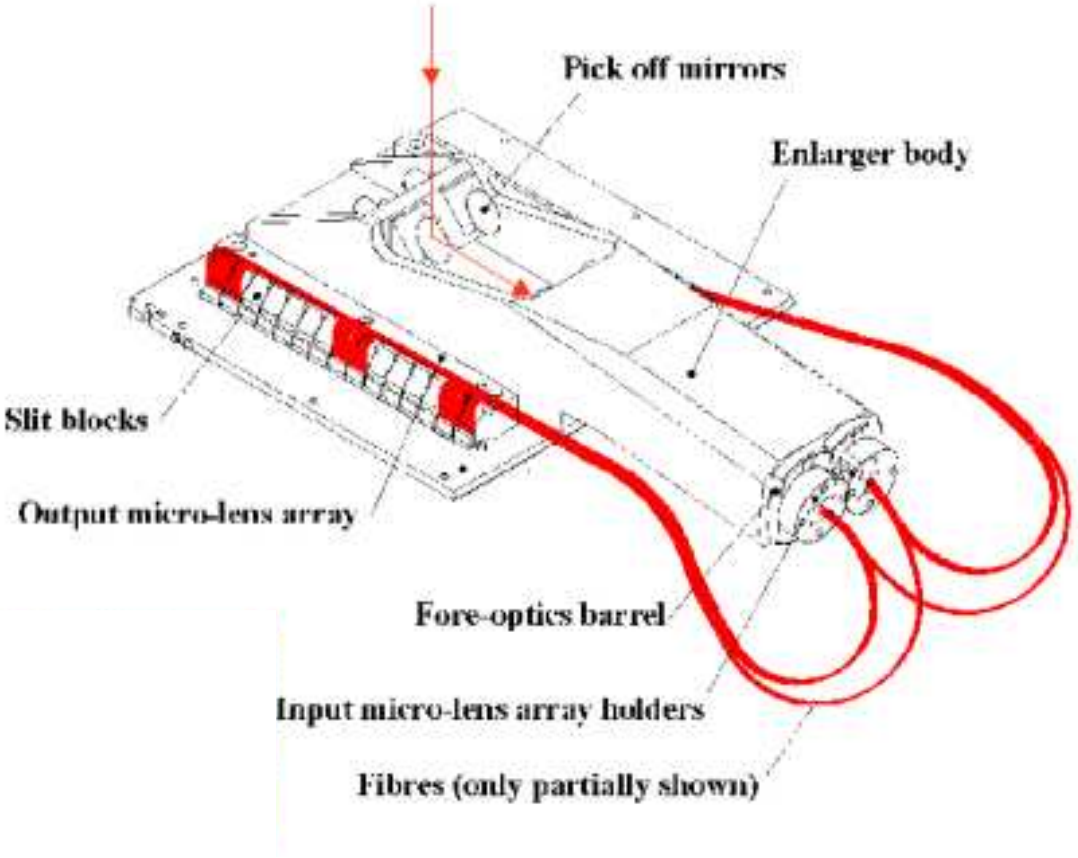

Figure 2.4: Constructional details of the GMOS-IFU showing the input pick-off mirrors, the science and sky fields (within the Enlarger body) and the re-formatted fibers forming the two pseudo-slits, one on each side of the main body. (*Reproduced with permission from Gemini Telescope Facility*)

For our pilot spatially resolved spectroscopy, we utilized the then recently com-

missioned GMOS-IFU (Aug 2002 - Jan 2003 observing semester) on the Gemini North telescope. The Integral Field Unit (IFU) provides the added capability of spatially resolved spectroscopy to the Gemini Multi-Object Spectrograph (GMOS). The GMOS is the optical imager and spectrograph on the Gemini North and South telescopes and is designed for broad band and narrow band imaging as well as longslit and multi-object spectroscopy (MOS). For observing programs requiring spatially resolved spectroscopy, the IFU is inserted into the incoming light beam (in the place of a MOS mask) at the front of end of the spectrograph. The design of the IFU, (see Figure 2.4) uses two pick-off mirrors at the focal plane of the telescope to direct the incoming light beam on to two corresponding rectangular arrays of lenslets; corresponding bundles of optic fibers behind the lenslet arrays pick up the light beams and reformat them into two pseudo-longslits for dispersion by the grating arrangement in the spectrograph (Figure 2.5).

The two arrays contain a total of 1000 lenslets arranged in regular rectangular grids. The corresponding optic fibers are packed in fiber blocks of 50 fibers each. The IFU is thus capable of providing 1000 independent spectra with a spatial sampling of $0''.2$ from a fixed $5'' \times 7''$ patch of sky (called the *science field*) within the larger $5'.5 \times 5'5$ field of view of the GMOS. For sky subtraction, a set of 500 fibers, identical to those used for the science field, is arranged to map a $3''.5 \times 5''$ patch of blank sky, called the *sky field*, at a distance of $1'$ from the science field. The orientation of the IFU has to be carefully chosen during the preparation of the observing program to ensure that the sky field is free of faint objects; this is done using sky catalogs or any available previous imaging. The science and sky fibers are inter-leaved within the two pseudo-longslits (called *blue* and *red* slits, shown schematically in Figure 2.6) to avoid systematic distortion or losses due to the optical elements. In the pseudo-slits, the fibers from either two or three science blocks are bracketed by blocks of sky fibers. With this arrangement of fibers, the dispersed spectra form two columns of 750 spectra each on the CCD, as seen in Figure 2.7; as

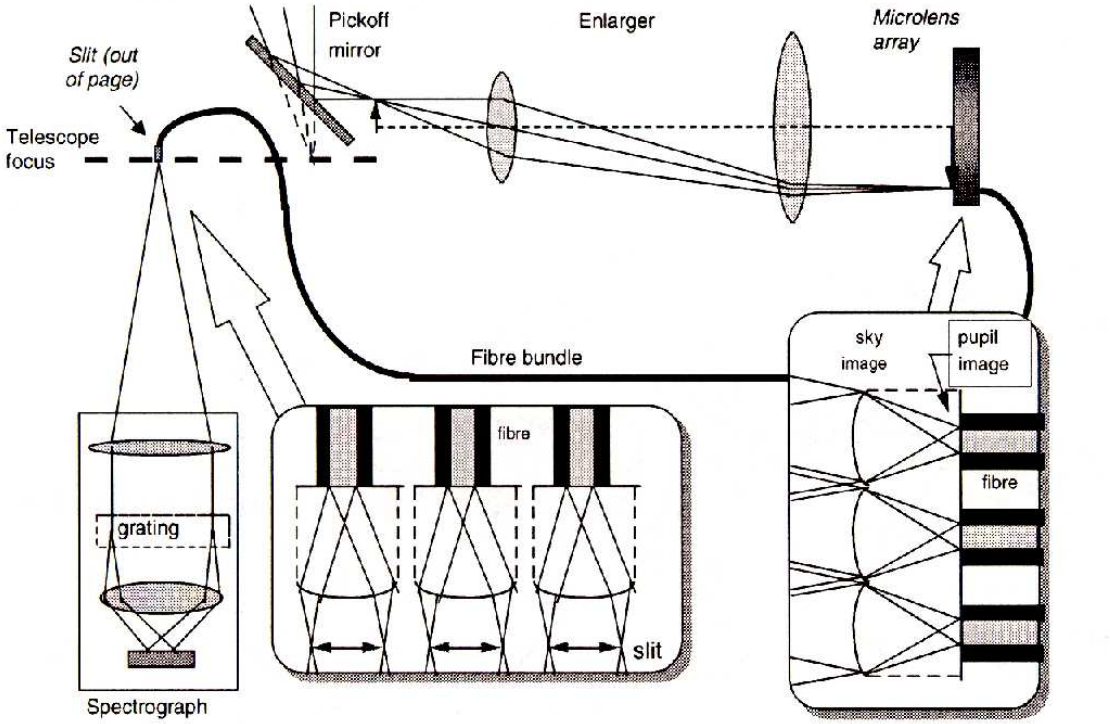

Figure 2.5: Cross-sectional view of the GMOS-IFU, showing the fiber layout from the enlarger body to the pseudo-slit (Allington-Smith et al., 2002). The dispersion arrangement with the grating and the CCD, both of which form part of the GMOS spectrograph, are also schematically shown. (*Reproduced with permission from Gemini Telescope Facility*)

in the pseudo-slits, the science spectra are bracketed by the sky spectra, thus reducing instrumental errors in sky subtraction. In the 'IFU 2-slit' mode, each spectrum can use only half the width of the CCD and an order sorting filter is necessary to avoid spectral overlap. However, when observing small targets, as in the case of CFRS03, half the science and sky fields may be masked off at the entrance pupil; in this 'IFU 1-slit' configuration, the science FOV is reduced to $5'' \times 3''.5$ but the permitted spectral length on the CCD is consequently doubled. It must be pointed out that due to the interleaving, adjoining spectra on the CCD may not necessarily

correspond to contiguous patches on the sky; the reduction pipeline therefore uses a CCD-to-sky map to reconstruct the observed science field.

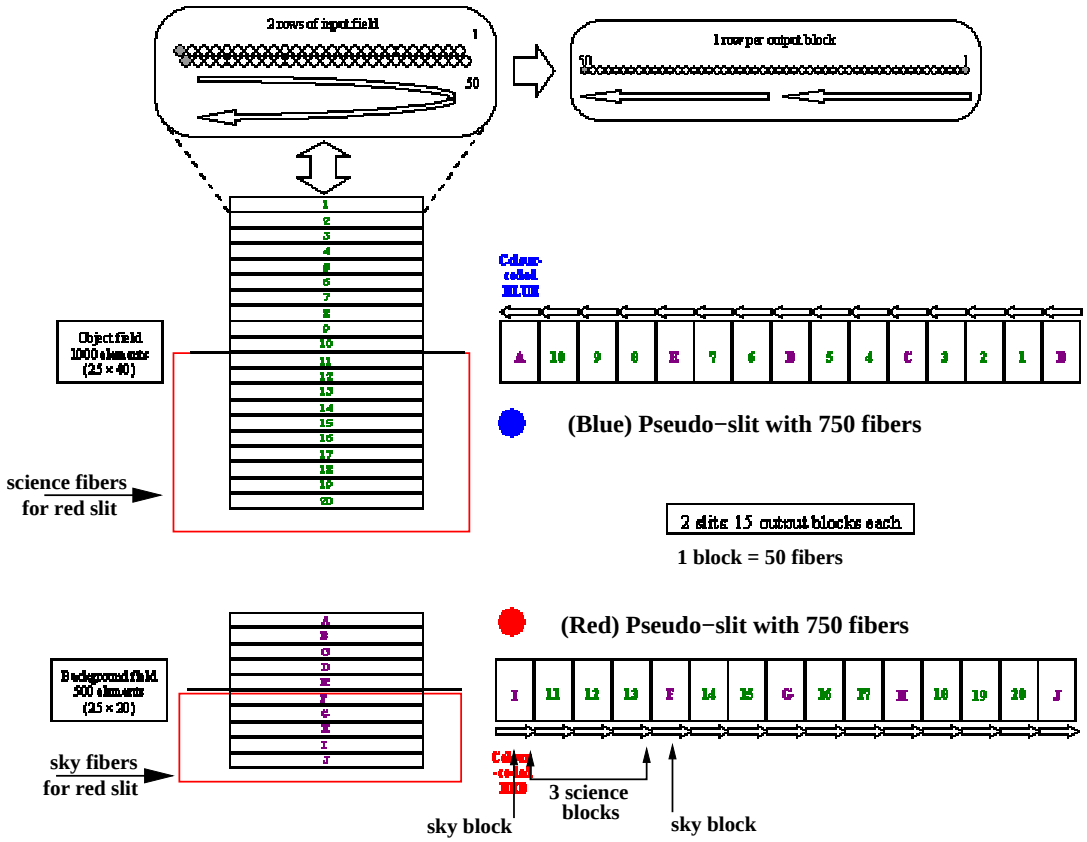

Figure 2.6: Schematic of the mapping of the optic fibers from the input science and sky fields to the two pseudo-slits of the IFU; highlighted regions show the science and sky regions used in the 1-slit mode (*Reproduced with permission from Gemini Telescope Facility*)

With this design, the IFU user may access all the grating and filter combinations available in the GMOS, provided care is taken to avoid spectral overlap while in the 2-slit mode. The effective width of the IFU pseudo-slits is $0''.31$ which gives a spectral resolution of 1080 to 7100, depending on the chosen grating. A complete description of the construction of the GMOS and the design characteristics of the

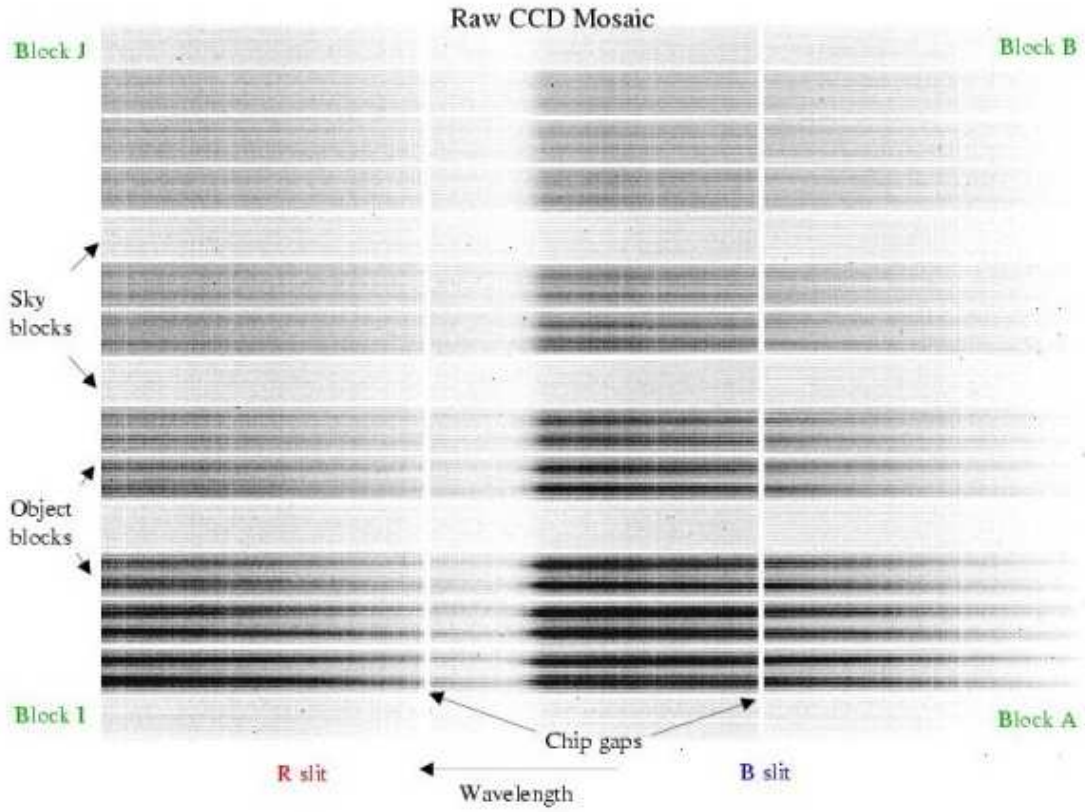

Figure 2.7: Placement of the 1500 spectra (1000 science + 500 sky) from the 'red' and the 'blue' pseudo-slits on the 3-chip GMOS CCD; the chip gaps are also shown. (*Reproduced with permission from Gemini Telescope Facility*)

gratings, filters and the CCDs may be found at the Gemini Telescope website *, from where Figures 2.4 - 2.7 are reproduced. The Gemini reduction pipeline for GMOS-IFU data and the changes we implemented to improve sky subtraction are discussed in Section 2.6.

*http://www.gemini.edu/sciops/instruments/gmos/gmosIndex.html

2.5 GMOS-IFU Observations of CFRS03

The principal focus of our GMOS-IFU observations (Gemini North program GN-2002B-Q-22, PI D.Crampton) was the elliptical galaxy, as set forth in Section 2.3; however, the IFU 1-slit field of view was large enough to fit the lensed arc (the source) completely, see Figure 2.1, thus providing us with data for the additional science goals related to the lensed star forming galaxy as well.

For the CFRS03 observations we used the GMOS-IFU with the R400 grating set at central wavelength, $\lambda_c = 8630$Å, and the OG515 order sorting filter with passband, $\lambda \geq 6150$Å. The chosen grating setting with on-chip 2x spectral binning provided a spectral resolution, $R = 1547$ at the central wavelength (corresponding to a velocity resolution of $100\,\mathrm{km\,s^{-1}}$ in the rest frame of the elliptical galaxy). Eight exposures each of 1800s were taken for a total on-source integration time of 14.4ksec. After the first set of four exposures, the grating was dithered by 50Å to $\lambda_c = 8680$Å to cover the gaps on the three-chip GMOS CCD (seen in Figure 2.7); during each set of four exposures, spatial dithers of $0''.1$ in a grid pattern were used to compensate for the throughput variation across the cross-section of each fiber. All standard calibrations including observations of the spectro-photometric flux standard G191B2B were taken.

2.6 IFU data Reduction

Initially we used the standard Gemini GMOS-IFU pipeline to reduce, flux calibrate and combine the separate science exposures into a single 3D data cube; details of the steps involved in the reduction process are provided in the following section. Systematic analysis of the final data cube indicated a higher than expected level of residuals from the sky subtraction; the assessment methods used and quantitative values of the residuals are given in the following section. Efficient sky subtraction is crucial for improved S/N in these spatially resolved, spectroscopic observations of

low surface brightness targets. Therefore, in order to understand the source of the residuals and to improve sky subtraction, we systematically characterized the data reduction process and developed an in-house reduction script, designed to work in conjunction with the Gemini pipeline. We present the standard Gemini IFU reductions in the next subsection, followed by a description of the characterization of the IFU in Sections 2.7.1 - 2.7.3, and then the improvements we incorporated and the resulting 3D cube in Section 2.7.4.

2.6.1 Gemini IFU pipeline reduction

The Gemini reduction package is a set of Subset Preprocessor (SPP) scripts designed to use available IRAF tasks and work as an external package within IRAF. Only those tasks related to our reductions are discussed, where necessary; complete details on the construction and use of the Gemini reduction package may be found at the Gemini Telescope website [†].

In the Gemini pipeline, each IFU science exposure, composed of three individual FITS extensions for the 3-chip CCD, is bias subtracted, the extensions mosaiced together and then flat fielded using a calibration flat; the calibration flat is taken contiguously during night time science observations so that it may be used as a reference frame to extract the 1D spectrum corresponding to each fiber. Fiber-to-fiber throughput variations are corrected using a normalized twilight flat. During extraction of 1D spectra, the five rows on the CCD corresponding to each IFU fiber are summed together with the option of variance weighting. The extracted spectra are then wavelength calibrated using a standard calibration arc spectrum. For sky subtraction, all the spectra from the sky fibers are combined to form a high signal-to-noise ratio (SNR) master sky spectrum, which is then subtracted from each of the science spectra. In producing the master spectrum, the user is provided the choice of discarding one or more columns of sky fibers, if light contamination from

[†]http://www.gemini.edu/sciops/data/dataIRAFIndex.html

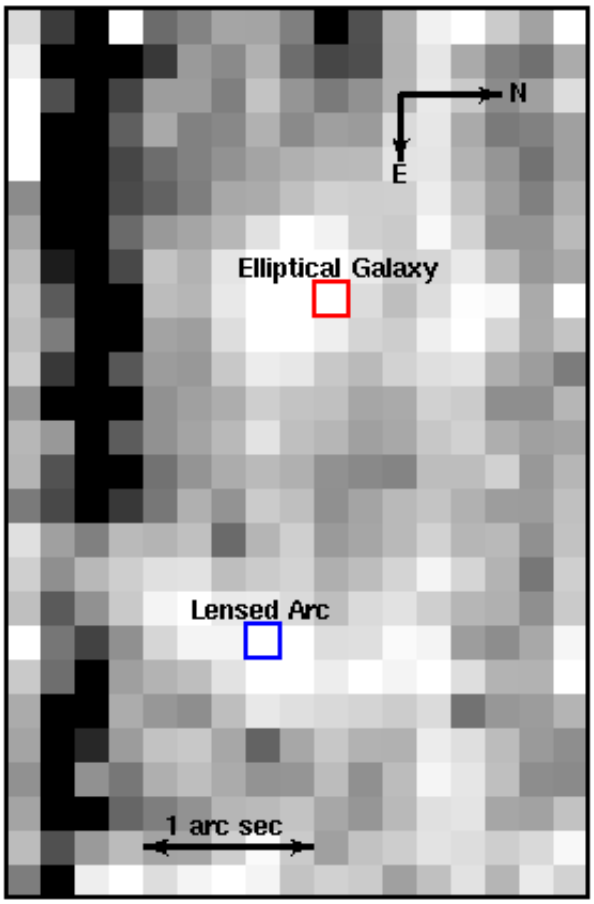

Figure 2.8: White light image of CFRS03 from the co-added 3D cube from the Gemini pipeline reductions. The red square indicates the pixel from which the elliptical galaxy spectrum, Figure 2.9 was taken; similarly the blue square, for the lensed star forming galaxy, Figure 2.10. Fiber blocks which have been over- and under-sky subtracted are seen as the dark and bright bands

an unforeseen faint source in the sky field is suspected. The spectra are next flux calibrated using spectro-photometric standard star observations, if available. The pseudo-slit-to-sky map for the IFU is then applied to re-arrange the spectra, as seen on the CCD, into a 3D data cube, in which two spatial dimensions correspond to the sky positions of the fibers and the third is the spectral direction. Finally, the 3D cubes from all the science observations are combined to improve the overall

SNR.

Figure 2.8 shows the white light image from the Gemini pipeline reduction of the CFRS03 data; the image is made by projecting the co-added 3D cube in the spectral direction, with each pixel corresponding to a $0''.2$ IFU fiber. The locations of the elliptical galaxy and the lensed arc are visible though not delineated as in the HST image (Figure 2.1) not only due to the larger IFU pixel size and seeing effects, but also due to the presence of sky residuals. Spectra extracted from single IFU pixels from the elliptical galaxy and the arc, indicated by the red and blue squares in Figure 2.8, are plotted in Figures 2.9 and 2.10 along with the expected 1σ noise, estimated as the Poisson noise in the corresponding pixels prior to sky subtraction. These two IFU pixels were chosen for illustration since they had the highest flux in the regions corresponding to the elliptical galaxy and the arc in the white light image.

The effect of over- or under-sky subtracted residuals in these sky noise dominated observations is seen in the white light image as bands of dark and white columns respectively; comparison with the HST image, Figure 2.1, shows that these blank sky areas should only have residual flux at the level of the sky noise with no features. These columns of poorly sky subtracted fibers therefore indicate the presence of some systematic effect along the spatial direction of the CCD, since these contiguous IFU pixels correspond to adjacent spectra on the CCD; the IFU fibers are grouped in blocks of fifty as seen in Figure 2.7. In additiion, the comparison of the elliptical and arc spectra with their respective sky noise spectra shows not only pixel-to-pixel variations in the residuals but also a systematic trend in the spectral direction; this is more clearly seen in the low order continuum fits, shown overplotted in the respective figures, where high continuum levels coincide with spectral regions of high sky flux, indicative of the *possible* presence of scattered light.

In order to quantify sky residuals, we carry out a similar comparison using sky subtracted sky spectra in the 5 sky blocks; this avoids any contribution from the

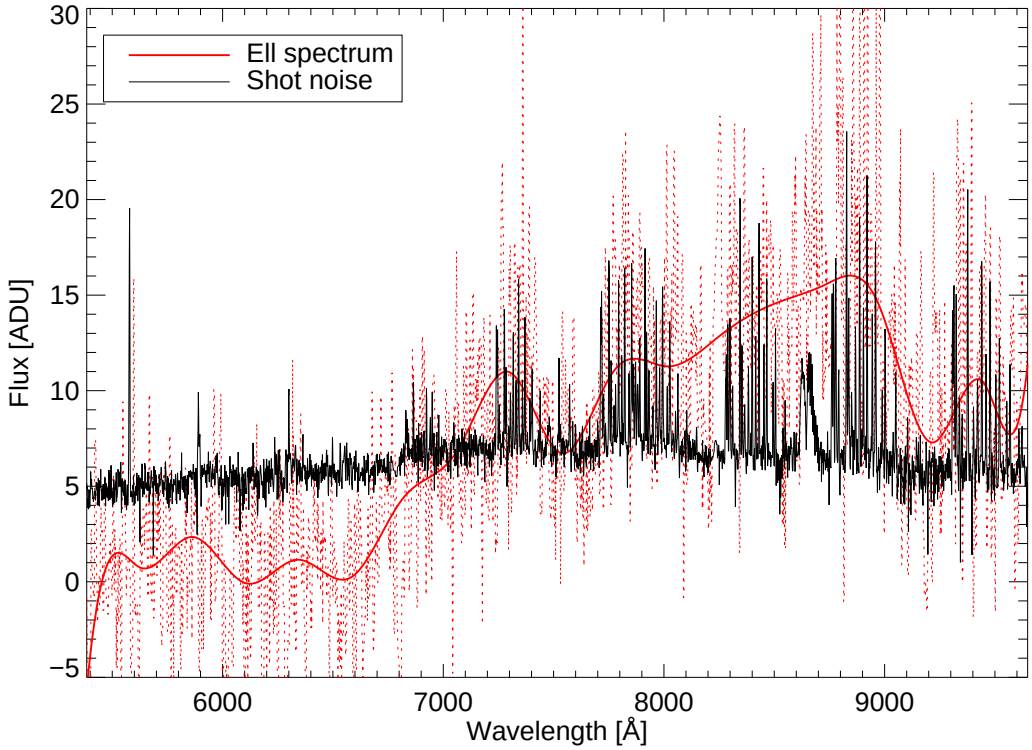

Figure 2.9: Gemini GMOS-IFU pipeline reduced spectrum of the elliptical galaxy at z=0.94, which is the deflector in CFRS03. The spectrum is extracted from a single IFU pixel in the co-added 3D cube, marked in Figure 2.8. Overplotted is a low order continuum fit to illustrate the sky limited nature of these observations, which therefore need good sky subtraction. The expected noise spectrum is plotted to the same scale to show that regions of high residuals coincide with spectral regions of greater sky flux

underlying spectrum of the object being observed. A sample of such an assessment for the Sky Block I (labeled in Figure 2.6) is shown in Figure 2.11, where the median of the fifty sky subtracted sky spectra as well as a continuum fit to the median combined spectrum are compared with the expected noise spectrum (derived from the same fibers prior to sky subtraction). For this sky block, a systematic over subtracted trend in the continuum along the spectral direction is seen. In addition,

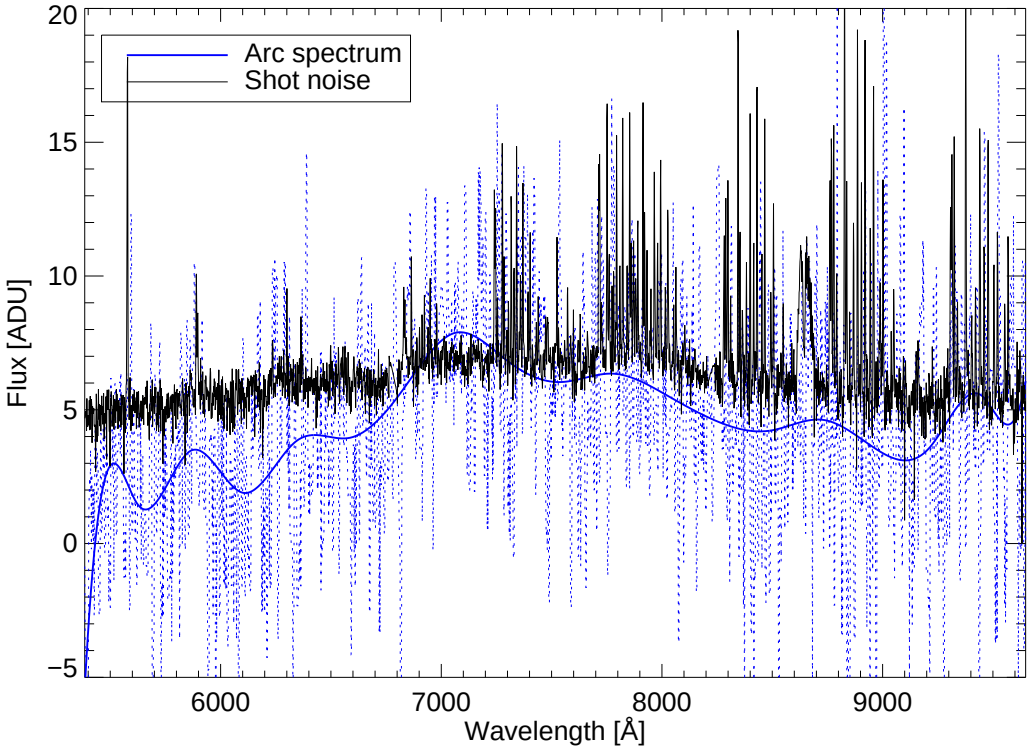

Figure 2.10: Gemini GMOS-IFU pipeline reduced spectrum of the lensed star forming galaxy at z=2.94, which is the source in CFRS03. The spectrum is extracted from a single IFU pixel in the co-added 3D cube, indicated in Figure 2.8; overplotted is a low order continuum fit. The expected noise spectrum is plotted to highlight regions of strong sky residuals and consequent low S/N achieved from these reductions

Figure 2.12, shows a similar continuum fit to the median combined sky subtracted sky spectra in all five sky blocks; the arrow indicates their positions along the CCD (also refer to Figure 2.7). Along with a variation in the spectral direction, a systematic variation in the residuals along the spatial direction of the CCD is clear. Expressing the *relative sky residual* as,

$$R_{sky}(\lambda) = \frac{\mid F_{ss} \mid}{F_{ns}} \tag{2.1}$$

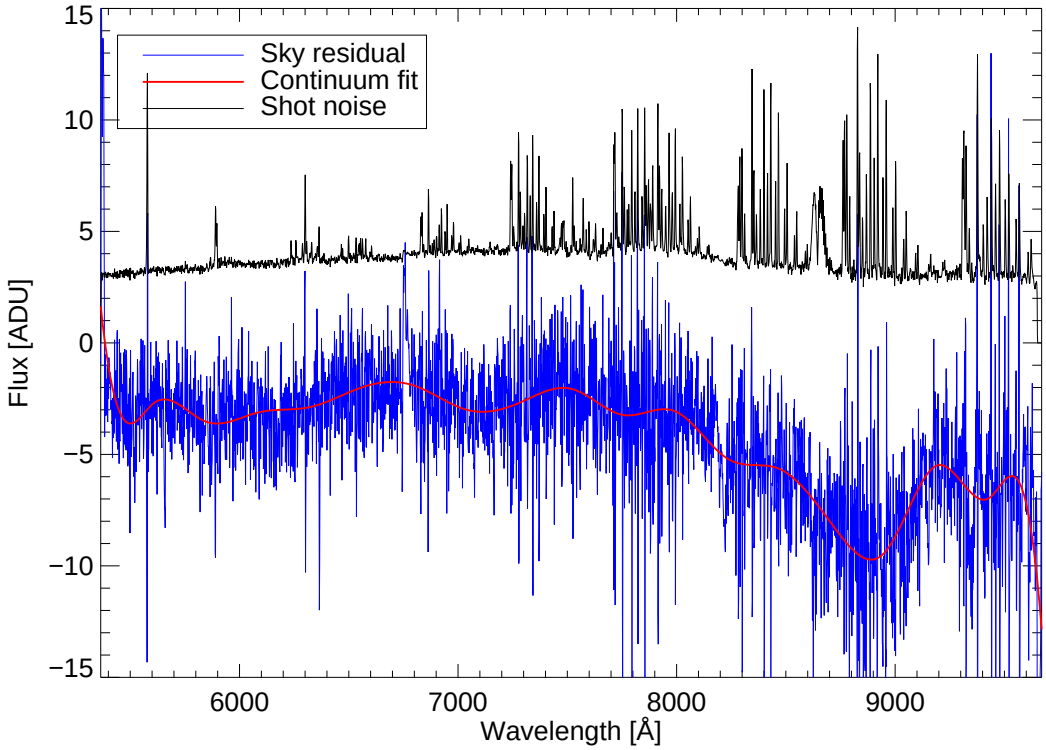

Figure 2.11: Residual flux after sky subtraction in GMOS-IFU pipeline reductions. The sample spectrum shown is the median spectrum of the 50 fibers in Sky Block I after sky subtraction. The expected residual spectrum, which should equal to the Poisson noise of the sky spectrum, is overplotted to highlight the residuals

where, F_{ss} and F_{ns} are the continuum flux (in ADU) in the sky subtracted sky spectra and in the corresponding noise spectra, shown in Figure 2.12; neglecting the contribution from read noise, in the ideal case, this ratio should be 1 and higher values, > 1, measure the contribution of the sky residuals. For the IFU reductions, the relative sky residual values are consistently higher, with the maximum residuals occuring in the fiber blocks, I and J at the top and bottom ends of the CCD; the median value of the residual, as given by Equation 2.1 is 1.5 for these two blocks and decreases to 1.1 for the other sky blocks. Of particular note, the spectral region where the sky residual is high in these spectra coincides with a region of strong sky

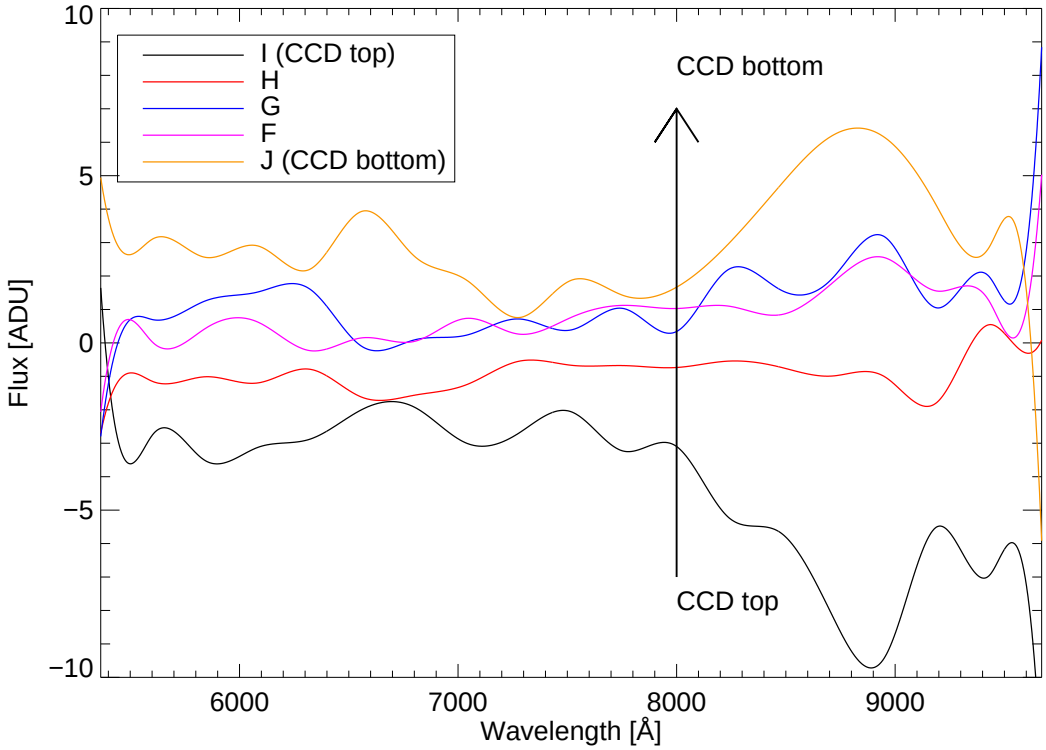

Figure 2.12: Sky residuals measured by sky subtracted sky spectra in the 5 sky fiber blocks; each spectrum is the median combined sky residual spectrum of a block of 50 fibers. The positions of these blocks in the psuedo-slit and correspondingly on the CCD are indicated to show the variation of the scattered light in both the spectral and spatial directions.

lines, which if scattered within the camera will give rise to the strong, featureless sky residual spectra, seen in Figure 2.12.

In order to assess and correct for these residuals, we first carry out a systematic characterization of the IFU in Section 2.7. It must be noted that the 2002B semester, during which our observations were taken, was the first in which the GMOS-IFU was available for queue scheduled observations; the characterization was therefore aimed at improving our understanding of the performance of the IFU as well as that of the Gemini reduction pipeline. Based on these tests, we have de-

veloped and applied an improved sky subtraction procedure to the final reductions described in Section 2.7.4.

2.7 IFU characterization and improved sky subtraction

In the IFU reduction process, sky residuals result from three independent, equally important sources, namely, (i) poor flat fielding, principally inadequate correction for fiber throughput and illumination variations, (ii) differences in the observed wavelengths or the widths (FWHM) of night sky emission lines between individual IFU spectra and (iii) the presence of under- or over- sky subtraction due to scattered light on the CCD. Poor throughput and illumination correction as well as scattered light affect the residual continuum levels while differences in the observed characteristics of the sky lines result in narrow residual features. In the following subsections, we investigate the presence of these three effects individually in the GMOS IFU and their effect, if any, on the reduction process.

2.7.1 Effect of fiber throughput correction

Optic fiber throughput variations result from differences in their intrinsic material properties as well as due to mechanical stresses induced by flexure and fiber packing in the IFU (Barden, 1998). In addition, the placement of the IFU fibers in the casement, seen in Figure 2.5, results in a non-uniform illumination pattern, and thus to differences in the observed flux. To measure and compensate for these unavoidable variations in throughput, the Gemini pipeline uses a calibration twilight flat field. Twilight flat fields are taken at dawn so that the the IFU is illuminated with a uniform light source; the grating and filter settings match those of the observing program for which the flat field is intended. For these twilight flats,

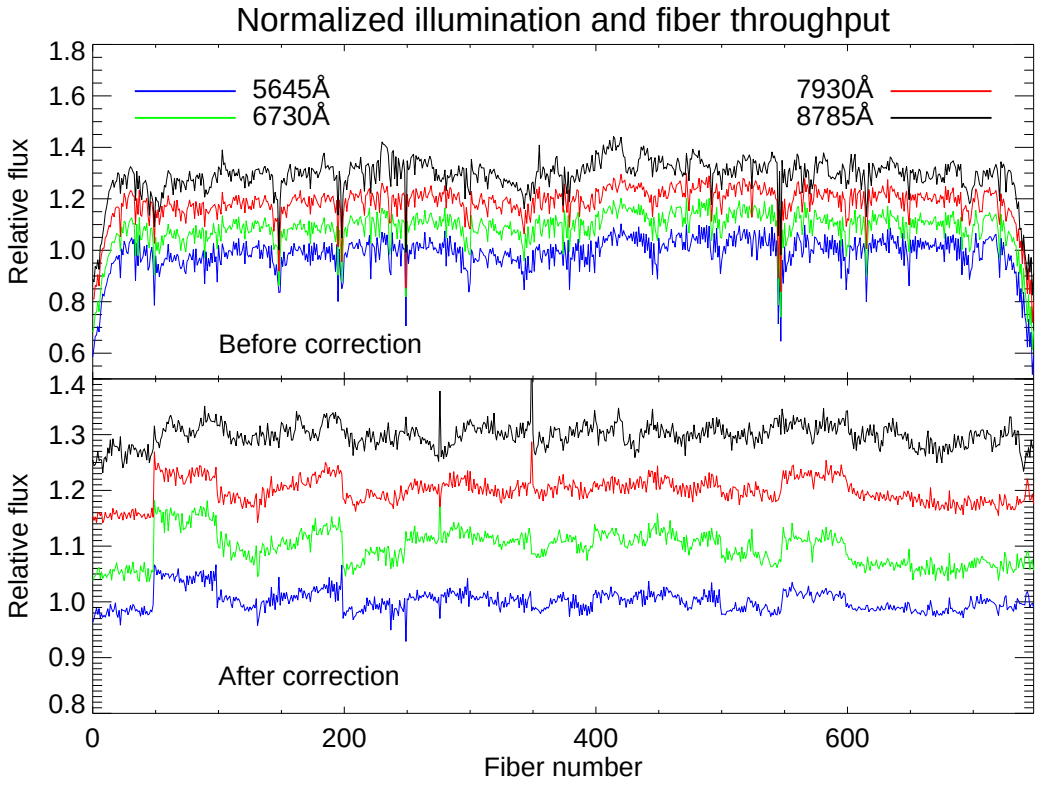

Figure 2.13: Variation in the throughput and illumination of the IFU fibers measured as the normalized total flux in the twilight flat fields, as observed (top panel) and after correction (lower panel). The fiber numbers refer to the order in which they appear in the pseudo-slit and on the CCD. The flux measurement is done in the four wavelength bins indicated, to assess any systematic wavelength dependencies; the plots are offset by 0.1 unit from each other for clarity

after subtracting the bias, the total light throughput from each fiber is measured by projecting the spectra in the spectral direction and normalizing these total flux values with their mean or median value. Figure 2.13, (upper panel), shows the resulting normalized throughput pattern in a typical twilight flat field; in this case, the normalization is done with the median value. In order to test for wavelength dependency, we have carried out the comparison in four spectral bins, distributed from the blue end to the red end in the wavelength range of our observations; the

four plots are offset by 0.1 unit from each other for clarity. The plots show that the throughput is lower by $\sim 40\%$ for the fibers at the top and bottom ends of the CCD compared to the median value, with a scatter of $\sim 10\%$ around the median for the other fibers; however, no systematic wavelength dependency is observed.

In order to compensate for this throughput variation, the *inverse* of the normalized profile, Figure 2.13, is multiplied with the calibration flat field taken with the science exposure; the calibration flat field corrects pixel-to-pixel sensitivity variations. This scaled *master* flat field is used for correcting the science observations for both sensitivity, fiber throughput and illumination variations. To assess the efficacy of this correction, we corrected the twilight flat field with the master flat; the result is shown in the lower panel of Figure 2.13, again estimated in the same four wavelength bins. The median variation in throughput after correction is $\leq 2\%$ with even the maximum difference less than 5%. The higher values of relative sky residuals ($\geq 10\%$) and the spectral dependency seen in Figure 2.12 indicate that improper throughput correction makes only a minor contribution, if any, to the sky residuals.

2.7.2 Spectral line centroid and PSF variations

For effective sky subtraction, the spectrum of the observed object and of the master sky spectrum should be aligned in wavelength and the widths of corresponding sky lines in both spectra should be matched (assuming the spectral flux in both spectra have been matched by the flat fielding, as discussed in Section 2.7.1). Figure 2.14 (upper panel) shows the *observed* positions of two unsaturated lines in the calibration arc spectra for the 750 science and sky IFU fibers. The comparison is shown for two lines, one at the blue end (7272.94Å) and the other at the red end (8667.94Å) of the observed range to test for any wavelength dependency; the plotted ordinate is the relative shift (measured in pixels) of each spectrum measured with respect to the median value. The shifts are significant and are caused by the

characteristics of the grating and by the camera optics. The non-linear spectral shifts are rectified by wavelength calibration using either a calibration arc spectrum or a set of strong night sky emission lines, if present in the observed spectral range. For our observations, the presence of these strong atmospheric *Meinel bands*, seen in the noise spectrum in Figure 2.11 for example, permitted us to apply and compare both calibration methods; for calibrating with the night sky lines, the required line lists were taken from Osterbrock et al. (1996, 1997). We estimate the error in wavelength calibration using the difference between the nominal and the calibrated wavelengths of unsaturated lines in a wavelength corrected calibration arc spectrum; we carry out this comparison for the two spectral lines chosen. The bottom panel of Figure 2.14 shows the error, after calibration with the arc spectrum, measured relative to the nominal central wavelengths indicated. The error for both the blue and the red lines is $\leq$ 0.2Å; the corresponding velocity error due to wavelength mismatch, at the central wavelength of 8630Å, is $\leq 10\,\mathrm{km\,s^{-1}}$ at z=0.94. Using the night sky lines for calibration results in a similar error value. In addition, Figure 2.16 (right panel) shows that the errors in the two lines are not correlated, thus ruling out systematic spectral trends.

In the case of the IFU, the intrinsic width of a spectral line is further broadened by the characteristics of the optic fiber as well as by the camera optics in the spectrograph (Barden, 1998). We estimate this *instrumental broadening* as the full width at half maximum (FWHM) of a Gaussian profile fitted to an unsaturated spectral line in the calibration arc spectra which have been wavelength calibrated. The arc spectral lines may be reasonably assumed to have no intrinsic width, hence the measured FWHM is solely due to instrumental broadening. Figure 2.15 shows the measured FWHM for the 750 spectra, measured at 7272.94Å and 8667.94Å; the measured median instrumental broadening is 2.4Å and no systematic differences either between the sky and science fibers or in wavelength are seen, as shown by the scatter in Figure 2.16 (left panel). The measured small errors in wavelength cali-

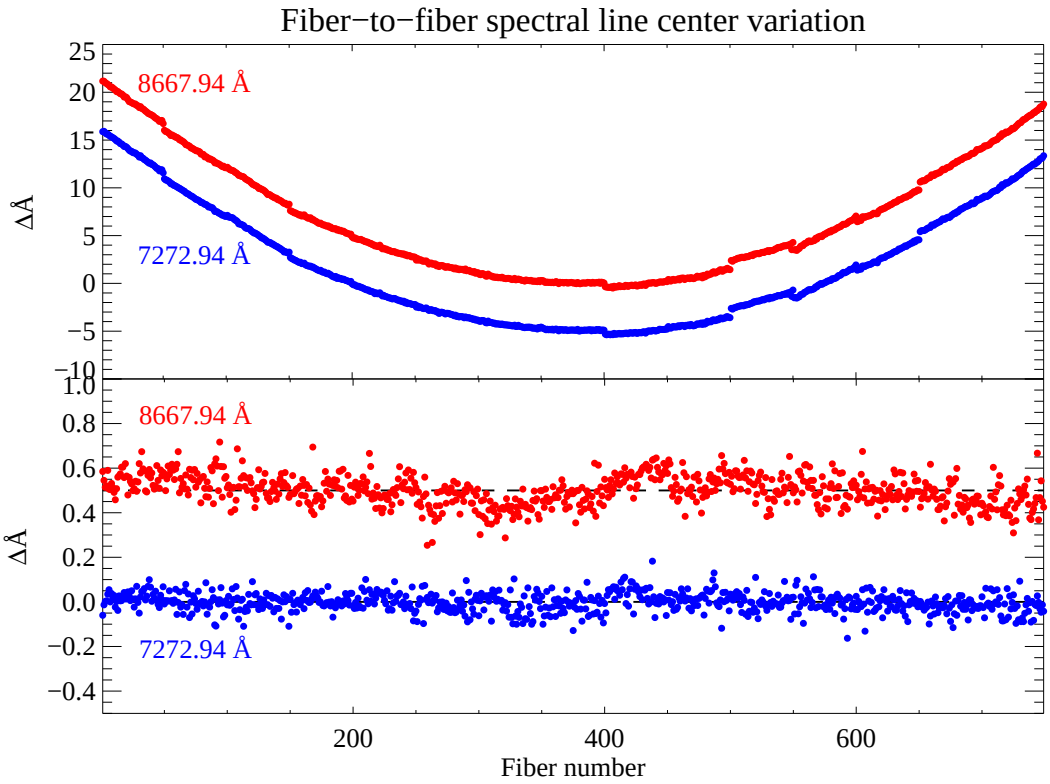

Figure 2.14: Measured variations in the positions of the IFU spectra on the GMOS CCD, compared before and after applying the wavelength calibration. The relative positions are measured as the centroids of two unsaturated calibration arc lines; the positions are measured relative to the median value (before correction) and relative to the wavelength of the spectral lines in a CuAr spectrum used for calibration (after correction). The ordinate shows the relative positions in units of ΔÅ. The fiber numbers on the abscissa relate to the fiber positions in the pseudo slit and therefore on the CCD. The plots for the 8667Å lines are offset by 5 and by 0.5Å respectively for clarity

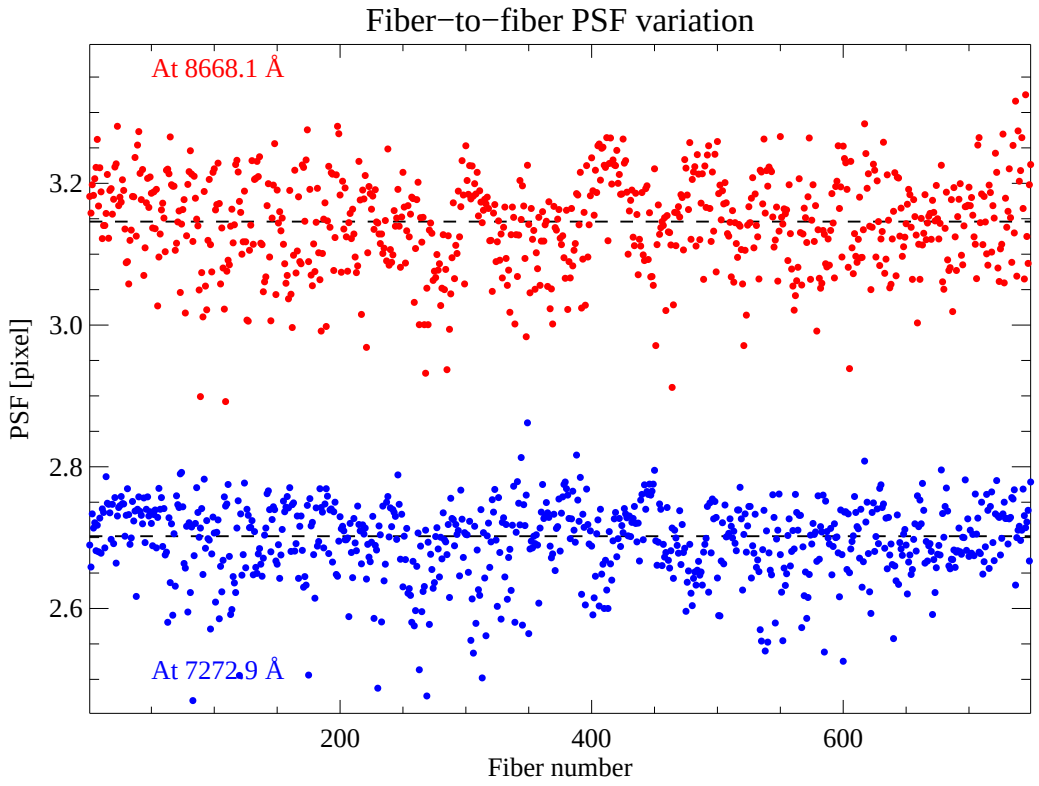

Figure 2.15: Measured variations in the PSF between the IFU fibers measured using unsaturated calibration arc lines. The measurements are shown for two lines at 7272.93Å and 8668.02Å to test for wavelength dependency; the median value at each wavelength is indicated by the dashed line. The values for the red line are offset by 0.5 pixel for clarity

bration and PSF indicate that they are not the principal cause of the sky residuals.

2.7.3 Scattered light

In order to estimate possible contamination by scattered light within the GMOS, we reduce a twilight flat field exposure using the same reduction steps, including sky subtraction, as used for the science exposures. Since all the IFU fibers in a twilight flat are exposed to the same uniform light source, this comparison offers a

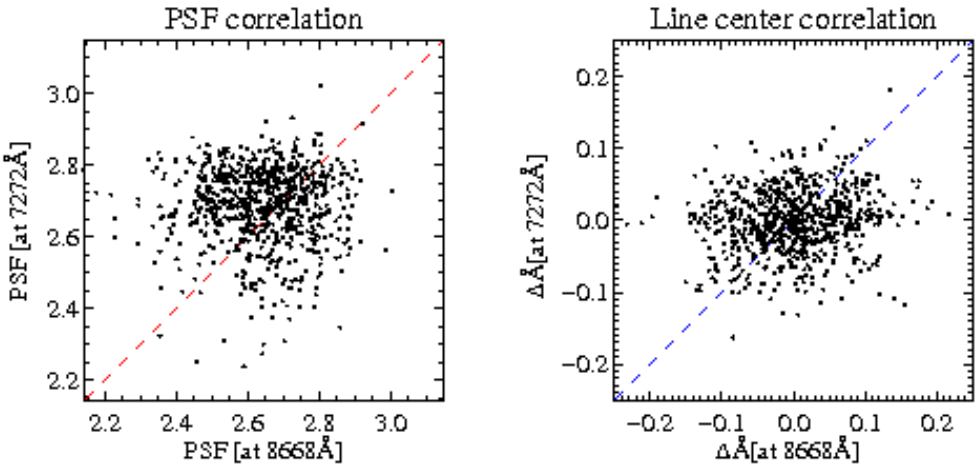

Figure 2.16: Correlations between the measured PSF and the variation of spectral line centroids at a red (8668.02Å) and a blue (7272.93Å) line to test for systematic wavelength dependencies in both these quantities.

direct measure of sky residuals due to scattered light in the individual fiber blocks as well as any systematic trends along the spatial direction of the CCD. In order to improve the S/N, we median combine the fifty sky subtracted twilight spectra in each fiber block and then fit a low-order continuum to the median spectrum, since the scattered light is generally characterized by a slowly varying continuum devoid of any spectral features. Figure 2.17 shows a smoothed surface fit through all the continua, arranged in the order in which they appear on the CCD; light and dark areas in this grey scale image indicate under- and over- subtracted regions due to the presence of scattered light. Over plotted in the figure is the continuum fit to the master sky spectrum, which is used for sky subtraction (the median of the spectra in all the sky fibers); this plot is only used to indicate the shape of the continuum and highlight regions of high flux; hence the units are arbitrary. The comparison shows that the region with significant scattered light residuals coincides with the spectral region of high flux (shown demarcated with vertical lines).

The trend in the scattered light along the spatial direction of the CCD is better

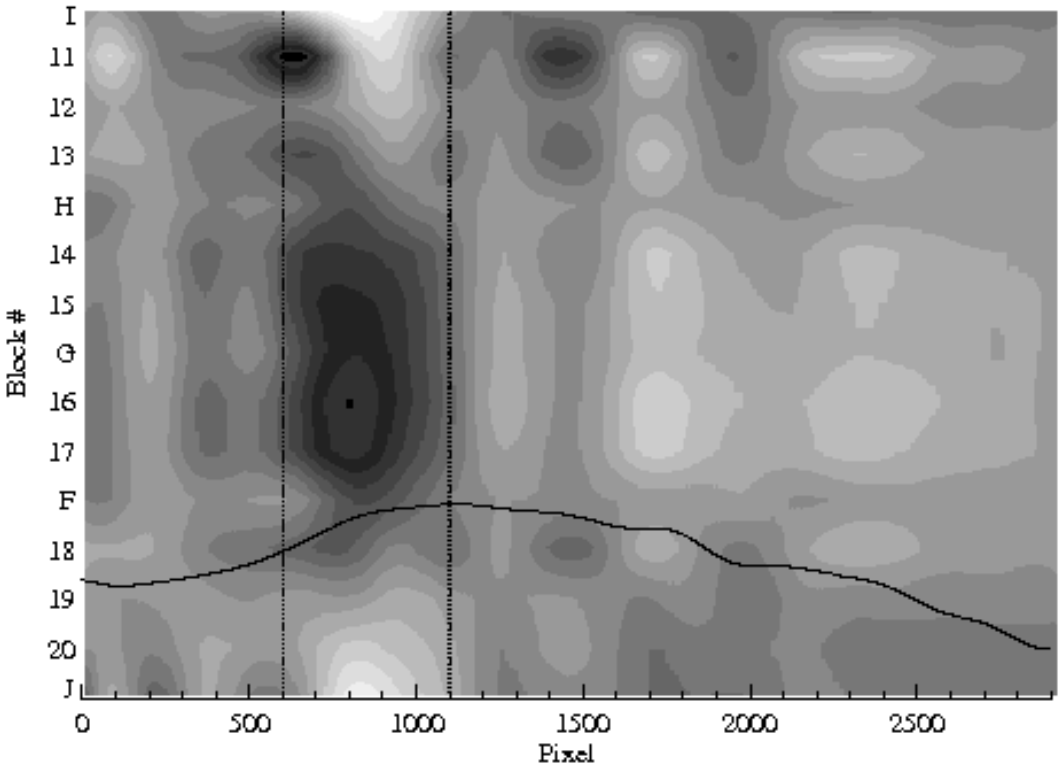

Figure 2.17: A surface fit to the observed level of scattered light in the GMOS-IFU, measured in a fully reduced twilight flat spectrum; dark regions indicated over-subtraction while the white regions show high residuals due to scattered light. The overplotted spectrum is a continuum fit to the nominal twilight spectrum while the vertical lines delineate the region used in Figure 2.18 to compare residuals in the sky and science blocks .

seen in Figure 2.18 (top panel), which is a plot of the median sky residual in each IFU fiber block, estimated only in the scattered light region marked on Figure 2.17; blue points refer to sky blocks and red to science blocks with the error bars indicating 1σ scatter for the fifty fibers in each block. The expected Poisson noise in the region is over plotted for comparison. The trend shows the amount of scattered light is high on the top and bottom ends of the CCD, which are the I and J sky blocks; this matches the trend seen in Figure 2.12, thus lending support to the scattered

light hypothesis. The residuals in both these blocks are $\sim 4\times$ the expected residual, leading to under subtraction in these blocks, while the middle fiber blocks are over subtracted to the same degree. The presence of scattered light and the resulting increase in the noise in the science fiber blocks leads to a consequent drop in the S/N obtained.

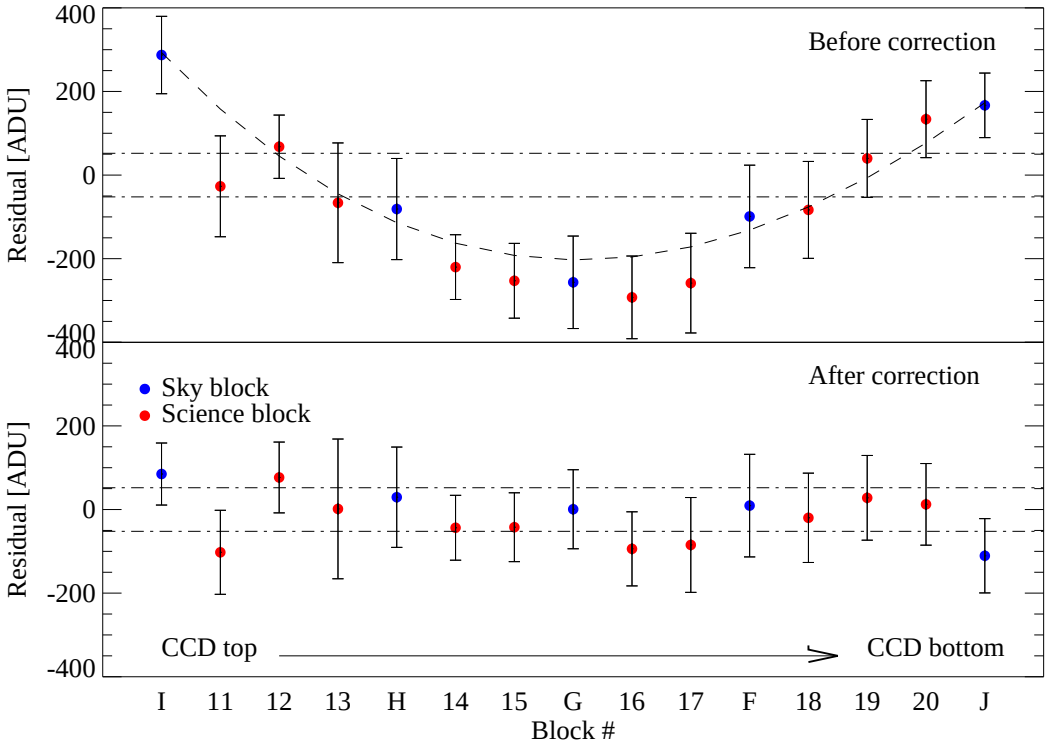

Figure 2.18: The sky residuals in the IFU science and sky blocks before and after applying the correction for scattered light. For illustration, a sample cubic polynomial, used for scattered light correction, is shown fitted to the median residual values in the plot. The chained lines indicate the nominal Poisson noise levels in this spectral region and are shown for comparison with the residual values

Given the diffuse nature of the scattered light, direct modeling and correction of the sky residual is not feasible. Instead, the strategy we use to correct for this scattered light is to fit a least squares cubic polynomial to the residual values in

only the sky blocks along each column of the CCD (perpendicular to the dispersion direction); the science blocks are not used in this fit since these fibers would normally have light from the object being observed. The cubic polynomial fit provided the best compromise between adequately modeling the trend without fitting into noise features. The correction spectrum for scattered light for each science and sky block, obtained by interpolation from this fit, is then subtracted from the 50 spectra in the corresponding block. The median and scatter in the residuals in each block after applying this correction, shown in the lower panel of Figure 2.18, indicates that the sky residuals in all the science blocks are within $\sim 1.3\times$ the expected noise (expressed in ADUs) and are more uniform along the CCD.

2.7.4 Scattered light corrected science exposures

The correction method for scattered light, described in Section 2.7.3 is applied to each science exposure as the final step in the reduction procedure. For this, the residuals in the sky blocks after sky subtraction, similar to those shown in Figure 2.12, are used for estimating the cubic fits and the scattered light correction spectra. The individual science exposures are then stacked into 3D cubes, which in turn are then combined to make final data cube. The white light image, obtained by projecting the combined 3D data cube in the spectral direction, is shown in Figure 2.19.

On comparison with the white light image from the Gemini pipeline reductions, (Figure 2.8), the improvement achieved by the correction method we have adopted for scattered light is clearly noticeable; in *both* images, the scaling was adjusted to bring out the features to the best possible extent. It is seen that with the removal of scattered light from the sky regions surrounding the elliptical galaxy and the arc, both objects are better delineated ; even the foreground objects seen in the HST image, Figure 2.1, are resolved. The price we pay for this improvement, however, is that a fraction of the object continuum flux is also lost due to the

polynomial fit and subtraction of the residuals; this is seen in the comparison of the sky subtracted flux in the science blocks in Figure 2.18, Block 11 for example, before and after correction. In addition, the correction applies only to scattered light residuals in the continuum, while the narrow sky line residuals from the strong Meinel bands, which extend redward of $\sim$ 7500Å (over half the wavelength range in our observations) remain as a dominant source of noise in comparison with the weak absorption features present in the elliptical and arc spectra. The ramifications of this uncorrected noise on the SNR achievable from such observations, its effect on the integration time requirements as well as alternate strategies that we propose are discussed in detail in Section 2.11

In the final data cube, we use spectral cross correlation against standard galaxy templates to identify the fibers corresponding to the elliptical galaxy and the lensed high redshift star forming galaxy. The cross correlation is done in Fourier space with the IRAF task *fxcor* using continuum subtracted IFU and template spectra. For identifying the elliptical galaxy, the correlation is done using E, S0 and Bulge template spectra from the *Kinney* catalog, (Kinney et al., 1996), while the six available star burst templates from the same catalog are used for the lensed source. An added advantage of using *fxcor* is that the Tonry *r-value*, which is computed as part of the correlation process, may be used for weighting individual spectra during subsequent co-addition; the *r-value* of the correlation is proportional to the strength of the correlation peak and the associated SNR in the spectral features (Tonry and Davis, 1979). Given our science goals, which place more importance on the SNR in the regions with absorption features than in the overall spectral continuum, we choose to use the correlation *r-value* instead of the conventional scheme with spectral signal-to-noise for weighting during co-addition.

The results from the cross correlation are shown in Figure 2.19 in which the fibers associated with the elliptical galaxy are marked in red boxes, while the blue boxes correspond to the lensed source; the regions over which the cross correlation

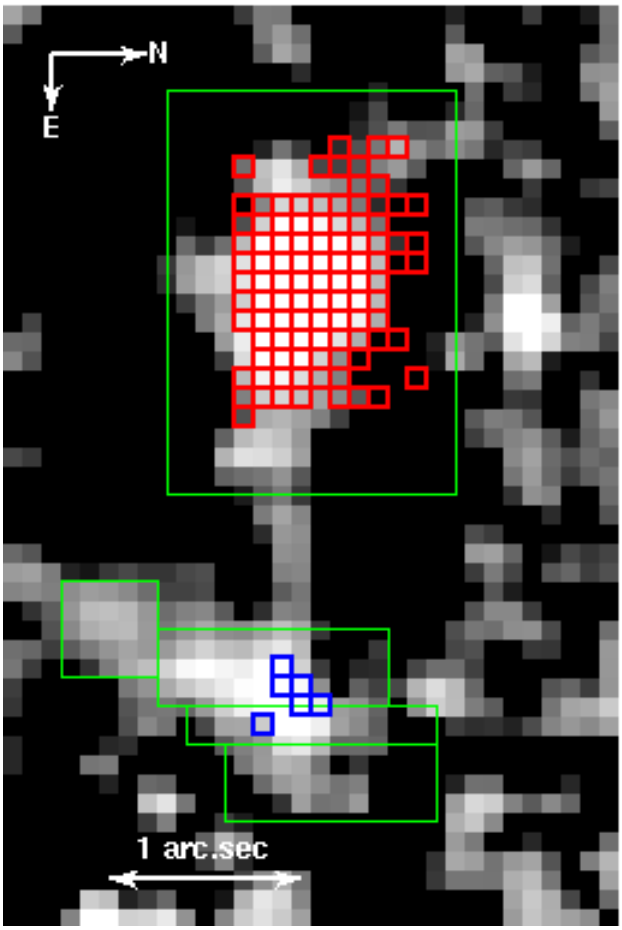

Figure 2.19: Projected white light image of the scattered light corrected 3D cube. Overplotted in red squares are fibers identified by spectral cross correlation as being associated with the elliptical galaxy; the blue squares indicate the fibers associated with the lensed star forming galaxy. The fibers on which the cross correlation was carried out are demarcated in green boxes.

was carried out are demarcated by green boundaries, the regions being chosen based on the flux ($\geq$ 40% of the peak flux of the elliptical and lensed SF galaxy). Only those fibers whose spectra correlate within ± 0.005 of the published redshifts of the elliptical galaxy, $z = 0.938$, and of the lensed galaxy $z = 2.94$ respectively, and with r-values ≥ 5 are chosen. For the case of the lensed arc, this stringent selection chooses only 6 pixels even though several other pixels show comparable flux levels

in the white light image, Figure 2.19. However, our objective to identify the lensed counter image by cross correlating the co-added arc spectrum against the elliptical galaxy spectra and look for correlation peaks from anomalous lines associated with this star forming galaxy (as explained in the following section). Using a co-added arc spectrum based on flux levels led to poor results in this cross correlation with no pattern seen; however, basing the choice on the presence of the absorption features, which is assured by the strength of the correlation peak and the *r-value*, gave more consistent results, shown in Figure 2.22.

The identified spectra are then weighted by their r-values and co-added to make the final elliptical and star burst galaxy 1D spectra, shown in Figures 2.20 and 2.21, with their associated sky noise spectra. Typical absorption lines in Elliptical and star burst galaxy spectra, which provided the strength of the cross correlation, are marked at their observed wavelengths for reference. From the cross correlation, the (r-value) weighted mean redshift of the elliptical galaxy is 0.9363 ± 0.0018 while that of the lensed galaxy is 2.9429 ± 0.0017, with errors computed from the weighted variance.

2.8 Location of lensed counter image

The size of the field of view of the IFU and the position of the elliptical galaxy in it, permits us to search for the location of a counter image to the lensed arc. The lens model developed by Crampton et al. (2002) predicted two likely locations for the counter image, both of which fell within the IFU FOV. Since the spectrum of the counter image should match that of the lensed arc, we correlate the co-added arc spectrum, shown in Figure 2.21, against the spectrum of each IFU fiber within a select region with a high likelihood of containing the counter image for the given lens geometry. In order to avoid spurious noise signals, the cross correlation is done using a 100 pixel window centered on each of the spectral lines marked

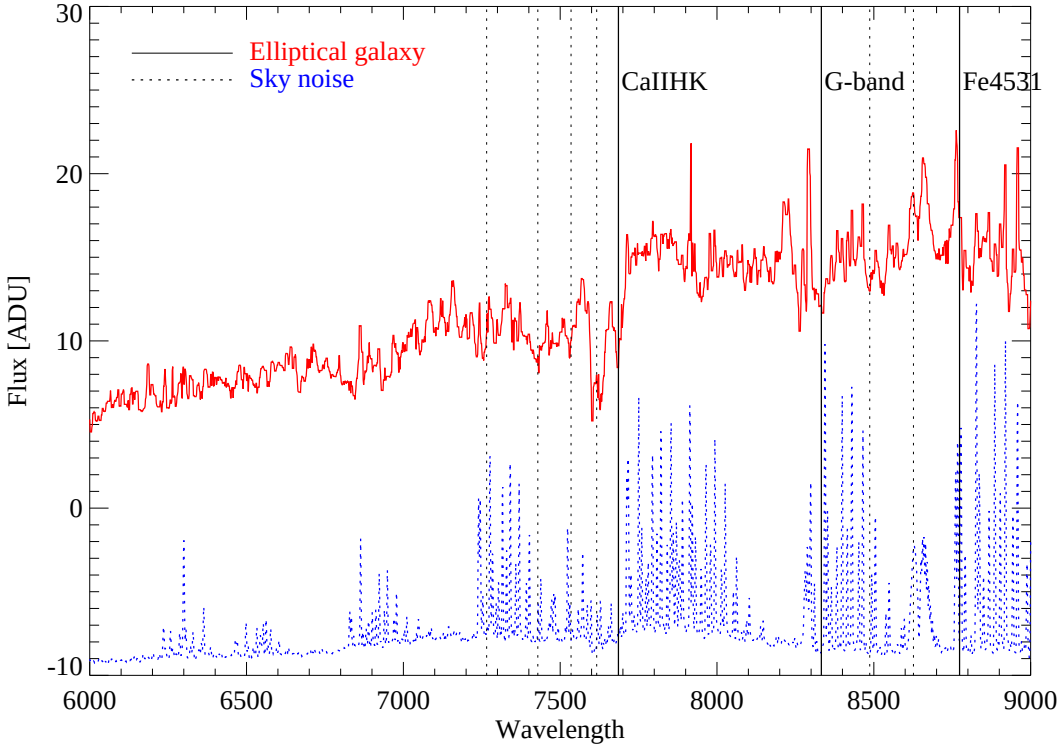

Figure 2.20: Co-added 1D spectrum of the elliptical galaxy, obtained as the weighted mean of the spectra identified by cross correlation; the *r-value* is used for weighting (see §2.7.4 for details). The spectrum has been median smoothed to the spectral resolution; the associated Poisson noise spectrum, (shown offset by -15ADU for clarity), highlights spectral lines free of sky noise regions. Overplotted are typical spectral lines found in elliptical galaxies (strong feature = solid line and labeled; weak spectral feature = dashed line)

in Figure 2.21; the correlation is done in pixel space using *fxcor*, as described in Section 2.7.4 and is run for each spectral line separately. For each spectral line, only fibers which correlate within a pixel of the co-added arc spectrum and whose correlation strength, given by the *r-value*, is greater than 10 are selected and the fiber position with the maximum *r-value* is identified as the most likely location of the counter image. The cross correlation is carried out for each of the twelve lines

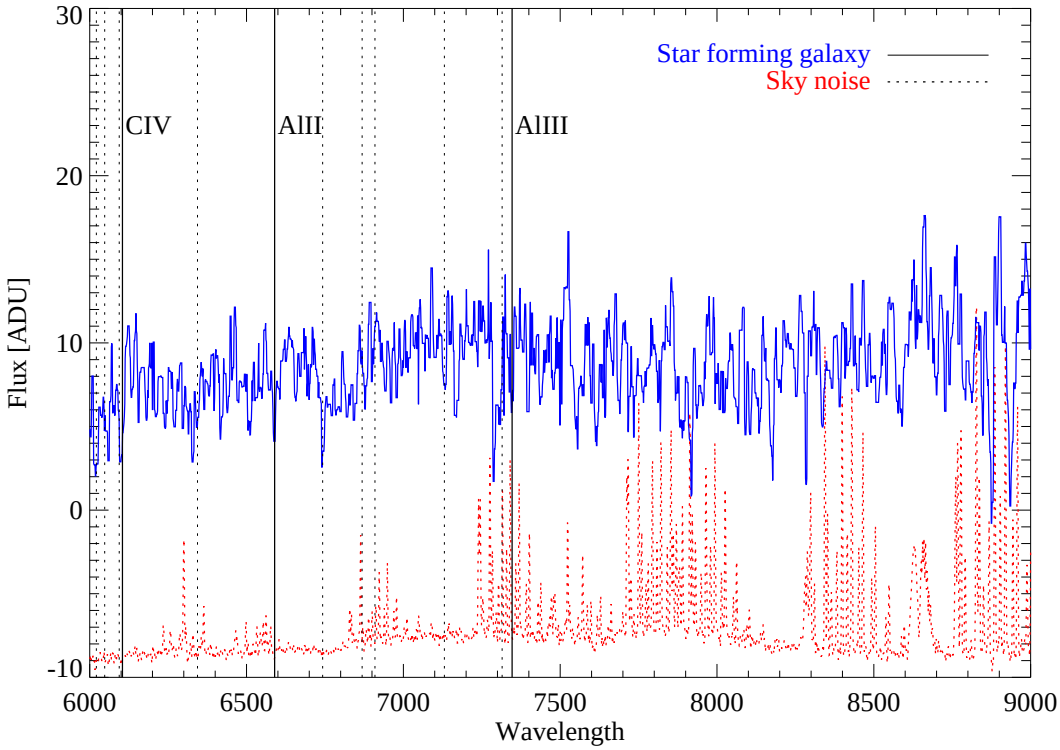

Figure 2.21: Co-added 1D spectrum of the star forming galaxy at z=2.94, obtained as the weighted mean of the spectra identified by cross correlation; the spectrum has been median smoothed to the spectral resolution; the associated Poisson noise spectrum, (shown offset by -15ADU for clarity), highlights spectral lines free of sky noise regions. Overplotted are typical spectral lines found in star burst galaxies (strong feature = solid line and labeled; weak spectral feature = dashed line); the identified spectral lines are listed in Table 2.2

available within the observed spectral range, as listed in Table 2.2. On Figure 2.22 the best locations identified for ten spectral lines are shown by the different colored symbols; two of the spectral lines did not meet the selection criteria. It must be noted that the locations of two pairs of lines coincided exactly, therefore leaving only 8 distinct symbols seen in the figure. Table 2.2 lists the spectral lines, corresponding rest frame wavelengths and the best correlation values and corresponding locations.

The region over which the correlation was carried out is demarcated in green.

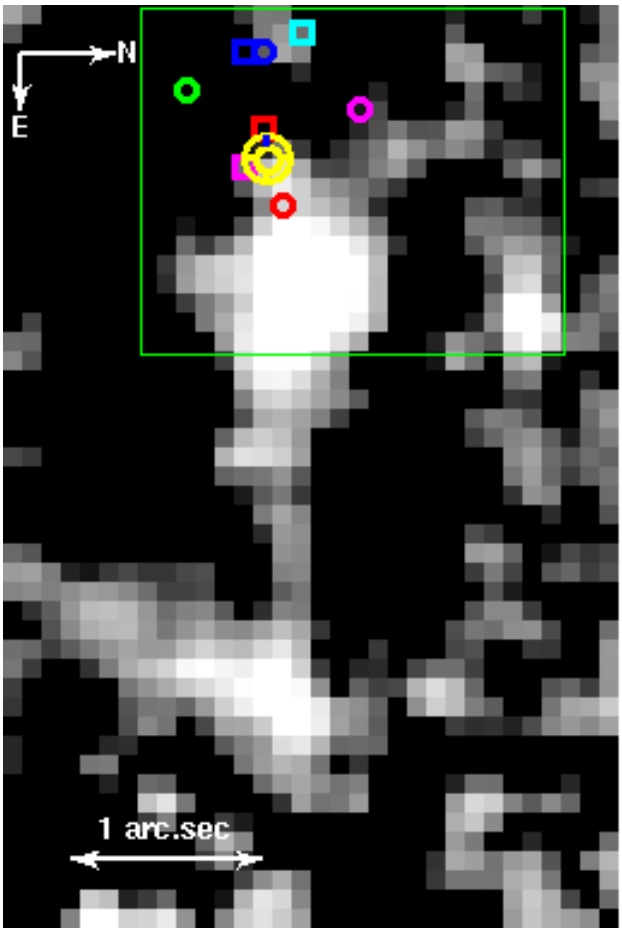

Figure 2.22: Likely locations of the counter image identified by cross correlating the co-added arc spectrum with each fiber spectrum in the region demarcated in green. The different symbols represent the positions of maximum *r-value* for each of the 10 spectral lines which met the selection criteria. The weighted barycenter of the counter image is denoted by the yellow annular symbol

The locations identified by the 10 lines are then combined using the corresponding *r-value* as weights; the barycenter of the counter image thus deduced is marked with a yellow annular symbol in Figure 2.22. The location thus identified coincides with a small bright region on the periphery of the elliptical galaxy and also with the likely location of the counter image identified by Crampton et al. (2002) using

Table 2.2: Details of spectral lines identified in the lensed counter image

Line	λ_0 Å	TDR	x pixel	y pixel
SiII	1526.7066	46.8	14	42
SiII*	1533.4312	47.0	14	42
CIV	1548.195	22.0	13	46
CIV	1550.77	18.1	16	47
FeII	1608.4511	16.6	13	40
AlII	1670.7874	37.9	15	38
NiII	1709.6	20.0	10	44
NiII	1741.549	-	-	-
NiII	1751.91	18.1	14	46
SiII	1808.0126	20.2	10	44
AlIII	1854.7164	-	-	-
AlIII	1862.7895	93.7	19	43
$\Sigma r, (x, y)_b$		340.4	15.0	42.7

List of spectral lines which met the selection criteria for inclusion in the search for the counter image; their rest frame wavelengths, the maximum *r-value* of the correlation and the fiber (x,y) position corresponding to the maximum value are listed; the coordinate origin in Figure 2.22 is the bottom, left corner. The last row lists the total *r-value* and the weighted barycenter of the counter image in pixel (x,y) coordinates. The two spectral lines, which did not meet the selection criteria are included for completeness, though they are not used for computing the barycenter

their lens model. The implications of this coincidence and the contribution to an improved lens model are discussed further in the summary of results in Section 2.11.

2.9 Velocity dispersion of deflector galaxy

As stated in Section 2.5, one of our principal objectives was to determine the velocity dispersion of the elliptical galaxy and thus test whether this galaxy had indeed followed an evolutionary path different from the Fundamental Plane prediction, as proposed by (Crampton et al., 2002) from their CFHT long slit spectroscopy. In addition, given the spatial information from our IFU observations, we aimed to de-

rive the radial velocity dispersion profile, depending on the S/N achieved in various radial bins. The velocity profile reflects the total (i.e, dark matter + baryonic) mass enclosed within a given radius, and would thus provide tight constraints on the 2D mass distribution of the galaxy and therefore on the lens model..

The observed spectrum of a galaxy is a composite of the intrinsic spectra of its stellar population, but broadened by the kinematic motion of the stars in the gravitational potential of the galaxy (reflected by the velocity dispersion and measured by the line of sight velocity dispersion, LOSVD) and by the instrumental profile of the telescope and spectrograph; the intrinsic stellar spectrum is already broadened by atmospheric effects in each star, such as due to pressure and rotation. Since the observed absorption lines in the galactic spectrum are well fit by Gaussians, both the LOSVD and the instrumental broadening are normally modelled as convolutions by Gaussians (Rix and White, 1992); but see Saha and Williams (1994) for a non-parametric approach. However, in their Fundamental Plane studies of elliptical galaxies, Kelson et al. (2000) note that deviations from a guassian profile account for less than 10% variation in the LOSVD.

The basic task may therefore be stated thus: given the observed galaxy spectrum, a representative stellar template and a known instrumental broadening function, one must derive the parameters for the broadening function describing the LOSVD. Since the first systematic approach by Simkin (1974), several methods have been proposed for the extraction of both the the bulk velocity (or redshift) and the velocity dispersion of a galaxy. Earlier methods utilized the computational advantage of the Fourier domain and Fast Fourier Transforms for the deconvolution, such as the Direct Quotient method (Sargent et al., 1977), the Fourier Cross Correlation method (Tonry and Davis, 1979) and variations of these basic approaches (Franx and Illingworth, 1988, Bender, 1990, Statler, 1995). For observed spectra of low redshift galaxies with S/N $\sim$ 100, the Fourier methods provide an efficient approach and have found extensive use. However, a significant drawback of Fourier

based methods is that noisy segments in the observed spectrum are folded into the Fourier decomposition and there is no straightforward method of masking them. This is specially important for galaxies at $z \geq 1$ for which the absorption lines at wavelengths redward of the Balmer break (at $\lambda = 4000$Å) normally used for LOSVD measurements, have been redshifted to the spectral region with strong night sky emission lines (at $\lambda \geq 7500$Å); for such spectra, it would be distinctly advantageous to be able to mask an absorption line that falls directly on a strong sky emission feature while using other lines in the spectrum with acceptable S/N values. Other drawbacks include 'ringing' either due to the abrupt discontinuities at either end of the spectrum or other sharp noise features such as residuals from sky subtraction (see Rucinski (1999) for a more detailed discussion).

The alternate approach is to work in pixel space, which permits direct masking of noisy spectral regions. Under the assumption that the broadening function has a parametric form, pixel-space methods use a χ^2 minimisation technique for estimating the parameters (Rix and White, 1992, van der Marel et al., 1994, Gebhardt et al., 2000, Kelson et al., 2000, Rucinski, 2002, Cappellari and Emsellem, 2004); the methods differ either in the parametric representation of the broadening function (Hermite polynomials are included with the Gaussian for complex kinematic profiles) or in the numerical minimization scheme adopted. Of these different methods, we have adopted the Singular Value Decomposition (SVD) method, described in detail by Rucinski (1992) and references therein. The deconvolution is recast as a series of over-determined linear equations, which the SVD is particularly efficient in solving. Due to its numerical efficiency for such applications, the SVD algorithm has been incorporated in many numerical toolboxes including IDL, which we use. Rucinski et al. (1993), Rucinski (1999) have successfully applied this method to obtain the complex kinematic profiles of contact binaries. A summary of the pertinent details of the method are given below; a detailed description of the methodology and a discussion of the advantages of SVD are provided in Rucinski (1992, 1999),

Press et al. (1992)

The (digital) convolution of a representative stellar template S, by the broadening function, B, to obtain the observed spectrum, P, may be expressed in matrix form as an over-determined system of linear equations,

$$[S]\{B\} = \{P\} \tag{2.2}$$

The stellar template is assumed to be either a set of single stellar templates each of high S/N or a linear combination of such templates. The template is redshifted to the best estimated redshift of the galaxy; corrections to the redshift are obtained as part of the SVD solution. The templates are resampled to the instrumental resolution of the spectrograph; the instrumental resolution is determined by fitting a Gaussian to one or more high S/N but unsaturated emission lines in the calibration arc spectrum. In the matrix representation adopted in our approach, the length of the observed spectrum, represented by the column vector, P, determines the number of linear equations, n. The number of spectral pixels, m, required to adequately sample the LOSVD determines the length of the column vector, B; since the parameters of the broadening function are unknown apriori, the length has to be chosen iteratively. For the LOSVD of the elliptical galaxy, we adopt a Gaussian parametrization. For this parametrization, we find that the solution converges for a broadening function of 51 pixels or less. With these dimensions for the columm vectors, the convolution of the template by the broadening function may be represented in matrix form as the product of a $(m \times n)$ 'design' matrix, S, by the columm vector, B. In the SVD method, the design matrix is then decomposed into a product of three matrices as

$$[S] = \{U\}[W]\{V\}^T \tag{2.3}$$

in which, U and V^T represent orthonormal basis vectors and W is a diagonal matrix of weights, (the eigen values), associated with each basis vector. The power of the SVD comes from this decomposition, which makes it feasible to invert each matrix

and thus solve directly for the broadening function, B, as,

$$\{B\} = \{V\}[W^{-1}]\{U\}^T\{P\} \tag{2.4}$$

Finally, the parameters of the broadening function are recovered by fitting a Gaussian to the elements of the column vector, B. The LOSVD is the full width at half maximum (FWHM) of the Gaussian while the centroid and the normalisation provide the redshift correction, if any, as well as the flux scaling between the template and the galaxy spectrum. In SVD, as in all other methods, the choice of the stellar template plays a crucial role in the solution. One of the advantages of SVD is that regions of the template which are devoid of spectral features have correspondingly smaller matrix elements during decomposition and may thus be identified and exluded (ie, set to zero after inversion).

2.9.1 Implementation of the SVD method

We have implemented the SVD method for velocity dispersion estimation in IDL, making use of the available toolboxes in this programming environment. For the stellar templates, we use the publically available templates from the Sloan Digital Sky Survey (SDSS). The SDSS template set consists of 1D spectra of 32 G and K gaint stars in M67 observed with a velocity resolution of $90\,\mathrm{km\,s^{-1}}$ [‡], which matches the GMOS-IFU resolution for our observations. The typical spectral S/N of these templates is ~ 100. We test and calibrate our SVD implementation in several steps as described below.

2.9.2 Effect of the spectral S/N and the Gaussian FWHM on the recovery efficiency of the SVD method

In order to assess the SVD method's efficiency in recovering the parameters of the broadening function at varying spectral S/N levels, we convolve one of the SDSS

[‡]http://www.sdss.org/dr5/algorithms/veldisp.html

stellar templates with a Gaussian, whose FWHM is chosen to correspond to a realistic velocity dispersion in early type galaxies (in the range $150 - 300\,\mathrm{km\,s^{-1}}$); we add Poisson noise to the broadened spectrum to mimic S/N values from 10 - 100 and then test the recovery of the input Gaussian parameters, specifically the width, σ, by the SVD method; the FWHM = 2.35σ. Table 2.3 lists the parameter values used in these tests. For each S/N value, we repeat the test with 100 different realizations of the noise spectrum added to the same broadened object spectrum, to obtain statistical estimates of the recovery process. The template spectrum used for the SVD solution is the unbroadened stellar template; we estimate the effect of using different templates in the recovery in a subsequent test.

The procedure used to test the recovery efficiency of the SVD method is illustrated by the four panels in Figure 2.23. Each panel pertains to the trials done for one of the Gaussian widths; the plots chosen for illustration refer to S/N = 15. In each of the four panels, the upper plot shows the input *normalized* Gaussian (in red) used as the broadening function. The stellar template is convolved with the broadening function and then Poisson noise is added to make the *observed* spectrum, P, in Equation 2.2. The level of noise added is chosen such that the spectrum, P, has the required S/N value. Using the unbroadened stellar template as the *template* spectrum, S, the Equation 2.2 is solved for the *broadening function*, B, using the SVD method. The test is repeated 100 times with a new realization of the Poisson noise spectrum added to the observed spectrum, P. The overplotted Gaussians, shown in blue in Figure 2.23, have been generated using the parameters recovered by the SVD method in these 100 trials done for each S/N value. The differences between the input Gaussian and the 100 fitted Gaussians are plotted in the lower panel to show graphically where the main differences between the *shapes* of the input and fitted Gaussians lie. The trends seen in these plots are discussed along with the other results below.

The results from these tests are shown in Figure 2.24 and the numerical values

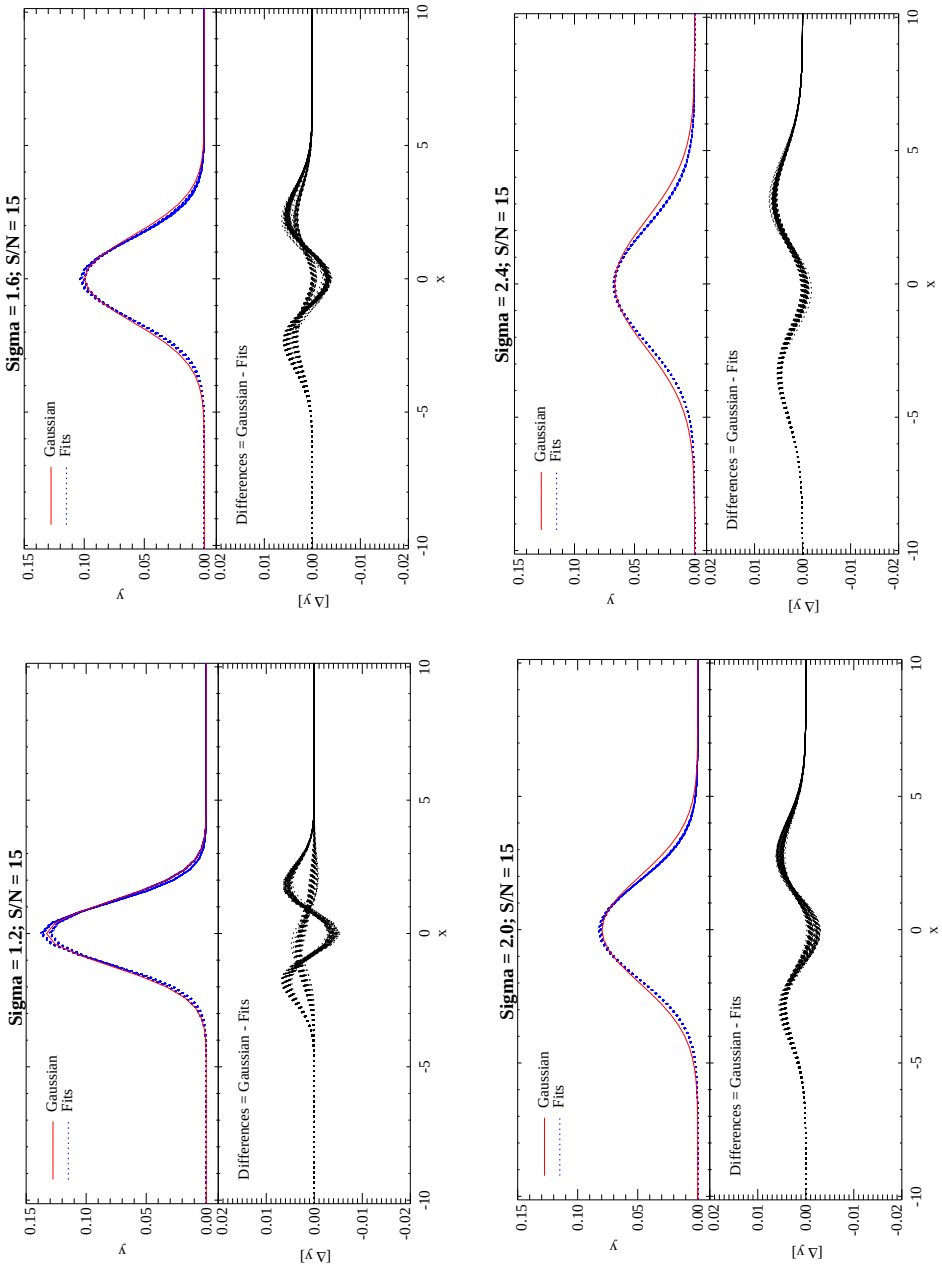

Figure 2.23: The four panels show the efficiency of recovery of the Gaussian width by the SVD method; the results pertain to a S/N of 15 for the four σ values used. The lower panels show the error in the fit as the difference between the input Gaussian and the fitted one

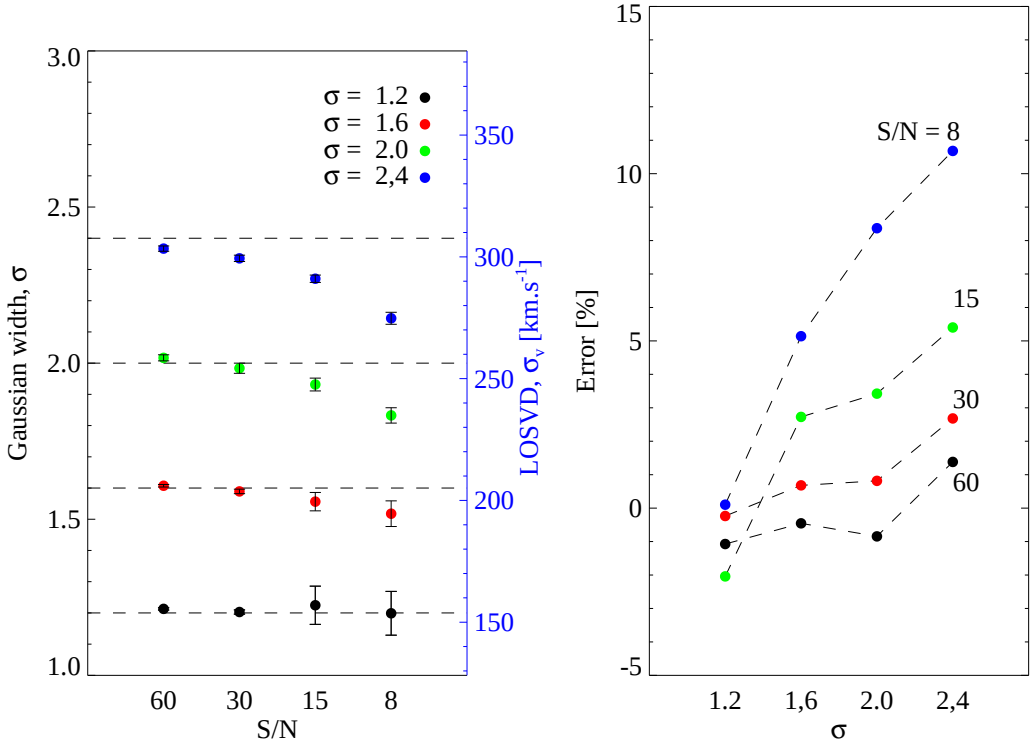

Figure 2.24: Errors in the fitted Gaussian width for the four values of σ as a function of the spectral S/N. The left panel shows the effect of decreasing the S/N for a fixed input Gaussian width. The percentage errors at fixed S/N but with increasing Gaussian width are shown in the right panel.

summarized in Table 2.3. The *error* in the SVD fit value is defined as,

$$error = \frac{(\sigma_{in} - \sigma_{fit})}{\sigma_{in}} \; [\%] \tag{2.5}$$

The results show that the SVD method recovers the input Gaussian width with errors $\leq 5\%$ for the range of values of σ used in these trials and for S/N ≥ 10; for lower S/N, the errors are below this margin only for $\sigma \leq 1.6$ and then increase rapidly at higher values. Since the σ values used represent the expected range of LOSVD values for elliptical galaxies, we therefore stipulate a minimum S/N of 12, erring on the side of caution, for acceptable error margins of $\leq 5\%$. The increase

Table 2.3: Gaussian parameters used to test the SVD method and results obtained

σ_{in} Å	FWHM Å	LOSVD $\mathrm{km\,s^{-1}}$	S/N -	σ_{fit} Å	Error1 %	Error2 %
1.2	2,83	154	60	1.213 ± 0.004	-1.1	-2.94 ± 0.61
			30	1.203 ± 0.007	-0.5	
			15	1.225 ± 0.061	-0.8	
			8	1.119 ± 0.07	1,4	
1.6	3.77	205	60	1.607 ± 0.004	-0.2	-0.09 ± 0.73
			30	1.589 ± 0.007	0.7	
			15	1.556 ± 0.029	0.8	
			8	1.518 ± 0.041	2.7	
2.0	4.71	257	60	2.017 ± 0.010	-2.0	-1.31 ± 0.38
			30	1.984 ± 0.016	2.7	
			15	1.932 ± 0.021	3.4	
			8	1.833 ± 0.025	5.4	
2.4	5.65	308	60	2.367 ± 0.009	0.1	4.25 ± 0.35
			30	2.336 ± 0.010	5.1	
			15	1.270 ± 0.012	8.4	
			8	2.144 ± 0.019	10.7	

List of Gaussian widths used to test the efficiency of recovery of the SVD method at different S/N values. The LOSVD values corresponding to these input parameters are also given. The fit values and their corresponding spread (measured as the inter-quartile distance from 100 trials) as well as the corresponding errors (Error1) are listed in the next two columns. The final column lists the bi-weight mean and spread of the errors associated with stellar template mismatch discussed in Section 2.9.3

in the errors for lower S/N values at any given Gaussian width is as expected. However, the differences between the input and the fitted Gaussians, seen in Figure 2.23, as well as shown by the trend in errors seen in Figure 2.24, indicate that at smaller values of σ, the SVD method overestimates the width, though the error in the fit is only $\leq 2\%$ for all the S/N values; with higher values of *sigma*, the method underestimates the width and the resulting error is then a function of the S/N, being $\leq 5\%$ only for S/N $\geq 15\%$, which is acceptable for our application. Since the SVD method relies on a direct solution of a system of linear equations without any

tunable parameters, it may be interesting to investigate the reason for the trend and correct for it, as part of a future development.

In order to verify that there is no wavelength dependency in the fitted errors, the upper panels in Figure 2.25 show a 500Å spectral region of the input broadened stellar templates for the four values of σ used in these trials (spectra shown in red); the spectra chosen for these plots pertain to S/N=15. Overplotted in blue are the 100 *fitted* spectra, which are the stellar template broadened by the broadening functions recovered by the SVD solution in the 100 trials; the fitted spectra are hardly distinguishable from the input spectrum due to the close match. The lower plots show the differences between the input and the fitted spectra; for ease of comparison, the units of flux used in both panels are the same. The results support that there is no wavelength dependency in the fitted errors; trials using other stellar templates produced similar results.

2.9.3 Effect of stellar templates on the recovery efficiency of the SVD method

In order to assess the effect of different stellar templates on the recovery efficiency and to obtain the error introduced due to template mismatch, we run the SVD method on the broadened stellar template prepared in Section 2.9.2, but use the 31 other SDSS stellar templates to obtain the broadening parameters. The tests are done for all four Gaussian widths but only for S/N = 15 to obtain an upper bound on the error introduced; higher values of S/N result in progressively smaller errors (N.B: the error referred here follows the definition given in Equation 2.5).

Results are shown in Figure 2.26, each panel representing a different value of σ used for broadening. Each point and the associated errors bars represent one of the SDSS templates. It must be emphasized that no information about the exact spectral types of the templates is available, and is therefore not used in the SVD method; the order in which the templates are numbered in the plot is therefore

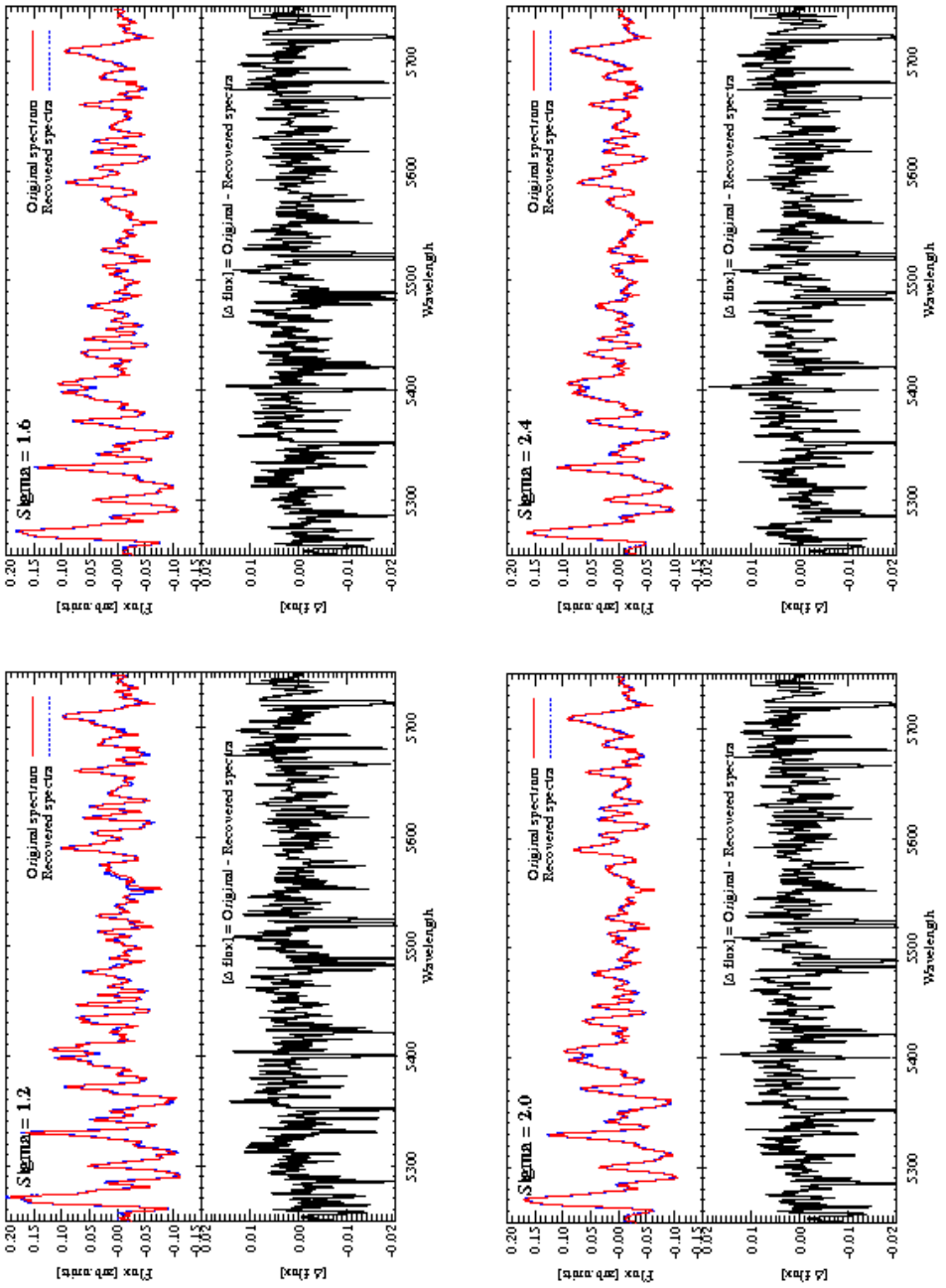

Figure 2.25: The four panels show the four broadened stellar templates (a 500Å region) with noise added (S/N=15) in red and the spectra fitted by the SVD method overplotted in blue (for the 100 realizations); the lower plots, which show the differences between the input and fitted spectra, show that there are no spectral dependencies observed in the fit

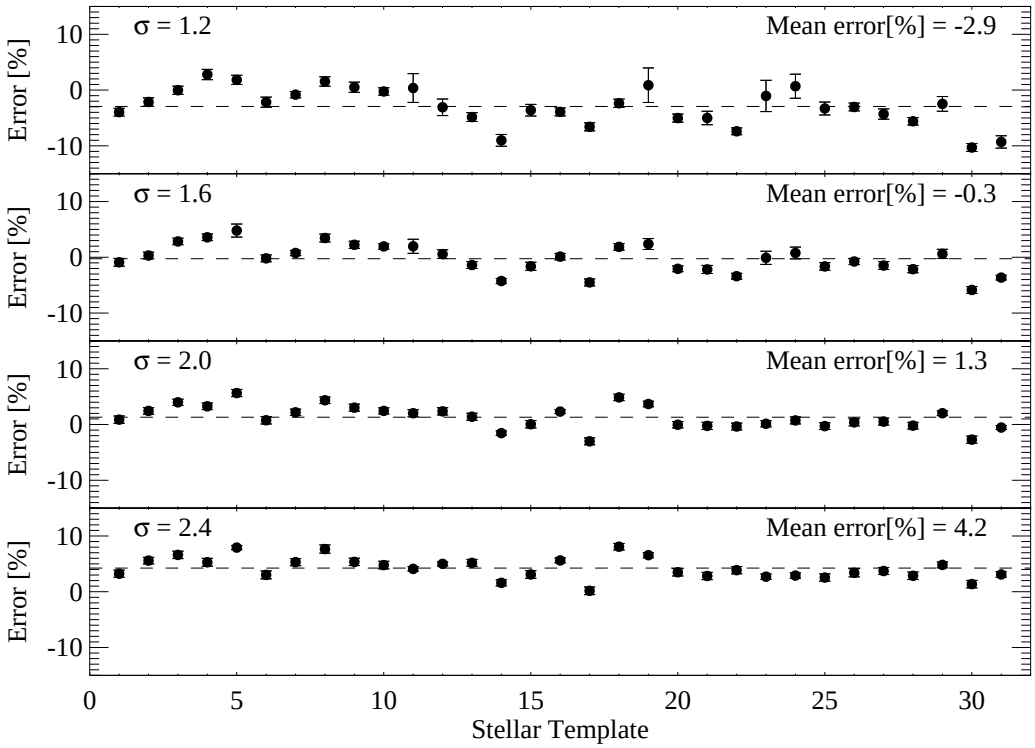

Figure 2.26: Plots showing the effect of using different stellar templates on the recovery efficiency of the SVD method and the consequent errors in the fitted Gaussian width. The test is carried out on the broadened template described in Section 2.9.2 for four different values of σ and S/N = 15 to obtain an upper bound on the error.

arbitrary. The trials for each template is repeated 100 times for the different realizations of noise, as described in Section 2.9.2 and the mean and IQD values are derived for each template (indicated by the symmetric error bars). Finally, the biweight mean and spread of the errors from all the templates is used as the measure of the overall Gaussian width and error; these values are listed in the last column of Table 2.3.

The effect of template mismatch is more evident for smaller values of σ as indicated by the scatter in the individual values of width as well as the spread in the associated errors; however, the scatter even for $\sigma = 1.2$ is less than 1%. The bi-

weight mean error shows the same increasing trend with increasing Gaussian width, as discussed in Section 2.9.2 reaching a maximum of 4.2% for $\sigma = 2.4$, which we accept as the upper bound on the error due to template mismatch associated with the SVD method.

2.9.4 Calibration against SDSS velocity dispersion values

Having assessed the intrinsic performance of the SVD method, we then calibrate it against published velocity dispersion values available at the SDSS on-line galaxy catalogs. The SDSS catalogs provide velocity dispersion and redshift values, as well as position and photometric details, of elliptical galaxies with spectroscopic observations taken as part of the survey; the corresponding spectra and the associated noise spectra are also available to the public. The SDSS collaboration use both the Fourier and the Direct fitting methods, described in Section 2.9, to obtain two independent velocity dispersion estimates, the mean and rms error of which are the values published in the catalog; their minimum acceptable S/N, determined by calibration trials, is 12. Since we use the SDSS stellar templates for the SVD method, the SDSS results provide a robust benchmark of our implementation.

Figure 2.27 illustrates intermediate steps in the implementation of the SVD method on an *observed* elliptical galaxy spectrum from SDSS, plotted in the upper left panel along with the associated noise spectrum. The galaxy used in this trial is an elliptical galaxy at a redshift, z = 0.284 and with velocity dispersion of $228 \pm 22\,\mathrm{km\,s^{-1}}$. The corresponding S/N spectrum, median smoothed for clarity, is used to select the spectral region (S/N $\geq$ 12) over which to apply the SVD method. Overplotted are lines representing strong spectral absorption lines taken from the reference line list available at the SDSS website; the lines have been appropriately redshifted to match the observed galaxy. It must be mentioned that in an earlier version of the SVD method, each line was individually fit with the SVD solution and the biweight mean of the values was taken as the LOSVD of the galaxy. The

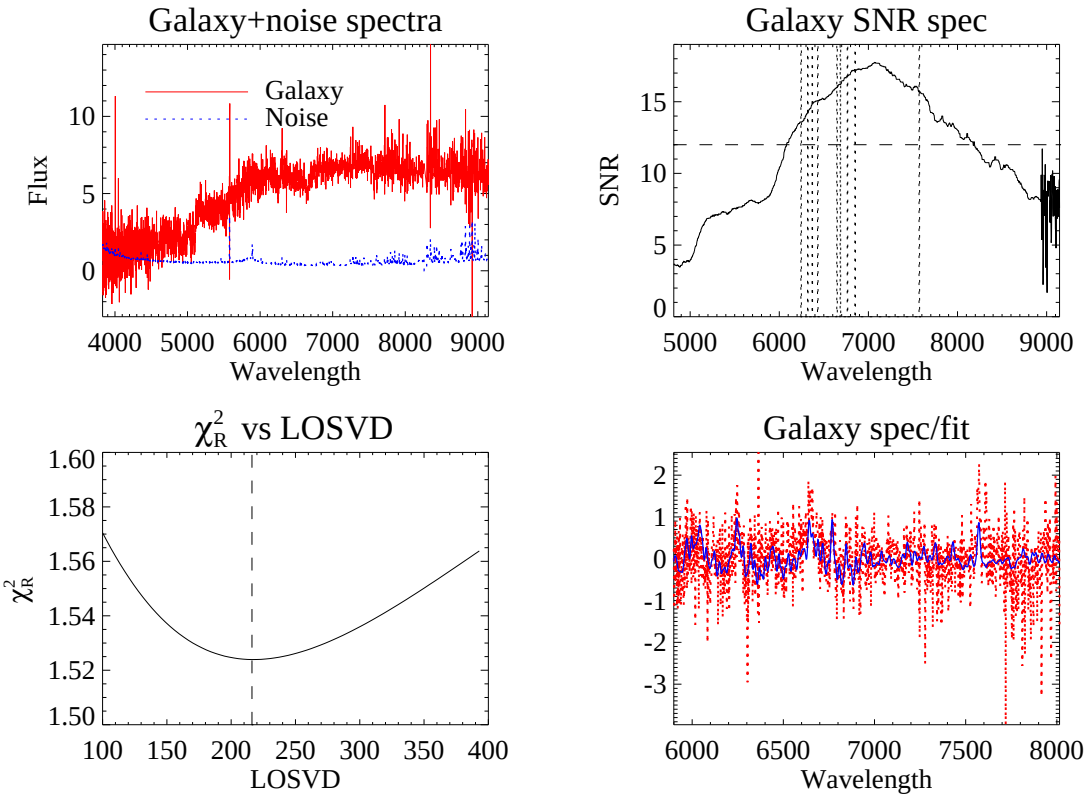

Figure 2.27: The four panels show intermediate steps in the implementation of the SVD method on observed elliptical galaxy spectra, discussed in Section 2.9.4. The observed spectrum and the associated noise spectrum (top, left) are used to compute the median smoothed S/N spectrum (top, right). Overplotted are spectral lines from the reference line list which lie in the region with S/N higher than the cutoff, ≥ 12. The lower left panel shows a preliminary estimate of the reduced χ^2, with the minimum value providing a first guess for the LOSVD. The continuum subtracted galaxy spectrum with the broadened template spectrum overplotted is shown in the lower, right panel

method worked well for galaxies with strong spectral features matching the line list but failed on those where several lines were weak or absent. Therefore, in the current implementation, the complete spectral range above the threshold S/N value is used.

In our implementation, we have chosen to use each SDSS stellar template independently and take the biweight mean of the LOSVD values to represent that of the galaxy. This choice is based on the uncertainty in knowing the stellar make up of individual galaxies and thus on the proper weighting scheme to be used to make a linear combination of stellar templates. Our approach therefore applies equal weight to all stellar templates.

For each stellar template, we obtain a preliminary estimate of the broadening parameters using the reduced χ^2 computed for an assumed range of observed velocity dispersions (lower left panel). The estimate is then iteratively refined using the SVD method within a minimization routine. It must be noted that during this minimization, we estimate best fit values for the midpoint, scale and the FWHM of the broadening Gaussian function, as well as error estimates associated with the minimization of all three parameters. A non-zero value for the fitted mid point indicates the correction to be applied to the assumed value of the redshift. The velocity dispersion is finally scaled to the rest frame of the galaxy. The lower, right plot in Figure 2.27 shows the continuum subtracted galaxy spectrum in the spectral range used for the SVD solution overplotted with one of the stellar templates broadened using the best fit broadening parameters.

Figure 2.28 shows the LOSVD values and the associated fit errors for this elliptical galaxy derived using the individual stellar templates and the bi-weight mean and spread (velocity dispersion $= 221 \pm 18\,\mathrm{km\,s^{-1}}$) computed from this set (blue square). For comparison, the SDSS velocity dispersion value and the error margins ($228 \pm 22\,\mathrm{km\,s^{-1}}$) for this galaxy, taken from their catalog, are overplotted (red triangle). The calibration was repeated for a set of 25 elliptical galaxies from the SDSS

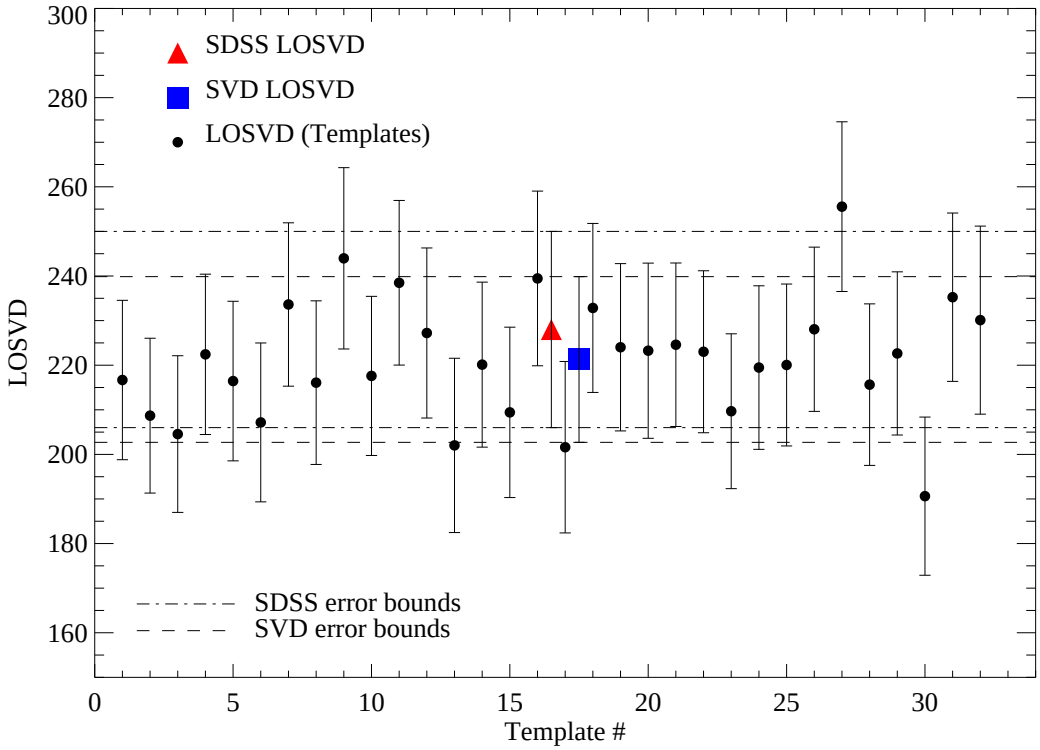

Figure 2.28: Plot showing the individual LOSVD estimates from the SVD method obtained using each stellar template individually and the bi-weight mean (blue square) and associated error values derived from them. Overplotted is the LOSVD and the associated error from the SDSS catalog for this z=0.284 elliptical galaxy.

catalog and the velocity dispersion values matched within the respective errors in all cases but one (at z=0.36) which had only two spectral lines in the spectral region above the S/N cutoff (while other galaxies had on average 6 or more lines). This case underlines the importance of the presence of strong spectral lines for the SVD method, as it is for any velocity fitting algorithm.

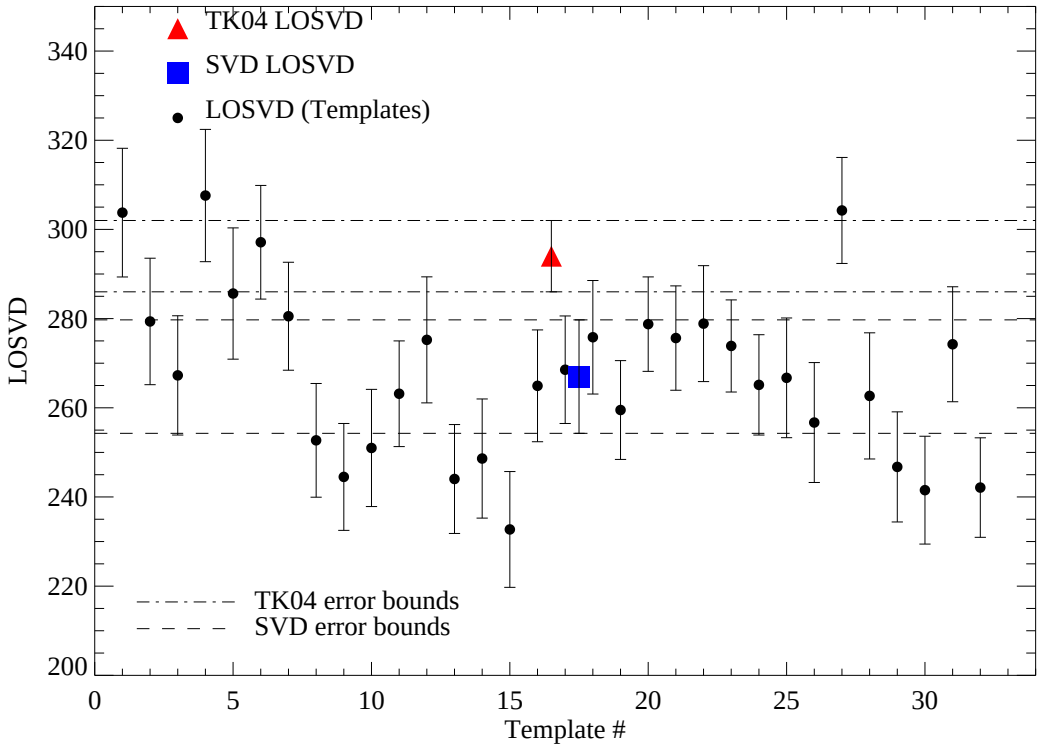

Figure 2.29: Plot showing the LOSVD estimates and associated errors for the elliptical galaxy in CFRS03, obtained using individual stellar templates; the combined value and error margin are overplotted (blue square). For comparison, the velocity dispersion for this system obtained by Treu and Koopmans (2004) from their best fit *lens model* and the associated error values are overplotted (red triangle)

2.10 Application of the SVD method to CFRS03

We finally implement the SVD method on the co-added spectrum of the elliptical galaxy of CFRS03 (Figure 2.20 described in Section 2.7.4). At the redshift of this galaxy, six strong absorption lines (Ca H, Ca K, SII, Hδ, G-band and Hγ) fall within the spectral window with S/N $\geq$ 15. The individual template solutions of the LOSVD and associated errors are shown in Figure 2.29 with the overall mean

and error margins ($267.5 \pm 12.7\,\mathrm{km\,s^{-1}}$) shown by the blue square. We compare our estimate of the velocity dispersion with the value of $294 \pm 8\,\mathrm{km\,s^{-1}}$ published in Treu and Koopmans (2004), which they obtain from their best fit Singular Isothermal Sphere (SIS) *lens model*. Even though our spectroscopic estimate of the LOSVD differs from this model by $\sim 10\%$, both values are more consistent with the velocity dispersion of a passively evolving galaxy and exclude the higher value derived by Crampton et al. (2002). These results are discussed further in the conclusions, which follow in the next section. Finally, the spatially resolved velocity dispersion measurements for this elliptical galaxy will be carried out along with the development of the lens model planned for future work.

2.11 Conclusions

This chapter describes in detail the pilot program applying our observational technique of IFU spectroscopy of gravitationally lensed systems to study baryonic physics in high redshift, star forming galaxies with sub-galactic scale resolution. The program was successfully carried out on the confirmed gravitational lens system, CFRS03+1077, using the Gemini GMOS-IFU spectrograph to carry out the observations. With this work, we achieved two important observational goals: (i) we tested the feasibility of our approach with a modest 4h observation and (ii) we gained valuable experience both in data acquisition and in analysis with the then newly commissioned GMOS-IFU. From the observations, we verified that the $0''.2$ IFU fibers adequately sample the median PSF from ground based observations and provide enough independent spatial elements on the lensed image, as needed for our spatially resolved investigations.

Pre-processing the observations using the Gemini pipeline resulted in appreciable residuals after sky subtraction and consequent low SNR for this low surface brightness target. Therefore, we carried out a series of tests aimed at characteriz-

ing the performance of the IFU and the efficacy of the data reduction steps, and thus improve the sky subtraction. The tests indicated significant contamination of the spectral continuum from scattered light. We have therefore incorporated an extra step in the Gemini pipeline to estimate and then apply a correction for the scattered light in the individual IFU fiber blocks. The simple procedure uses the residual flux in sky fibers after sky subtraction to estimate the level of scattered light in these fiber blocks; the corresponding amount of scattered light in the science blocks, which are interleaved with the sky blocks, is then obtained by interpolation. We assessed the improvement achieved by applying the correction to the processing of a twilight flat field; since the twilight field exposes all the IFU fibers to a uniform light source, this test provides a direct estimate of residuals with and without scattered light correction. On average, the sky residuals *in the continuum* are decreased by 25% of their levels without correction, with the reduction being $\sim 50\%$ in the extreme cases. In all the fiber blocks, the sky residual levels after correction are consistent within 10% of the expected Poisson noise level. We have applied this correction step in the data reduction of all the science observations.

It must be mentioned that due to the design layout of the sky fiber blocks in the pseudo-slit of the IFU, the correction procedure can only use these 5 regions to sample and then interpolate for the scattered light level in the 10 science blocks. The interpolation with a least squares cubic polynomial fit, may therefore leave some residual scattered light or to the loss of useful signal from the science blocks along with the scattered light due to overcorrection. The association that is seen between the spectral region with high flux and the corresponding CCD columns with scattered light, indicates that the probable cause is reflections within the GMOS camera or from the CCD. However, due to the complex pattern of the scattered light from multiple reflections within the camera optics, it is difficult, if not impossible, to assess the loss of useful flux or to correct for it. We propose two alternate approaches to overcome this drawback in the developments planned for

future, which are discussed with the concluding remarks in Chapter 6.

The principal scientific objective for this program was to test the hypothesis put forth by Crampton et al. (2002) that the elliptical galaxy, which is the deflector in CFRS03, has followed an evolutionary path different from that predicted by the Fundamental Plane model. With IFU spectroscopy, we proposed to verify their measurement of the LOSVD, which formed the basis for their finding. We developed a stringent selection procedure with spectroscopic cross correlation to identify fibers associated with the elliptical galaxy. This approach assured us of identifying only those fibers in which the spectral features, used for LOSVD measurement had S/N values ≥ 15. For determining the LOSVD at this SNR value, we adopted a direct fitting method which permits us to selectively mask out noisy spectral regions, thus giving a distinctive advantage over the Fourier based methods for this application. Our method uses χ^2 minimization to determine the parameters of the Gaussian representing the LOSVD; we employ the SVD method for the solution of the set of linear equations during the minimization. We have characterized and calibrated the recovery efficiency of our method using SDSS stellar template spectra as well as spectra of elliptical galaxies from the SDSS public spectroscopic catalogs, which have published velocity dispersions. Our calibrations indicate that our SVD method is able to recover the LOSVD in the typical velocity range observed in elliptical galaxies with errors $\leq 5\%$ from spectra with SNR ≥ 15 in the spectral regions used for the velocity measurement; it is for this reason that we adopted the spectral cross correlation method to identify the fibers instead of the conventional S/N in the continuum. We have assessed that the error introduced by mismatched stellar templates is $\sim 2\%$, with the error being $\leq 5\%$ even in the worst case; these levels of error are reported by the SDSS for their measurement methods. In our comparison with 25 published SDSS velocity dispersion measurements, the SVD values matched 24 within the associated error bars; the spectrum of the galaxy for which the values did not match, had only two spectral features with adequate SNR for LOSVD fitting

(compared to 6 or more features in all the other spectra with successful matches); this is the likely reason for the difference in the velocities determined for this one case by the SDSS and the SVD methods.

We have used the SVD method to determine the LOSVD of the elliptical galaxy in CFRS03 as $267.5 \pm 12.7\,\mathrm{km\,s^{-1}}$. Our velocity differs by over 5σ from the value of $380\,\mathrm{km\,s^{-1}}$ determined by Crampton et al. (2002), thus arguing against their hypothesis. Our velocity determination is more consistent with the estimate of $294\,\mathrm{km\,s^{-1}}$ by Treu and Koopmans (2004), with both results supporting the passive evolution of elliptical galaxies predicted by the Fundamental Plane model. Using the spatial resolution offered by the IFU observations, we plan to extract a radial velocity dispersion of this elliptical galaxy and thus estimate its dynamical mass distribution. This will form part of the work on building lens models for the systems we have observed, including those described in Chapters 4 and 5, and is discussed in the overall thesis summary in Chapter 6.

Even though these observations were tuned primarily for the LOSVD of the elliptical galaxy, the presence of the lensed arc within the IFU FOV encouraged us to attempt spatially resolved observations of this $z = 2.94$ galaxy, which if successful,would be a redshift milestone for such observations. However, the spectral S/N per IFU pixel, even with the improvements incorporated in the data reduction, was of order ~ 1 from the 4h of integration, and attempts to measure velocity offsets between different regions in the lensed image using the *weak absorption* features in the rest frame UV spectral region, gave inconclusive results.

As a positive outcome, however, the coadded arc spectrum, constructed using the spectral cross correlation technique we developed for these observations, permitted us to identify the location of the lensed counter image. This location matches a bright feature seen on the periphery of the elliptical galaxy in the HST image and falls close to the *likely* position proposed by Crampton et al. (2002) using their lens model. The location of the counter image provides an additional and strong

constraint for the development of the lens model.

Finally, this experience with IFU observations of a low surface brightness target ($\sim 22\,\mathrm{mag.arc.sec}^{-2}$) has helped us assess the integration time requirements for similar observations; the S/N of ~ 1 per spatial element from the 4h integration time corresponds to $\sim$ 25h per lensed galaxy to reach even the minimum S/N ~ 5 to measure velocity offsets between the (absorption) lines. However, the successful results from a similar observation by Swinbank et al. (2003) using the strong [OII]3727Å *emission* line on a z=1.034 lensed star forming galaxy using the same instrumentation, the GMOS-IFU, with 5h integration time, clearly highlights the feasibility of this technique - the presence of a strong emission line is tantamount to success at the current state of fiber optic and IFU technology. This equates to an upper bound on the accessible redshift as ≤ 1.5 for GMOS IFU observations.

The key challenge at present is to increase the sample size of lensed star forming galaxies in this redshift interval with sufficient surface brightness for spatially resolved observations. Chapters 3 and 4 describe the progress we have achieved in identifying and *confirming* suitable gravitational lenses using the CFHT Legacy Wide survey imaging data.

Chapter 3

Search for lensing galaxy groups and clusters in CFHTLS-Wide

3.1 Introduction

Recent observational results have clearly shown that baryon physics play a key role in galaxy evolution though our understanding of these potentially complex processes is far from complete. Detailed observations of such processes at work in individual low mass galaxies - principal star formers at all redshifts - are therefore a pressing requirement. Spatially resolved observations (spectroscopy and multi-color imaging) of the stellar and gaseous components will provide answers to the many fundamental questions discussed in detail in Chapter.1.2.1.

Toward this end, we have devised an observational approach using gravitational lensing combined with IFU spectroscopy for sub-galactic scale observations of high redshift galaxies. Results from our pilot study of CFRS03, described in Chapter 2, have shown the viability of this method for emission line galaxies at redshifts up to $z \sim 1.5$; the accessible redshift range for such studies may be extended in the near future with advances in instrumentation. Our conclusions from this pilot study are fully supported by results from other successful studies in the published

literature (Swinbank et al., 2003, 2006, 2007) using the same technique. The success of such studies have depended on two key observational features: (1) gravitational lensing, which conserves the surface brightness of these high redshift objects, and (2) the presence of bright emission lines for adequate spectral S/N. Consequently, the number of such detailed observations have been limited mainly due to the lack of a significant sample of bright, lensed galaxies to carry out these investigations.

Our first goal therefore is to build a catalog of confirmed lensed, emission line galaxies within the appropriate redshift interval, ($z \leq 1.5$) and with adequate surface brightness, ($\mu_i \leq 23\,\mathrm{mag.arc.sec}^{-2}$), for follow-up IFU observations. These constraints are solely for observational reasons: for ($z \leq 1.5$), the redshifted [OII]3727Å emission line, expected to be strong in star forming galaxies (and is therefore used as a star formation rate calibrator (Kennicutt, 1998)), falls within the accessible wavelength range of the GMOS. The surface brightness value is chosen to provide a S/N ~ 5 per IFU pixel in the [OII] emission line at $z \sim 1.5$ even with a moderate exposure time ($\sim 5h$), as calculated using the Gemini GMOS-IFU Integration Time Calculator *; this S/N is adequate for our science goals,

The extensive imaging data from the Canada France Hawaii Telescope Legacy Survey (CFHTLS) offers a suitable dataset in which to carry out our search. In particular, we have chosen the Wide component (CFHTLS-W) with a sky coverage of 195 square degrees and have designed our search strategy specifically to work with the multi-filter (g,r and i minimum) and deep ($i_{AB} \leq 24.0\,\mathrm{m}ag$) photometric data from this ongoing survey; pertinent details of this survey are given in Section 3.2 .

In this search for lenses in a wide field imaging survey, we narrow the search area first by detecting galaxy clusters and then carry out a dedicated search for strong lens images in these cluster regions. The rationale for this approach is that the large mass concentrations in clusters ($\mathrm{M} \geq 10^{14}\,\mathrm{M}_{\odot}$) lead to significant

*http://www.gemini.edu/sciops/instruments/itc/ITCgmos.html

lensing cross sections and therefore a high likelihood of lensing background objects (Kochanek et al., 2004). An order of magnitude estimate of their lensing cross section may be used to illustrate this; Appendix A contains a description of the geometry and relevant equations used. The deflection angle, α, in gravitational lensing depends on the local surface mass density, Σ, (Eqn. A.6), which is the projection of the three dimensional mass distribution on to the lensing plane. In this discussion, mass refers to the total dark matter and baryonic mass; and of this, the 80% dark matter content (WMAP 5 year results, Komatsu et al. (2008)) is expected to be the principal component. On the lensing plane, strong lensing, in which the background source is distorted to form multiple images, may only occur in regions where the surface mass density exceeds a critical value, Σ_{crit}, (Eqn. A.10). This is the case for all points within the Einstein angle, θ_E, (Eqn. A.5) or the equivalent projected Einstein radius, R_E; both quantities are functions only of the enclosed mass for given source and deflector redshifts Therefore, the Einstein angle or radius offer a direct scale of comparision of strong lensing cross sections of different mass distributions. For a galaxy cluster, with ($M \geq 10^{14}\,M_\odot$) at a redshift of 0.5, the Einstein angle is of order 10", when the background galaxy is at $z = 1.2$; we assume a centrally concentrated mass distribution for simplicity, noting that a more realistic mass parametrization leads to an Einstein angle of the similar size. Since the Einstein angle scales as the square root of the total mass,(Eqn. A.5), the θ_E for a cluster is 10 times larger than that of even a massive field galaxy with mass, $M \sim 10^{12}\,M_\odot$; this corresponds to an increase of two orders of magnitude in the lensing cross section and therefore a similar boost in the likelihood of lensing background galaxies with a given volume density and distribution with redshift.

In addition, centrally concentrated clusters lead to higher magnification of the lensed images, and can produce giant arcs of length ∼10". Due to the large image radius, the lensed arc is also well separated from the brightness of the central galaxies, which dominate the core of clusters. With the modern 8-m class ground

based telescopes, the arcs are marginally resolved along the minor axis, normally in the radial direction. The resulting surface area of these giant arcs combined with the surface brightness, which is conserved by gravitational lensing even for a high redshift source, provide the magnification boost to carry out spatially resolved IFU spectroscopy.

Therefore, we have chosen to search for giant arcs around galaxy clusters as a first step in constructing this catalog of lensed galaxies. We do accept that our present technique is not tuned for the detection of galaxy-galaxy lenses, similar to CFRS03. However, this work is being done as part of a larger, international collaboration, the Strong Lensing Legacy Survey, (SL2S). Within our collaboration, a sub-group is working on the detection and follow-up of galaxy scale lenses in the CFHTLS-Wide. Our cluster scale sample will therefore form a good complement to their work.

To summarize, we have adopted a three-step process to compile the catalog of lensing galaxy clusters from the CFHTLS-W photometric data:

- first, we detect galaxy groups and clusters with an efficient search method which uses the color and position information available for each Wide Field;
- second, within a pre-defined aperture around each detected group or cluster, we use a search algorithm tuned to identify arc-like objects;
- finally, we prioritize each detection by visual inspection, in conjunction with photometric redshift estimates based on available colors. Final spectroscopic confirmation is achieved with follow-up longslit or multi-slit (MOS) observations.

This chapter is devoted to a description of our cluster detection method, the tests for selection function, completeness and contamination and the resulting cluster catalog. The arc detection method and results from the longslit and MOS observations to confirm lensed galaxy candidates follow in Chapter 4. We begin in

Section 3.2 with a summary of pertinent details of the CFHTLS-W, the data set on which we carry out our search. Next, in order to explain the motivation behind the design of our cluster detection method, we review various published methods based upon *optical* data in Section 3.3. The strengths and limitations of each method and its applicability to the CFHTLS-W data are pointed out. We introduce our cluster detection method in Section 3.4, highlighting its relevance and specific advantages for this particular photometric data. The Monte-Carlo simulations we have used to test the selection bias, completeness and false detection rate of our detection algorithm are described in Section 3.5. In Sections 3.6 and 3.7, we present our cluster catalogs, categorized into high, medium and low quality based on the detection likelihood. As a comparison with other cluster detection methods applied to the CFHTLS observations, we apply our method to the XMM-LSS clusters (Pierre et al., 2007), and the candidate clusters in the Matched Filter catalog (Olsen et al., 2007). We conclude the chapter in 3.8 with a discussion of these comparisons, an outline of improvements in progress and future plans.

3.2 The CFHTLS-Wide survey

The soon to be completed CFHTLS photometric survey is an open collaboration between the Canadian and French astro-communities and is being carried out at the Canada-France-Hawaii 4m telescope on Mauna Kea, Hawaii. The survey is designed around the wide field imager, *MegaPrime*, at the heart of which is *MegaCam*, a thirty six CCD camera with 1 square degree field of view. CFHTLS is designed to address various cosmological as well as galactic science goals for which it has been granted 450 nights of observing time spread over 5 years (2003 - 2008). This section summarizes the survey parameters for the Wide component of the survey which is relevant to our work. Further details of the survey as well as the sky locations of

the survey fields may be found at the CFHTLS webpage [†].

The principal goal of the *Wide* survey is to map structure formation in the universe using cosmological weak lensing. To accomplish this, the survey will map 195 square degrees in 4 different sky patches (W1, W2, W3 and W4) to a depth of $i' \leq 24.5mag$. All the fields in the survey area will eventually be imaged in the full five filter $u^*g'r'i'z'$ set, closely matching the Sloan filters. The fields are initially observed with only the $g'r'i'$ filters with seeing better than 0".9; imaging with the u^* and z' filters as well as re-imaging with the r' are done later during a second pass through each Wide field. As of July 2008, the areal coverage (in square degrees) in the gri filters completed in the four fields are W1(44), W2(20), W3(41) and W4(16); the field-to-field variation in the total integration time in the different filters will be evened out as the survey proceeds toward completion.

Our principal objective is to discover a large sample of clusters at redshifts ≤ 0.8, which have a high likelihood for lensing emission line galaxies in the redshift range of interest to our IFU survey ($1. \leq z \leq 1.5$). The CFHTLS-Wide survey with its extensive sky coverage, adequate imaging depth and a minimum of three filter passbands provides a rich data set for which we tune our detection algorithm.

3.3 Review of cluster detection methods

From as early as 1937, following Zwicky's insightful prediction of the presence of dark matter deduced from observations of the Coma Cluster (Zwicky, 1937), galaxy clusters have been recognised as valuable probes of large scale structure formation in the universe as well as laboratories for studying galaxy evolution. Catalogs of clusters at ever increasing redshifts needed for such studies therefore continue to be published, each using innovative detection techniques that have kept pace with the advances in observational technology. Pioneering work in optical detection of

[†]http://www.cfht.hawaii.edu/Science/CFHLS/

clusters was carried out by George Abell (Abell catalog, (Abell, 1958)) and by Fritz Zwicky (Clusters of Galaxies catalog, (Zwicky et al., 1968)), both catalogs being based on meticulous visual examination of photographic plates with quantitative selection criteria. These methods have since been superseded by automated methods applied to digital data from CCD cameras, especially data from recent large surveys such as the Sloan Digital Sky Survey (SDSS) as well as surveys using large format CCDs such as the MegaCam on the CFHT; these automated methods form the core of this review. In addition, cluster catalogs are also constructed with detections at other wavelengths, such as in X-rays emitted by the hot gas trapped in the deep gravitational potential of clusters (e.g. Pacaud et al. (2007)), as well as in microwave wavelengths from inverse Compton scattering of the Cosmic Microwave Background radiation by the hot electrons in the intracluster medium, termed the thermal Sunyaev-Zel'dovich effect (LaRoque et al., 2003); however, this review focusses only on optical methods in keeping with the nature of our detection scheme.

Optical detection methods aim to identify the member galaxies of the clusters, utilizing one or more of their properties observed uniquely in the cluster environment to isolate them from their field counter parts. For the sake of completeness therefore, we first describe these defining properties of cluster members in optical observations, highlighting those which are particularly relevant to our detection scheme.

3.3.1 Optical properties of clusters

Clusters reside at the high mass end ($M \sim 10^{14}\,\mathrm{M}_{\odot}$) of virialised structures in the universe. In the hierarchical ΛCDM structure formation paradigm, clusters occur at the nodes of the mass filaments where they accrete infalling galaxies and gas in the inter-cluster medium. Dark Matter is the principal contributor (85%) to the mass budget of a cluster while hot gas, observed in X-rays, is typically (10%) with the visible galaxies making up the remaining (5%) only (Voit, 2005). In optical surveys however, it is the enhanced density of galaxies that is the most visible marker of

the presence of a cluster. A rich cluster like Coma contains over 3000 galaxies (with r $\leq$ 20mag) within a radius of $\sim$ 1Mpc (corresponding to a volume density of $\sim 1000 Mpc^{-3}$) (Komiyama et al., 2002), while even the much smaller Fornax cluster has a galaxy density of $\sim 500 Mpc^{-3}$ in its central 0.25Mpc (Ferguson, 1989); these greatly enhanced galaxy densities stand out in sharp contrast, as seen in Figure 3.1, against the number density of field galaxies which yeilds only one bright L^* galaxy within a volume of $\sim 100 Mpc^3$, based on the normalisation of the observed field galaxy Luminosity Function (Fried et al., 2001); the galaxy density enhancement between cluster and field environments is therefore 3-4 dex.

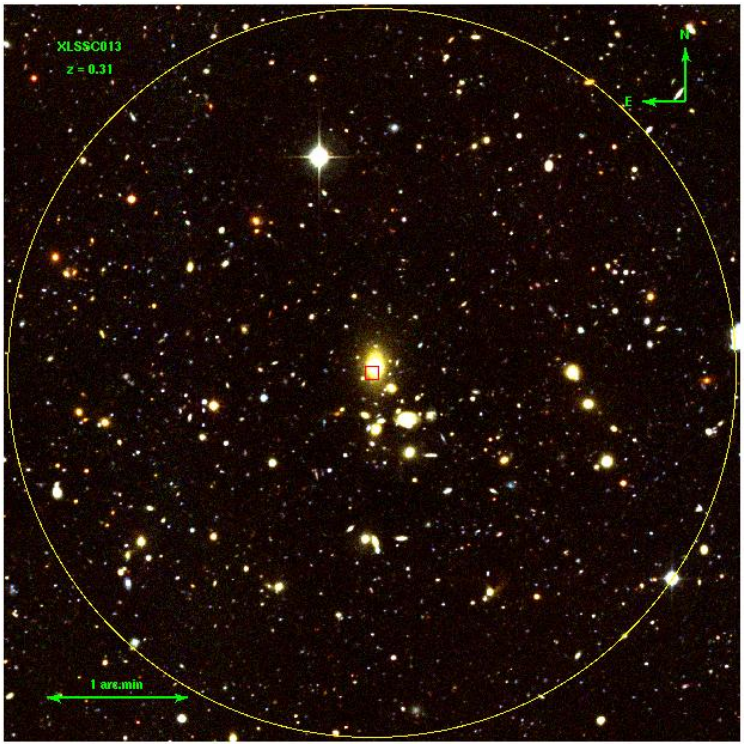

Figure 3.1: RGB color image of confirmed Xray cluster, XLSSC013, at redshift 0.31 from the XMM-LSS cluster surey (Pierre et al., 2007). Red square marks the center of Xray emission and the yellow circle shows the inner 0.5Mpc

This contrast between the galaxy densities in cluster versus field enviroments is futher enhanced by the 'Morphology - Density', $(T - \Sigma)$ relation, first observed

by Dressler (1980) in a sample of 55 rich clusters. The study showed that there was an increasing fraction of early type E+SO galaxies in the higher density cores of these low redshift clusters while the late type galaxies were preferentially found in lower density environments. This enhancement of the (E+S0) population in the cluster core is clearly seen in Figure.3.2, which shows the 15 spectroscopically confirmed early type members of the X-ray cluster, XLSSC013, at $z = 0.31$, from the XMM-LSS cluster survey (Willis et al., 2005). This radial trend of galaxy morphology in cluster environments has since been verified by several studies for low and intermediate redshifts (see for example Helsdon and Ponman (2003) and references therein). Recently, Smith et al. (2005b) have confirmed that this higher E+S0 fraction was in place even by $z = 1$; however, they find an evolution in the $(T - \Sigma)$ relation, with the fraction, $f_{(E+S0)} = 0.7$ being lower at $z = 1$ compared to the value of 0.9 observed in the local universe. This evolution in the E+S0 fraction is consistent with the 'Butcher-Oemler' effect (Butcher and Oemler, 1984) in which high redshift clusters are observed to have an excess of blue galaxies in their cores, indicative of ongoing star formation, compared to their low redshift counterparts. The Butcher-Oemler effect, also termed the 'Star Formation Rate - Density', $(SFR-\Sigma)$ relation, is measured as an increase in the blue fraction, f_b with redshift, and has been observationally validated using a variety of star formation indicators by several studies (see for example Gerke et al. (2007) and references therein). In their DEEP2 survey, Gerke et al. (2007) also find that at a given redshift, the more luminous galaxies are preferentially red and that richer clusters have a lower f_b.

Combining the two effects, there is a higher density of E+S0 galaxies in the cores of clusters compared to the field and the color of these galaxies evolves toward the red with cosmic time. Several mechanisms have been put forth as being responsible for this morphology transformation and color evolution in cluster enviromments though a fully consistent picture has not been agreed upon yet. Gerke et al. (2007)

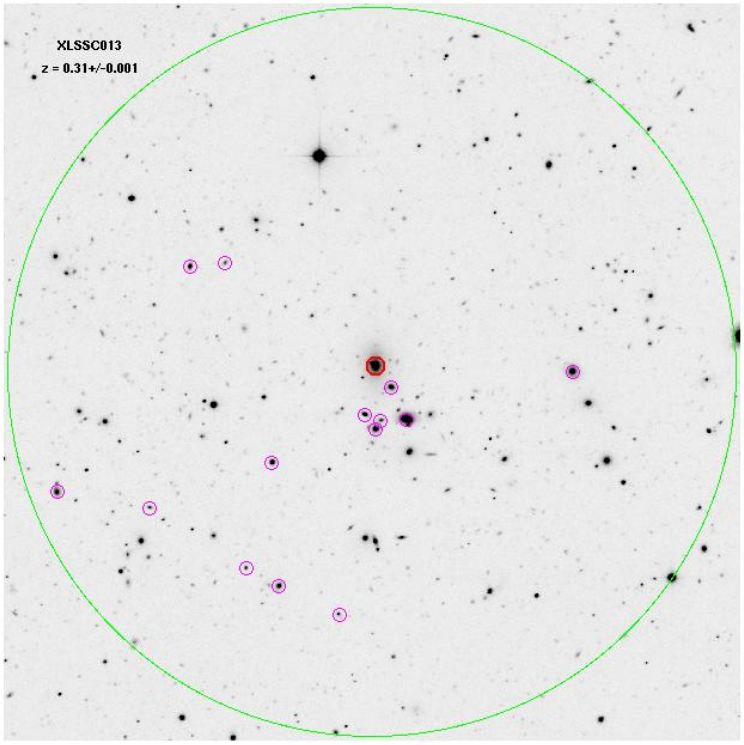

Figure 3.2: Spectroscopically confirmed early type (E+S0) member galaxies (maroon circles) and the BCG (red circle) of XLSSC013 within the inner 0.5Mpc (green circle) core of Xray cluster XLSSC013. This central enhancement in the population of luminous, early type galaxies highlights the Morphology-Density relation for this cluster at $z = 0.31$

point out that though the effects may be related, the mechanisms responsible for late to early type morphology transformation may be different from those responsible for quenching star formation and leading to the color evolution. Though a full summary of this interesting and ongoing debate is beyond the scope of this work, for cluster detection using photometric data, which is our focus, the clustering of early type galaxies offers a consistent and easily detectable signal.

In addition to their physical clustering, the (E+S0) galaxy population in a cluster, especially those within the central core regions, have been observed to possess a strong correlation between color and absolute magnitude. This *Color-Magnitude*

Relation (CMR) is seen as a tight ridge, the 'Red Sequence' (Gladders and Yee, 2000), which extends over several magnitudes with small scatter ($\leq$ 0.1mag) in a color-magnitude diagram (CMD). In addition, brighter, and hence more massive galaxies (assuming a simple mass-to-light ratio), are observed to have redder colors than less massive ones, which therefore leads to a small slope of $\sim$ 0.1 mag/mag in this color sequence (Kodama et al., 1998). For illustration, the Red Sequence of $XLSSC013$ is shown in Figure 3.3; the confirmed cluster members (red dots) lie along the red sequence defined by the bright central galaxy, BCG, indicated by the black square, thus distinguishing them from the field galaxy population (black dots) in a rest frame 1Mpc aperture centered on the cluster; shown in blue dots are the candidate cluster members identified by our cluster detection algorithm, which is described in detail in Section 3.4.

de Vaucouleurs (1961) first noted the existence of the correlation between the absolute magnitude and the ultra-violet colors of E+S0 galaxies in a survey of 148 galaxies. Visvanathan and Sandage (1977) confirmed the existence of the CMR with a systematic comparison of Virgo with eight other low redshift clusters, and also measured a uniform slope of 0.1mag/mag in all these clusters. With a similar comparison of the Virgo and Coma clusters, Bower et al. (1992) proposed that the homogeneity in the observed colors of early type members in clusters at similar redshift and the observed evolution in the slope of the CMR could be used as a cosmological distance indicator, as indicated earlier by Visvanathan and Sandage (1977) . The correlation has since then been well tested in clusters at increasing redshifts up to $z \leq 1.5$ (e.g. (Stanford et al., 1998, Kodama et al., 1998, Blakeslee et al., 2003, De Lucia et al., 2007)); recent results using near infra-red observations indicate that the CMR may have already been in place in proto-clusters as early as $z \sim 3$ (Kodama et al., 2007).

From this general body of work, there is consensus that the observed tight red sequence indicates that the stellar populations in cluster ellipticals are homoge-

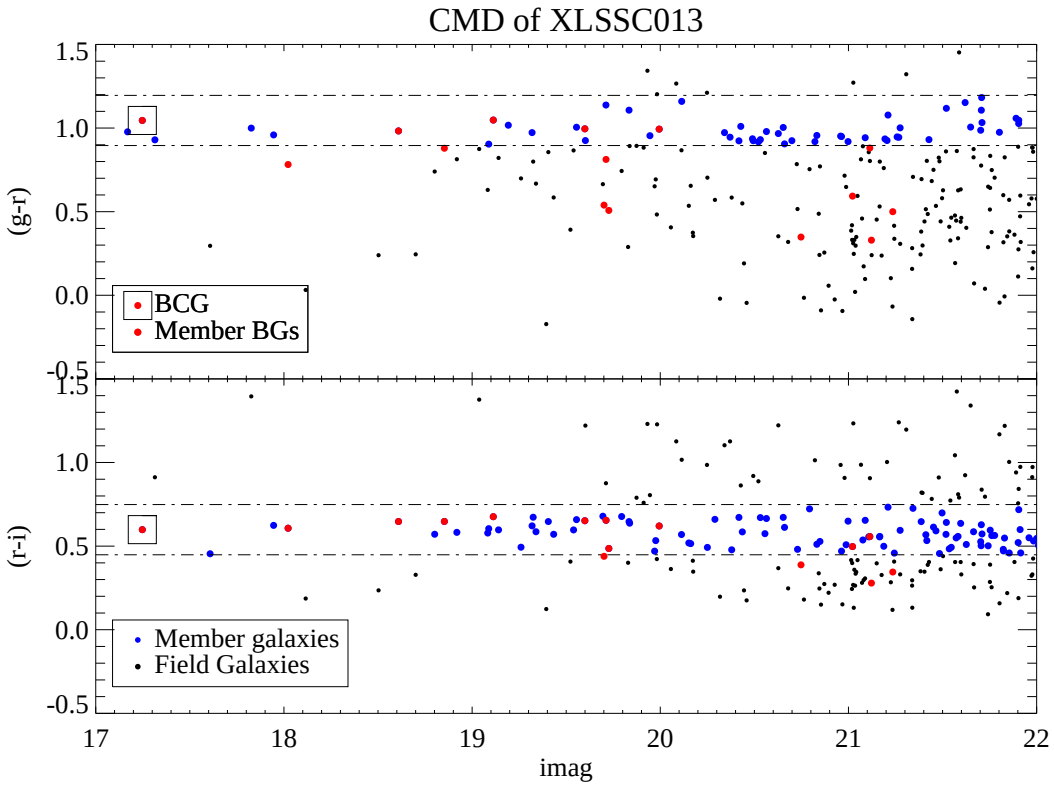

Figure 3.3: Color-magnitude diagram of confirmed X-ray cluster, XLSSC013 at $z = 0.31$, showing the Red Sequence of confirmed early type (E+S0) cluster members (Cluster BGs, red dots) defined by the BCG (demarcated in a black square). The two lines define the color cuts we use for selecting likely cluster members (blue dots) in our cluster detection algorithm, described in Section 3.4. The field galaxies within the detection aperture are shown as black dots

neous, formed very early ($z >> 1$) and have been passively evolving since then. In addition, the evidence clearly shows that the CMR is universal, being present even in poor clusters and is also identical in zero point and slope -within photometric uncertainties- in any two clusters at the same redshift. The measured intrinsic scatter of only a few centimags may indicate that star formation in all these galaxies happened in a single burst and was subsequently quenched in the cluster environment (Kodama and Bower, 2003, Kodama et al., 1998), which is expected in the

monolithic collapse model for elliptical galaxies (Eggen et al., 1962); however, De Lucia et al. (2006), Kauffmann and Charlot (1998) argue that the correlation may also be reproduced using the hierarchical assembly scenario of Λ-CDM cosmology. On a related question, Kodama et al. (1999) also show that the slope of the CMR is primarily a metallicity effect and not due to age (the deeper potential wells of more massive galaxies retain the metals from the initial burst of star formation while galactic winds drive them out of the less massive ones); recent work (e.g. (Brough et al., 2007, de Rossi et al., 2007)) challenge this simple interpretation arguing that the star formation in cluster ellipticals is more complex than the single burst model and that the slope arises due to a combination of metallicity and age effects. Though further discussion on this interesting question is outside the scope of this review, it is important to summarize the following properties since they are key to our cluster detection method:

- There is a higher density of early type E+S0 galaxies in the cores of clusters
- These (E+S0) galaxies have old, quiescent stellar populations (formation redshift $z >> 1$) which show no evidence of recent or ongoing star formation
- Due to the single burst of star formation followed by passive evolution, the (E+S0) cluster galaxies have homogeneous colors; due to their very early formation epoch, these stellar populations have redder optical rest frame colors than those in any other galaxy at the same redshift.
- The color clustering is universal and is found even in poor clusters; the scatter in color in any cluster is very small (typically a few centimags)
- Due to the increasing star formation rates in this cluster core (E+S0) population with redshift, there is a color evolution toward blue at earlier cosmic times

- However, the CMR in two clusters at the same redshift match in zero point and slope within photometric uncertainties (and hence may be calibrated to be redshift indicators).

- Due to luminosity segregation, the galaxies at the cluster core are brighter than those at greater distances from the center, thus making their detection easier.

Given these strong observational results, we have chosen to focus on this position and multi-color clustering of the (E+S0) cluster members for efficiently identifying clusters from the field galaxy population in the available multi-color optical photometric data.

3.3.2 1D methods

In this review, a detection method which uses only a single cluster property for detection, is referred to as a 1D method; 2D and higher dimensional algorithms are those that use correspondingly more properties. The most basic property of a cluster is the physical clustering of galaxies (as seen in projection on an image, without any redshift information). This is reflected as an enhancement in the density of galaxies per unit area compared to the statistical value for field galaxies. Used by both Abell (1958) and Zwicky et al. (1968) for visual detection of clusters, this enhanced galaxy density was used in the automated *Counts in Cells* method by Lidman and Peterson (1996). For the moderately deep, single filter data ($I \leq 22.5$mag) from their Anglo-Australian Telescope survey, Lidman and Peterson (1996) computed the *contrast* between the galaxy density in cells over the field value and detected clusters as enhancements above a threshold value. To avoid spurious noise peaks, they used the Schechter luminosity function to weight their detections. From the 13 square degrees of survey area, they detected 105 cluster candidates.

The count in cells method is well suited to single filter data, is easy to implement

and needs only low computational power (though this may not be a major advantage at present). However, the binning of the data leads not only to a loss of information but also dependency of the detected structures on the bin size chosen. An additional, and more serious, drawback is contamination due to projection effects since the method relies entirely on galaxy positions in the 2D plane of the sky. Moreover, this method does not utilize any color information, even when available, and so is a poor choice for the multi-color CFHTLS data.

Vornoi Tessellation, (VT), first proposed by Ebeling and Wiedenmann (1993) for source detection in images and later extended for cluster detection by Kim et al. (2002), Ramella et al. (2001), is an allied method, which enhances and detects the clustering density of galaxies. In this two-step method, all the sources (galaxies) in the detection image are first demarcated into contiguous Vornoi polygons, the area of each being an inverse measure of the local galaxy density. A percolation algorithm, such as the 'Friends-of-friends', (Huchra and Geller, 1982) is then used to detect associated peaks from this density map. VT retains all the advantages of the *Count in Cell* method while overcoming the disadvantage due to binning. However, the method is still prone to projection effects and is also not designed to include available color information, as in the CFHTLS.

3.3.3 2D methods

A powerful generalization of the simple count in cells was implemented by Postman et al. (1996) in the *Matched Filter* (MF) method. The contrast in this case is obtained by applying a filter which combines the expected (Schechter) luminosity function of cluster members as well as their radial (circularly symmetric) distribution. In this method clusters are detected as enhancements in the resulting density map. The method was first applied to 5 square degrees in the Palomar Distant Cluster Survey with a resulting catalog of 79 cluster candidates in the redshift interval $z \leq 1.2$. In a more recent application of the MF method, Olsen et al. (2007)

have used it on the 4 square degrees of CFHTLS-Deep fields to produce a catalog of 162 clusters complete to $z \sim 0.7$. This catalog provides a test set against which we may compare our detection method and we discuss results from this comparison in Section.3.6.

In the Matched Filter method, the reliance on an 'ideal' cluster model is both the strength and the drawback. By fitting a fiducial cluster model to the data, the method derives important cluster parameters, such as the richness and redshift, as part of the detection process. The method is ideal for deep, single filter data and can be tuned for different cluster models. At the same time however, the dependency on a cluster model biases the method against clusters which do not fit the assumed profile. This drawback becomes greater at higher redshifts, where the higher merger rates produce significant differences among clusters (Cohn and White, 2005). In addition, this method too is prone to projection effects since it fits all galaxies, including projected field galaxies, that lie within the aperture to the assumed cluster model.

This model dependence may be reduced by searching for clusters entirely in color space by using the Red Sequence of the (E+S0) cluster members, discussed in Section. 3.3.1. First proposed by Gladders and Yee (2000) in the *Cluster Red Sequence* (CRS) method, this approach comes with two major strengths: (i) by using color, it effectively reduces foreground and background contamination independent of the redshift of the putative cluster and (ii) it does not rely on an 'ideal' model for the radial distribution of the cluster members as the Matched Filter method does, thus reducing the selection bias. However, such methods need imaging in at least two filters for the necessary color information, which may not be the case in all surveys.

First results from their ongoing 'Red Sequence Cluster Survey' show 429 candidate clusters from nearly 10 square degrees (Gladders and Yee, 2005). By fitting a slope to the CMR (described in Section 3.3.1), and using the color evolution of

elliptical galaxies, the CRS method also derives the likely redshift of the detections; of the candidates in their first results, 67 lie in the redshift interval ($0.9 \leq z \leq 1.4$). In an associated publication, which is of relevance to our search for lensing clusters, Gladders et al. (2003) present 8 strong lensing candidates discovered by visual inspection of their RCS imaging. They use their results to argue that the observed higher incidence of lensing clusters at $z \geq 0.6$ in the RCS sample may indicate that the greater ellipticity or presence of substructure seen in high redshift clusters may boost their lensing cross section. This hypothesis can be tested using the statistically significant sample of lensing clusters detected from our current lensing cluster search.

It is important to point out that the RCS is a dedicated cluster survey and uses matched R_c and z' filters to isolate the strong $4000\mathring{A}$ break in early type galaxies, thus increasing the detection efficiency only in a specific redshift interval; this flexibility in choosing the filters may not exist in surveys designed for science goals other than cluster detection. Hence, in our method we adopt the approach of color cuts in multiple colors as used by Goto et al. (2002), discussed below, instead of detecting and fitting to the red sequence as in the CRS method.

In a similar detection scheme using color information, the *Cut and Enhance* (CE, Goto et al. (2002)) method applies a series of 34 color cuts to the objects in the photometric catalogs for 395 square degrees of SDSS early release imaging data. Each cut thus aims to isolate subsets of galaxies with similar colors from the three filter (Sloan gri) data. For each galaxy subset, this clustering in color is next combined with the galaxy density computed within cells on a grid covering the imaging area to create a color-position density map. In this computation, the clustering signals are amplified by using a weighting scheme based on the inverse square of the separation in color and position; smaller separation translates to a higher weight. The computed weights in each cell are converted into 'gaussian clouds' and added together to make a smooth density map. Next, the object detection software, 'Sex-

tractor' (Bertin and Arnouts, 1996) is used to detect peaks in each density map and thus produce one cluster catalog per color cut. Finally the detections in all the catalogs are combined, using selection rules described in the paper, to produce the final cluster catalog.

A closely related technique is the *MaxBCG* (Hansen et al., 2005), also developed to work with SDSS early release data. Here, each galaxy is tested for the likelihood of being a Bright Cluster Galaxy (BCG) using a combination of two estimators: (i) the number of galaxies within a color cut centered on the galaxy's colors, thus testing for a red sequence and (ii) the fit to an empirical BCG evolutionary track. The likelihood function is tested at a series of redshift slices and peaks in the estimated values are used to locate BCGs and the clusters in which they occur. This method obtains the richness and redshift of the cluster as part of the fit. A drawback is the use of the BCG evolutionary model since recent resutls from De Lucia and Blaizot (2007), Bild (2007) indicate that BCGs in certain rich clusters have ongoing star formation with colors up to $\sim$ 1mag bluer than the red sequence; such clusters would not be identified by the MaxBCG. In addition, the dependency on an empirical evolutionary track for all BCGs adds a further selection bias.

After investigating the methods reviewed here, we designed our color-based cluster detection method drawing upon the strengths of the CE and MaxBCG schemes (with significant changes to the likelihood estimation, see Section 3.4.1). The principal reason for our choice is that these color based approaches effectively reject foreground and background contamination with little dependency on a model. Our data, the CFHTLS-Wide, is also observed with Sloan filters and in at least two colors (see Section 3.2), and hence is well suited for such color-based schemes. Our investigations showed that using the galaxy positions for detection (as in MaxBCG) is more effective in rejecting noise peaks than using a density map on a grid (as in the CE method). However, our method does not rely on the modeled color evolution of elliptical galaxies like the RCS nor of BCGs as in MaxBCG; similar to the

CE, our method too does not seek any preferred radial distribution nor luminosity function reducing the selection bias further. Unlike both the CE and MaxBCG, our method estimates cluster richness and redshift only subsequent to the detection. We decided to separate the two steps since our principal aim is to detect mass density enhancements as likely locations to find gravitationally lensed arcs; estimating cluster properties is secondary and may be accomplished by using any suitable approach independent of and subsequent to the detection process. Finally, our method does not require any fine tuning or choice of parameters like the Matched Filter and may be easily applied to other multi-color imaging (using any filter system) with only minor changes.

3.3.4 3D and higher methods

Knowledge of the redshift of even a subset of the galaxies in the survey area provides a third dimension and a very stringent constraint that may be employed for cluster detection. The redshift may be measured directly from a spectrum or may be photometric, inferred from available colors. At the time of development of our cluster detection method, only (g-r) and (r-i) colors were available for most of CFHTLS-Wide survey area and spectroscopic information for a subset of bright galaxies is currently available only where the SDSS footprint falls on the CFHTLS fields. Using available SDSS spectroscopic redshifts, we have tested the accuracy of estimating photometric redshifts with HyperZ (Bolzonella et al., 2000) using only two colors. Our results indicate that for $\sim$ 30% of the galaxies the method fails catastrophically thus making 3D cluster detection methods inadvisable when only two colors are available. However, we include 3D methods in this review since we aim to include photometric redshifts in our detection method as CFHTLS-W u and z filter data become available in the near future.

By incorporating the redshift information, Kepner et al. (1999) refined the basic Matched Filter algorithm (Postman et al., 1996) into a $2\frac{1}{2}$ dimensional (using photo-

metric redshift) or a 3 dimensional (if spectroscopic redshifts are available) *Adaptive Matched Filter* (AMF) method. The AMF retains all the powers of the basic MF and significantly reduces or removes the noise in the model fit due to foreground and background contamination. With redshift information, the method provides better estimates of cluster membership and richness. However, the dependency on a cluster model still leaves it prone to miss clusters which do not match the input model. Kim et al. (2002), in a systematic comparison of the MF, the AMF and the Vornoi Tessellation methods on 25 square degrees of simulated SDSS imaging data, find that with the inclusion of luminosity and redshift information, the Matched Filter methods outperform Vornoi Tessellation both in detection efficiency and in estimating the cluster parameters.

The C4 algorithm (Miller et al., 2005), implemented on 2600 sq. degrees of SDSS data, incorporates position, five filter photometry and spectroscopic redshifts for cluster detection. Processing each galaxy in the catalog in turn, the method uses a 3D position bin (α, δ, z) around each galaxy to pick a set of neighboring galaxies ; next, with color cuts in the four colors available, the number of likely cluster members is estimated and quantified as a 'number count' for the galaxy being tested. By comparing the number counts obtained for 100 galaxies chosen at random but using the same position bin size and color cuts, the cluster likelihood is estimated. Using mock SDSS catalogs as well as clusters from N-body simulations, the method is tested to be over 90% complete and 95% pure for clusters with mass $\geq 10^{14}\mathrm{M}_{\odot}$ and up to redshift 0.12. The main drawback of this method, especially for detecting clusters at higher redshift, is the dependency on spectroscopic redshifts, which at present is expensive in terms of observing time.

This review illustrates that though there are a variety of published methods for optical detection of clusters, all of them rely on one or more of the well defined properties of early type galaxies observed in cores of all clusters. The available observations dictate the appropriate properties to be used. Given the well calibrated

astrometry and multi-color photometry of the CFHTLS-W described in Section 3.2, we base our detection method to fully utilize both these properties.

3.4 Cluster search in CFHTLS-W

Given the multi-color and deep CFHTLS photometric data, our natural choice is a detection method that uses both galaxy positions as well as all available colors. As mentioned in Section 3.3, in our design we have incorporated the ideas and advantages of four other methods from published literature. Details of our detection algorithm and its specific characteristics are given in this section.

The principal idea behind our method is to identify simultaneous density enhancements in the projected 2D positions of the galaxies as well as in the two colors, that are available for each CFHTLS-Wide field; this method may be extended to include more colors, as they become available. Clusters candidates are identified using a well defined metric computed with the position-color enhancement. Our method draws upon the strengths of four other methods reviewed in Section 3.3.3, with improvements tailored for the CFHTLS-W data: -1- the *C4* (Miller et al., 2005) though without redshift information, -2- to the *Cut and Enhance* (Goto et al., 2002), with a galaxy based density enhancement estimate, -3- the *MaxBCG* (Hansen et al., 2005) without relying on a BCG evolution model and -4- to the *Cluster Red Sequence* (Gladders and Yee, 2000) though we stipulate a minimum of two colors to increase the robustness of the detections. Our method *does not* impose a luminosity distribution or a modeled radial distribution of cluster galaxies,thereby minimizing any selection bias in the detections.

We compute this position-color enhancement (referred as the *weight*) within a predefined aperture around each galaxy in a magnitude selected set. This magnitude cut is user defined and is based on the depth of the available photometry; the default has been set at $i' \leq 20$mag for the CFHTLS-Wide data. The radius of the aperture

is also a user defined parameter; in our detection, it corresponds to a co-moving distance of 1Mpc at a redshift of 0.5. We chose the aperture size using results from simulations and the reasons are discussed in detail in Section.3.5. Using this (two colors + position) enhancement as a metric, we test for the likelihood of the galaxy being a member of a cluster. Galaxies with density enhancement (referred as the *significance*) greater than a threshold value are flagged as candidate cluster members. We determine this detection significance for each galaxy independently using a statistical estimate of a 'field galaxy' weight; the method used to obtain this field estimate is explained in Section 3.4.1. A 'friends-of-friends' algorithm, using color and position, then links the detected members into candidate clusters. We found that by locating the detection filter at each galaxy and not on a grid defined over the survey area (as is done in both CE and in RCS methods), our approach becomes more efficient in rejecting false positives due to noise peaks. This galaxy centered approach instead of a positional grid has been adopted in both the *Adaptive Matched Filter* (Kepner et al., 1999) and the *MaxBCG* (Hansen et al., 2005) methods specifically for this advantage.

3.4.1 Implementation

For cluster detection, we use processed images, with well calibrated astrometry, produced in-house for each 1 square degree CFHTLS-Wide field. The pre-processing and astrometric calibration of individual exposures for each filter is done by D. Balam as part of the CFHTLS-Wide reduction process; kind permission to use these images for the present project is gratefully acknowledged. We stack the individual processed images for each field and for each filter using the public software, 'Swarp ver. 2.16.4' from the Terapix group (author E. Bertin).

Object detection and photometry is done on the stacked images using 'Sextractor' (Bertin and Arnouts, 1996). The Sextractor output catalogs contain the position and color information required by our detection method. We use a pho-

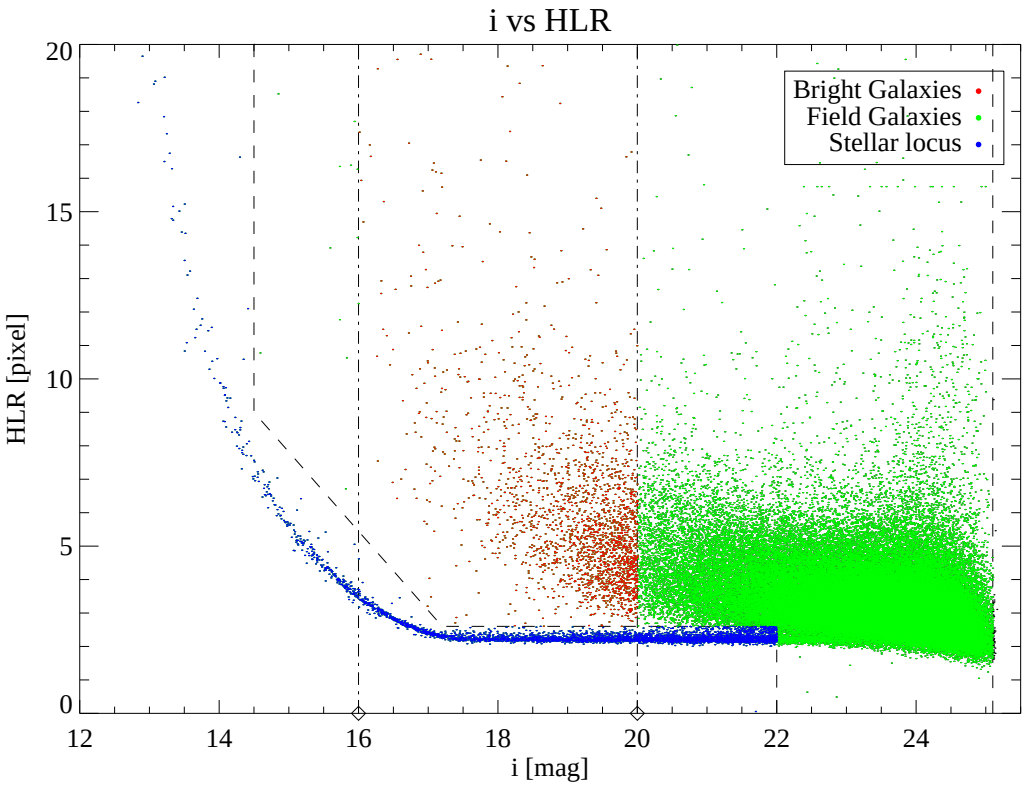

Figure 3.4: Plot of i' magnitude versus half light radius (HLR) of all objects in one CFHTLS-Wide field (sky coverage=$1deg^2$). The stellar locus defined by the HLR is used for star-galaxy segregation. The user defined magnitude and HLR cuts used are marked in dashed lines and the classification identifies stars (in blue), bright galaxies (red dots) and faint field galaxies (in green). Overplotted are the magnitude cuts (chained lines) used for selecting the bright galaxies which are then tested for cluster membership as described in §3.4.1

tometric zero point of 30 for all filters in Sextractor. The photometry is then re-calibrated to the Sloan system by matching objects found in common between the CFHTLS-Wide field and the SDSS DR4 imaging catalog [‡], where available. For Wide fields without overlap with the SDSS, the zero points are propagated from calibrated CFHTLS-Wide fields using objects in common between the two images

[‡]Available at http://cas.sdss.org/astrodr4/en/tools/search/IQS.asp

(typically a few hundred objects).

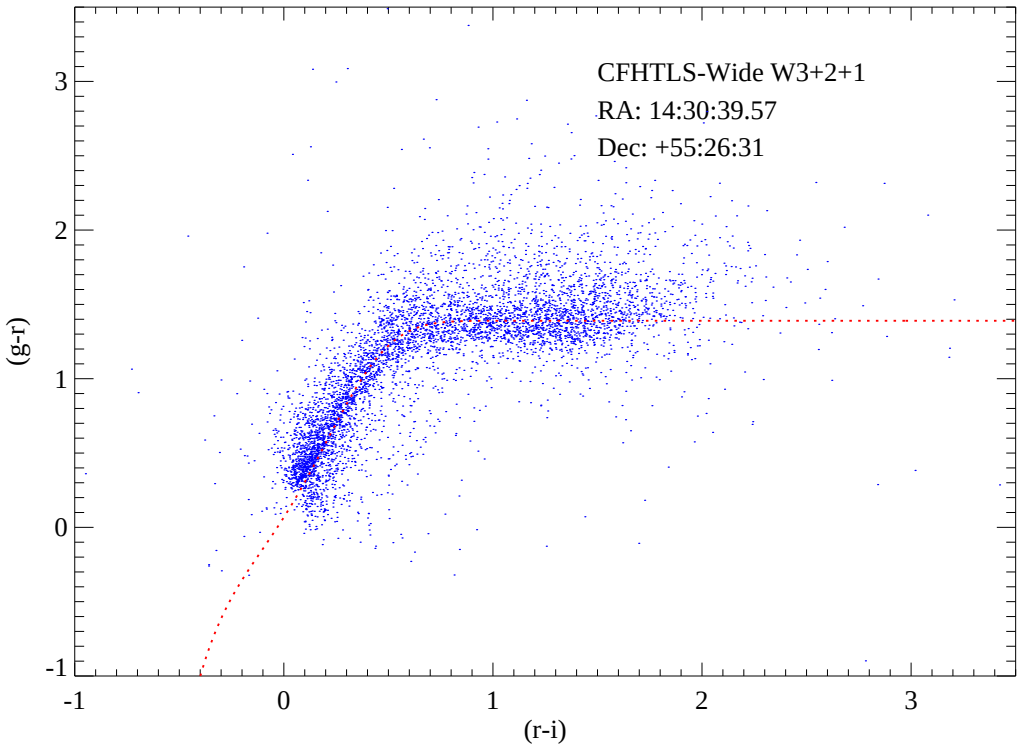

Figure 3.5: Effectiveness of our photometric calibration illustrated by a comparison of the observed stellar locus (blue dots) on a color-color diagram versus the empirical stellar color locus (red dashed line) derived from all the SDSS fields ((Finlator et al., 2000), with coefficients of fit from D.Balam, private communication).

We also tested for any systematic differences between the use of point sources and of extended objects for this photometric calibration. Using an i vs half-light-radius (HLR) cut we segregated point sources (stars, unresolved galaxies) from extended objects; a typical plot, Figure 3.4 shows the stellar locus and the HLR and magnitude cuts used. We then derived two independent zero point corrections, first for the point sources by comparing with SDSS PSF magnitudes and second for the extended objects using model maginitudes [§]. The difference in the zero

[§]Refer to http://cas.sdss.org/astrodr4/en/help/docs/ for details on SDSS magnitudes

point corrections between the two methods was typically less than 0.01mag for any filter; in comparison, the color cuts we use for cluster detection are typically larger, ~ 0.15mag. For our work, therefore, we only apply the zero point correction from extended objects using SDSS model magnitudes to all objects in our catalogs. In Figure.3.5, we illustrate the effectiveness of the zero point correction with a comparison between the corrected colors and the empirical stellar (gr vs ri) color locus derived from all the SDSS fields ((Finlator et al., 2000), with coefficients of fit from D.Balam, private communication)

For each CFHTLS-W field, the photometrically calibrated catalog forms the input to the cluster detector; for each object detected by Sextractor, the catalog contains the ID number assigned by Sextractor, (α, δ) in J2000 coordinates, x,y positions on the (20k x 20k) image, the HLR, and g, r, i Sextractor Kron magnitudes with corresponding photometric errors. We use simple magnitude (i $\leq$ 24mag) and HLR ($\leq$ 30 pixels) cuts to reject all objects with poor photometry. In addition, we exclude objects which are not detected in all three filters or have photometric errors greater then a user defined maximum (=0.5 mag in our implementation). We use the i - HLR relation Figure 3.4 to select the bright galaxies, referred as *BG* (shown as red dots) to be tested for cluster membership. The field catalog, (referred hence as *Fld*), consists of all objects in the observed field, which meet the magnitude and photometric selection criteria mentioned above. Each CFHTLS-Wide field typically contains of order 2000 BGs and 150,000 Fld objects.

Our cluster detection routines are a group of IDL (Integrated Development Language) procedures packaged into a single project file for portability. The cluster detection algorithm processes each BG in turn for the computation of its (position + color) weight; the (g-r) and the (r-i) weights are computed independently and the results are combined only in the last step of the detection process, when candidate cluster members are linked to identify clusters. For each BG, we select *all* objects (field objects as well as other BGs) within a fixed aperture of radius 0.5Mpc at

redshift $z = 0.5$, which corresponds to an angular size of 164 arc.sec.; this physical radius corresponds to half the virial radius of a typical cluster of virial mass, (M$\sim 10^{14}$ M$_{\odot}$). The chosen aperture size adequately covers the cluster core from which (E+S0) galaxies contribute the majority of the position and color weight. Other detection methods, e.g. Hansen et al. (2005), Kim et al. (2002), adopt a similar aperture size for this reason. In addition, we have chosen to keep the radius fixed after our Monte Carlo simulations showed that the detection significance was unaffected by the size of the aperture (refer to the discussions in Section 3.5.2). ¶

For the set of objects within the aperture, we then apply a color cut centered on the color of the BG to locate likely co-cluster members. The width of the color cut, (= 0.15mag), corresponds to the photometric color error of a galaxy at the faint magnitude end ($i' = 24$mag) of our field sample. The *cluster weight*, as a measure of the BG being a cluster member (our null hypothesis), is computed as,

$$W_c = \sum_{i=1}^{n} \frac{1}{(\delta_d + \epsilon_d)} * \frac{1}{(\delta_c^2 + \epsilon_c)} \tag{3.1}$$

where the position and color separations, δ, are measured with respect to the BG; suffixes refer to the separation in distance (d, measured in pixels) and in color (c, in mags). The summation is carried out only for the objects, which lie within the aperture as well as within the imposed color separation from the BG; these position and color cuts normally yield a few tens of objects per BG. Softening parameters, ϵ (¿ 0), are used to prevent numerical errors due to division by zero; the softening

¶We also tested the feasibility of basing aperture size on the photometric redshift of the BG estimated using HyperZ with g, r and i magnitudes, which were the only three filters available for the Wide fields at the time of these tests. Due to the use of *only two colors* during the photometric redshift estimation, our results showed that the fits fail catastrophically for a significant number ($\sim 30\%$) of galaxies. Therefore, we decided not to use a photometric redshift dependent aperture. However, when data in five filters becomes available, our detection routines can be easily modified to incorporate adaptive aperture radii based on the photometric redshifts of the BGs, as discussed under future work in Chapter 6.

parameter for distance is a tenth of the astrometric error (in pixels) and for color is a tenth of the color error for a galaxy at the bright end of our BG sample (the softening parameters, ϵ, represent a small fraction of the smallest expected error values in position and color).

Next, we compute the *field weight*, which is a measure of the BG being just a field galaxy (the alternate hypothesis). For this we use the field catalog with shuffled x, y positions for all the objects; their colors remain unchanged. The BG is placed at 1000 random positions in this shuffled field and at each position the weight is computed using Eqn. 3.1. The median and the inter-quartile distance of this set of 1000 weights is taken to be the field weight, W_f, and a measure of the scatter σ_f. Finally, the *significance*, which is the metric that we use to measure the likelihood of the BG being a cluster member, is calculated by,

$$S_c = \frac{W_c - W_f}{\sigma_f} \tag{3.2}$$

We repeat this computation for all the galaxies in the BG catalog. The computation of the cluster and field weights for all the BGs in a single CFHTLS-W field takes ~ 15 minutes on a single processor PC.

Detected cluster members are those with significance greater than a threshold, (3σ in our case), in *both* the $(g-r)$ and the $(r-i)$ colors. This threshold value was determined using the detection efficiency from our Monte-Carlo simulations, Section.3.5.2.

In the preceding steps, each BG is tested individually if it is a member of a cluster; subsets of these BGs may be members of the same clusters. We therefore group together individual cluster members (BGs with significance greater than the threshold) using a 'Friends-of-friends' algorithm (Huchra and Geller, 1982) in which galaxies within a certain linking length are combined into a single group. We use both colors and physical separation for linking member galaxies; our chosen link lengths are the aperture radius (in pixels) and the width of the color cuts used.

Finally, we separate the detected clusters further into *gold, silver and bronze* categories depending on their maximum detection significances being greater than 5σ in both colors, greater than 5σ in just one color or less than 5σ in both, respectively; note that all these cluster members satisfy the minimum detection significance of 3σ, as mentioned earlier.

3.5 Monte Carlo tests for completeness and contamination

In the design of our detection method, we have incorporated a fully automated pipeline requiring no user intervention during the cluster selection, thus minimizing any selection bias due to human error. In addition, the method fully utilises all the available observational data and is flexible enough to incorporate additional information (e.g. photometry in the u^* and z' filters, photometric redshift estimates), when available. We have also maintained the dependency on a cluster 'model' to a minimum, thus minimizing bias against clusters which do not fit the fiducial model. In addition, this low dependency on a cluster model minimizes the need for fine tuning of parameters. By keeping the dependency on parameters to a minimum, we are able to run the detection on each CFHTLS-Wide field consistently with the same set of detection parameters.

Despite these safeguards, the method is still prone to selection bias since it assumes the universal presence of the CMR in *all* clusters, including poor clusters with few members. We test this assumption using two approaches, first with Monte Carlo tests on synthetic catalogs as detailed in this section and then with a comparison with two published CFHTLS cluster catalogs, the XMM-LSS and the Matched Filter catalogs, discussed in Section.3.6. In addition, we use these simulations to estimate the contamination of our cluster catalog from false positives, e.g. chance superpositions of galaxies with matched colors, as well as completeness for a spec-

ified cluster richness and redshift. It is with these results that we have set the detection threshold of 3σ for candidate cluster members.

3.5.1 Simulation methodology

In published literature two methods are normally adopted to carry out Monte Carlo simulations, either using synthetic clusters planted amongst observed field galaxies whose positions have been shuffled, or by placing synthetic clusters in a synthetic field. Our detection depends sensitively on color matches, hence the photometric field and cluster catalogs used in the tests should be self-consistent in colors. We investigated the method of synthetic clusters on shuffled CFHTLS-W photometric catalogs and found that our recovery rate was unrealistically high (100% even at $z \sim 1$) because of the significant difference between the synthetic colors of cluster members and the observed colors of the field galaxies. Therefore, we have adopted the latter approach of simulating synthetic clusters in a synthetic field, taking care to mimic actual observations by using published and well tested empirical relations or theoretical results in constructing the photometric catalogs used in the simulations.

We assume a total field galaxy population of 150,000, the median number of galaxies with $i' \leq 24$mag found in a 1 square degree CFHTLS-W imaging field, see Section 3.4.1. We first generate the field galaxy number distribution, $n(z, r')$, as a function of redshift and apparent r-magnitude, using the model source galaxy distribution commonly used in weak lensing studies (Brainerd et al., 1996)

$$n(z, r') = \frac{\beta z^2 e^{-(z/z_0)^\beta}}{\Gamma(3/\beta) z_0^3} \tag{3.3}$$

where, $z_0 = z_0(r)$. This normalized, parametric fit to observed galaxy distribution in deep redshift surveys is applicable up to redshift $z \sim 1$ and $20 \leq r \leq 24$, and is thus well matched to our range of interest.The form of the distribution function for four apparent magnitude bins is shown in Figure 3.6, using the values of the fitted parameters from Brainerd et al. (1996). In this field galaxy population, we assume

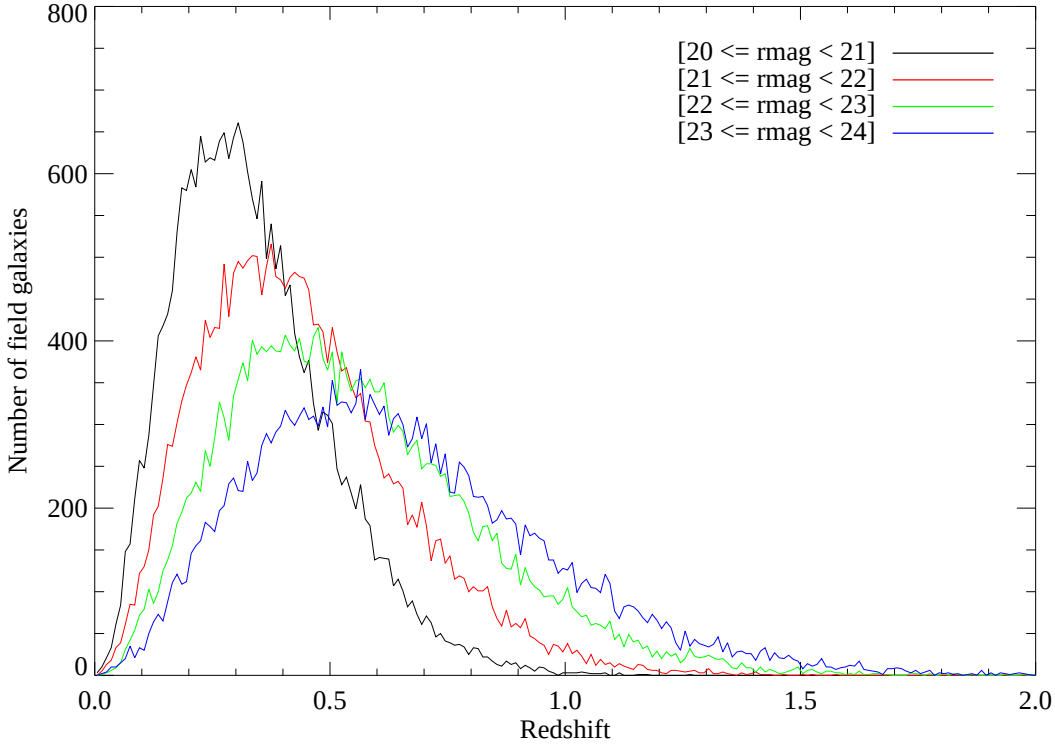

Figure 3.6: Synthetic field galaxy distribution with redshift as a function of r' magnitude generated using Equation 3.3 and values of the fitted parameters from (Brainerd et al., 1996); each distribution contains galaxies in 1mag bins in the interval $20 \leq r'mag \leq 24$

that there are equal numbers of early type E and S0 and late type Sb galaxies. Observations of field galaxy luminosity functions and their evolution with redshift for different galaxy morphologies have however shown that the field population is dominated by late types and that their luminosity functions evolve toward higher luminosity with redshift, while early and intermediate types show little evolutionary trend (e.g. Canadian Network for Observational Cosmology, CNOC2, survey Lin et al. (1999)). Therefore our assumption of equal numbers assigns a higher number density of (E+S0) galaxies to the field than the observed value; consequently, there is an increase in the field weight (more red galaxies in the field matching the color

of the BGs) and therefore a reduction in the detection significance; in other words, the detection significance from our Monte Carlo trials may be taken to be lower limits, making them a more stringent test of our detection method.

For these three galaxy types, we compute the synthetic colors with the evolutionary galaxy SED models (Bruzual and Charlot, 2003) and the transmission functions of the CFHT gri filters, assuming a uniform formation redshift, $z = 10$. We have verified that varying the parameters of the SED models, such as formation redshift or metallicity, have little effect on the results of our simulations since such changes affect both the field and the cluster galaxy colors equally; for our simulations, it is necessary that the field and cluster galaxy colors be consistent *relative* to each other, their absolute values are of little import. To the generated colors, we add photometric errors using the prescription in Sextractor (Bertin and Arnouts, 1996) with the published CFHTLS magnitude limits for the different filters. The positions of the field galaxies are distributed randomly within the (20k×20k) field.

Our objective is to test the effectiveness of our method in detecting clusters with different numbers of members and Abell richness (Abell, 1958) and at various redshifts. Therefore, for generating each synthetic cluster, we start with a prescribed number of member galaxies and select their absolute magnitudes from the Schechter luminosity function. For our simulations, we use published values of Schechter function parameters, $M^* - 5log(h) = -20.67$, faint end slope $\alpha = -1.2$ and normalization, $\phi^* = 0.0146h^3Mpc^{-3}$; these values are taken from Blanton et al. (2003), and apply to the Sloan r-band filter for galaxies at z=0.1. With the generated absolute magnitudes, converted to corresponding apparent magnitudes at z=0.1, we then compute the Abell richness of the synthetic cluster. We iterate this procedure till the generated cluster richness matches the Abell richness value for which the simulation is carried out.

We assign the morphologies and projected positions of member galaxies using observed results from literature for the morphology-density relation and the lumi-

nosity segregation of cluster galaxies. Applying the observed luminosity segregation from the ESO Nearby Cluster Survey (ENACS, (Biviano et al., 2002)), we designate all cluster members with absolute magnitude $M_r \leq -22.$ as elliptical galaxies, which populate only the cluster core. Probability density functions, derived from Figure 4 in Biviano et al. (2002), are used to assign the projected radial distribution of these bright galaxies; their angular distribution is randomly assigned, assuming circular symmetry. The cluster members, fainter than $M_r = -22$mag are assumed to follow the Plummer radial distribution; their angular distribution is assumed to be circularly symmetric and is therefore randomly assigned. Depending on the radial position of each member, the morphology (E, S0 and Sb) is determined using the observed morphology-density results from Thomas and Katgert (2006) (the required probability densities are computed from results in Figure 2 of the publication). The colors of the E, S0 and Sb cluster galaxies are obtained from the *same* SED models for these morphologies used for the field galaxies, thus maintaining color consistency. At the assumed cluster redshift, member galaxies with apparent magnitudes below the survey limit of $i > 24$mag are not included during detection. Photometric errors for the cluster members are assigned using the same method as for the field galaxy population, thus maintaining consistency in their photometry. Finally, we wish to emphasize that though we use the Schechter luminosity function and the Plummer radial distribution function to generate the synthetic cluster, our detection method *does not* rely on these models and uses only cuts in position and in colors for locating candidate cluster members.

The synthetic cluster is then merged with the field by placing it at a random position in the 20k x 20k field and converting the radial and angular positions of the cluster members into field x,y positions. The BG catalog for detection contains cluster members brighter than the magnitude cut (see Section 3.4.1); all cluster members are treated as part of the *Fld* catalog as well. These two catalogs form the input to the cluster detector, thus following the methodology we use for the actual

CFHTLS-W fields. The detection routine is repeated for a user defined number of trials (typically 100 times) for each synthetic cluster, with a different cluster location for each run. The (g-r) and (r-i) detection significances as well as their median and inter quartile values are written to file for analysis. The completeness and contamination results from these Monte Carlo simulations are discussed in the following section.

3.5.2 Monte Carlo results

We first test the rate of false positives for different significance thresholds, (Eqn.3.2), in order to check for any underlying bias in our multi-color based cluster detection method, for instance due to a chance superposition of galaxies being classified as a cluster. For this we select 100 bright galaxies (with $i' < 20$mag, the magnitude cutoff we impose for BGs in our cluster detector) and compute the median and scatter in their field weights, (Eqn.3.1), from 100 random locations in the field, repeating this process in redshift increments of $\Delta z = 0.05$ in the interval $0.1 \leq z \leq 1$. The false positive rate is taken to be the percentage number of times a galaxy in a random field position is flagged as a cluster with significance greater than the chosen threshold in a particular color. The histograms, shown separately for the $(g' - r')$ and the $(r' - i')$ colors in Figure.3.7, are compilations of the median false positive rates for a representative set of galaxies, each bar representing a redshift bin; results for different significance thresholds are represented by the colors indicated. We test the false detection rates for significance thresholds of 1, 2, 3 and 5σ.

The results show that a 1σ detection threshold leads to an appreciable contamination due to false positives of $\sim 20\%$ in both colors; the contamination rate shows no clear correlation with redshift, since the detections are based on galaxy colors and not on magnitudes. The false positive rate decreases to $\sim 5\%$ at a threshold of 2σ and drops to $1 \sim 2\%$ at 3σ; with further increase to 5σ detection significance, the contamination drops essentially to 0. In addition, during cluster detection, we

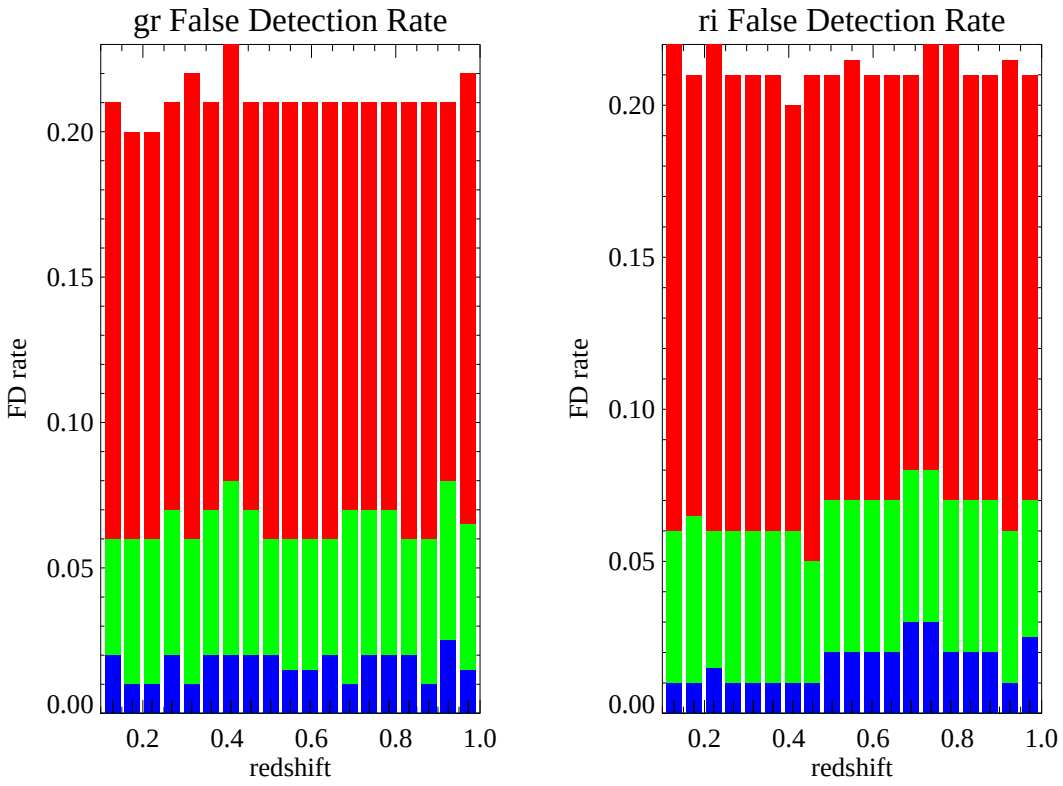

Figure 3.7: False detection rates for our cluster detection method estimated from Monte-Carlo simulations using significance thresholds of 1σ (red), 2σ (green), 3σ (blue) and 5σ (essentially zero)

impose the more stringent constraint that the significance should exceed the detection threshold in *both* colors; therefore, we have accepted the 3σ threshold, with a combined contamination $\sim 1\%$, for cluster detection. It must be mentioned that in this False Positives test, we included bright galaxies with various magnitudes up to the magnitude cut of $i' \leq 20$mag and did not find any dependency on the magnitude of the BG.

As a further test, we compute the completeness of our cluster detections using the recovery rate of synthetic clusters which are generated to resemble three observed clusters of different Abell richness classes. The results presented in Figure.3.8 pertain to clusters which resemble Coma (Abell richness class $A_c = 2$, with number

of member galaxies, $N_{gal} = 500$ with apparent magnitude $i' \leq 24$mag at $z = 0.1$, our magnitude limit for cluster detection), Fornax ($A_c = 1$), and a poor WBL cluster ($A_c = 0$) (WBL named after the authors of the catalog of poor clusters, White, Blyton and Ledlow, (White et al., 1999)); in the discussion we refer to these three classes by the names of their template clusters. The figure shows the detection significances in each color (*left panel* (g-r), *middle* (r-i)), as well as for the both colors combined (*right panel*), for these clusters as a function of redshift. These results pertain to 100 realizations of each class of cluster (ie. 100 Coma-like clusters generated using the method described in Section 3.5.1 and similarly for the other classes); the detection significance, (Eqn.3.2), for each cluster is computed at 100 random locations in the field in redshift increments of $\Delta z = 0.05$ in the interval $0.1 \leq z \leq 1$.. The magnitudes and colors of each cluster, generated at the fiducial redshift of 0.1, are computed taking into account cosmological dimming and k-corrections; at each redshift, member galaxies fainter than the magnitude limit ($i' = 24$mag), are not included in the computation. In these plots, the significance for each cluster at each redshift is taken to be the median of the significances computed at the 100 locations. The completeness in each color at each redshift step is then computed as the fraction of clusters with median significance greater than 3, the threshold we have set for cluster detection based on the false detection estimates. Figure 3.9 plots the median significance values with the 1σ scatter indicated; the significance threshold is also indicated.

The comparison shows that the detections are complete to $\geq 80\%$ for Coma in both the (g-r) and (r-i) colors at all redshifts up to $z \sim 0.8$; the detection efficiency drops rapidly at higher redshifts and asymptotes to a few percent (essentially equal to the false detection rate) by $z \sim 0.9$. This high detection efficiency is driven mainly by the bright early type galaxies in the core; their color clustering increases the detection significance while their bright magnitudes ensure that they are above the $i' \leq 24$ magnitude limit of the survey even at the higher redshifts. In addition,

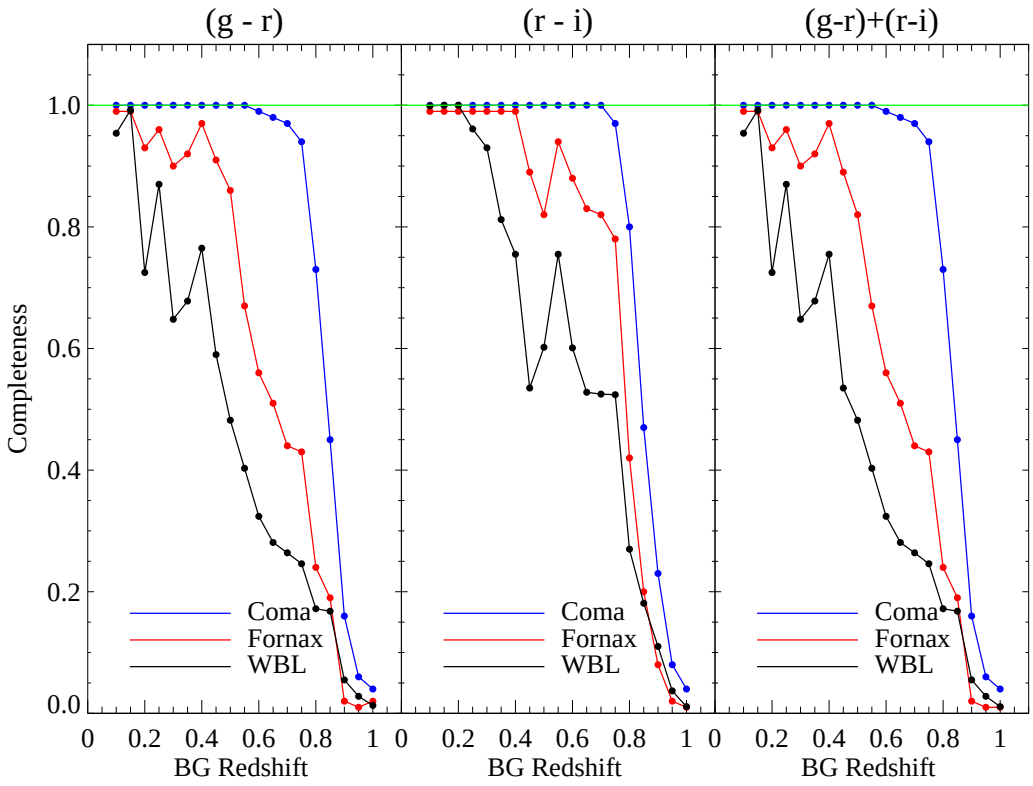

Figure 3.8: Completeness as a function of redshift for a Coma-like (blue), Fornax-like (red) and a poor WBL cluster (black); the completeness values have been estimated for the (g-r) and (r-i) colors separately, as well as for both colors combined

at all redshifts, the (r-i) detection significance is higher, as is expected from the homogeneous red colors of the early type galaxies in the cluster core; the combined detection significance, (right panel), therefore closely mimics the (g-r) significance, which is the smaller of the two significances. In the other cluster classes, the Fornax clusters are detected at efficiency $\geq 80\%$ only to $z \leq 0.6$ while the WBL retain this efficiency only till $z \sim 0.3$. It must be pointed out that though the early type (E+S0) cluster members are the principal contributors to the detection significance, the late type galaxy colors fall within the color cuts at certain redshift intervals. This leads to a corresponding increase in the detection efficiency at these redshifts, as seen in Figure 3.8, with the rise and fall of significances, instead of a monotonic decrease.

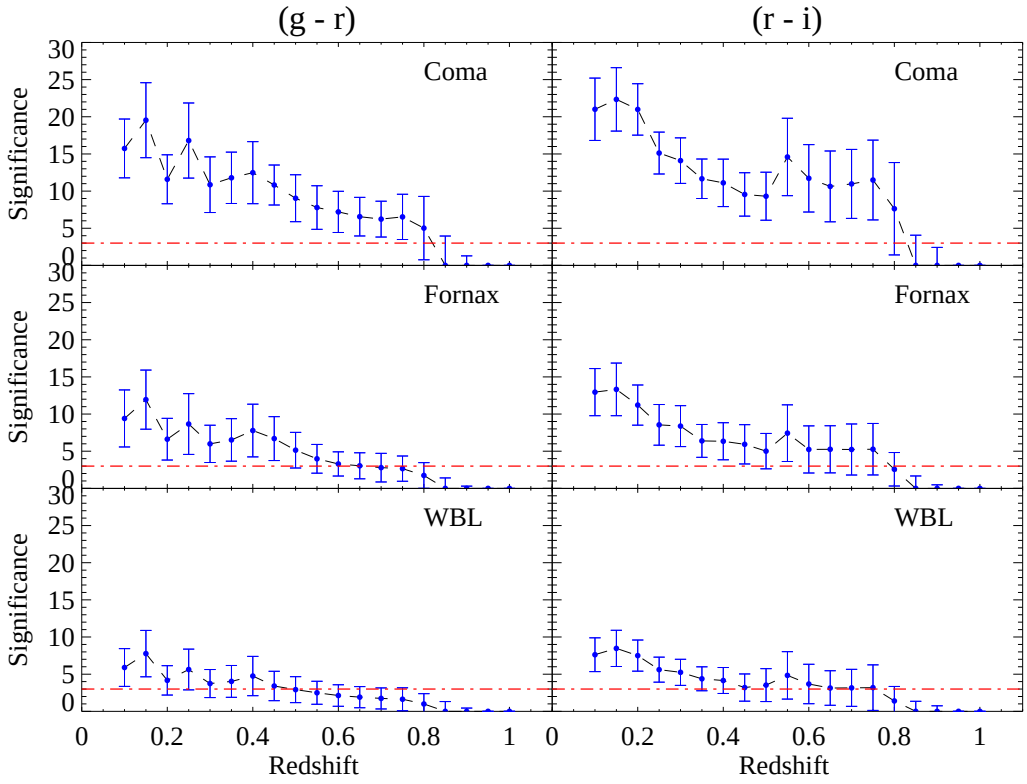

Figure 3.9: The median and 1σ scatter in the detection significance values as a function of redshift computed for the Coma-like, Fornax-like and a poor WBL cluster; the significance values are shown separately for the (g-r) and (r-i) colors. The red line indicates the 3σ threshold we have adopted for cluster membership

Our principal goal is to identify simultaneous enhancements of galaxy density and color as seen in photometric data and use these as proxies to signal the presence of mass enhancements due to clusters, therefore with the increased likelihood of detecting strongly lensed background galaxies. With the Monte Carlo simulations, we have tested the efficacy of our multi-color based detection scheme and have also determined the optimal detection parameters for this approach.

3.6 Cluster Catalogs, Deep Fields

As the first application of our cluster detection method, we applied have it to the CFHTLS-Deep fields, which cover four patches each of $1\deg^2$ within the larger Wide fields. Other than just being proof of concept, the resulting catalogs permit us to compare our detections with those of two other existing cluster catalogs for the CFHTLS-Deep fields, -1- The Matched Filter cluster catalogs (the MF catalogs, (Olsen et al., 2007), for the four CFHTLS-Deep fields) , and -2- the XMM-LSS cluster catalogs, (X-ray Multi-Mirror mission Large Scale Structure survey, (Pierre et al., 2007) for the CFHTLS-Wide field 1, which includes Deep field 1).

Table 3.1: Comparison of cluster detections in CFHTLS-Deep

Field	N_{gold}	N_{silver}	N_{bronze}	N_{total}	MF_A	MF_B	MF_C	MF_{total}
Deep 1	18	8	7	*33*	19	13	14	*48*
Deep 2	29	17	17	*63*	17	18	10	*45*
Deep 3	23	19	8	*50*	8	6	6	*20*
Deep 4	10	7	6	*23*	11	16	9	*36*

Comparison of the numbers of clusters detected in the four CFHTLS-Deep fields by our method with those in the Matched Filter Catalog (Olsen et al., 2007)

Details of the numbers of clusters detected in each of the CFHTLS-Deep fields by our method are given in Table.3.1, separated into *Gold, Silver* and *Bronze* categories (as defined in Section 3.4.1). In addition, a sample of RGB color composites of representative candidate clusters (2 each from the Gold, Silver and Bronze categories) drawn from the D1 field are shown in Figure.3.11 to visually highlight the presence of red sequence galaxies in the cores of these clusters, which is picked up by our method. In Table.3.1, the number of detections by the Matched Filter method (Olsen et al., 2007) are also listed for comparison; Olsen et al. (2007) use *visual inspection* of gri color images to classify the MF cluster candidates as follows: *Class A* show a clear overdensity of galaxies with homogeneous colors; *Class B* show an overdensity but do not exhibit clustering in colors and, *Class C* visually indicate

little enhancement either in position or color of their likely member galaxies. The numbers listed under these three classes for the MF clusters are taken from their public catalogs ‖.

Table 3.2: MF clusters in CFHTLS-D1 detected also by cluster detector

MF class	Number	N_{gold}	N_{silver}	N_{bronze}	N_{ND}
A class	19	12	-	-	7
B class	13	2	3	2	6
C class	14	6	1	1	6

Breakdown of the MF cluster detections in CFHTLS-Deep 1 which are also detected by our cluster detection method, classified by the assigned class and a non-detections (ND); details of the classification scheme are described in §3.6

The results in Table.3.1 show that there is noticeable field to field variation both in the number of clusters detected by our method as well as in the make-up of the categories of these detections. Other than cosmic variance due the presence of large scale structure along the lines of sight of these 1 deg^2 patches, the differences arise due to the variations in the observed depths in the three filters in these fields, especially in the case of D4, which was added to the survey three years after commencement of observations. This field to field variation in detected numbers in the three classes is evident in the Matched Filter results as well, though the pattern of variations is different from that seen in our method.

Carrying this comparison a step further, Table 3.2 lists the breakdown of each detection class in the MF cluster catalog, which are also detected by our cluster method in this blind trial; the results pertain to the Deep 1 field, with similar breakdown values obtained for the other Deep fields. To generate this classification, the positions of the candidate clusters in our cluster catalog are matched with those of the MF clusters, with a match being assigned if the positions fall within a distance equal to our detection aperture. It must be noted that during this match up, it

‖http://webviz.u-strasbg.fr/viz-bin/VizieR-2, J/A+A/461/81

was found that $\sim 30\%$ of our clusters contain more than one MF cluster; this was specially true of our high significance *Gold* category. The reason is because we link together detected BGs within one detection aperture radius of each other into a single cluster candidate; the MF method on the other hand, treats each detection location as an independent cluster.

The comparison shows that our detection method matches all the MF Class A detections that lie at redshifts z $\leq$ 0.8; the 7 non-detections lie at higher redshifts, according to the photometric redshift value assigned by the MF cluster filter. Similarly, the $z \geq 0.8$ MF candidates in Class B and C are not detected by our method along with $\sim$ 25% of cluster detections at redshift below 0.8; nearly all these low redshift non-detections lie at z $\leq$ 0.2. One possible cause may be that our detection aperture size is not including all the galaxies in the core of these low redshift clusters to provide the 3σ minimum detection significance. However, this effect is not observed in the Monte Carlo tests, where we observed the converse in that the detection significance was insensitive to aperture size above a certain minimum radius; this is the justification for the fixed detection aperture we use. An adaptive aperture based on photometric redshift, planned for a future version of cluster detector, may address this cause, if present. The other possible reason for the mismatch between MF and our detections at z $\leq$ 0.2 may be that the MF method, relying solely on galaxy density enhancement in a single filter, is more prone to contamination at lower redshifts, where the number of galaxies above the magnitude threshold is higher, leading to enhanced density.

For a visual support of the arguments for the mismatches at higher redshift, the three RGB images in the left column of Figure 3.12 show cluster candidates detected by *both* the MF and our method (top), by the MF only (middle) and by our method only (bottom panel). The top panel clearly shows that a 'typical' cluster to the eye is detected by both methods consistently. On the other hand, a cluster with multiple central galaxies or without a radial symmetry (as seen in

the middle panel) is missed by the MF perhaps due to the method's reliance on a fiducial cluster model; our detection method, which relies solely on position and color matching of the cluster members, is able to identify such cluster candidates. Our method, however, does not detect high redshift candidates, mainly because of the faint magnitudes and associated color errors, which are greater than the color cuts used for selecting member galaxies.These high redshift non-detections match the completeness trend predicted by our Monte Carlo simulations, presented in Section 3.5.2, which indicate a steep drop in detection efficiency even for a rich Coma-like cluster at $z \geq 0.8$. The higher z' magnitude of these high redshift red galaxies may provide better S/N values, and therefore, this redshift boundary may be advanced to $z \geq 1$ with the planned inclusion of the (i-z) color in a future development of our detection method.

Finally, it must be emphasized that the MF uses only the i' photometric catalog during the detection process and thus has no color information, even though data for the Deep fields are available in all five filters; the only use of color in the MF method is to classify their detections into the three classes, as mentioned above. Differences in detection efficiency between the detection methods have been shown to be significant by Kim et al. (2002) in their comparison of the Matched Filter method with Vornoi Tessellation, the principal reason being the assumption of a uniform background by the MF scheme. In our scheme, the inclusion of color makes it less susceptible to contamination by the background and this may be the reason for the differences in detection numbers as well as in the assignment of the detection classes.

The availability of the spectroscopically confirmed *Xray* clusters from the XMM-LSS survey region which overlaps the CFHTLS-Deep 1 field (Pierre et al., 2007), provides a more stringent test for our cluster detection method; since Olsen et al. (2007) have carried out a similar comparison with their Matched Filter catalogs, we also gain some insight into the detection bias of these two optical methods

from these comparisons. We match the cluster detections in our catalogs with the published XMM-LSS cluster positions using the same method we adopt to match the MF clusters; a detected cluster BG in our catalog (with $i' \leq 20$ mag, detection significances in gr and ri ≥ 3), which lies within a distance equal to our detection aperture radius measured from the published central positions of X-ray emission is taken to be a match. We take these XMM-LSS positions from Olsen et al. (2007) (Table 5) in order to maintain consistency in our comparison with the MF method. The detection parameters we use to make the Deep 1 catalog are the same as those used normally for all Wide fields and each cluster, if detected, is classified as Gold, Silver and Bronze based on their significance thresholds (refer to Section 3.4.1). The detection results provided in Table 3.3 list whether each XMM cluster is detected by our method (GD) and by the Matched Filter (MF) scheme (as given in Olsen et al. (2007)) as well as the detection significances in the $(g - r)$ and $(r - i)$ colors and the corresponding cluster classification. As a visual check of this comparison, the three RGB images in the right column of Figure 3.12 show, (*top panel*) a representative XMM-LSS cluster also detected by our method, (*middle*) an X-ray cluster not detected by our method and (*bottom panel*) one of our *Gold* clusters in Deep-1, which does not have any associated X-ray emission and hence is not part of the XMM-LSS catalog.

The comparison shows that our method detects 12 of the 17 XMM clusters. It is significant to note that our method detects all the X-ray clusters upto $z = 0.8$; all 5 clusters which are not detected are faint, high redshift clusters at redshifts ~ 0.8 or higher. As seen in the middle panel of Figure 3.12, the faint members of these high redshift clusters are indistinguishable against the field galaxies in the foreground; the i' magnitude cut used fails even to locate a BG for XLSSC029 at $z = 1.05$. On the other hand, the high significance *Gold* cluster in the bottom panel and which visually resembles a 'typical' cluster with a BCG and member galaxies with homogeneous colors, is not part of the XMM-LSS catalog, perhaps due to a lack of

associated X-ray emission. These results are fully consistent with our results from the Monte-Carlo simulations in which the detection significances in both colors and therefore the completeness are $\geq 80\%$ even for Fornax-like clusters up to redshift 0.6 and then drop steeply off beyond $z = 0.8$ even for a Coma-like cluster with Abell richness = 2. However, as emphasized under Section.3.5.2, our *principal* focus at present, using only the available (g-r) and (r-i) colors, is to identify clusters up to redshift ~ 0.6; we aim to extend this to higher redshifts once the fields have also been observed in the z' filter.

The MF success rate for the XMM clusters is 10 out of 17. It is interesting to note that it fails to detect three clusters at $z = 0.29, 0.34,$ and 0.46, all of which are detected with high significance by our method while it successfully detects two higher redshift clusters at $z = 0.92,$ and 1.05, though with redshift errors of ~ 0.1; at the same time the MF fails on a $z = 0.92$ cluster which is detected as a marginal 'Gold' detection by our color based scheme.

To summarize, the Monte Carlo results show that our cluster detection method is complete ($\geq 80\%$) up to a redshift of 0.6 for clusters of richness matching or higher than Fornax; for poorer clusters, the completeness remains at $\geq 80\%$ till z=0.3 and declines to $\sim 60\%$ by z=0.6. These simulation results are supported by the comparison of our catalogs against clusters detected by the MF method as well as the XMM sample of X-ray selected clusters in the CFHTLS-Deep 1. Given the expected correlation between richness and the lensing cross section of a cluster, the completeness level achieved by the cluster detector is adequate for the current application of searching for lenses.

3.7 Cluster Catalogs, Wide Fields

We have applied our cluster detection method to the 41 deg^2 of CFHTLS-W3 fields for which g, r and i observations are available. We chose to run the detector first

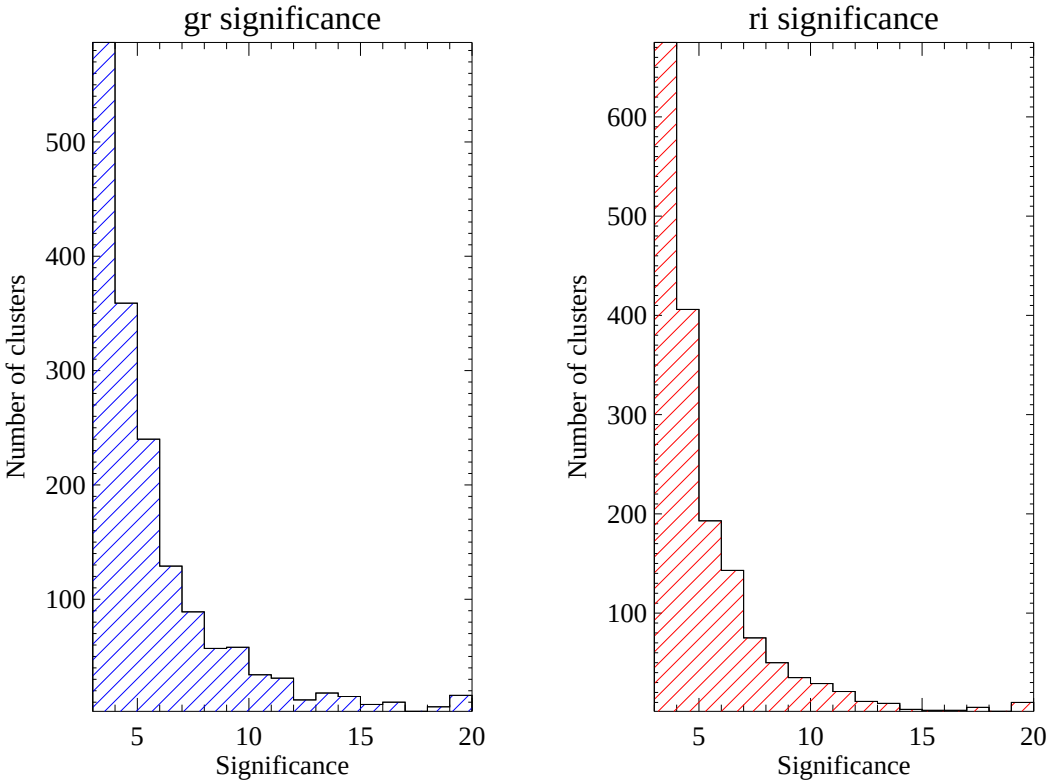

Figure 3.10: Histograms showing the distribution of gr and ri detection significances for the cluster candidates detected in the 41 deg^2 of CFHTLS-W3 for which g, r and i images are available

on the W3 fields because they contain 4 of the 9 lens candidates detected by earlier visual examination of each 1 deg^2 field during data processing; this increases the likelihood of detecting more lens candidates by the dedicated visual search of the RGB stamp images of the detected clusters. The preparation of the cluster catalogs for the other three Wide fields will be complete in the near future.

We use the *Terapix T04* stacked images and photometric catalogs from the Canadian Astronomy Data Center (CADC) to construct our cluster catalogs. The cluster catalogs list the cluster name, J2000 (α and δ), the i magnitude and gr and ri colors of the BCG, the gr and ri detection significances, the number of bright cluster members with i $\leq$ 20 mag (the BG magnitude limit) and the Abell richness using

the T04 i magnitudes of *all* the member galaxies (which fall within the detection aperture as well as within the color cuts for selection).

The catalogs for the 41 fields contain a total of 1671 cluster candidates (gold 650, silver 461 and bronze 560). All four visually selected lensing clusters in the W3 fields have been detected in the gold category. The median number of candidates per field is 40 with an interquartile distance (IQD) of 20; amongst these, the median(iqd) fractional distributions for gold are 0.38(0.21), silver 0.29(0.14) and bronze 0.33(0.20). Figure 3.10 shows the distributions separated by the gr and ri detection significances, running from the minimum value of 3 (the threshold for selection as a candidate) to a maximum of 20, chosen for the plot. In either distribution, objects with significances greater than 20 are added to the highest significance bin; there are 11 candidates with gr significance > 20 and 7 objects with similar significances in ri color. The distributions show that there is a significant fraction of candidates ($\sim 40\%$), in either color with detection significances > 5, which puts them in the gold category. Separated by the Abell richness classes, 1609 candidates fall in richness class 0 and lower (WBL-like clusters), 39 are Fornax-like (richness $= 1$) and 23 have richness above 1, thus in the Coma class. The next step is to estimate photometric redshifts of these candidates in order to draw clearer inferences from the distributions of these color dependent detection significances. The refinements will also make the cluster catalogs useful for other cosmological investigations. The immediate focus is to prepare and visually inspect the color images for these candidates. Visual examination of a sample RGB images of the richer candidates shows the expected cluster of galaxies with early type morphologies and colors. Automating the process of preparing the RBG images for all the candidates is underway. With a total of 62 Fornax-like and richer cluster candidates, there is a high likelihood of detecting more lenses in these fields.

3.8 Conclusions and future direction

We have developed an automated detection method to build cluster catalogs using two-color, wide field imaging data; these cluster catalogs form the first step toward our ultimate goal of building a catalog of lensed $z \sim 1$ star forming galaxies suitable for IFU follow-up. Since the mass concentration in clusters have a higher likelihood of gravitationally lensing background objects than galaxies in the field, our strategy is to systematically search only the regions around the cluster candidates either visually or with an automated search method for lensed images; this reduces the search to only $\sim 10\%$ of the total survey area. The cluster search method is designed for two-color photometric data and is tuned for the g, r and i images from the public CFHTLS-Wide survey, which covers 195 deg^2 in four patches. The algorithm adopts a well defined detection metric, based on position and color clustering of the dominant early type galaxy population in the core of clusters. We have reviewed published observational results to adequately justify our chosen detection strategy.

Using Monte Carlo simulations, we have determined the contamination rate from false detections as well as the completeness function of our method. We have tested the completeness for clusters of three representative Abell richness values, namely for rich Coma-like clusters. for moderate Fornax-like clusters and for poor (*WBL*) candidates, which resemble galaxy groups. The detection method is $\geq$ 80% complete for Fornax-like and richer clusters up to a redshift of 0.6, which is the principal redshift range of interest in our search for lensing clusters; for WBL clusters, the detection method is only complete at this level for redshifts up to 0.3 and drops to 60% by z=0.6. However, the lensing cross section of these low mass systems show a consequent steep decline with redshift and the likelihood of detecting lensed images in poor clusters at high redshift is low; therefore the lower completeness does not pose any disadvantage for our application.

As an additional stringent test of our detection method, we have compared our cluster candidates in the CFHTLS-Deep fields, which are 1 deg^2 patches within the

larger Wide fields, against two published cluster catalogs from the same imaging fields, namely, the Matched Filter catalog by Olsen et al. (2007) and the spectroscopically confirmed clusters in the XMM-LSS catalog (Pierre et al., 2007). The comparison has confirmed that our candidates match those in both catalogs up to a redshift of 0.8, which encompasses our principal region of interest; due to the faint magnitudes of galaxies at higher redshift, the associated color errors become larger than the color cuts we use for detection, leading to the observed drop in the detection efficiency.

Supported by these successful test results, we have applied the cluster detection to 41 deg^2 of CFHTLS-W3 fields for which g, r and i imaging are currently available; catalogs for the other Wide fields will be completed in the near future. Using an automated method, RGB color images of the high likelihood candidates have been generated for a visual search for lensed arc images; the catalog of candidate lensed images from this visual search as well as preliminary results from an automated search scheme are presented in the following chapter, as well as results from our spectroscopic confirmation of these lens candidates.

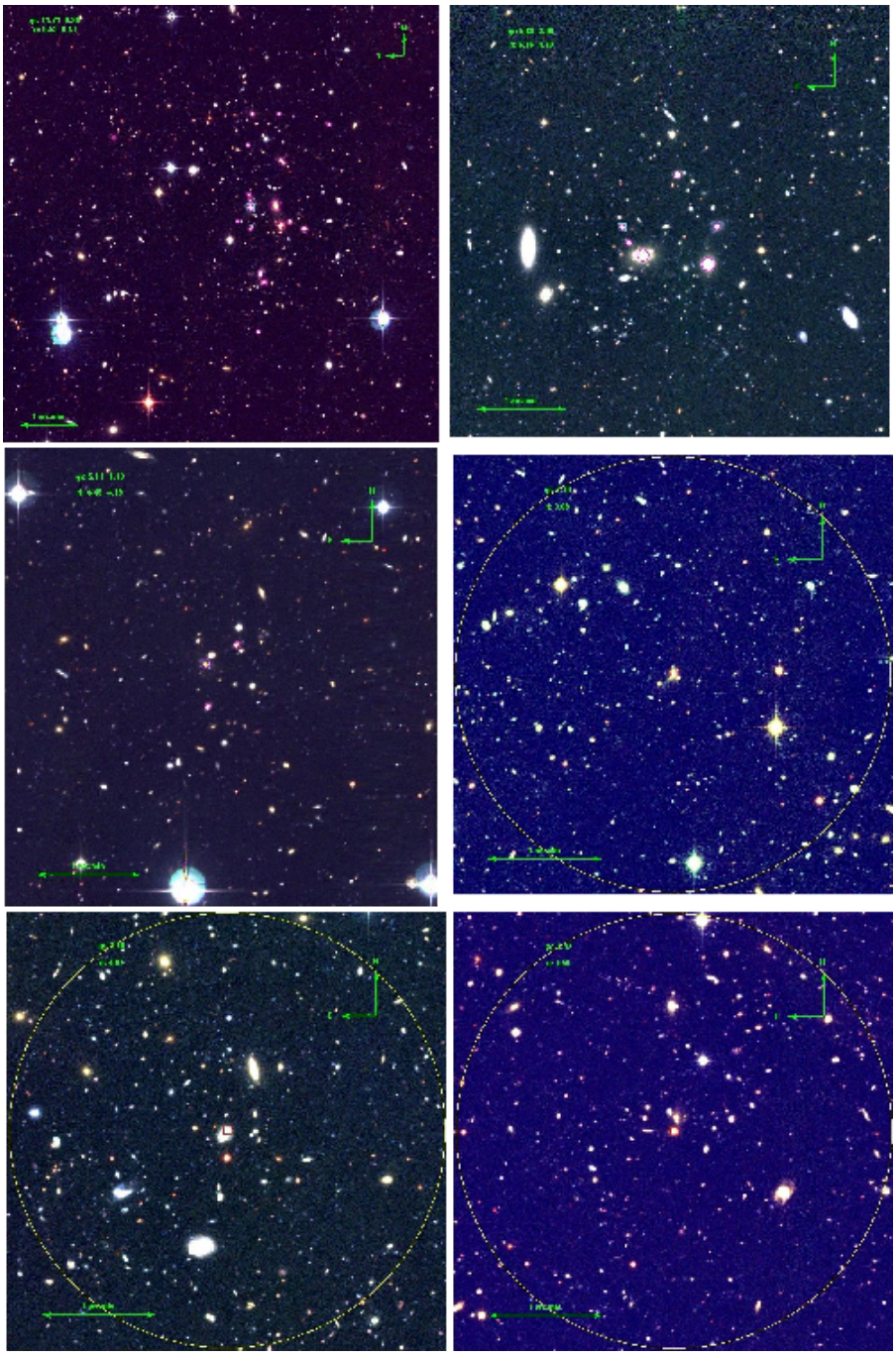

Figure 3.11: Mosaic of RGB color images of representative *Gold* (top row), *Silver* (middle) and *Bronze* (bottom row) clusters candidates from CFHTLS-Deep1 field; see §3.6 for details. Full scale individual images available online at http : //astrowww.phys.uvic.ca/ ∼ karun/Thesis_JPGs/D1/

Table 3.3: Comparison of XMM-LSS X-ray cluster detections in CFHTLS-Deep 1

XMM ID	R.A.(de.g.)	Dec.(de.g.)	z_{sp}	GD	S_{gr}	S_{ri}	Class	MF
XLSSC029	36.0172	-4.2247	1.05	N	0.00	0.00	-	N
XLSSC044	36.1410	-4.2376	0.26	Y	12.90	9.38	G	Y
XLSSJ022522.7-042648	36.3454	-4.4468	0.46	Y	20.52	9.76	G	N
XLSSC025	36.3526	-4.6791	0.26	Y	9.27	10.77	G	Y
XLSSJ022529.6-042547	36.3733	-4.4297	0.92	Y	5.27	9.23	G	N
XLSSC041	36.3777	-4.2388	0.14	Y	10.47	10.58	G	Y
XLSSC011	36.5403	-4.9684	0.05	Y	11.08	3.25	S	Y
XLSSJ022609.9-043120	36.5421	-4.5226	0.82	N	2.51	7.57	-	N
XLSSC017	36.6174	-4.9967	0.38	Y	15.38	10.13	G	Y
XLSSC014	36.6411	-4.0633	0.34	Y	14.27	7.50	G	Y
XLSSJ022651.8-040956	36.7164	-4.1661	0.34	Y	5.03	3.37	S	N
XLSSC005	36.7877	-4.3002	1.05	N	-0.56	-0.10	-	Y
XLSSC038	36.8536	-4.1920	0.58	Y	3.26	3.04	B	Y
XLSSC013	36.8588	-4.5380	0.31	Y	12.53	9.66	G	Y
XLSSC022	36.9178	-4.8586	0.29	Y	14.39	11.64	G	N
XLSSJ022534.2-042535	36.3925	-4.4264	0.92	N	1.01	3.30	-	Y
XLSSC005b	36.8000	-4.2306	1.00	N	1.07	1.25	-	N

Comparison of the detections of the spectroscopically confirmed XMM-LSS X-ray clusters in the CFHTLS-D1 field (Pierre et al., 2007), using our detection method (GD) against the results with the Matched Filter scheme (MF) for the same clusters given in Olsen et al. (2007). Our detections are classified further as Gold (G), Silver (S) or Bronze (B), as given in Section. 3.4.1

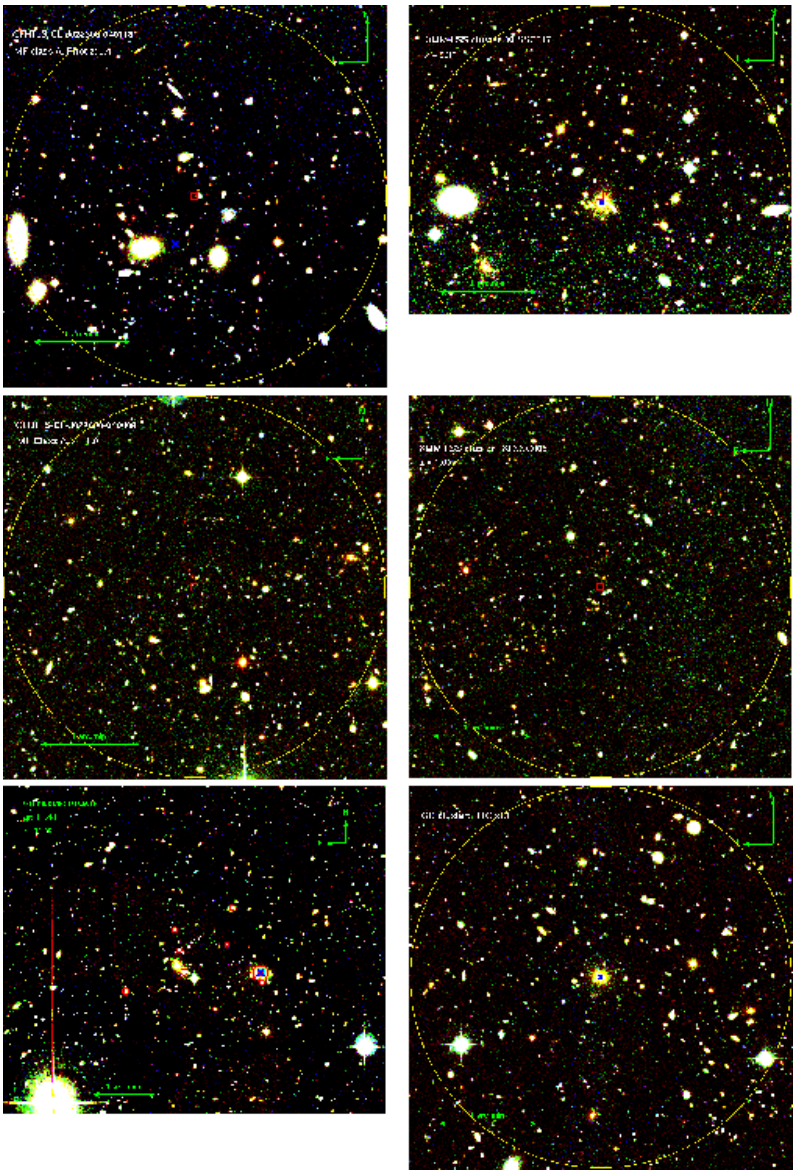

Figure 3.12: Mosaic of RGB color images of representative Matched Filter (*left panels*) and XMM-LSS clusters (*right panel*) matched against cluster candidates in our catalog for CFHTLS Deep-1 field. See §3.6 for a description of each panel. Full scale individual images available online at http : //astrowww.phys.uvic.ca/ ∼ karun/Thesis_JPGs/D1/

Chapter 4

Detection and Spectroscopic Confirmation of Lensed Arcs

4.1 Introduction

The focus of the work reported in this chapter is to compile a catalog of confirmed *lensing* clusters from amongst the cluster candidates in the CFHTLS-Wide catalogs described in Chapter 3; in this context, *lensing* clusters refer to those clusters with mulitple, strongly lensed images of background objects. The ultimate aim of this work is to develop a catalog of gravitationally lensed $z \sim 1$ star forming galaxies suitable for IFU spectroscopy in order to address the science goals set forth in Chapter 2.

Our initial search strategy was to use a dedicated visual search for likely lensed images in the RGB color images of either the 1 deg^2 CFHTLS fields or of the stamp images of the candidate clusters. Aiding our visual search is the distinctive blue color of these lensed images, due to the high UV continuum associated with star formation, being redshifted (at $z \leq 1.5$) into the blue end of the optical spectrum; these blue, lensed images stand in sharp contrast against the red colors of the early type galaxies in the cluster core, the region of the cluster which has the highest

strong lensing cross section (see Appendix A for details on strong lensing). In addition, the principal lensed images (those with significant magnification) also generally have a distinctive arc-like geometry, making their visual detection easier; the RGB panels in Figures 4.2-4.5 at the end of Section 4.4 show several illustrative examples of these lensed arcs. Our cluster catalog from each 1 deg^2 CFHTLS-Wide field contains $\sim$ 60 candidates in total in the three detection classes (gold, silver and bronze); the visual search for lenses takes $\sim 2h$ for the cluster candidates from each field.

Despite the advantage of simplicity, visual search is slower compared to automated schemes and is prone to human error and selection bias. False detection rates, such as due to contamination from foreground star forming galaxies or galaxies with disturbed morphologies, are difficult to quantify as is the completeness as a function of redshift and surface brightness. Therefore, in conjunction with the systematic cluster detection method we have developed, we have also implemented an automated method for detecting lensed arcs, developed by Lenzen et al. (2004). This scheme was chosen as appropriate for the CFHTLS data after a systematic evaluation of the performance of three different approaches in published literature. A survey of these automated methods for detecting gravitational lenses, highlighting merits and limitations of each method is presented in Section 4.2. Results from our comparisons of the performance of three available methods specifically on CFHTLS images follow in Section 4.3 to support our choice of *Arc_Detector* (Lenzen et al., 2004). For our application, we have tuned the method to work with minimal user intervention on the cluster stamp images from our cluster detector; in Section 4.3, we also report pertinent details of the implementation. Results of the performance of *Arc_Detector* on visually detected lens candidates are given in Section 4.4.

In order to confirm these gravitational lens candidates, we have initiated an observational campaign using longslit and MOS spectroscopy with the Gemini GMOS. Section 4.5 describes the observational approach, highlighting in sub-section 4.5.2

the improved B-spline based reduction procedure we have developed for these low surface brightness targets observed under marginal sky conditions. Observational results follow in Section 4.6. The chapter concludes in Section 4.7 with a summary of this work on the detection and confirmation of lensed arcs, as well as plans for future improvements.

4.2 Survey of arc detection algorithms

The majority of gravitational arcs known at present have been discovered either serendipitously in spectroscopic or imaging surveys (usually focussed on other science goals) or by visual examination of images over small regions of the sky in dedicated lensing surveys (eg. 2 lenses discovered in the CFRS (Hammer et al., 1995) discussed in Chapter 2, and 7 new serendipitous discoveries in RCS (Gladders et al., 2003) mentioned in Chapter 3) . With the commissioning of large multi-CCD mosaic cameras such as the Megacam and the availability of public surveys such as the SDSS, the need to automate this detection process has been recognized, as shown by the growing number of techniques proposed in recent literature.

These detection techniques may be broadly classified based on the type of data on which they may be applied (spectroscopic vs imaging) and also on the type of strong lenses they detect (galaxy-galaxy lenses vs cluster lenses). Please note that in the following discussion, we focus only on detection methods for extended arc-images of lensed background galaxies, (in keeping with the focus of the thesis), and do not include methods for point-images of lensed quasars.

The automated detection algorithms designed for imaging data rely principally on the morphology of the gravitationally lensed arcs - elongated along one direction (typically tangential to the cluster radius) and narrow in the transverse direction (i.e., radial); the length-to-width ratio may be $\sim$ 10 or more in the case of giant arcs, with the width being barely resolved ($\sim$size of the PSF). In the case where

the lensing is due to a single galaxy, as in CFRS03 described in Chapter 2, the symmetric mass distribution in the deflector leads to a classic arc-like image (see Figure 2.1); in a cluster however, the presence of multiple deflectors and the more complex mass distribution, often leads to a more extended (bigger radius of curvature, higher L/W ratio) but distorted image (eg. top panel in Figure 4.5). Detection methods for imaging data base their algorithms on these geometric properties, using either of two approaches, (i) direct detection of elongated objects followed by a rule-based selection of arcs or (ii) apply one of a variety of filtering schemes to enhance the geometric properties of arcs while suppressing contamination from other elongated structures (eg. an edge-on spiral galaxy); both methods are discussed in detail in the following sections. For spectroscopic data, an efficient strategy, first proposed by Hewett et al. (2000), is to identify anomalous emission lines of the background lensed galaxy superposed in the spectrum of the foreground deflector galaxy; to cite one example of the several successful applications, Willis et al. (2006) discovered five new galaxy-galaxy lenses in the SDSS-DR4 spectroscopic data with this technique. However, spectroscopy is expensive in terms of the required telescope time; additionally, this method relies crucially on the small separation of the lensed image from the deflector, so that the spectra of both the lensed and the lensing objects are superposed within a single slit or spectroscopic fiber, making this approach applicable only to galaxy-galaxy or galaxy-quasar lenses. In cluster lenses, the lensed image separation from the principal deflector galaxy is typically ~ 10", which makes this detection method unsuitable. Therefore, cluster lens detection relies mainly on imaging surveys and we devote this review to arc detection techniques designed for wide field, photometric data such as the CFHTLS-Wide survey.

4.2.1 Sextractor based *Arc finder*

The most direct approach is to use an efficient object detection program such as Sextractor (Bertin and Arnouts, 1996) to identify all the elongated objects in the

field and then search through the detections for arc-like candidates using their specific morphological characteristics; this technique is particularly applicable to space based observations where seeing effects are minimized. Horesh et al. (2005) have implemented this method to detect simulated arcs in HST images in their study of the lensing cross sections of 10 X-ray selected $z \sim 0.2$ clusters. In their lensing simulations, they use the Hubble Deep Field as the background galaxy distribution which is lensed by these foreground clusters, with cluster mass distributions estimated from HST imaging (Smith et al., 2005a). To detect these synthetic lensed arcs, Sextractor is run repeatedly six times, each time with a carefully chosen set of object detection parameters; at each step, detected objects with length-to-width ratio lower than a user defined threshold are eliminated to produce a final catalog of arc candidates. Results from their simulation indicate all arcs with integrated r-magnitude ≤ 21 are recovered though the detection efficiency drops steeply to 0.5 at $r \sim 23$mag; it must be noted that no observational effects, such as blurring due to seeing, were included in their simulations. A comparison with the *Arc_Detector* by Lenzen et al. (2004) (discussed later in this section) indicated that detection at brighter magnitudes ($r \leq 21$mag) were on par for both methods; however, the efficiency of the Lenzen et al. (2004) method remained at 80% even till $r \sim 23$mag compared to the 50% for Arc finder. This higher detection efficiency at fainter magnitudes of the method by Lenzen et al. (2004) is particularly relevant for our lensing cluster search since $r \sim 23$mag is the median magnitude of the arc-candidates we have visually detected in our survey. This comparison, as well as results from our investigations discussed in Section.4.3 indicate that the Lenzen et al. (2004) scheme is the more viable method for automated arc detection in the ground based CFHTLS survey data.

Estrada et al. (2007) adopted a similar Sextractor-based approach in their search for lensed giant arcs in SDSS galaxy clusters. The catalog of detected objects from Sextractor is then categorized using the ratio of the sizes along the major and

minor axes of each object (measured from their light profiles) to identify a subset of elongated objects (with major-to-minor axis ratio ≥ 1.4). Final selection of lensed arc-candidates is done using a neural network. An application of this method to 825 clusters detected in SDSS Data Release 5 by the MaxBCG method ((Hansen et al., 2005), discussed in Section 3.3.3) did not find any giant arcs. Visual inspection of these clusters was used to support this null result, with which the authors constrain the arc production efficiency of clusters in the redshift interval $0.1 \leq z \leq 0.3$. This null result is surprising since Willis et al. (2006) have reported 5 new lenses with their spectroscopic search method implemented on SDSS DR4 catalogs. In addition, we have discovered 9 lensing cluster candidates in 102 deg^2 of CFHTLS-Wide, with an areal coverage smaller than the SDSS (though the imaging is deeper). In the face of these results, it would be instructive to test the arc detector developed by Estrada et al. (2007) on the CFHTLS lenses and also compare the MaxBCG catalogs with our clusters (there is sizable overlap between the CFHTLS and SDSS fields).

4.2.2 Arc detection from computed object ellipticity and orientation

As a refinement to this direct object detection, the ellipticity (or elongation) and orientation of each object, determined using higher moments of its light distribution, may be used to refine the search. Designed to work on large imaging surveys, such as the CFHTLS, the method proposed by Alard (2006) uses a local estimator of elongation based on the second moments of the light distribution; the moments are computed at every point in the image within a window of size a few times that of the PSF. For suppression of false detections from noise, such as diffraction spikes, the image is first filtered with a Mexican hat band pass filter. The estimation of elongation is done in two steps: second moments of the light distribution are computed to identify any elongated structure that may be present at the point, as well as the orientation of its principal axes in the global image coordinates; if

an elongated structure is detected, the image axes are rotated to coincide with the principal axes of the structure and an estimator is used to determine the L/W ratio of the structure in these local coordinates (the image rotation improves the S/N of this estimation). This two step process effectively isolates gravitational arcs and also provides their properties, such as the orientation and radius of curvature, as part of the detection process. Results from an application to a single ($1k \times 1k$ pixels) CFHTLS i' image indicate that the method is capable of recovering the arc-candidate, which is visible in this field. Results from the independent tests we carried out on this method are presented and discussed in the following Section 4.3.

Seidel and Bartelmann (2007) have adopted the same approach for their *Arcfinder* algorithm, but they compute the ellipticity and orientation in cells (chosen with a user defined scale size) to improve the SNR of their estimator. Contiguous cells with matching values are then linked to identify larger arc-like features. Results from preliminary tests on HST images of two clusters with known lensed features, carried out mainly to fine tune the detection parameters, indicate that the method recovers the arc features; however, it is mentioned that the method suffers from appreciable contamination from diffraction spikes, though a quantitative assessment of the characteristics is postponed for a future publication. No results from ground based observations are provided.

4.2.3 *Arc_detector*, using anisotropic diffusion filtering

To improve the detection of arc-like structures in ground based imaging, Lenzen et al. (2004) use the anisotropic diffusion filtering method, which identifies and selectively enhances their edges only along the direction of elongation without affecting their brightness distribution in the transverse direction. The observed surface brightness of lensed arcs is typically at the level of the sky background, (eg. $22\,\mathrm{mag.arc.sec}^{-2}$ at Mauna Kea, (Krisciunas, 1997)); therefore, the filter is applied only to image pixels whose flux lies within user defined minimum and maximum

thresholds. This selective rejection of bright objects improves the computational efficiency of this method while the minimum threshold avoids spurious noise features. The filtered image is then partitioned into contiguous pixels belonging to objects, with the remaining pixels forming the background region; due to the edge enhancing effect of anisotropic filtering, only extended objects are identified by the partitioning algorithm in this *segmentation* step. In the final step, user defined selection criteria are applied to isolate arcs from the detected set of elongated objects. As proof of concept, Lenzen et al. (2004) have applied their algorithm to two HST images of cluster A1689 and one ground-based image of cluster RXJ1347-1145 and have successfully detected all the known giant arcs in these two lensing clusters. It must be noted that these tests were carried out on two lensing clusters in which the incidence of lensed arcs is greater than that of contaminating features, thereby biasing the tests in favor of the detection method. We therefore ran a blind test on the CFHTLS Deep 1 field to test for false detections; the results are discussed in Section 4.4. *Arc_detector* also performed with very encouraging success when we compared it against the methods proposed by Horesh et al. (2005) and Alard (2006), testing all three methods on CFHTLS-W data; details of these trials are given in the following section. Based on these results, we have adopted the anisotropic diffusion method for the automated detection of arcs in the CFHTLS cluster catalogs. The details of the implementation and results from our tests are discussed in Section 4.4.

4.3 Automated arc detection in CFHTLS clusters

For arc detection in CFHTLS, we were able to obtain the computational codes for both *Arc_detector*, the anisotropic diffusion filtering method (Lenzen et al., 2004) and the Sextractor based *Arc finder*, Horesh et al. (2005), both of which

are available from the authors on request; in addition, the beta version of the code by Alard (2006) was also made available for our trials (R.Cabanac. private communication). Therefore, we decided to independently test and choose a scheme appropriate for cluster lens detection in the CFHTLS imaging, instead of developing our own algorithm.

In these trials, we tested the detection efficiency of each method on fields containing candidate giant arcs around clusters, all of which had been detected earlier by visual examination of CFHTLS-W fields during image processing (D. Balam, private communication). Our trials indicated that *Arc_detector*, the anisotropic diffusion method (Lenzen et al., 2004), designed for cluster lens detection in ground based imaging, was able to match 6 of the 9 visually detected candidate lensed arcs with only minor changes to the set of default detection parameters (changes mainly to account for differences in the photometric zero points and PSF in the images). These results as well as possible reasons for the 3 non-detections are discussed further in Section 4.4.

On the other hand, in our trials the Sextractor based method by Horesh et al. (2005) was unable to locate the arcs in the test fields using the default parameter set; our findings were confirmed by the authors (A.Horesh, private communication) who acknowledged that the parameter set had been fine tuned for HST imaging only and may not be applicable for the smearing effects due to seeing in ground-based imaging. However, for efficient detection, the method relies on tuning a large number of parameters during the six consecutive runs of Sextractor, thus making this approach difficult to adapt to ground based photometry, such as from CFHTLS. Similarly, the method by Alard (2006), designed principally for close separation galaxy-galaxy lensing was unable to detect the giant arcs in the test fields. Tuning the filter parameters and the detection rules did not improve the detection rate.

Therefore, based on the above results, we have selected *Arc_detector* and carried out further tests only to fine tune the detection parameters for CFHTLS-W imag-

ing; the scope of this thesis does not permit tests to understand the completeness of detections and contamination from false positives. However, we have shared our experience from the CFHTLS trials with the authors with future plans of quantifying the selection function and fine tuning it for our cluster catalogs. For the sake of completeness, we discuss pertinent operational details of *Arc_detector* in the following paragraphs, before presenting results from our trials in the next section.

Table 4.1: Critical *Arc_detector* parameters for CFHTLS-W images

Step #	Parameter	Value	Step #	Parameter	Value
1. Scaling			**3. Detection**		
	Min	740		$Minlevel$	0.1
	Max	840		$Minsize$	5
	$Mode$	4		$Mindiff$	0.3
				$Maxthick$	35
2. Smoothing			**4. Selection**		
	τ	12		$Minecc$	0.7
	κ	0.0001		$Minthick$	2
	σ	2		$Mindiff$	0.3
	ρ	12			

Values of *Arc_detector* parameters used for detecting lensed arcs in CFHTLS-W images; refer to Lenzen et al. (2004) for a description of the effect of each parameter on the associated process

Arc_detector is available as a C-based set of source programs, which is compiled using a standard Linux compiler and linked with the *cfitsio* library *. The code is designed to accept image files in FITS format, thus making it readily compatible with the output from standard astronomical reduction tools such as IRAF. For arc detection, the method uses four consecutive steps: *scaling* the flux in the input image, *filtering* the scaled image with the anisotropic diffusion filter, *segmentation* of individual objects in the filtered image and finally, *selection* of arc candidates based on a set of rules. The user defined control parameters for these steps are provided in a separate input file. The four steps must be executed in the sequence

*http://heasarc.nasa.gov/fitsio/fitsio.html

given above; however, in order to help optimize the parameters, intermediate results from each step are saved so that user may stop and resume execution at any point. Further details of the installation and use of the method are described in Lenzen et al. (2004) as well as in the user's guide provided with the tarball containing the source code. For reference, Table 4.1 lists the principal parameters and the values we used for arc detection in the CFHTLS-W images.

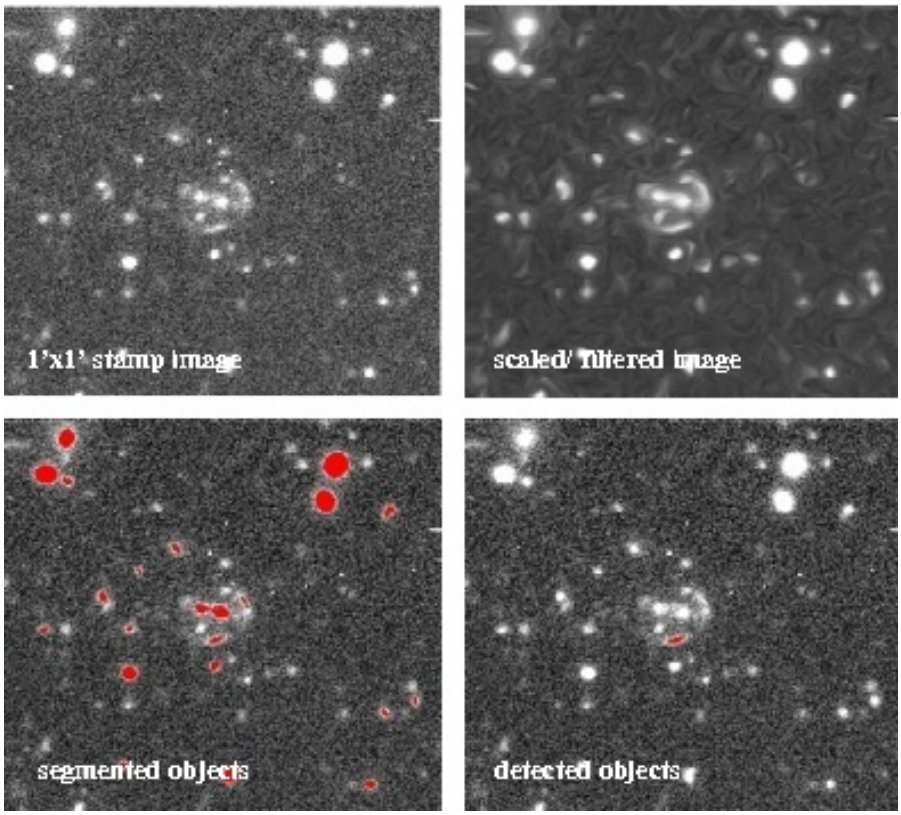

Figure 4.1: Sequence of operations carried out by *Arc_detector* on the $1'x1'$ images centered on bright cluster members: (from top left) the input stamp image is scaled and filtered using the anisotropic diffusion filter, objects are segmented (23 in this case) and finally elongated objects (lensed arcs) are selected

For arc detection, we use $(1' \times 1')$ image sections centered on each candidate cluster member in our catalogs; this aperture is adequate to cover the typical separation of ~ 10" of the lensed arc from the deflecting galaxy. We base our detection

principally on g'-images since star forming galaxies at $z \leq 1.5$ -the principal focus of our work -usually have higher flux in this waveband due to the redshifted UV continuum from the star formation. The blue arcs stand out in greater contrast against the red cluster members. We use an automated script to cut out the stamp images around each candidate cluster member and pipe them to *Arc_detector* for processing. Figure 4.1 shows the effect of each step in the arc detection sequence; we have chosen a section containing a lensed arc specifically to highlight the efficacy of the detection process. The top panels show the original stamp image (on the left), followed by the scaled and filtered image; the effect of the anisotropic filter in enhancing the extended morphology of the arc is noticeable. The bottom panels show the segmented objects (left panel) and the lensed arc isolated by the final selection process (right).

At present, we have only tested *Arc_detector* on lensed arc candidates, which were detected by an earlier visual search. Of the 9 arcs on which this test was carried out, the detector identified 6 (both detections and non-detections are discussed in detail in subsequent sections); in these trials, the highlighting done by detector, seen in Figure 4.1, isolates the arcs from the background objects. When used for arc detection, such highlighted objects may be identified by subsequent visual examination of each field after running *Arc_detector* on it. Implementation of this automated search and tests for completeness and contamination are planned for future work, discussed in Section 4.7. Results from our comparison between visual detections and those from *Arc_detector* are discussed in the following section.

4.4 Results from *Arc_detector*

Visual inspection of the CFHTLS-W fields during image pre-processing and stacking for the Weak Lensing survey, led to the serendipitous detection of 9 strongly lensed arc candidates (shown in Figures 4.2 - 4.5, plates included at the end of

this section) and two other candidates, shown in Figure 4.6, with lower likelihood of being lenses, either due to the geometry (left panel) or faint surface brightness (right panel). As mentioned in Section 4.1, all these lens candidates were detected by visual inspection of the individual 1 square degree Wide fields; visual inspection of RGB stamp images of our cluster candidates is ongoing as the cluster catalogs are prepared for the Wide fields for which gri imaging becomes available. Of the 9 lenses, 8 are first time discoveries; only the arc candidate, SL2SJ141911+532616 was discovered serendipitously in the Red Sequence Cluster Survey (Gladders et al., 2003) as RCS1419.2+5326, though without spectroscopic confirmation. The positional details of all these candidates were kindly made available for our lensing cluster survey (D. Balam, private communication). The results presented in this section pertain only to these lenses; we will extend our search for more lenses as we continue building our cluster catalogs. In the discussions, we use the naming convention for lenses as adopted by our Strong Lensing Legacy Survey (SL2S) collaboration.

Stamp images of the 6 visually detected arc candidates, which were also flagged as high likelihood detections by *Arc_detector*, are shown in Figures 4.2 - 4.4. For each candidate, the top panel is a $1' \times 1'$ g' stamp centered on the cluster BCG, the middle panel is the corresponding RGB color composite from the gri images and the bottom is the detection image from *Arc_detector*. In the Arc_detector image, high significance arc candidates are color coded red, mediocre, green and low likelihood objects are yellow. Figure 4.5 shows the three visually detected arc candidates, which were not detected by *Arc_detector*. For each candidate, the RGB color composite is shown on the left panel and the g' stamp on the right. In the following discussion of these detections, we focus only on the performance of *Arc_detector* on these lenses, and postpone a presentation of the properties of each lens candidate for Section 4.6, where we include results from the follow-up spectroscopy. In addition, i' stamp images of the two low likelihood gravitational

lenses detected visually are also shown in Figure 4.6; both these arcs are not detected by *Arc_detector* due to their faint surface brightness, as explained later in this section.

It must be emphasized that for all these trials, we used the same set of detection parameters without any fine tuning for specific lenses. The initial parameter selection was done on the candidate arc, SL2SJ141911+532616 (right column, Figure 4.3). For this lens, the minimum and maximum scaling values were set based on the average flux in the g' image, and the smoothing parameter was chosen to match the PSF; all other parameters were held at the default values suggested by Lenzen et al. (2004) for detecting giant arcs. It is therefore encouraging that the method detected $\geq$ 60% of the arcs, including the faint, small arc SL2SJ085915-034515 (right column, Figure 4.4).

Of those candidates *not* detected, shown in Figure 4.5, we notice that they fall in two broad categories: (1) the arcs have small separation from the bright central galaxy and are therefore not isolated as independent, extended objects after filtering, (eg. SL2SJ022025-044817) or, (2) the arcs are faint (surface brightness $\leq$ $0.25\,\mathrm{mag.arc.sec}^{-2}$ above the sky background) and hence fall below the lower cutoff threshold during scaling, (eg. SL2SJ022546-073738); for these candidates, lowering the threshold resulted in the detection of not only the arcs but also numerous spurious background noise ridges.

A simple estimate of the false detection rate in a typical $1\mathrm{d}eg^2$ CFHTLS field was obtained by applying *Arc_detector* to the candidate cluster members in CFHTLS-Deep1 cluster catalog. We chose to test this field since it had been carefully examined visually and no lens candidates had been reported, either from the examinations (D. Balam, private communication) or in available literature. Our cluster catalog for D1 contains 33 clusters composed of 140 bright ($i' \leq 21$mag) cluster members. Using a wrapper script, *Arc_detector* was run on $1' \times 1'$ stamp images centered on each cluster member; the output detection images as well as the details

of the detected objects were piped out for analysis. There were 12 independent detections from the 140 images; of these two were repeatedly detected due to the associated member galaxies belonging to the same cluster. Visual examination of these detections showed that edge-on spiral galaxies (Figure 4.7, left panel) dominated the false detections (10 out of 12); two were interacting galaxies with disturbed, extended morphology (Figure 4.7, right panel). Our trials indicate that the type (giant arcs, arclets, contaminants such as edge-on spirals) and number of detections (fitting to noise features) depend crucially only on the 3 parameters governing the anisotropic diffusion filter and on the final object selection rules after segmentation. We have shared all our findings with the authors of the algorithm to motivate improvements to the detection efficiency in future versions.

To summarize, our current results indicate that *Arc_detector* locates bright arcs ($\geq 0.5\,\mathrm{mag.arc.sec^{-2}}$ brighter than the sky background, typically $22\,\mathrm{mag.arc.sec^{-2}}$), which are well separated ($\geq$ 5arc.sec) from the deflector galaxy. These properties are consistent with the types of arcs we need for IFU follow-up, hence *Arc_detector* offers a viable automated detection method which matches the objectives of our cluster lens survey. At present, having tuned *Arc_detector* to work in conjunction with visual examination, our aim is to extend it to be a wholly automated detection process with a well understood selection function.

4.5 Spectroscopic confirmation of candidate arcs

Longslit and MOS spectroscopy on the Gemini North and South telescopes were used to confirm the lensing hypothesis of these gravitational lens candidates (by measuring the redshifts of the deflector and source) and, more pertinently, to assess the suitability of each system for deeper IFU follow up; the IFU selection criteria, which are based on our experience with CFRS03, are (i) surface brightness,

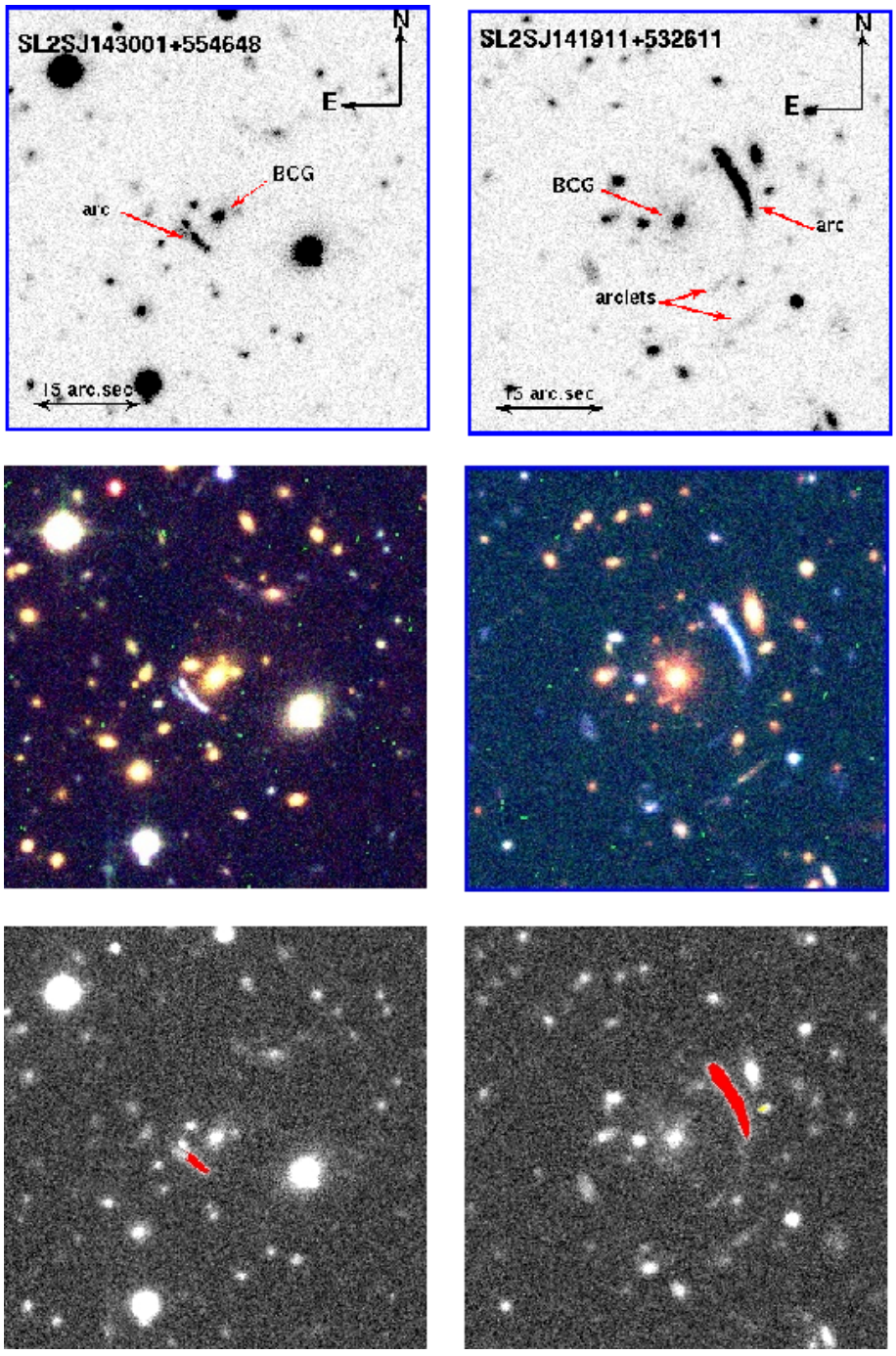

Figure 4.2: Stamp images ($1' \times 1'$) of the visually detected arc candidates are shown in each column. (*Top panel*) g' image centered on the principal deflector, (*middle*) corresponding RGB color composite and (*bottom*) detection image from *Arc_detector*, with *red* = high detection significance, *green* = medium, and *yellow* = low significance. Relevant photometric details of each candidate are given in Table 4.3

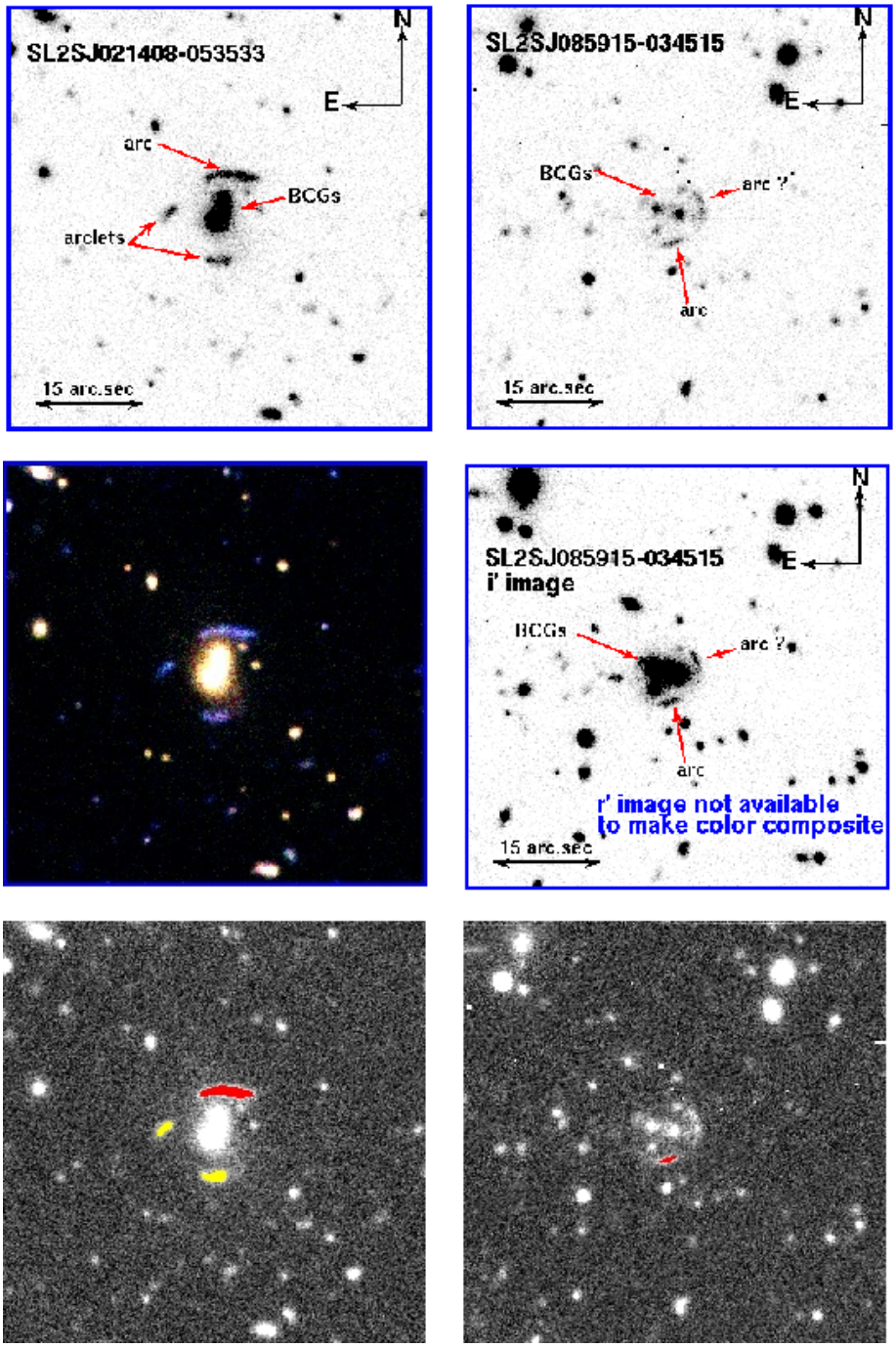

Figure 4.3: Stamp images of visually detected arcs and corresponding output images from *Arc_detector*, in a format similar to Figure.4.2

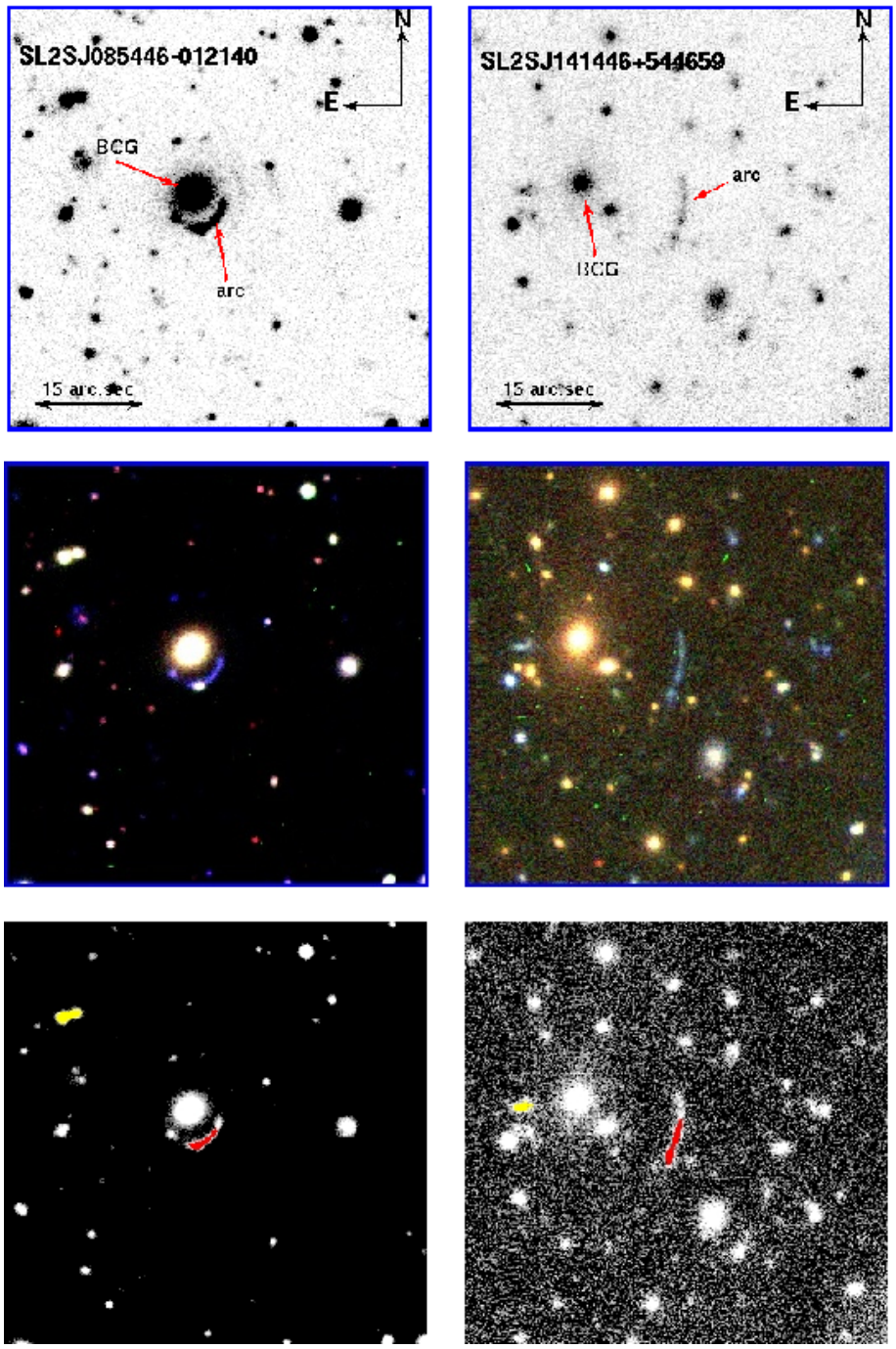

Figure 4.4: Stamp images of visually detected arcs and corresponding output images from *Arc_detector*, in a format similar to Figure.4.2

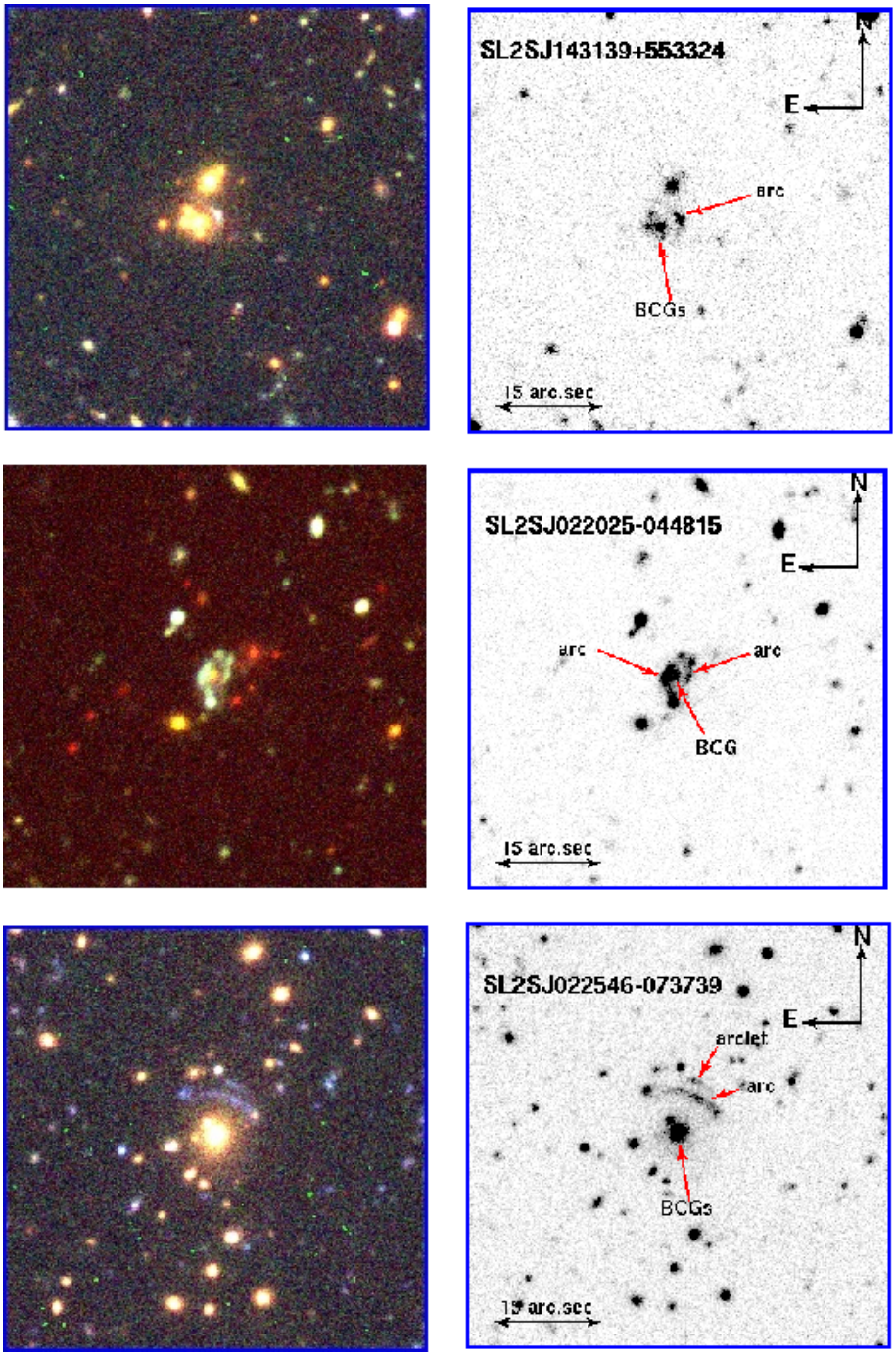

Figure 4.5: RGB images (*left panels*) and g' stamp images (*right*) of three visually detected arcs, which are *not* detected by *Arc_detector* using the standard set of parameters *without tuning* for individual cases

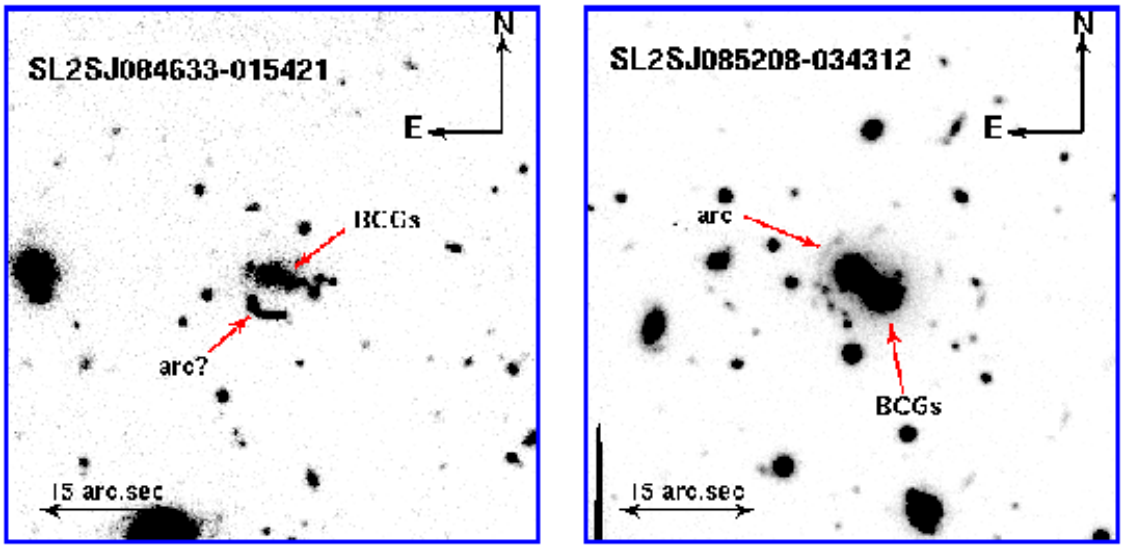

Figure 4.6: Stamp i' images of two arcs, which have low likelihood of being lenses, as mentioned in §4.4; both were detected, along with other candidates, by visual inspection of the CFHTLS-W 1 deg^2 fields

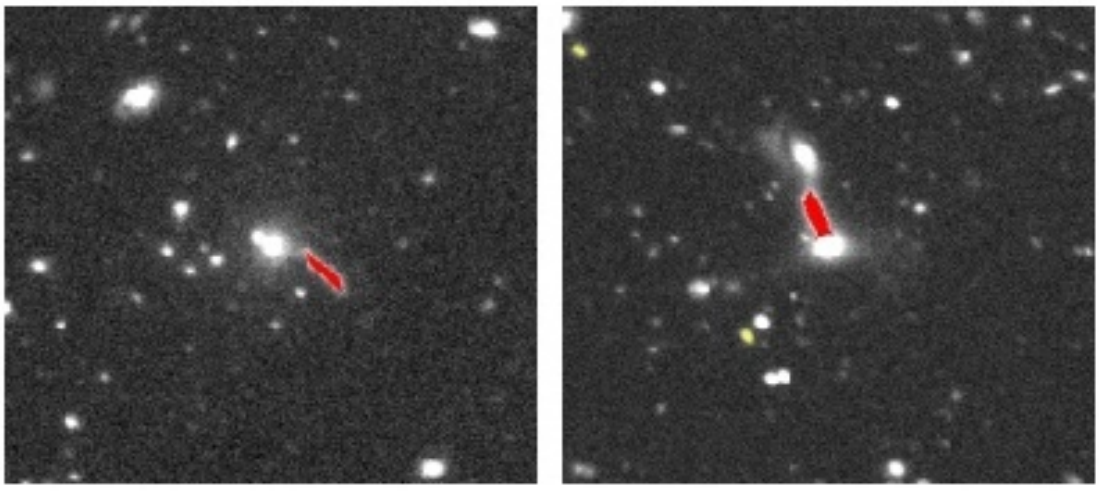

Figure 4.7: Stamp images from CFHTLS-D1 showing the two typical types of false detections - edge on spiral galaxies or tidal disruption features due to galactic interactions - flagged as lensed arcs by *Arc_detector*

$\mu_i \leq 22 mag.arc.sec^{-2}$ (which may be measured from available CFHTLS photometry) and, (ii) the presence of one or more emission lines in the observed spectrum, in regions clear of strong night sky emission bands (which needs spectroscopic confirmation). A description of the observing approach adopted and the data reduction, specifically the improved sky subtraction method using B-splines that we have implemented, are given in the following subsections before presenting the results.

4.5.1 Observing approach

In the three observing semesters since we began this survey, we have observed 6 of the 9 visually selected candidates lenses; all these observations were carried out either at the 8m Gemini North or South telescopes. Pertinent details of our observing programs for each candidate, including the Gemini program ID, are given in Table.4.2; a description of the general characteristics of the Gemini GMOS spectrograph is provided along with the IFU design in Chapter 2 (Section 2.4). For these GMOS spectroscopic observations, we initially chose a 1 arc.sec. longslit. The slit width was consistent with the expected seeing of $1''.1$ under the 'poor weather' observing conditions we had requested. Such 'poor weather' programs are specifically designed to tolerate a wide range of sky conditions, including patchy cloudy skies and 'grey' sky brightness, and thus may be scheduled in queue at over 80% of the available time during the semester; this greatly enlarges the window of opportunity for these observations at these heavily subscribed telescope facilities, For our long slit program, however, during the first semester of observations it became evident that setting up the slit on these low surface brightness targets, especially under poor observing conditions, was challenging, if not impossible. We therefore revised the instrument configuration to use MOS instead of the longslit, using the bright galaxies in the lensing cluster for mask acquisition. The bonus of this revised strategy is that we simultaneously obtain spectroscopic redshifts of several group members, for which we relied earlier on photometric estimates only.

Table 4.2: Details of spectroscopic follow-up observations of candidate arcs

SL2S ID	RA	Dec	CFHTLS-W	Date	Gemini	GMOS	Int time
-	hh:mm:ss	dd:mm:ss	field	Observed	Program	Instrument	s
SL2SJ022025-044815	02:20:25.26	-04:48:15.86	W1+1+2	Jan 2007	GN-2006B-Q-95	LS+R400	3840
SL2SJ022025-044815	02:20:25.49	-04:48:16.36	W1+1+2	Jan 2007	GN-2006B-Q-95	LS+R400	3840
SL2SJ084633-015421	08:46:32.75	-01:54:20.90	W2-2+2	Jan 2007	GN-2006B-Q-95	LS+R400	3840
SL2SJ085208-034312	08:52:07.46	-03:43:12.20	W2-1+1	Jan 2007	GN-2006B-Q-95	LS+R400	3840
SL2SJ143000+554648	14:30:00.65	55:46:47.90	W3+2+1	Jun 2007	GN-2007A-Q-114	LS+R400	3750
SL2SJ022546-073738	02:25:46.13	-07:37:38.70	W1+2-1	Sept 2007	GS-2007B-Q-52	MOS+R400 S	2570
SL2SJ022546-073738	02:25:46.13	-07:37:38.70	W1+2-1	Sept 2007	GS-2007B-Q-52	MOS+R400	2680
SL2SJ085914-034514	08:59:12.52	-03:45:18.50	W2+1-0	Jan 2008	GS-2007B-Q-52	MOS+R400	2200
SL2SJ085914-034514	08:59:12.52	-03:45:18.50	W2+1-0	Jan 2008	GS-2007B-Q-52	MOS+R400	2200

Details of Gemini GMOS spectroscopic follow-up observations of candidate lensed arcs. For each target, the columns are the Strong Lensing Legacy Survey (SL2S) ID, sky position (J2000 α, δ), the corresponding CFHTLS-Wide field, date of observation, the Gemini Observing program (with GN=Gemini North, GS=Gemini South), the GMOS instrument + grating used and the total on-source integration time. For lenses with two arcs, separate rows provide observational details for each arc

We used the R400 grating (with 400 lines/mm) set at a central wavelength of 7500Å for both the longslit and the MOS observations (both using 1" slit width); the consequent spectral resolution (R=959 with 2x spectral binning) permits measurement of the redshift to an accuracy, $\Delta z = \pm 0.001$, which is adequate for confirming the gravitational lensing hypothesis of the observed system. The grating central wavelength at 7500Å permits a spectral coverage of $5500 - 9500$Å, corresponding to the redshift range, $0.47 \leq z \leq 1.55$ for the [OII]3727 emission line doublet; the [OII] emission line is associated with star forming galaxies and the strength of the line is therefore used as one of the standard calibrators of the rate of star formation (Kennicutt, 1998). At the chosen grating central wavelength however, the spectra of these low surface brightness lensed arcs are dominated by strong night sky emission lines; since the observations were also carried out under poor weather conditions, there was a consequent increase in the sky noise. Using the standard Gemini pipeline for data reduction and extraction of these sky dominated spectra resulted in high residuals from both the sky subtraction and inadequate fringe correction (a quantitative comparison follows in sub-section 4.5.2). Therefore, we have developed and incorporated a B-spline based sky subtraction procedure first proposed by Kelson (2003) and have extended it for preparing the fringe correction frame as well; the method is adapted with minor modifications for both MOS and longslit data. Details of this new reduction technique are discussed first in sub-section 4.5.2 before we present our results from the observations. We include a comparison with results from the Gemini pipeline to illustrate the improvement achieved.

4.5.2 B-spline reduction procedure

The principal difference between the B-spline method (Kelson, 2003) and the reduction procedure commonly used for optical spectroscopy lies in the application of the *wavelength calibration*. In longslit or MOS spectroscopy, the observed spectrum on the CCD is distorted by the camera optics as well as by other effects such as a tilt

in the slit. This non-linear distortion, usually seen in both the x and y directions of the 2D spectrum, is rectified using a wavelength calibration, which maps the intrinsic (x,y) coordinates of the CCD to the observed wavelength (λ), and spatial coordinate, y'; this mapping is obtained using emission lines of known wavelength in either calibration arc spectra or unblended, strong night sky emission lines seen in the science observations themselves.

The usual reduction procedure - which is adopted by the Gemini pipeline as well- is to estimate and *apply* the wavelength calibration as one of the first steps in data reduction, usually after bias subtraction and flat fielding of the spectra. Sky subtraction is only done subsequently on the spectra which have been rectified and *resampled* to the linear (λ,y') coordinate system of the CCD. This linearisation is necessary since the sky spectrum is fitted using a parametric fitting function in these rectified coordinates.

Kelson (2003) points out that the key to improving sky subtraction is to avoid the resampling of the observed 2D spectrum- resampling of the strong sky lines leads to correlated noise in the adjoining pixels, which then unavoidably gives rise to the sharp over- and under-subtracted residuals during sky subtraction. The problem is made worse in regions around pixels affected by cosmic rays or by CCD defects, where the noise level is higher. To circumvent the introduction of correlated noise, Kelson (2003) propose using the wavelength calibration only as a map of the sampling of the sky spectrum along each row of the CCD. The small non-linear shifts in wavelength from one CCD row to the next due to camera distortions or tilted slitlets ensure that all the sky lines are well sampled. Instead of resampling to linearized coordinates, the B-spline method stacks all the rows together (assuming the dispersion direction is along the rows) to make a well sampled 1D sky spectrum as a function of observed wavelength (which is known from the wavelength calibration). This approach thus fully utilizes the sampling of the sky spectrum, which is lost during the linearisation adopted in the traditional sky subtraction methods.

Without the resampling and linearisation however, the common parametric functions for fitting the sky spectrum cannot be used. Instead B-splines, a family of non-parametric, piecewise linear functions, are used for fitting. B-splines find extensive application in engineering design; Farin (1988.) provide a complete treatment of their properties and the generating functions. The added advantage of this approach is that cosmic rays may be easily rejected using a robust sigma clipping algorithm during the fitting procedure; bad pixels and other defects may similarly be excluded with a suitable mask.

For this non-parametric fitting of the sky spectrum, we use the extensive B-spline library available within IDL. The steps involved in our reduction procedure are illustrated in the five panels shown in Figure.4.8; each panel is the same 800Å spectral window, $(7650 - 8450\text{Å})$, of a typical MOS 2D spectrum taken from our Gemini GMOS observations of SL2SJ022546-073738.

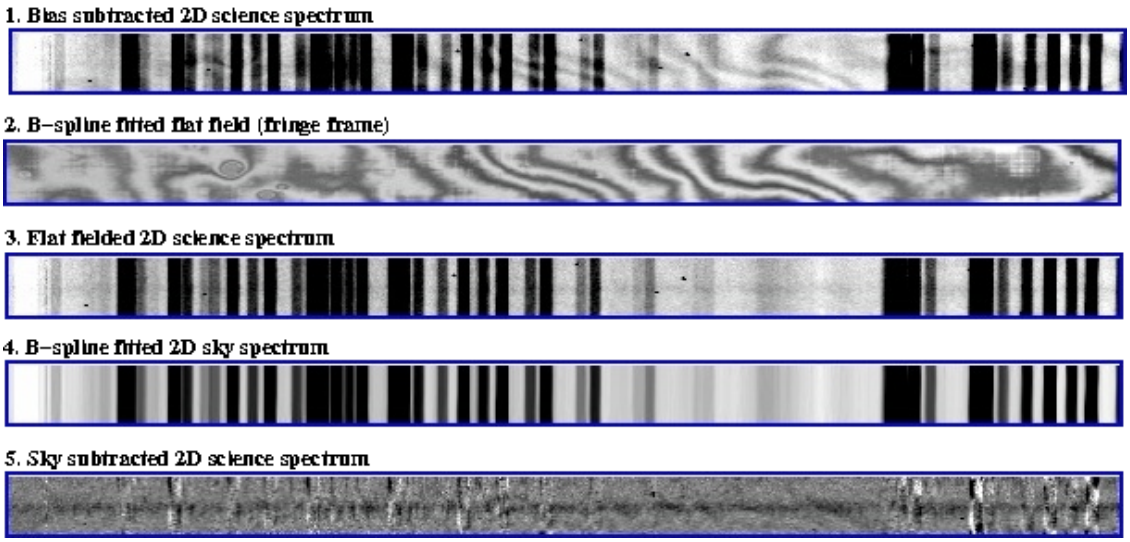

Figure 4.8: The steps involved in our B-spline reduction procedure are illustrated in these five panels; each panel is the same 800Å spectral window, $(7650 - 8450\text{Å})$, of a typical MOS 2D spectrum taken from our Gemini GMOS observations of SL2SJ022546-07373A

The first panel in Figure.4.8 shows a bias subtracted 2D spectral section; this wavelength section has been chosen since it contains two bands of strong night sky emission lines, which are seen as the dominant dark lines in the inverse grey scale image; at this early stage of the reduction process, the galaxy spectrum is not even visible against the high background level of sky emission and clearly illustrates the challenges of sky limited observations. Some of the cosmic ray spikes in this 1h exposure are also visible. Of particular note in this panel are the wavy patterns due to the severe fringing in the GMOS CCD at wavelengths $\geq$ 7500Å; we have estimated variations of $\sim$ 40% in the ADU counts along a sky line due to fringing in the red end of the detector. This appreciable, *wavelength dependent* variation in the flux in the sky lines poses a further major challenge to sky subtraction, especially for the low surface brightness targets observed. In addition, for MOS observations, this wavelength dependency causes abrupt changes in the fringe patterns from one slitlet to the next due to the changes in the position of the slits in the mask as well as any tilt in the slit, if used.

In the standard Gemini pipeline, the calibration flat field, taken contiguously with the science exposure, is also used for fringe correction. The fringe frame is prepared by fitting and normalizing the flat field with a parametric fitting function; there is no built-in flexibility to fit different functions or orders to match the changes in the fringe patters from one slitlet to the next. We have therefore developed a method of fitting an appropriate order of B-spline that matches the changing continuum in each slitlet; the method takes into account the wavelength dependency of the fringe pattern during fitting by using the wavelength solution. The second panel shows the fringe frame prepared from the calibration flat field; the third panel shows the flat fielded science exposure, where the effect of the fringing has been significantly reduced.

The sky spectrum in the flat fielded frame is then fit with a B-spline, taking the wavelength variations from one CCD row to the next into account. We use a

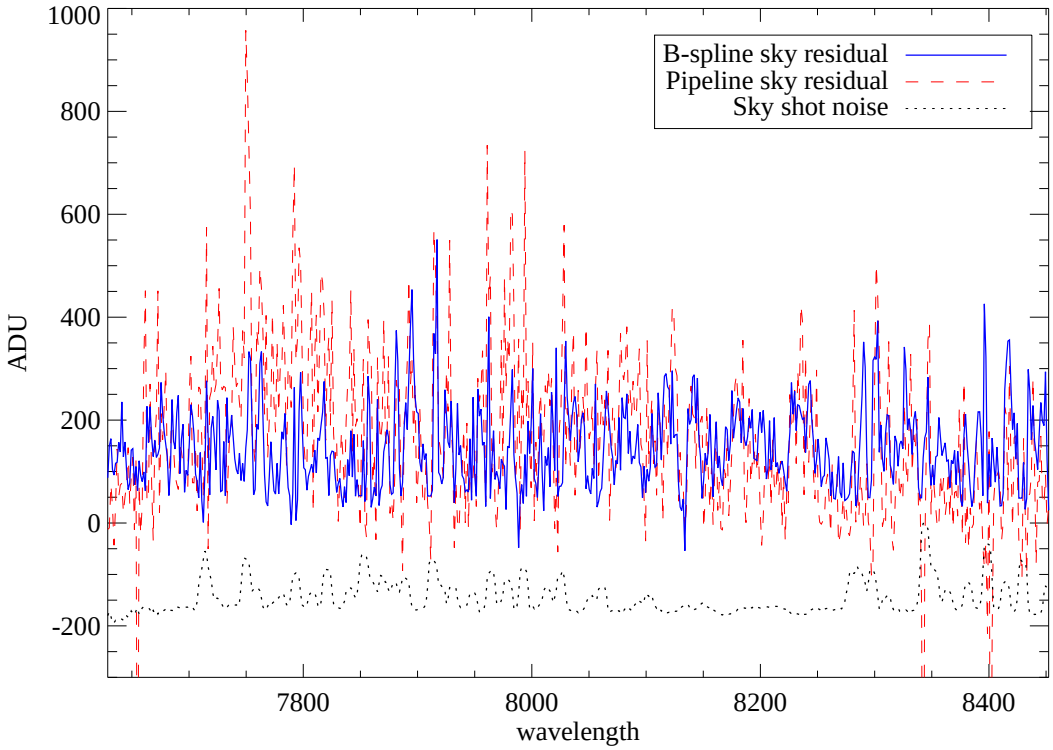

Figure 4.9: A comparison of sky subtraction residuals, (as defined in §4.5.2), from B-spline and Gemini GMOS-MOS pipeline reductions. The 1D extracted spectral section shown is the 800Å window in Figure 4.8; the corresponding shot noise from the sky lines is also shown (offset by -250ADU for clarity)

3σ rejection to exclude cosmic rays and a mask to exclude bad pixels and longslit bridges from the fit. The fitted sky spectrum is then propagated to all the rows to make a 2D sky spectrum, shown in the fourth panel, which is then subtracted from the flat fielded science frame. The 1D object spectrum is extracted from the resulting sky subtracted spectrum, (bottom panel).

A comparison of the sky residuals in the extracted 1D spectrum from this B-spline approach with those from the Gemini Pipeline reductions is shown in Figure.4.9; the shot noise, computed from the sky spectrum, is also shown to highlight areas of expected higher residuals. For this comparison we have chosen a region

with strong sky residuals and low object continuum; the sky 'residual' for this sky dominated spectrum is therefore taken to be the sky subtracted object spectrum itself. The pipeline reduced spectrum shows the under- and over-subtracted skylines due to the resampling. On average, the sky subtraction residuals are reduced by a nominal 30% by using the B-spline method. However, the residuals in the B-spline reductions are still $\sim 2\times$ what is expected from Poisson scatter alone. Most of the contribution to this noise comes from inadequate fringe correction and associated noise, which are visible as the dark and white bands on either side of the galaxy spectrum in the bottom panel of Figure.4.8. Though further improvements by more efficient fringe correction may be possible, we use the B-spline method in its current form and counter-check the extracted 1d spectra with those from the Gemini Pipeline for good measure.

Finally, it must be emphasized that the requested integration times for our observations were designed to confirm the presence of a strong [OII] emission line (rest frame EW ≥ 15) providing a S/N ratio of 5 or higher However, the practical limitation of a modest ($\sim 1h$) integration time coupled with the relaxed observing constraints means that when the emission line is not present, the continuum spectrum alone from these low surface brightness lensed arcs rarely provides adequate SNR for redshift confirmation.

4.6 Results from Longslit and MOS spectroscopy

Results for each lens candidate from our longslit/MOS spectroscopic campaign as well as from the available CFHTLS-W photometry are presented in this section; a summary of pertinent properties of each candidate obtained from these observations is also provided in Table 4.3, The redshift of each lensed galaxy is estimated by cross correlating the extracted and co-added 1D spectrum against a set of 6 star burst

galaxy templates (Kinney et al., 1996), as well as templates of late type spirals (Sa, Sb and Sc) from the same catalog. Spectra of the deflectors, where available, are correlated against early type galaxy templates (E, S0 and Bulge). The Fourier cross correlation package, *Fxcor* available within IRAF is used for the correlations. The Tonry *r-value* (Tonry and Davis, 1979), which is proportional to the ratio of the strength of the correlation peak and the associated noise, is used as the measure of the accuracy of the redshift estimation. The redshift errors from the correlation are quoted in units of cz $\mathrm{km\,s^{-1}}$ in Table 4.3; since the rms error from wavelength calibration is typically ≤ 0.1Å or a difference of cz $\leq 10\,\mathrm{km\,s^{-1}}$, it is neglected. It must be noted that during our longslit observations of the lensed arcs, our request for contiguous spectroscopy of the central galaxies of the lensing clusters was not awarded time; therefore, for the lensing clusters observed with the longslit, we estimate photometric redshifts with available CFHTLS-W photometry. Such photometric estimates are flagged accordingly in Table.4.3.

We start our summary with results for the two lenses which show [OII] 3727Å emission, our leading candidates for IFU follow-up. In the cross correlation, we also tested spectral regions containing H_α and other emission lines commonly observed in star burst galaxies; these gave lower correlation peaks than the [OII] region or the fits did not converge. Therefore we are reasonably confident that the observed emission features are consistent with redshifted [OII] lines; the redshift of the deflector, where available lends support to our assumption. For each candidate the results presented are, the 2D spectral section showing the emission line, the extracted, continuum subtracted 1D spectrum used for the cross correlation, the best fit galaxy template redshifted to match that of the arc, and the expected sky noise spectrum. The best fit template is the one with the highest *r-value*. Given the low continuum flux in the arc spectrum, the overall S/N per spectral pixel is low; however, the given sky noise spectrum shows that the spectral features, mainly the emission lines, lie clear of the strong night sky emission lines. Finally, since the ob-

servations were taken as poor weather programs, no flux calibration is attempted; this is not a drawback since the objective is to only estimate the redshift from the spectral line centroids.

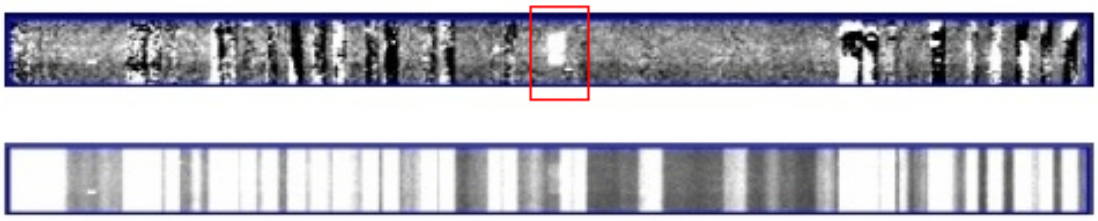

Figure 4.10: [OII] 3727Å emission line (highlighted in red box) in processed 2D spectral window ($8750 - 9450$Å) of SL2SJ143000+554648 (top panel); the unprocessed spectral section (bottom panel) shows that the line lies clear of the strong Meinel bands on either side. The effect of the significant fringing on sky subtraction in this far red end of the CCD is clearly visible

SL2SJ143000+554648: With a classic lensing geometry, a background galaxy at a redshift of 1.435 is lensed by the BCG of a galaxy cluster at a redshift of 0.501. The g' image and the RGB color composite are shown in Figure 4.2; also refer to the RGB color composite, Figure 5.5, for the $5'.5 \times 5'.5$ GMOS-MOS observations described in Chapter 5. The processed 2D *longslit* spectrum, Figure. 4.10, shows an emission feature lying between two strong Meinel bands in the extreme red end of the CCD. Even though the sky residuals are significant due to the severe fringing at these wavelengths, the emission feature is unaffected by the sky noise. In the extracted 1D spectrum, the emission feature (Figure 4.11), is seen to lie clear of the sky lines. From cross correlation with the Kinney spectral templates of star forming galaxies, we estimate the line to be [OII] $3726, 3728.7$Å, though the doublet is unresolved with the chosen 1" slit width and R400 grating combination ($\Delta\lambda = 12$Å at $\lambda_c = 7500$Å). The redshift of the deflector is spectroscopically confirmed from our MOS observations obtained as part of our survey for the dark

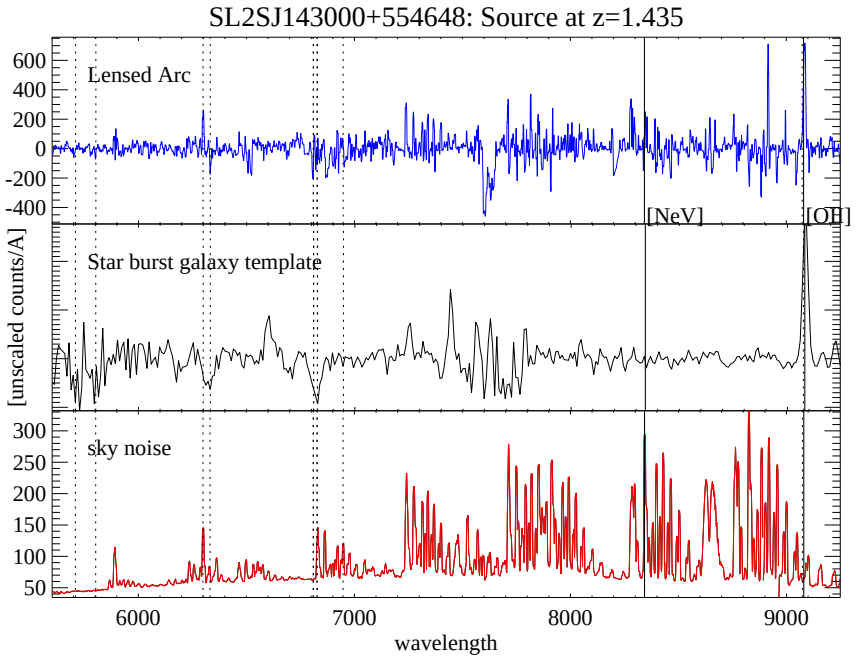

Figure 4.11: Extracted 1D spectrum of SL2SJ143000+554648 at redshift z=1.435 (top panel), compared with the redshifted best fit star burst galaxy template from the Kinney et al. (1996) catalog (middle) and sky noise spectrum (bottom panel). Typical spectral features indicative of star formation (Pettini et al., 2000) are marked (*expected* strong features with rest frame equivalent width ≥ 2 = solid lines and labeled; weaker features in dashed lines)

matter profile of lensing groups, which is discussed in detail in Chapter 5.

SL2SJ022025-044815: As a more tentative gravitational lens candidate, two arc-like structures are observed around a galaxy with an early type morphology, Figure 4.5. The arcs are bluer than the central galaxy in the RGB color composite (constructed using ugi images, since the r'-image of this region was corrupted due to a dead Megacam amplifier). In our *longslit* observations, each arc was observed with an independent pointing, with the slit oriented along the length of the arc. Each 2D spectrum clearly shows a strong emission feature at the same redshift of 1.059; the emission feature lies within the strong Meinel bandhead between

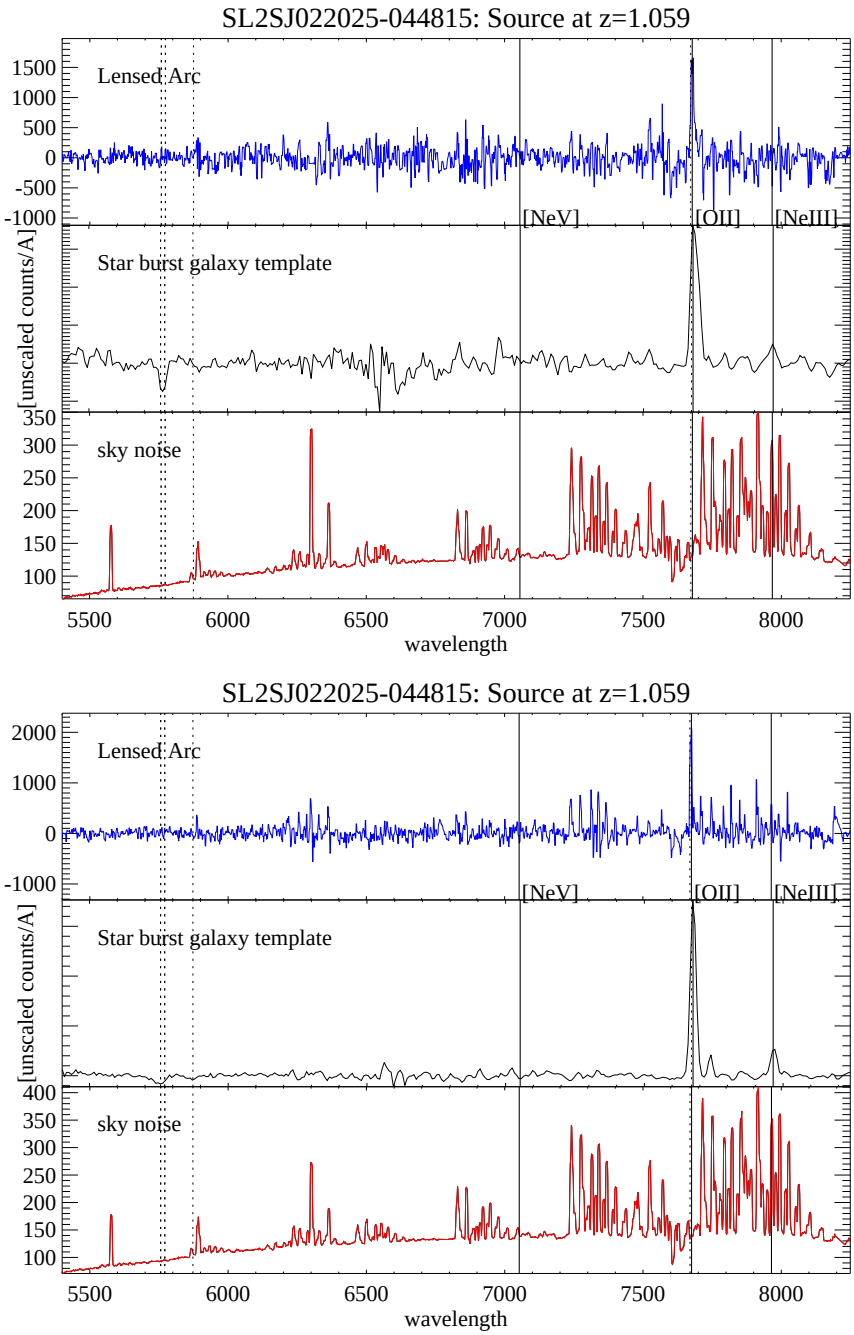

Figure 4.12: Extracted 1D spectra of SL2SJ022025-044815 at redshift z=1.059, Arc 1 (*top*) and Arc 2 (*bottom*), compared with the redshifted best fit star burst galaxy template and the sky noise spectrum. Typical spectral features are also marked as in Figure 4.11

$7600 - 8000$Å (Figure 4.12) but is strong enough to be seen even in the 2D spectra prior to sky subtraction. In cross-correlation with star burst galaxy templates, the strongest peak corresponded to the [OII] doublet, though the doublet is unresolved; no other spectral features are seen in the observed spectral range. The measured 3".5 distance between the arcs in the g'-image corresponds to $\sim$ 32kpc in the rest frame. This is marginally consistent with the object being just a face-on spiral galaxy with a bright bulge. However, the measured angular separation of the two lensed images, the redshift of the source and the probable redshift of the deflector judging by its color, are highly indicative of a gravitational lens. With only the available ugi images, the photometric redshift estimate of the deflector gave inconsistent results with large errors in the fit, probably due to light contamination from the blue arcs in the u and g images. Our proposal for GMOS longslit spectroscopy of the central galaxy was not awarded time. Therefore, the nature of the object remains unconfirmed and can be resolved with additional (IFU) observations.

Table 4.3: Measured properties of lensed arcs and BCGs

SL2S ID	Arc					BCG				
	μ_i	r	l	z_s	cz	i	$g-r$	$r-i$	z_s	cz
SL2SJ143000+554648	22.3	4.3	5.6	1.435	230	18.9	1.85	0.97	0.501	141
SL2SJ022025-044815	22.7	1.9	3.6	1.059	197	19.96	-	-	-	-
SL2SJ022546-073738	22.8	6.	10.1	-	-	19.8	1.8	1.01	0.511	179
SL2SJ085914-034514	22.4	4.6	4.4	-	-	20.12	1.76	1.41	0.644	157
SL2SJ084633-015421	21.76	4.1	5	-	-	20.12	1.62	1.35	-	-
SL2SJ085208-034312	22.93	6.	4.9	-	-	18.61	2.01	0.94	-	-

Measured properties of candidate arcs and BCGs from Gemini GMOS longslit/ MOS spectroscopy and from CFHTLS photometry. Properties and units listed are: (Arc) surface brightness, μ_i mag.arc.sec^{-2}; radius, r arc.sec; length, l arc.sec; spectroscopic redshift, z_s; redshift error, $cz\,\mathrm{km\,s^{-1}}$: (BCG) i ABmag; g-r color, ABmag; r-i color, ABmag; spectroscopic redshift, z_s; redshift error, $cz\,\mathrm{km\,s^{-1}}$. For lenses with two lensed arcs, only details for the principal image are provided; arc and BCG spectroscopic redshifts are listed only where available

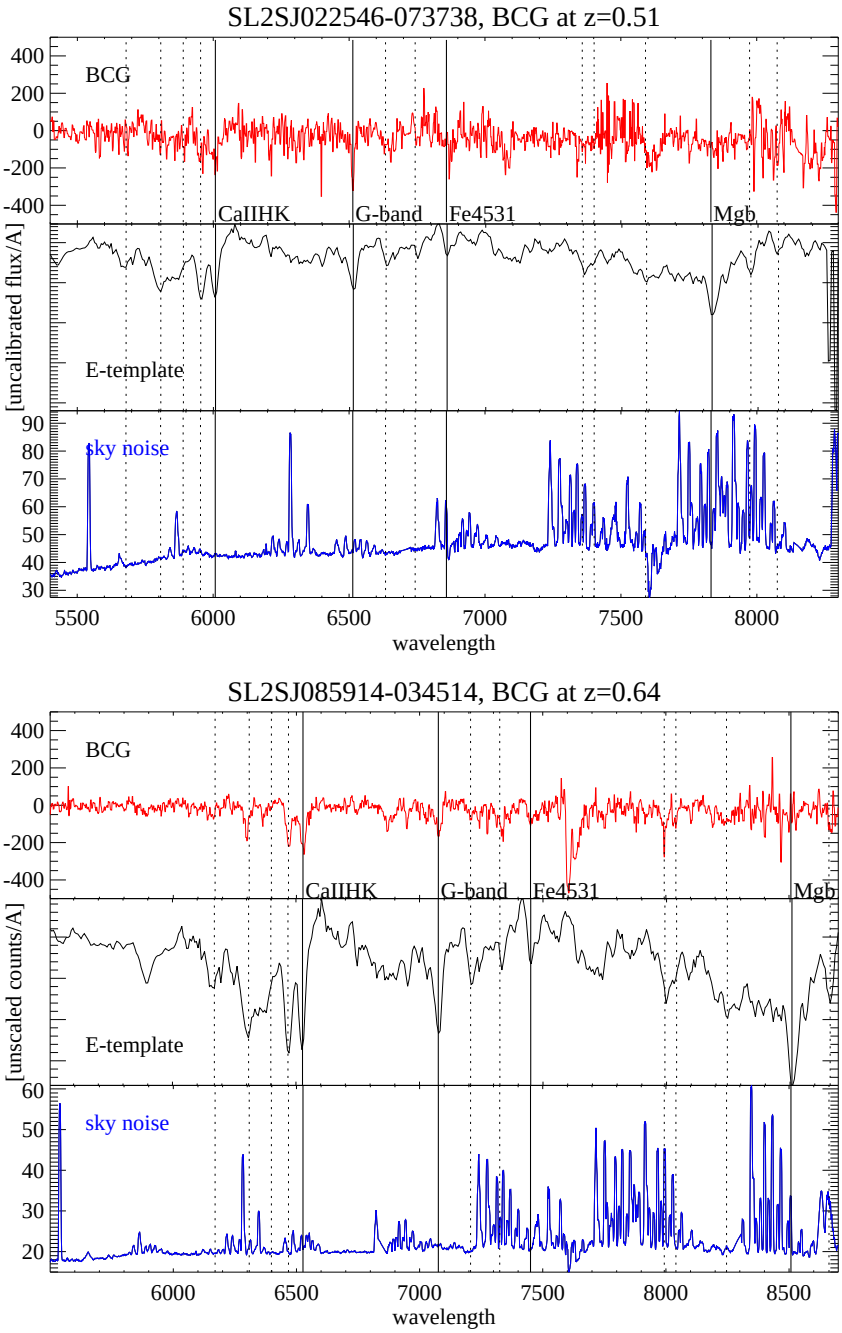

Figure 4.13: Extracted 1D spectra of the BCGs of the lensing cluster SL2SJ022546-073738 (z=0.51) (*top*), and of SL2SJ085914-034514 (z = 0.64) (*bottom*); the BCG spectra are compared with redshifted Elliptical galaxy template and the corresponding sky noise; typical absorption features indicative of an old, passively evolving stellar population are marked (strong features = solid lines with labels; weaker features in dashed lines)

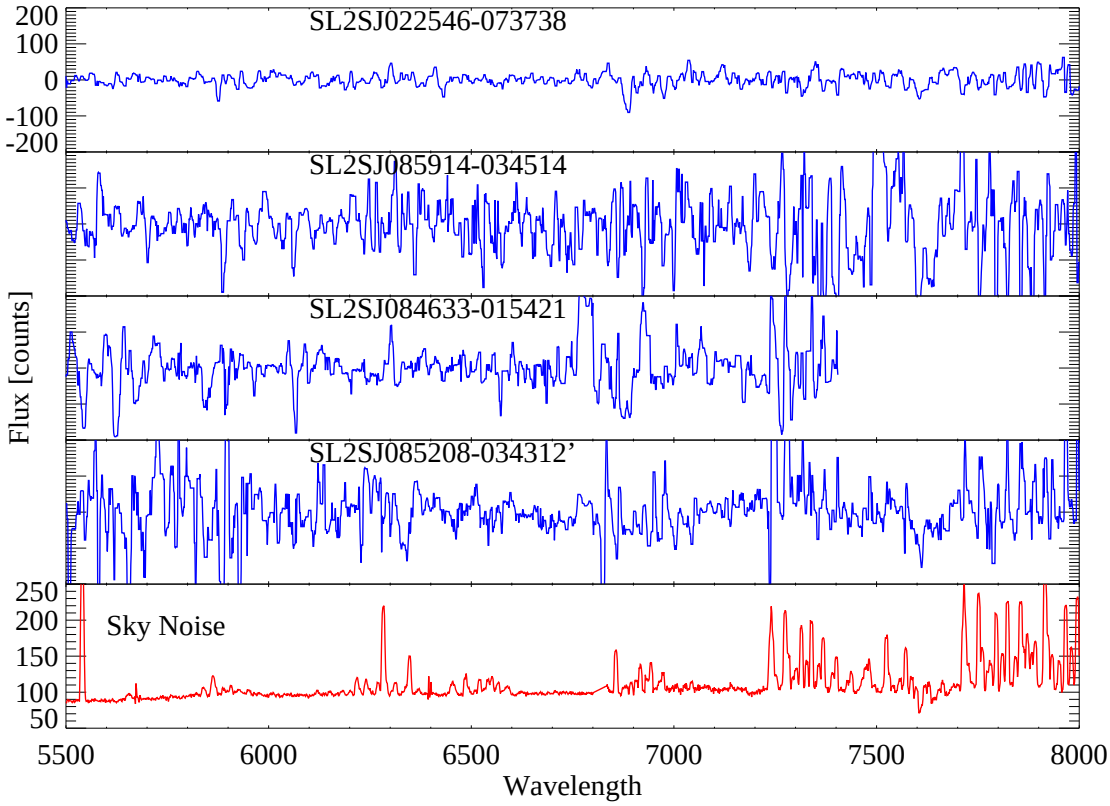

Figure 4.14: Extracted 1D spectra of lensed arcs in SL2SJ022546-073738, SL2SJ085914-034514, SL2SJ084633-015421 and SL2SJ085208-034312 for which the redshifts could not be determined due to low S/N and the lack of emission lines. The continuum subtracted spectral regions used for cross correlation are plotted, with flux in unscaled counts. A corresponding sky noise spectrum is shown for comparison

SL2SJ022546-073738: This lens candidate shows a distinct blue arc and tentatively a smaller arclet, both of which are centered on the BCG of a cluster (Figure 4.5). The longer arc (length $\sim$ 10", $l/w \sim 5$) lies at a radius of $\sim$ 6" from the brightness peak of the central galaxy measured in the i' image. The CFHTLS g' photometry of this arc indicated only two small regions with surface brightness, $\mu_g < 23.\,\mathrm{mag.arc.sec}^{-2}$, the magnitude limit imposed by the observing conditions

and our modest integration times. In our *MOS* observations therefore, the field was oriented such that two slitlets (length $\sim$ 15") covered these two regions and had adequate sky regions; this configuration permitted us to also place a short $\sim$ 5" slitlet on the central galaxy, with two sky slitlets placed beyond the slitlets for the arcs. In this field orientation, however, most of the bright (i' mag $\leq$ 20) candidate cluster members could not be observed since they lie along the line connecting the BCG and the arc. The extracted spectra of the arcs do not show any emission features; the spectrum of the brighter arc is shown in the top panel of Figure 4.14. Cross correlation of the continuum against star burst galaxy templates did not yield any consistent results, thus the redshift of the source remains unknown. For the BCG however, the extracted 1D spectrum (*top panel*, Figure 4.13) gave a strong correlation peak at z = 0.51 with early type galaxy templates, the strongest being with that of an elliptical galaxy. The measured redshifts of three other objects in the field on which we had placed slitlets, are consistent with that of the central galaxy; the median redshift and associated error are listed in Table 4.3.

SL2SJ085914-034514: Exhibiting an interesting configuration, four galaxies lie in a tight group with the candidate lensed arc approximately centered on the geometric center of the group (Figure 4.4). Close examination reveals that the arc extends nearly into a full Einstein ring (radius $\sim$ 4"), with two other segments visible above the sky background; for our MOS spectroscopy, however, only the arc segment lying to the South of the galaxy group has sufficient surface brightness. For the observations, the mask was oriented to place a slitlet along the length of this arc segment; a second slitlet was placed on the central galaxy group. No emission lines are observed in the extracted spectrum of the arc, (panel 2, Figure 4.14), therefore we are unable to determine the redshift of the background galaxy. Cross correlation of the deflector galaxy spectrum gave a strong peak at $z = 0.64$, with a strong Balmer break and several other spectral features seen in an elliptical galaxy (*bottom panel*, Figure 4.13). The measured redshifts of the other objects

on which we placed slitlets did not match the redshift of the central galaxies; this may indicate that the deflector galaxies form a compact galaxy group, warranting further detailed MOS/ IFU spectroscopy to determine the dark matter profile which is the focus of the work reported in Chapter 5.

SL2SJ084633-015421, SL2SJ085208-034312: In the visual inspection of stacked CFHTLS-W images, both these targets were flagged as candidate lensed arcs due to their extended morphology (Figure 4.6) , though their colors and geometry put them in a lower likelihood category than the 9 high priority candidates discussed in Section 4.4. Both targets were observed as part of the longslit program but the extracted 1D spectra have low continuum flux and are devoid of any indicative spectral features (panels 3 and 4, Figure 4.14). As a consequence, cross correlation against star burst galaxy templates did not provide any redshift estimate.

4.7 Conclusions and future work

With visual inspection of stacked CFHTLS-Wide color images as well as dedicated visual searches in stamp RGB images of the cluster candidates in our CFHTLS-Wide catalogs, we have compiled a set of 9 gravitational lens candidates, of which 8, if confirmed, are first time discoveries.

We have initiated a spectroscopic campaign of these candidates not only to verify the lensing hypothesis but also to assess the suitability of the lenses for deeper IFU follow-up aimed at addressing the scientific objectives set forth in Chapter 2. We have observed 6 of the 9 candidates at the current stage of the survey, using the Gemini GMOS with either longslit of MOS spectroscopy carried out at either the North or the South telescope, as warranted by the declination of the lens target.We have successfully confirmed SL2SJ143000+554648 as a classic lens (source at z=1.435, deflector at z=0.501) and in addition, have verified it as a

prime candidate for IFU spectroscopy due the presence of strong [OII] emission which lies clear of the night sky lines. A strong [OII] emission has been confirmed for the 'source' galaxy of SL2SJ022025-044815 at z=1.059; however, we are yet to be awarded time to determine the redshift of the deflector. The redshifts of the other 4 observed systems have not been confirmed due to the lack of emission lines; the continuum SNR in our 1h observations under marginal sky conditions are too low for redshift measurements. We are planning follow-up near Infra-red spectroscopy of these candidates in forthcoming observing semesters. Observations of the other lens candidates, including new ones discovered in the cluster catalogs under preparation, will be undertaken in future observing semesters.

In order to automate this search for gravitational lenses in the available 195 deg^2 of multi-color, CFHTLS-Wide imaging, we have implemented *Arc_Detector*, an algorithm developed by Lenzen et al. (2004) to identify lensed arcs in ground based, photometric data, using anisotropic diffusion filtering to enhance the elongated geometry of arcs and thus detect them. We have tuned the detection parameters for CFHTLS g' imaging and have matched the visual detections for over 60% of the candidates. We reserve a more comprehensive assessment of the method's completeness and false detection rate for future work to be carried out in collaboration with the developers of the algorithm. Correlating the detections in the g' image with those from the i' filter will help to understand the dependency, if any, of *Arc_detector* on the observed filter; this will be extended to the u*, r' and z' filters, after observations of depth comparable to the g and i filters ($\sim$ 24mag) become available.

Chapter 5

Dark matter distribution in galaxy groups

5.1 Introduction

Nature's telescope, gravitational lensing, provides a valuable cosmological probe not only to study the nature and evolution of high redshift galaxies, but also as a tool to map the distribution of gravitating mass in the universe and thus piece together structure formation at all mass scales ranging from massive clusters (mass $\geq 10^{14}$ $M_{\odot}$) down to that of individual field galaxies ($M \sim 10^{11}$ $M_{\odot}$). This latter application provides a well understood test of the model of heirarchical mass assembly, which in turn forms the corner stone of the concordance Λ-CDM model of cosmic evolution. Observations and simulations indicate that galaxy groups, which lie in the mass range ($10^{13} \leq M \leq 10^{14}$ $M_{\odot}$), form a crucial link between clusters, which are dark matter dominated, and galaxies, in whose structure baryons play a significant role. Open questions related to the contribution of dark matter in the distribution of mass in galaxy groups have been reviewed in Chapter 1. At that point it was discussed that only recently have observational results begun to address these issues. Our catalog of *confirmed* gravitational lenses from the CFHTLS-Wide fields provides a good sample of objects that, by their richness estimates, represent galaxy groups and hence suitable targets for a systematic study on the distribution

of dark matter in this mass scale.

Toward this objective, the Strong Lensing Legacy Survey (SL2S) collaboration, of which we are a part, has undertaken a multi-wavelength survey of these candidate groups and clusters; details of the survey are given in Chapter 1, §1.4. Within this broad framework, the focus of this chapter, is to estimate the mass distribution in these lensing systems from the kinematics of member galaxies, measured as the line of sight velocity dispersion (LOSVD) using MOS spectroscopy. Our results will complement the mass measurements from the lens model, describing the inner strong lensing core, the weak lensing studies, which are measured at radii outside the viral radius and from the Xray measurements which provide an estimate of the baryonic contribution. Taken together, these independent but complementary mass measurements will provide a more complete picture of the mass distribution than individual estimates using only one of these methods, which has normally been the approach in published work to date.

In Section 5.2, we use the substantial theory on galactic dynamics (eg. Binney and Tremaine (1987), to relate the underlying density distribution in a galaxy group to the projected mass and then to the LOSVD, which is the observable quantity in our work. We apply the formalism in subsection 5.2.1 to three *parametric* density profiles to characterize their effects on the LOSVD and thus to test how well our observations will distinguish one model from the other. Results from our theoretical comparisons for galaxy kinematics alone are presented in subsection 5.2.2, which are then refined in subsection 5.2.3 by adding the constraints provided by the projected mass estimated from a lens model. The observational and data reduction details of two lensing systems from our catalog, which have been observed to date, are described in Section 5.3, The kinematics of member galaxies deduced from these observations are presented in subsection5.3.3. A comparison of observations and the theoretical predictions follow in subsection 5.3.4, which includes a mass estimate under the assumption of a simple lens geometry. A full treatment of the lens model

will be undertaken with the SL2S HST Cycle 16 observations currently underway. The chapter concludes with an outline of work in progress and future plans.

5.2 Model estimates of LOSVD for specific density profiles

The objective of this section is to compute the theoretical LOSVD models of three commonly used dark matter density profiles for galaxy group and cluster scale objects, and thus compare how well we are able to distinguish one from the other observationally. We compare three parametric density profiles, the Navarro, Frenk and White (NFW (Navarro et al., 1997)) and the Hernquist (HRQ, (Hernquist, 1990)) profiles and compare them against the *Softened* Isothermal Sphere, SIS, a generic model used to describe virialized mass distributions*. In the Softened Isothermal Sphere model, a non-zero core radius is used to prevent the singular behavior at r=0 of simple *Singular* Isothermal Sphere (Binney and Tremaine, 1987).

Our choice of the NFW and HRQ profiles for this comparison is motivated by published results, which indicate that at the scale of clusters, observations to date are unable to exclude one density distribution in favor of the other; this trend may extend to the lower mass scale of groups as well. As an example, the CIRS survey, (Cluster Infall Regions in the Sloan Digital Sky Survey, Rines and Diaferio (2006)), which mapped the mass distributions in 72 low redshift clusters ($z \leq 0.2$), found that equal numbers were fit with the NFW (36) and the Hernquist (35) profiles, with SIS being the best fit for only one cluster. The mass distributions in this survey were estimated by combining galaxy dynamics from Sloan observations with mass maps from archival X-ray measurements, On the other hand, Gavazzi et al. (2003), in their strong lensing analysis of cluster MS2137.3-2353, found that the

*The abbreviation, SIS, used in this chapter consistently represents a *Softened* Isothermal Sphere only

locations and brightness of the images are better fit under the assumption of a SIS dark matter profile than with a NFW distribution. Therefore, we also include the SIS as a baseline for comparison. However, we do not test alternate density parametrizations such as the Kravtsov model (Kravtsov et al., 1998), which differ from the NFW profile only in the inner slope at radii ≤ 0.1 times the virial radius; this difference has little effect on the LOSVD, which is measured within an aperture nearly equal to the virial radius. Finally, in this comparison, we assume spherical symmetry for all three profiles and neglect any effects due to triaxiality; this analysis may have to be refined in the future, if our observational results indicate the need to include triaxiality. In Section 5.2.1, we present the formalism we have employed for this comparison; we follow the methodology developed by Łokas and Mamon (2001) for their investigations of the properties of NFW profiles, though we generalize the formulations for all three density profiles used in our comparison. The results from our analysis are discussed in Section 5.2.2.

5.2.1 Formalism used for LOSVD computation

In this formulation, we use the standard representation of the three spherically symmetric density profiles, NFW (Navarro et al., 1997), HRQ (Hernquist, 1990) and SIS (Binney and Tremaine, 1987), which are given by,

$$\rho_{NFW}(r) \propto \frac{1}{\left(\frac{r}{r_s}\right)\left(1+\frac{r}{r_s}\right)^2} \tag{5.1}$$

$$\rho_{HRQ}(r) \propto \frac{1}{\left(\frac{r}{a}\right)\left(1+\frac{r}{a}\right)^3} \tag{5.2}$$

$$\rho_{SIS}(r) \propto \frac{1}{1+\left(\frac{r}{r_c}\right)^2} \tag{5.3}$$

where, the principal parameters describing the profiles are, r_s, the scale radius for NFW, a, the scale radius for HRQ and r_c, the core radius of SIS. For the second

parameter needed to set the normalization, we choose the mass enclosed within a prescribed radius. In the first part of the analysis, in which we compare the *model* characteristics of the three profiles against each other, we use the virial mass of a typical rich cluster, $M_v = 10^{15}$ $M_\odot$, for the normalization; this assumed virial mass also permits us to benchmark our results with similar results in Łokas and Mamon (2001) (for NFW alone) and in Willick and Padmanabhan (2000) (in their comparison of mass distributions from galaxy dynamics and weak lensing), both studies having used the same fiducial cluster mass. We set the virial radius, r_v to be the radius within which the mean density is 200 times the present critical density of the unverse, ρ_0^c. For the specified virial mass, the viral radius is obtained from,

$$M_v = \frac{4}{3}\pi r_v^3(\Delta\, \rho_0^c) \tag{5.4}$$

where, the chosen overdensity parameter, $\Delta = 200$. In the second part of this analysis, where we compare the estimated LOSVDs of lensing clusters, we use the mass enclosed within the Einstein radius as the mass constraint; thus we ensure that the strong lensing characteristics within the inner core of the cluster are identical for the three profiles and test for differences in the galaxy dynamics, as measured by the observed LOSVD, due to the intrinsic characteristics of the density distributions.

Along with introducing the normalization, we also recast the expressions of the HRQ and the SIS profiles in such a way that they may be defined using the same set of parameters as used for the NFW profile. This refinement leads to a consistent set of equations for the various properties of these profiles, which therefore lends well to a systematic comparison. Under this formulation and using the notation employed by Łokas and Mamon (2001), the *normalized* density profiles may be succinctly expressed as

$$\rho(s) = \rho_0^c\, \delta_c\, \eta(s) \tag{5.5}$$

where s is the scaled radius, r/r_v. The function, $\eta(s)$, which describes the shape of

the profile, is represented for the NFW, HRQ and SIS by,

$$\eta(s) = \frac{1}{(cs)(1+cs)^2} \qquad \text{NFW} \tag{5.6}$$

$$\eta(s) = \frac{1}{(cs)(1+cs)^3} \qquad \text{HRQ} \tag{5.7}$$

$$\eta(s) = \frac{1}{(cs)(1+(cs)^2)} \qquad \text{SIS} \tag{5.8}$$

where, the *concentration index*, c, is given by (r_v/r_s) for NFW, (r_v/a) for HRQ and (r_v/r_c) for the SIS profiles. The functional form of the *concentration parameter*, δ_c, which contains the normalization scale for each profile, is obtained by setting the expression for the enclosed mass within the virial radius, $M(r_v)$, equal to the virial mass, M_v

$$M(r) = \left(\int_0^r 4\pi k^2 \rho(k) dk \right) \Big|_{r=r_v} = \frac{4}{3}\pi r_v^3 (\Delta\, \rho_0^c) \tag{5.9}$$

Substituting the normalized density profiles, Equations 5.5 - 5.8 and carrying out the integral in Equation 5.9, yields analytical expressions for δ_c for the NFW, HRQ and SIS as,

$$\delta_c = \frac{1}{3} \frac{\Delta c^3}{\left(ln(1+c) \; - \; \frac{c}{(1+c)} \right)} \qquad \text{NFW} \tag{5.10}$$

$$\delta_c = \frac{2}{3}(\Delta c^3) \left(1 + \frac{1}{c} \right)^2 \qquad \text{HRQ} \tag{5.11}$$

$$\delta_c = \frac{1}{3} \frac{\Delta c^3}{(c \; - \; tan^{-1}(c))} \qquad \text{SIS} \tag{5.12}$$

Thus, in the first part of the analysis, we have chosen the virial mass, M_v, and the concentration index, c to describe these two-parameter, spherically symmetric density distributions. In our comparison, we use two typical values for the concentration index of the NFW profile: $c = 5$, which corresponds to typical cluster mass scale, $10^{14} \leq M \leq 10^{15} \mathrm{M}_\odot$ and $c = 10$, for cD galaxy scale halos, $\sim 10^{13} \mathrm{M}_\odot$ (Willick and Padmanabhan, 2000). The former, hereafter referred as NFW5, corresponds

to the typical lensing group or cluster in our sample while the latter (NFW10) includes the cases where the strong lensing is dominated by the central galaxy alone. It must be noted that this comparison of two concentration indices (at the same overall virial mass), is intended only to quantify the effect of the underlying scale radius on the LOSVD. Furthermore, Comerford and Natarajan (2007) have pointed out that the actual value of c in clusters may be $2 \sim 3$ times higher than the earlier estimates; in the current analysis, therefore, we avoid associating the NFW profiles with any names for the objects they represent. Using the NFW5 profile as the benchmark, the concentration indices for the HRQ and SIS are adjusted to match the profiles at the scale radius, r_s; this follows the approach adopted by Willick and Padmanabhan (2000) in their comparison of the NFW and Kravtsov profiles in weak lensing. The resulting density profiles, scaled by the critical density, are shown in Figure 5.1 and are discussed in Section 5.2.2.

With the enclosed mass distribution, Equation 5.9, quantities required to compute the LOSVD may be derived. Of these, the corresponding scaled circular velocity, $V(s)$, may be expressed as,

$$\frac{V(s)}{V_v} = \frac{M(s)}{s\, M_v} \tag{5.13}$$

where the circular velocity is scaled with the value at the virial radius, given by,

$$V_v = \frac{GM_v}{r_v} \tag{5.14}$$

For the chosen halo mass, $10^{15}\,\mathrm{M}_\odot$, the circular velocity at the virial radius, $V_v = 1434\,\mathrm{km\,s^{-1}}$. Next, the radial velocity dispersion, $\sigma_r(r)$, is obtained as the solution of the Jeans equation for hydrostatic equilibrium (Binney, 1980). In our radially symmetric analysis, we assume that the anisotropy factor, $\beta = 1 - (\sigma_\theta/\sigma_r)^2$, which is a measure of the radial and tangential velocity components, is negligible; σ_θ is the tangential velocity dispersion. Our assumption is based on results from dark matter simulations (Cole and Lacey, 1996) on cluster scales, which have borne out that $\beta \sim 0$, thus lending support to the assumption of isotropy in the radial

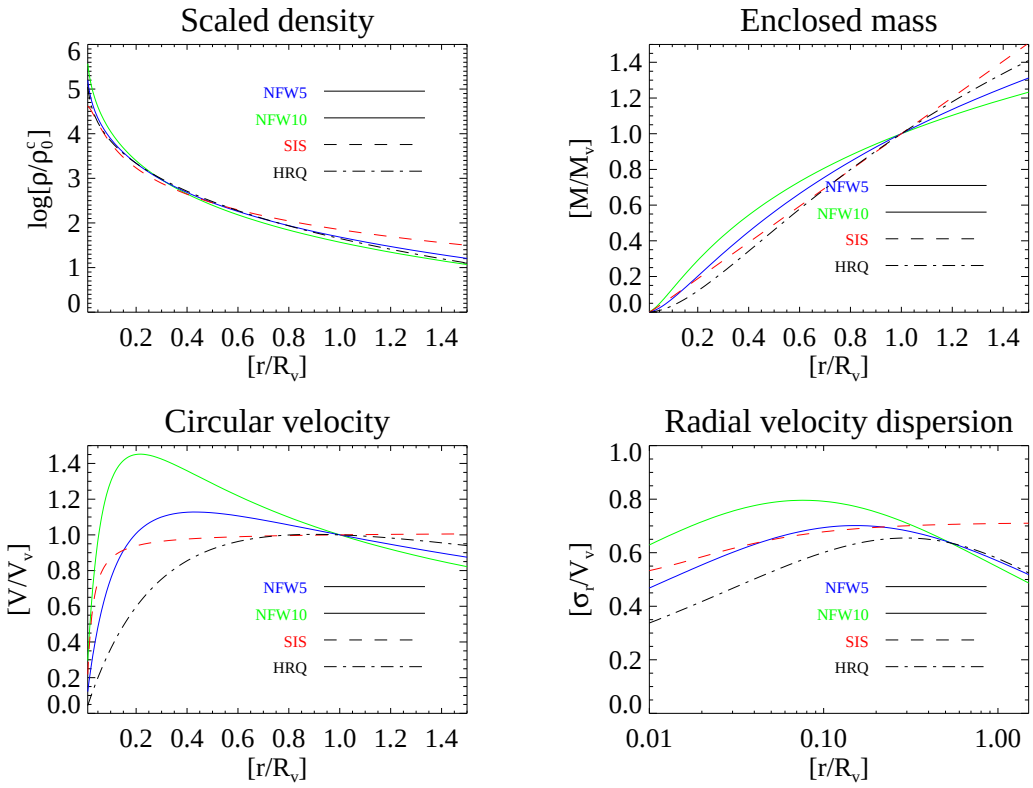

Figure 5.1: Comparison of properties of dark matter halos described by NFW, HRQ and SIS density profiles; for this plot, the profiles have been matched as described in Section 5.2.1. The top panels show the scaled density, $log(\rho/\rho_0^c)$ (left) and the enclosed mass, M/M_v (right) as functions of the scaled radius, r/r_v, while the corresponding bottom panels are the circular velocity, V/V_v and the radial velocity dispersion, σ_r/V_v.

velocity dispersion. Under this assumption, the scaled radial velocity dispersion may be expressed as,

$$\frac{\sigma_r^2(s)}{V_v^2} = \frac{1}{\rho(s)} \int_s^\infty \frac{\rho(k)M(k)}{k^2}\, dk \tag{5.15}$$

Using an IDL implementation of the numerical integration routines in *QUADPACK* (Piessens et al., 1983), we compute the unstable double integral for $\sigma_r(r)$. Published values in Łokas and Mamon (2001) for the NFW profile permit us to verify our methodology, and apply it to the HRQ and SIS profiles. The computed circular

velocities and radial velocity dispersions for the three profiles used in our comparison are shown in the bottom panels in Figure 5.1.

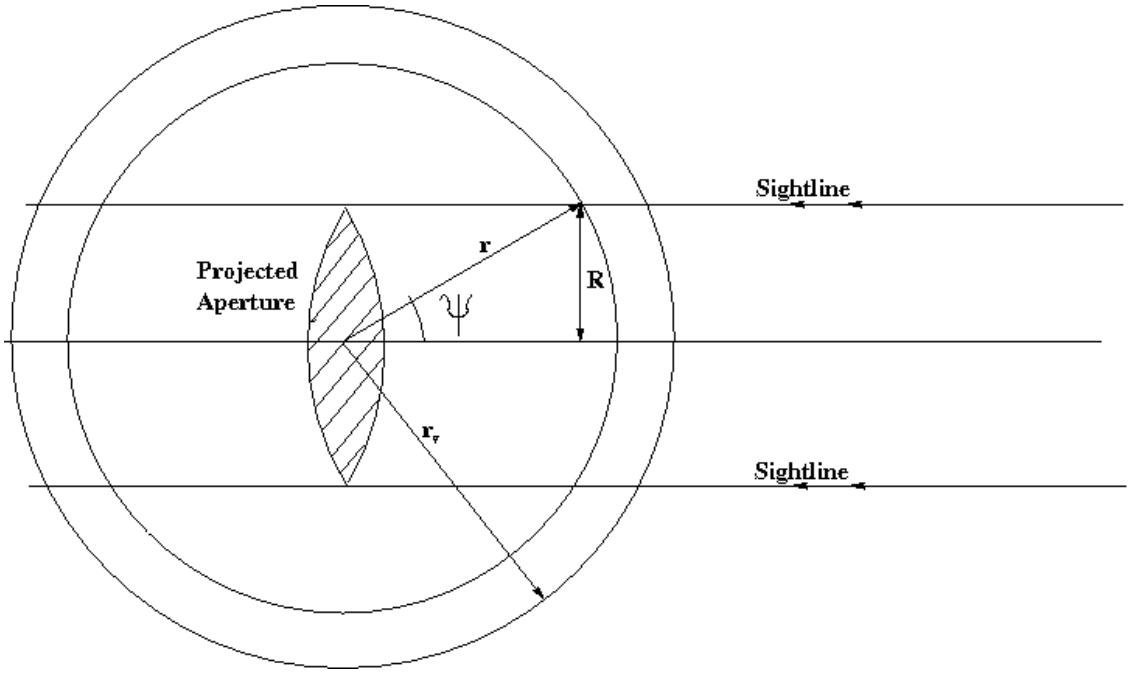

Figure 5.2: Geometry of the 3-D dark matter distribution with the projected aperture overplotted; 3-D variables indicated are virial radius, r_v, and intrinsic radius, r; corresponding projected variables are, aperture radius, R, and the angular variable of integration, ψ

For our comparison of strong lensing and galaxy dynamics in different dark matter density distributions, we need the projected mass and the LOSVD within an observed aperture, referred as the *aperture LOSVD*. Expressions for the projected properties of the halo, namely the surface density, Σ_m, the projected mass, M_p and the LOSVD, σ_{LOS}, are derived first by integrating the radial profiles of the corresponding halo properties along the line of sight. At an *observed* 2-D aperture radius, R, (indicated in the schematic Figure 5.2), the surface density is given by,

$$\Sigma_m(R) = \int_R^\infty \frac{r\,\rho(r)}{\sqrt{r^2 - R^2}}\,dr \tag{5.16}$$

where, r is the 3-D *intrinsic* radial coordinate. For numerical stability, we carry out the integration with a change to an angular variable, ψ, such that the *scaled* surface density may be expressed as,

$$\frac{\Sigma_m(R)}{r_v \rho_0^c} = \int_0^\pi R' \, \rho(R') cosec(\psi) \, d\psi \tag{5.17}$$

where the variable, $R' = R \, cosec(\psi)$. The projected mass within the observed aperture, R, obtained by integrating the surface density within the aperture, is given in units of $r_v^3 \rho_0^c$ by,

$$M_p(R) = \int_0^R K \, \Sigma_m(K) \, dK \tag{5.18}$$

with K being a variable of integration. The corresponding LOSVD, σ_{LOS}, at the 2-D radius, R, is obtained as the density weighted radial velocity dispersion. Using the results from Equations 5.9, 5.15 and 5.16, the *scaled* LOSVD may be expressed as,

$$\frac{\sigma_{LOS}^2(R)}{V_v^2} = \frac{1}{\Sigma_m(R)} \int_0^\pi R' \, \rho(R') \sigma_r^2(R') \, cosec(\psi) \, d\psi \tag{5.19}$$

where, as in Equation 5.17, the scaled radial coordinate, $R' = R \, cosec(\psi)$. Finally, the aperture LOSVD, σ_{ap}, is the surface density weighted value of σ_{LOS} within the observed aperture. Using Equations 5.16-5.19, the aperture LOSVD, in units of V_v^2, is obtained from,

$$\sigma_{ap}^2(R) = \frac{2\pi}{M_p(R)} \int_0^R K \, \Sigma_m(K) \sigma_{LOS}^2(K) \, dK \tag{5.20}$$

Comparative plots of these projected quantities for the different density profiles are shown in Figure 5.3 and discussed in the following subsection.

5.2.2 Results from LOSVD comparison - I

We first establish a baseline for our LOSVD predictions by matching the density profiles of the NFW, HRQ and the SIS distributions and then comparing their

intrinsic and projected characteristics. For this, we adjust the concentration indices of the HRQ and SIS distributions such that their scaled densities match with the NFW5 profile at the scale radius, $r_s = 0.2\, r_v$ (Figure 5.1); this matches the density distributions within the inner core and tests for differences in the consequent velocity fields. The NFW10 profile provides a comparison for variations in the concentration index; the scale radius is this case is 0.1 r_v. The virial mass in all cases is fixed at $10^{15}\,\mathrm{M}_\odot$ and provides the second constraint needed to determine the two parameters of these profiles. This cluster scale mass was chosen only because the NFW results could be compared against published values in Łokas and Mamon (2001) for the same virial mass; group scale masses, more pertinent to our work, are used in the second comparison, discussed in Section 5.2.3.

The intrinsic properties of the density distributions as functions of the scaled radius, r/r_v are shown in Figures 5.1, and their projected counter parts as functions of the scaled *aperture* (= projected) radius, R/r_v in Figure 5.3. Since the density distributions have been matched, the principal differences in the intrinsic properties arise mainly in the velocity profiles, with the radial velocity dispersion of the sharply peaked NFW10 profile showing a maximum at a smaller radius ($0.8V_v$ at $s = r/r_v = 0.08$) compared to the NFW5 ($0.7V_v$ at $s = 0.13$) and the Hernquist profiles ($0.66V_v$ at $s = 0.3$); for the assumed virial mass, the circular velocity at the virial radius, $V_v = 1434\,\mathrm{km\,s^{-1}}$. In comparison, the velocity dispersion of the SIS model remains constant at $0.56V_v$ within the core radius, where it is governed by the constant density distribution. The velocity dispersion then rises smoothly to plateau at ($0.71V_v$) at larger radii ($r \gg r_c$); this follows the trend expected from the Virial Theorem which indicates that the radial velocity dispersion for a purely isothermal sphere is a constant (Binney and Tremaine, 1987). The differences between the radial velocity dispersions however, are significant only within the core and the profiles, except the SIS, converge toward each other at larger radii (eg. at $r/r_v \geq 0.1$, the differences are $172\,\mathrm{km\,s^{-1}}$, $186\,\mathrm{km\,s^{-1}}$ and $315\,\mathrm{km\,s^{-1}}$ between the NFW10 and

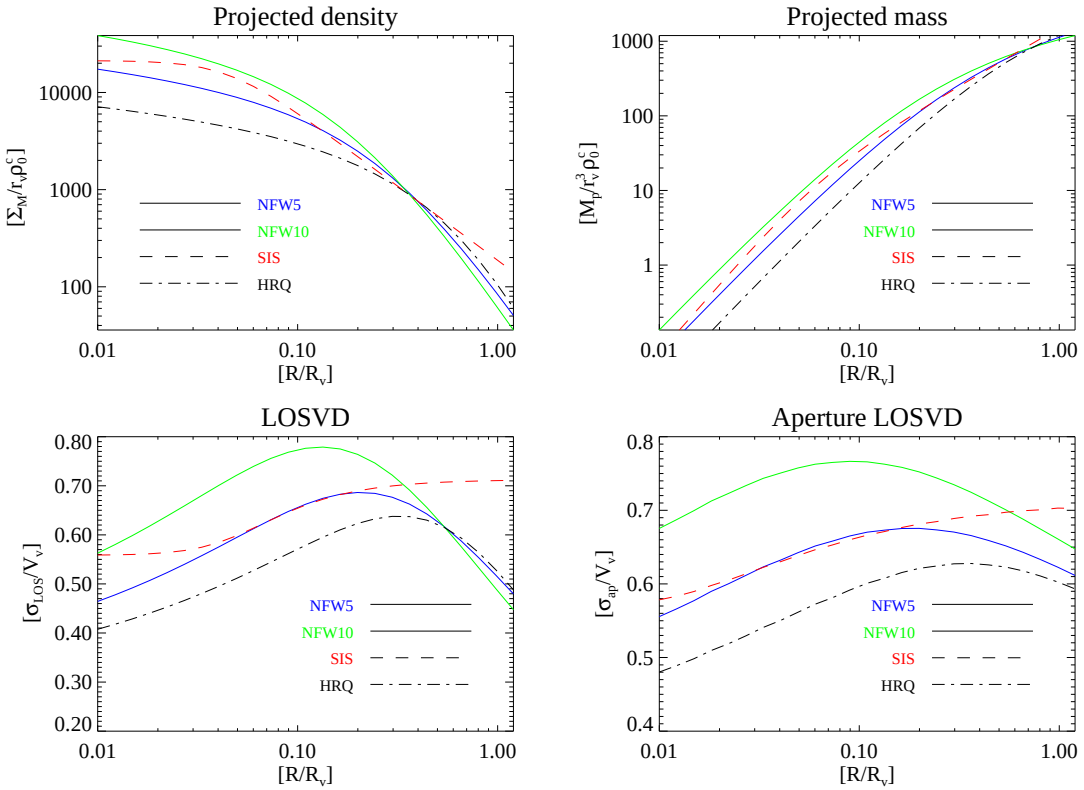

Figure 5.3: Comparison of the scaled *projected* properties of NFW, HRQ and SIS density profiles. The top panels show the scaled surface density, $\Sigma_M/r_v^3\rho_0^3$ (left), and the projected mass, $\Sigma_M/r_v\rho_0^3$ as functions of the scaled *projected* radius, R/r_v; the corresponding bottom panels are the LOSVD, σ_{LOS}/V_v at an aperture radius, R, and the aperture LOSVD, σ_{Ap}/V_v

the NFW5, SIS and HRQ profiles, but drop to $\sim 50\,\mathrm{km\,s^{-1}}$ at $r/r_v = 0.8$ for all profiles except for the SIS for which it is higher by $230\,\mathrm{km\,s^{-1}}$ and continues to increase with radius. Though the radial velocity dispersion is not directly observed, these radial trends affect the projected LOSVD, which is the measured quantity and is discussed below.

The projected properties reflect the cumulative variations between these profiles and show significant differences both in the projected mass as well as in the LOSVD. The variations in these observed properties are particularly relevant for

our work since lensing properties are governed by the projected mass and the galaxy dynamics, which are the focus of our observations, probe the aperture LOSVD. As expected from the variations seen in the intrinsic properties, the principal differences lie within the core regions and become smaller at larger aperture radii (eg, at $R/r_v = 0.8$, the observed LOSVD of NFW5 and HRQ are $75 - 100\,\mathrm{km\,s^{-1}}$ below that of NFW10 and $150\,\mathrm{km\,s^{-1}}$ lower than the SIS at this radius. Therefore, even in the case of matched densities, we expect to distinguish between the SIS and the two other density profiles with the observed LOSVD. The predicted differences between NFW5 and HRQ for this case however, are smaller than the expected errors in our observations, $\sim 100\,\mathrm{km\,s^{-1}}$, making it difficult to distinguish between the two; this prediction is consistent with the observational results from the CIRS survey, (Rines and Diaferio, 2006), discussed earlier in Section 5.2. It is for this reason that the additional constraints provided by strong lensing, which are sensitive to the projected mass distributions at smaller radii, $R/r_v \sim 0.1$, become particularly important. The effect of including the additional constraint provided by the lens model on the aperture LOSVD of the NFW, HRQ and SIS density distributions is discussed in the following subsection.

5.2.3 Results from Lensing + LOSVD comparison - II

We extend this comparison of LOSVDs to galaxy groups in which the presence of strong lens features provides additional constraints for the estimation of the mass distribution. Using the observed lens geometry, ie. the positions and brightness of the lensed images, and measured redshifts of the deflector and source, a lens model may be constructed to obtain the projected mass distribution of the deflector, the galaxy group in our observations. In this theoretical comparison of density distributions, we assume that the lens model is available, and match the *projected masses* within a chosen aperture, instead of matching the density at a chosen radius as in Section 5.2.2; for simplicity, the aperture radius for computing the projected

mass is taken to be the Einstein radius corresponding to the source and deflector redshifts. The redshifts used as an example in this comparison are those of the galaxy group, SL2SJ143000+554648 ($z_d = 0.501, z_s = 1.435$), which was observed as part of this project and is described in Section 5.3.

The comparisons are carried out for five different values of the virial mass, $10^{14} - 10^{15}$ $M_\odot$ in equal increments, to cover the typical mass scale from galaxy groups to cluster values. For each virial mass, the concentration index of each profile is iteratively adjusted to match the projected mass, M_p, within the Einstein radius, r_E, to the mass value obtained from the lens model. For the assumed lens geometry and for a spherically symmetric density distribution, the projected mass within the Einstein radius is given by,

$$\theta_E = \sqrt{\frac{d_{ls}}{d_l d_s} \frac{4GM_p}{c^2}} \tag{5.21}$$

where, $\theta_E = r_E/d_l$ is the Einstein angle ; the cosmological distances, d_l, d_s and $d_l s$ refer to the angular diameter distances from observer to the deflector, to the lensed source and from deflector to source, respectively.

Figure 5.4 shows the resulting projected mass profiles (left panels) and the LOSVD (right) for the NFW, HRQ and SIS profiles as functions of the scaled aperture radius; the effects of increasing virial mass are shown in the five profiles plotted. Table 5.1 lists the pertinent numerical values: the first three columns tabulate the viral masses, corresponding virial radii (for an overdensity, $\Delta = 200$) and the circular velocity at the virial radii. The fourth column is the scaled Einstein radius, $s_E = r_E/r_v$; the observed Einstein radius of the lensing galaxy group, SL2SJ143000+554648, described in Section 5.3, is used as an example in this comparison. The projected mass and the observed LOSVD at a rest frame radius of $0.77 Mpc$ for the three density profiles are listed in columns five to ten; this radius corresponds to the aperture in our observations of this lensing group (see Section 5.3.3). Additionally, correlations of the aperture LOSVD for the three density distributions plotted against each other are shown in Figure 5.13; for clarity, only the

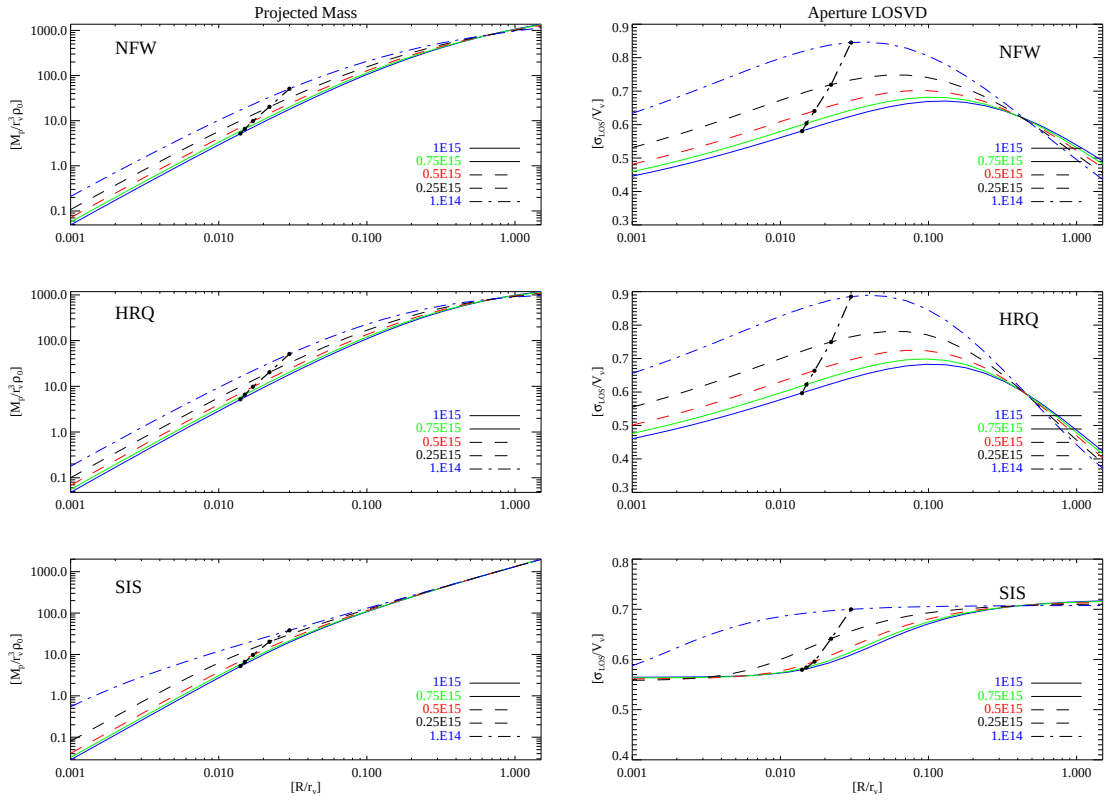

Figure 5.4: Effect of the virial mass of the galaxy group or cluster on the projected mass within an aperture (*left panels*), and the aperture LOSVD (*right*) for the NFW, HRQ and SIS density distributions respectively; refer to §5.2.3 for model parameters used in these plots. The locus of the projected mass and aperture LOSVD at the *scaled* Einstein radii corresponding to the virial masses is overplotted (chained line)

plots for virial mass of 10^{14} $M_{\odot}$ and 10^{15} $M_{\odot}$ are shown and the comparisons are discussed along with the observational results in Section 5.3.4.

The effect of *decreasing* virial mass for a fixed projected mass within the Einstein radius, seen in Figure 5.4 , is to increase the *fraction* of projected mass within the inner radii, as expected; the underlying density distribution becomes more peaked toward the center. The *scaled* aperture LOSVD consequently reflects this central concentration of mass and shows a higher relative peak in each profile as well as

Table 5.1: Modeled values of projected mass and LOSVD as functions of virial mass

M_v	r_v	V_v	s_E	M_p [$M_\odot$]			σ_{LOS} [$km\,s^{-1}$]		
[$M_\odot$]	[Mpc]	[$km\,s^{-1}$]	[-]	NFW	HRQ	SIS	NFW	HRQ	SIS
1.00E+15	2.09	1434.	0.014	5.67E+14	5.84E+14	5.65E+14	907.	889.	1011.
7.50E+14	1.90	1303.	0.015	4.76E+14	4.90E+14	4.71E+14	815.	794.	921.
5.00E+14	1.66	1138.	0.017	3.64E+14	3.74E+14	3.63E+14	696.	673.	806.
2.50E+14	1.32	904.	0.022	2.21E+14	2.23E+14	2.31E+14	526.	498.	640.
1.00E+14	0.97	666.	0.030	1.04E+14	1.01E+14	1.25E+14	353.	324.	472.

Modeled values of projected mass and aperture LOSVD as functions of virial mass, M_v, for the NFW, HRQ and SIS density distributions (column 1). The corresponding halo properties tabulated are virial radius, r_v, circular velocity, V_v, scaled Einstein radius, s_E, the projected mass, M_p and observed LOSVD, σ_{LOS}, for NFW, HRQ and SIS respectively; the listed projected mass and LOSVD are interpolated values corresponding to the Einstein radius (=29Kpc) and observed aperture radius (=0.77 Mpc) of the galaxy group SL2SJ143000 (see Section 5.2.3 for details)

an overall increase in the LOSVD for decreasing virial mass; however, the increase in the scaled LOSVD is largely offset by the decrease in the circular velocity, seen in column 3 in Table 5.1; the observed value of the LOSVD, in units of velocity, is therefore lower for a smaller virial mass.

The peaked trend in the aperture LOSVD for both the NFW and HRQ indicates a significant and *measureable* difference between the values within the core (eg. $0.2r_v$) and at a larger radius, $\sim r_v$; for example, for the NFW profile, the difference is $\sim 200\,km\,s^{-1}$ for a galaxy group scale object. The advantage of this approach is that it provides an additional constraint, thus removing the reliance on the unknown virial mass. This method may be applied with MOS observations, where the number of members with confirmed redshifts permits this binning. Depending on the number of members, a finer binning may also be adopted and the radial trend in the LOSVD may be derived. We have applied this novel approach to our GMOS-MOS observations of SL2SJ143000+554648, described in the next

section. Comparisons of the observed and predicted values of the LOSVD and the results inferred from them are discussed in Section 5.3.4.

5.3 Observations

We have complemented our theoretical models of the LOSVD with an observational campaign of MOS spectroscopy of lensing groups † from our catalog, presented in Chapter 4. The goal of the observations is to measure the redshifts of a sample of member galaxies of each group and thus estimate the LOSVD; *candidate* member galaxies are identified for spectroscopic follow-up using colors in the CFHTLS-W imaging as part of the cluster detection algorithm described in Chapter 3. At present, HST imaging of these galaxy groups is ongoing as part of a campaign by the SL2S collaboration (HST Cycle 16, PI. J-P. Kneib) and lens models are not available yet. Therefore, for the present comparison, we use the simplifying assumption that in each case the lensed arc lies on the Einstein radius, as discussed in Section 5.2.3. This permits us to obtain the projected mass without a full reconstruction of the mass distribution in the inner core of the group; this will be verified and refined as necessary when the lens models become available.

In this spectroscopic campaign, we have completed MOS observations of two groups, SL2SJ143000 + 554648 and SL2SJ143139 + 553323, both done as part of our Gemini North program, GN2007A-Q-92 during the observing semester spanning August 2007. We begin this section with a description of the instrument and target selection as well as the data reduction before we present and discuss the results from our analysis.

†For brevity, all the objects are referred as *groups* though their actual virial masses are yet to be determined with lens models using the SL2S HST observations

Table 5.2: Details of spectroscopic follow-up observations of candidate arcs

SL2S ID -	RA hh:mm:ss	Dec dd:mm:ss	Gemini Program	Date Observed	GMOS Instrument	Int time s
SL2SJ143000+554648	14:30:00.65	55:46:47.90	GN-2007A-Q-92	Aug 2007	MOS+R400	14400
SL2SJ143139+553323	14:31:39.00	55:33:23.00	GN-2007A-Q-92	Aug 2007	MOS+R400	14400

Details of Gemini GMOS observations of lensing groups to measure redshifts of member galaxies and the LOSVD. For each target, the columns are the Strong Lensing Legacy Survey (SL2S) ID, sky position (J2000 α, δ), the Gemini Observing program (with GN=Gemini North), date of observation, the GMOS instrument + grating used and the total on-source integration time

5.3.1 Instrument configuration and target selection

Our objective is to obtain the LOSVD of each lensing group from the statistical spread in the measured spectroscopic redshifts of its observed member galaxies. The strength of this estimate depends on the number of member galaxies observed as well as by their (well separated) radial distribution, In order to contiguously observe and obtain the redshifts of several galaxies ($\sim$ 20 or more) within an aperture spanning a few arc minutes, we chose the GMOS-MOS with a FOV of $5'.5 \times 5'.5$ and capable of both imaging and spectroscopy; by choosing target galaxies brighter than $i \sim 22$mag, we could use the GMOS-MOS in standard mode, ie. without nod and shuffle, for modest integration times ($\sim$ 2h), and thus maximize the accessible area of the observed field. With 1" MOS slitlets and the R400 grating set at a central wavelength of 6800Å, the spectral resolution was 480, which provided redshift sampling, $\Delta z = 0.002$. With this instrument configuration and the chosen $4\times$ spatial binning and $2\times$ spectral binning, the spectral S/N $\geq$ 5 per pixel was adequate for our observational goals. At the chosen grating setting, the consequent wavelength range of $4750 - 8750$Å permitted coverage of the strong 4000Å break in these early type galaxies in the redshift interval $0.2 - 1$, in which we expected these lensing groups to lie.

We chose to observe each field with two masks in order to increase the number of candidate member galaxies observed; the crowded regions in the centers of these lensing groups required judicious placement of the MOS slitlets. In addition, we oriented the field such that we could place a slitlet along the long axis of the lensed arc and thus aimed to obtain the redshift of the lensed source at the same time. The set of target galaxies were chosen using available CFHTLS colors and magnitudes. The top priority galaxy candidates were those that lay within a color difference $\leq$ 0.3mag (in both (g-r) and (r-i) colors) of the BCG and were brighter than i = 22mag, the magnitude limit which could be observed with a modest 2h integration time in the standard GMOS configuration. The chosen galaxies were further ranked by magnitude during slit placement, a brighter galaxy being chosen over a faint one in case of conflict. This high priority list included the visually identified bright central galaxy and the lensed arc, Regions in the slit mask, which were free after placement of these top priority targets, were filled with second priority galaxies that matched the BCG in one color only (within 0.3mag) or were brighter than the magnitude cut. This approach provided good slit placement over the observed field and permitted us to observe 20 galaxies on average per mask (plus two or three stars for mask acquisition) In addition, the observations were specifically designed to act as poor weather filler-programs in order to increase the window of opportunity. Complete details of the observations are listed in Table 5.2. All standard calibration observations were also obtained.

5.3.2 Data reduction and analysis

Both sets of MOS observations were processed using the b-spline based reduction procedure we have developed, described in Chapter 4; 1-D spectra were extracted using standard IRAF tasks and then co-added to make the final spectrum for each observed object. The spectra were continuum subtracted and then cross correlated against template galaxy spectra to determine the redshift; the continuum subtrac-

tion and cross correlation were carried out with in-house scripts designed for MOS data. For the cross correlation, performed in Fourier space, we used the IRAF task *FXcor*. Three template spectra from the *Kinney* catalog (Kinney et al., 1996, McQuade et al., 1995) corresponding to a galactic bulge, Elliptical and S0 galaxies were used for the cross correlation. The cross correlation was carried out in two steps for each template, first to obtain a nominal redshift and then a second run, with the template redshifted by the nominal value from the earlier step, in order to verify the estimated redshift and improve it, if necessary. The best fit template was determined as the one which gave the highest *R-value* in Step 1; the R-value is a combined measure of the strength of the correlation peak and the S/N in the spectrum (Tonry and Davis, 1979). For the best fit template, the redshift correction in the second step was smaller than the instrument resolution of $\Delta z = 0.002$ in all cases and was therefore neglected; this second step however provided a complementary check for the fits in the first step. The cross correlation range in the observed galaxy spectrum had to be restricted to wavelengths below 8300Å due to the noise from the strong sky bands as well as from residual fringe patterns. This restricted wavelength was not a disadvantage for the two groups we observed since the strong absorption features, which provided the majority of the correlation signal, fell well clear of the sky bands and fringe regions. This may have to be modified on a case by case basis for galaxy groups at higher redshifts by choosing spectral windows in between the Meinel bands for cross correlation. In the following section, results from our observations are discussed separately for each galaxy group.

5.3.3 Observational results

General results from our Gemini GMOS-MOS observations of the two galaxy groups are first described and discussed individually before being compared to the theoretical LOSVD predictions from the models presented in Section 5.2.3. As explained in that section, since we do not have an estimate of the total (virial) mass of these

objects, we compensate by applying our theoretical analysis to a range of virial masses.

N:B: The color plates, figures and tables accompanying the observational results are included at the end of the chapter for better presentation.

SL2SJ143000+554648: With a classic lensing geometry, a background galaxy at a redshift of 1.435 is lensed by the mass in the central regions of a galaxy group at a redshift of $0.5008^{+0.0008}_{-0.0001}$; the statistical method used for measuring the LOSVD, described in the following Section 5.3.4, also provides estimates of the group redshift. The redshift of the source was determined by longslit observations as part of our Gemini program, GN-2007A-Q-114, described in Chapter 4. The RGB color image, Figure 5.5, composed of $5'.5 \times 5'.5$ CFHTLS-W g, r, i images of the field, shows that the light in this core region of the group is dominated by the BCG, which may be assumed to contribute the majority of the mass in the region and therefore is the principal deflector; also refer to Figure 4.2, which shows a $1'$ square region in the core of the group. Using color and magnitude cuts, defined in Section 5.3.1, we identified 31 high priority galaxies (excluding the BCG and the lensed arc), and 19 objects of second priority for MOS observations; of these, the chosen field orientation and slitlet sizes (width $1''$, length typically $10''$) permitted observations of 39 galaxies, along with 3 acquisition stars and the lensed arc, using two MOS masks. Of the observed galaxies, 38 matched the early type templates during cross correlation and yielded secure redshifts. Of these, 19 galaxies are consistent within $\pm\Delta z = 0.01$ of the redshift of the BCG at $z = 0.4972$, as shown in Figure 5.6; these are taken to be members of this group. Their distribution on the sky, Figure 5.7, indicates that 10 members lie within a *projected* aperture radius corresponding to rest frame 0.5 Mpc, shown in the blue circle. The green and magenta apertures are used for LOSVD comparisons and are described in Section 5.3.4. Table 5.3 lists the spectroscopic redshifts, measured photometry and the sky positions relative to the BCG of the member galaxies. Figure 5.8 shows the velocity distribution of

the member galaxies as well as the fit to the LOSVD, both of which are discussed further in Section 5.3.4.

SL2SJ143139+553323: In this interesting, but at present *candidate* lensing group (unknown source redshift), shown in the $5'.5 \times 5'.5$ RGB color composite in Figure 5.9, four galaxies with colors consistent with early type galaxies are clustered within a *projected* aperture of radius ~ 3" (20kpc in the rest frame of this group at $z = 0.6694$). The blue lensed image, lying to the NE of these central galaxies, appears distorted by the complex mass distribution. Even though we devoted a slitlet on one mask to the lensed arc during these MOS observations, we have been unable to determine the source redshift due to the lack of any emission line in the observed wavelength range; the continuum flux level from 2h of integration per mask is inadequate for redshift determination from absorption lines with cross correlation against star burst galaxy templates. For target selection for these MOS observations, our color and magnitude prioritization provided 19 high and 24 second priority targets; of these, the chosen field orientation, permitted slitlet placement on 25 objects (of which 12 were high priority, including only one slitlet on the central galaxies, and one on the lensed arc) plus 3 acquistion stars on the two masks. Cross correlation of the extracted 1D spectra of these galaxies with the early type templates yielded secure redshifts for 22 objects; of the three remaining objects, two had spectra of low mass stars and the spectrum of the arc did not provide a redshift of the source. The redshift distribution, Figure 5.10, shows 9 galaxies consistent with a group at a median redshift, $z = 0.6694^{+0.0013}_{-0.001}$; the redshift of the central four galaxies is 0.6651 ± 0.0003. The projected radial distribution, Figure 5.11, shows that 7 of these members lie within a projected distance of 0.5Mpc of the center of the group, the barycenter being taken to coincide with the center of the light distribution of the four galaxies in the core. Measured values of spectroscopic redshifts, photometry and sky positions of the member galaxies are listed in Table 5.4; their velocity distribution and the LOSVD fit are shown in Figure 5.12 and

discussed in the following section.

5.3.4 LOSVD estimation and comparison with theoretical predictions

The statistical spread in the spectroscopic redshifts of the observed members of the galaxy groups provides a direct measure of their LOSVD within the observed aperture. By the Virial theorem, the LOSVD of these 'test particles' traces the gravitational potential, and thus the mass distribution, of the underlying -and dominant -dark matter distribution. Since we are working under the assumption that these are virialised galaxy groups, the LOSVD may be adequately described by a single Gaussian. However, given the limited number of member galaxies observed, the statistical estimators used to measure central location and the spread of the Gaussian, and thus the LOSVD of the group, must be resistant to errors due to small number statistics, especially due to outliers and any intrinsic departure of the velocity field from a Gaussian distribution. These outliers may arise either from measurement errors in the redshift or due to the intrinsic non-virialized nature of *individual* member galaxies, which may be in the initial phases of infall or may be undergoing interactions between themselves. In the presence of outliers, the classic estimators, namely the sample mean and the standard deviation, are prone to significant error due to the dominant first and second moments of these outlying points. Gebhardt and Beers (1991) and Beers et al. (1991) provide detailed discussions on these issues related to estimating the LOSVD using small samples of redshifts as well as effects due to the non-Gaussian nature of the velocity field. Based on these discussions, a comprehensive review of several alternate estimators, specifically applicable for the dynamical analysis of galaxy groups, is provided by Beers et al. (1990), who have incorporated various robust statistical methods into a public software package *ROSTAT*, which we utilize for our analysis. Based on their simulated comparisons of these methods, we adopt the *bi-weight* for estimating the central location and

spread for our samples, typically $n \sim 10 - 20$ galaxies with secure redshifts. The error in the redshift of each galaxy from the cross correlation is taken into account by ROSTAT during the estimation of the bi-weight spread. The values of the estimators for the two galaxy groups, corrected to their rest frame values, along with their confidence intervals are listed in Table 5.5. The 1σ confidence intervals on the spread, given in the table, are estimated in ROSTAT with a bootstrap technique (see Beers et al. (1990) for details on the methodology).

Figure 5.8 is a histogram of the velocity distribution of the 20 member galaxies of SL2SJ143000+554648 about the bi-weight mean redshift of the group, z = 0.5008. The LOSVD is $1081\,\mathrm{km\,s^{-1}}$ within the observed aperture using the spread in the measured redshifts as listed in Table 5.3; the overplotted Gaussian in Figure 5.8 shows the ROSTAT bi-weight fit to the velocity distribution from which the LOSVD was estimated. The estimated value corresponds to a rest frame LOSVD of $720^{+91}_{-110}\,\mathrm{km\,s^{-1}}$ within an aperture of radius 0.77Mpc at the redshift $z = 0.5008$ (shown in magenta in Figure 5.5).

Figure 5.12 shows the velocity distribution of the 9 observed cluster members of SL2SJ143139+553323 about the group redshift, z = 0.6694; the estimated LOSVD is $1005\,\mathrm{km\,s^{-1}}$, corresponding to a rest frame value of $563^{+87}_{-137}\,\mathrm{km\,s^{-1}}$ within an aperture of 0.912Mpc (indicated by the magenta circle in Figure 5.9).

We carry these LOSVD measurements an additional step by comparing its values at two (or more) aperture radii in galaxy groups where the number of members with measured redshifts permits such binning, eg. SL2SJ143000. Due to the peaked profile of the aperture LOSVD as a function of aperture radius, seen in Figure.5.3, we expect observable differences in these values; both the NFW and the Hernquist profiles show this trend. Therefore, the additional constraints provided by these differential measurements of the LOSVD at two or more aperture radii may be used both for estimating the parameters of the underlying density distribution as well as for distinguishing one profile from another. We apply this test to SL2SJ143000,

in which there are 6 members within a rest frame aperture of 0.2Mpc (shown as a green circle in Figure 5.5); this is the minimum number of galaxies needed for meaningful LOSVD measurement, according to results from ROSTAT simulations (Beers et al., 1990). The rest frame LOSVD for this subset of group members in the inner core of SL2SJ143000 is $784^{+126}_{-115}\,\mathrm{km\,s^{-1}}$.

Figure. 5.13 shows a comparison of the rest frame aperture LOSVD for the two apertures in SL2SJ143000, plotted along with the predicted values for NFW, HRQ and SIS profiles; the error bars are 1σ confidence intervals returned by the ROSTAT bootstrap method. The left panel is for a virial mass of $10^{15}\,\mathrm{M}_{\odot}$ while the right pertains to $0.5\times10^{15}\,\mathrm{M}_{\odot}$. The rest frame LOSVD of SL2SJ143139 is also overplotted, though only for reference; a more complete comparison of this group can only be done once the source redshift of this system is known, thus permitting a lens model. The theoretical predictions are computed assuming that the projected mass within the lensed arc (assumed to be the Einstein radius for now) is known from the gravitational lens model; the parameters of the density distribution are calculated using interpolation for each virial mass, using the projected mass from the lens model as the constraint, as discussed in Section 5.2.3. In this simplified model, the contribution of the baryonic mass of the BCG (a few$\times10^{12}\,\mathrm{M}_{\odot}$) to the projected mass has not been taken into account ; the effect of including this additional mass in the core however, will only shift the LOSVD profile vertically and will not affect the general trend, namely, radius corresponding to the maximum LOSVD and the slope at larger radii, which are the principal results of this analysis.

For SL2SJ143000, the comparison favors a virial mass of $0.5\times10^{15}\,\mathrm{M}_{\odot}$ compared to $10^{15}\,\mathrm{M}_{\odot}$ for this galaxy group. In addition, the LOSVD and the differential values are consistent with either a NFW or a Hernquist distribution and rule out the SIS profile, in which the aperture LOSVD increases with radius; this increase in the observed velocity dispersion for the SIS profile is due to the integration of the constant isothermal value up to larger aperture radii. As expected the limited data

cannot differentiate between the NFW and the HRQ profiles; though preliminary, this is consistent with observational results from the CIRS survey (Rines and Diaferio, 2006) in which the mass distribution in equal numbers of local clusters were fitted by the NFW and the HRQ profiles. Though, the LOSVD of SL2SJ143139 appears consistent with these results, this can only be confirmed once the source redshift and thus the lens model are available. A full reconstruction of the LOSVD profile of galaxy groups and parameter estimation of the underlying density distribution are planned for future work and will be undertaken with the accumulation of observations of other lensing groups as our observational campaign progresses.

5.4 Conclusions and future work

The focus of the work reported in this chapter is to map the distribution of mass, i.e., dark matter as well as baryonic components, in galaxy groups and thus address broader issues related to the hierarchical assembly of mass in this crucial scale, which links the dark matter dominated clusters with the scale of field galaxies, where baryons provide the bulk of mass. The key feature of the method we have developed to achieve this objective is that it combines the complementary constraints from gravitational lensing and from observed galaxy dynamics, to map the mass distribution from the core of the galaxy group to a radial distance up to the virial radius. To obtain the mass estimate from galaxy dynamics, we use MOS spectroscopy of member galaxies in the sample of confirmed lensing galaxy groups and clusters in our CFHTLS-Wide catalogs described in Chapters 3 and 4. The gravitational lens models are obtained from complementary HST observations being undertaken by members of our SL2S collaboration.

In this chapter, we have presented details of our method and the associated formalism, developed specifically for three popular, parametric dark matter profiles for group and cluster scales, namely, the NFW, Hernquist and the Softened Isothermal

Sphere model. The objective of this theoretical work is to relate the LOSVD of the member galaxies to the underlying dark matter distribution which governs their dynamics. We have successfully verified the methodology against published results for specific cases, where available. Our goal is to use the observed LOSVD from our MOS spectroscopy along with the mass constraints from the lens model to identify the dark matter profile appropriate for the scale of galaxy groups and also extract the parameters describing the density distribution.

Gemini GMOS observations are complete for two of the groups in our catalogue, the *confirmed* lensing group, SL2SJ143000+554648 (deflector redshift, z=0.5008, source z=1.435, with 20 confirmed members, LOSVD = $720\,\mathrm{km\,s^{-1}}$ within a rest frame aperture of 0.77Mpc) and the *candidate* lensing group, SL2SJ143139+553323 (z=0.6994, source redshift yet to be determined, with 9 confirmed members, LOSVD = $563\,\mathrm{km\,s^{-1}}$ within a rest frame aperture of 0.912Mpc). For the confirmed lensing group, SL2SJ143000, we have combined the LOSVD measurement with a simple lens model to favor a virial mass of $0.5 \times 10^{15}\,\mathrm{M_\odot}$ for this galaxy group; this preliminary estimate will be refined when the lens model from HST observations becomes available. The same observational approach of MOS spectroscopy for galaxy dynamics and HST observations for constructing the lens models will be adopted for all the lensing clusters and groups in our catalog. We propose to submit proposals in the upcoming Gemini observing semesters to carry out MOS observations of the lensing groups in our catalogs.

In addition, we have devised a differential measure of the LOSVD, estimated at two or more apertures, in order to constrain the slope of the velocity profile and thus distinguish the underlying dark matter density profile. We have applied this approach to SL2SJ143000 using the LOSVD measurements of the 20 member galaxies taken at two apertures. Our results exclude the softened isothermal sphere model as viable for the dark matter distribution in this galaxy group. However, the estimated slope of the density distribution is compatible with either a NFW or a

Hernquist profile in this case. The accumulation of results from future observations will permit us to test whether this compatibility with both density models, which has been reported in literature for clusters, extends to the scale of galaxy groups as well.

Our observational campaign is being carried out as part of a multi-wavelength survey of lensing galaxy groups by the SL2S collaboration. Our mass estimates from galaxy dynamics and strong lensing will be extended to distances beyond the virial radius with weak lensing mass maps as well as refined with estimates of the baryonic and stellar mass contributions obtained from X-ray and NIR observations. By combining these independent and complementary mass measurements, we will achieve a complete picture of the mass distribution in galaxy groups, which is an important issue yet to be fully addressed in observational cosmology.

Figure 5.5: RGB color image of a $5'.5 \times 5'.5$ GMOS field of view centered on the lensing cluster SL2SJ143000, observed as part of our observational program, GN-2007A-Q-92. The color image was made from CFHTLS-W g,r,i images of the field

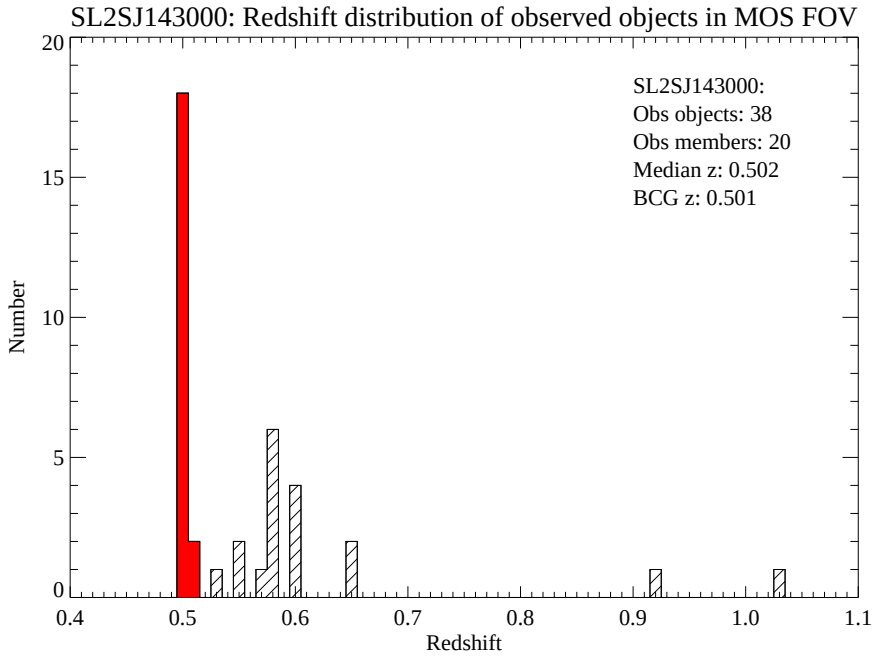

Figure 5.6: Histogram showing the redshifts of the observed galaxies in the SL2SJ143000 MOS field; the bin width used is 0.01. Of these, 19 galaxies (highlighted in red) are consistent with the red shift of the BCG

Table 5.3: Details of confirmed cluster members in SL2SJ143000+554648

ID	RA	Dec	i	(g-r)	(r-i)	z	Δz	RA offset	Dec offset
-	deg.	deg.	mag	mag	mag	-	$\mathrm{km\,s^{-1}}$	arc sec	arc sec
BCG	217.502833	55.779878	19.049	1.638	0.880	0.4972	112.4	0.0	0.0
#1	217.559250	55.764219	19.43	1.23	0.70	0.5038	72.8	203.1	-56.4
#2	217.456500	55.769869	20.09	1.55	0.81	0.4959	131.0	-166.8	-36.0
#3	217.446750	55.768939	20.10	1.65	0.92	0.4992	140.3	-201.9	-39.4
#4	217.550250	55.756489	20.32	1.71	0.87	0.5052	99.2	170.7	-84.2
#5	217.445417	55.767169	20.36	1.59	0.79	0.4988	128.6	-206.7	-45.8
#6	217.504583	55.780339	20.48	1.64	0.89	0.5009	170.3	6.3	1.7
#7	217.555208	55.792289	20.69	1.58	0.84	0.5024	109.4	188.6	44.7
#8	217.497292	55.775089	20.77	1.74	0.90	0.5019	82.4	-20.0	-17.2
#9	217.506000	55.788300	20.80	1.61	0.84	0.4969	126.8	11.4	30.3
#10	217.561667	55.765411	20.80	1.12	0.50	0.5081	117.8	211.8	-52.1
#11	217.515917	55.782339	20.80	1.69	0.87	0.4952	120.5	47.1	8.9
#12	217.459958	55.761981	20.81	1.34	0.63	0.4987	120.5	-154.4	-64.4
#13	217.513917	55.772692	21.04	1.66	0.90	0.5018	128.3	39.9	-25.9
#14	217.516000	55.773239	21.17	1.42	0.67	0.5018	115.1	47.4	-23.9
#15	217.507792	55.780000	21.20	1.42	0.70	0.5041	79.4	17.8	0.4
#16	217.557292	55.794850	21.23	1.54	0.68	0.5017	140.0	196.0	53.9
#17	217.533917	55.763511	21.25	1.37	0.72	0.4990	174.5	111.9	-58.9
#18	217.545917	55.756819	21.31	1.44	0.69	0.5047	114.5	155.1	-83.0
#19	217.497167	55.759511	21.34	1.40	0.65	0.5017	142.1	-20.4	-73.3

Details of the spectroscopically confirmed cluster members of lensing group SL2SJ143000+554648. The columns tabulated are member ID, sky position (J2000 α, δ), i magnitude, (g-r) and (r-i) colors, spectroscopic redshift, redshift error, positional offsets in RA and Dec measured relative to the position of the BCG

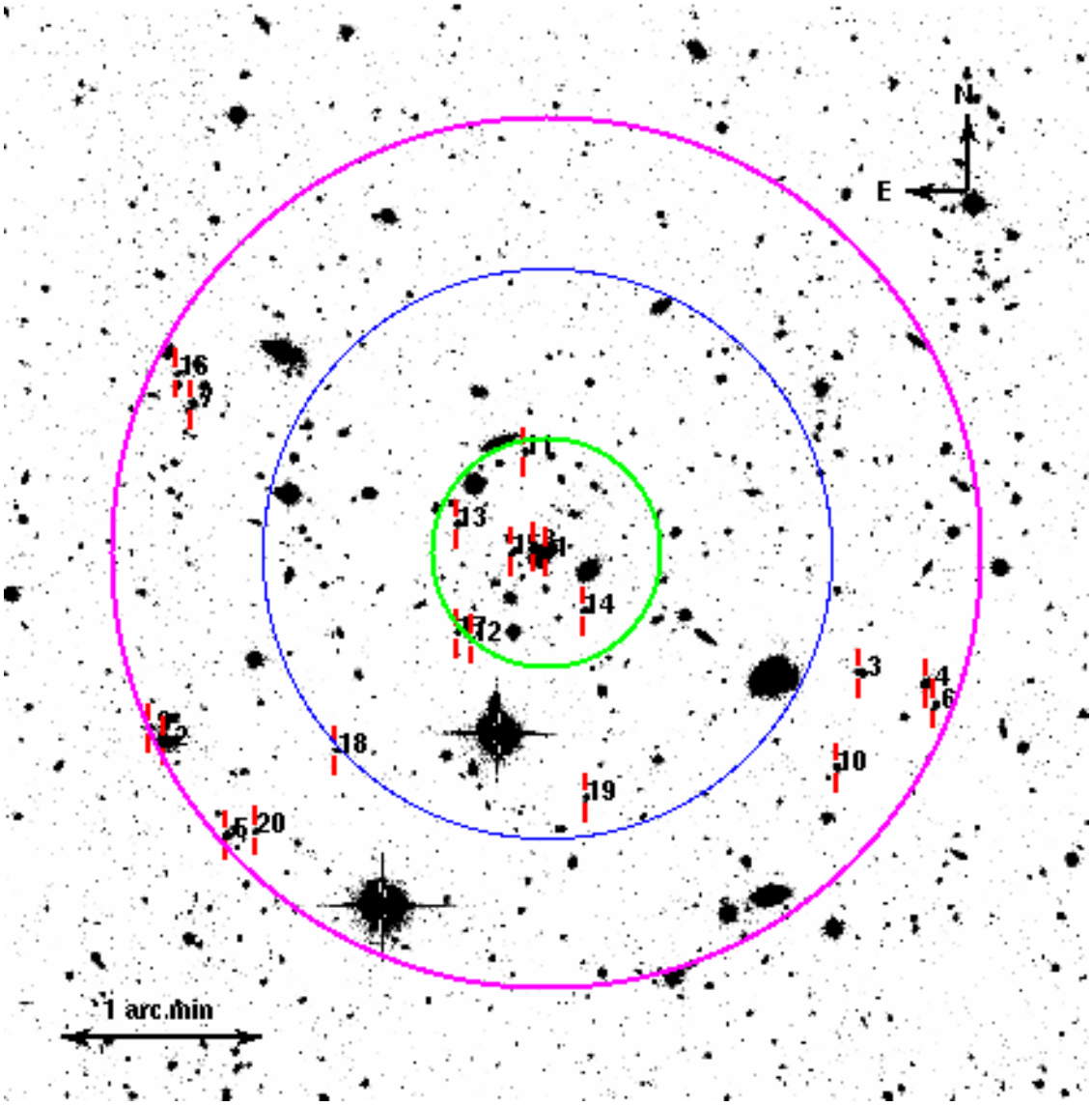

Figure 5.7: A 5′.5 × 5′.5 CFHTLS-W i'-image showing the observed GMOS-MOS field centered on SL2SJ143000 at z=0.502, with the confirmed cluster members indicated (numbered in descending order of brightness). An aperture corresponding to 0.5Mpc at the redshift of the cluster is shown (blue circle) for reference. Also shown are the inner (green) and outer (magenta) apertures used for LOSVD measurement (see Section 5.3.4

Table 5.4: Details of confirmed cluster members in SL2SJ143139+553323

ID	RA	Dec	i	(g-r)	(r-i)	z	Δz	RA offset	Dec offset
-	deg.	deg.	mag	mag	mag	-	$\mathrm{km\,s^{-1}}$	arc sec	arc sec
BCG	217.915500	55.556389	18.917	1.312	0.960	0.6651	84.2	0.0	0.0
#1	217.878583	55.551211	20.48	1.68	1.12	0.6690	203.3	-132.9	-18.6
#2	217.978333	55.565781	20.55	0.88	0.67	0.6722	95.6	226.2	33.8
#3	217.920000	55.570400	20.70	1.65	0.98	0.6747	150.5	16.2	50.4
#4	217.872750	55.562561	21.06	1.69	1.24	0.6694	70.2	-153.9	22.2
#5	217.886250	55.553411	21.07	1.23	0.93	0.6667	152.6	-105.3	-10.7
#6	217.933333	55.557511	21.07	1.67	1.15	0.6667	164.0	64.2	4.0
#7	217.950917	55.553389	21.14	1.11	0.88	0.6702	92.3	127.5	-10.8
#8	217.912333	55.570531	21.32	1.71	1.10	0.6731	149.9	-11.4	50.9

Details of the spectroscopically confirmed members of lensing group SL2SJ143139+553323. The columns tabulated are member ID, sky position (J2000 α, δ), i magnitude, (g-r) and (r-i) colors, spectroscopic redshift, redshift error, positional offsets in RA and Dec measured relative to the position of the BCG

Table 5.5: *ROSTAT* results of the LOSVD for two lensing groups

SL2S	Bi-weight	BCG	Rest frame LOSVD $[\mathrm{km\,s^{-1}}]$		Aperture radius [Mpc]	
ID	median z	z	Inner	Outer	Inner	Outer
SL2SJ143000+554648	0.5008	0.501	784^{+126}_{-115}	720^{+91}_{-110}	0.2	0.77
SL2SJ143139+553323	0.6694	0.67	-	563^{+87}_{-137}	-	0.912

Median redshift and LOSVD of confirmed members of the two lensing groups observed by our Gemini GMOS-MOS campaign; the statistical values tabulated are the bi-weight central location and spread computed by ROSTAT using the spectroscopic redshifts and errors. The 1σ confidence intervals on the rest frame LOSVD are bootstrap values from ROSTAT, converted to rest frame values using the redshift of the group

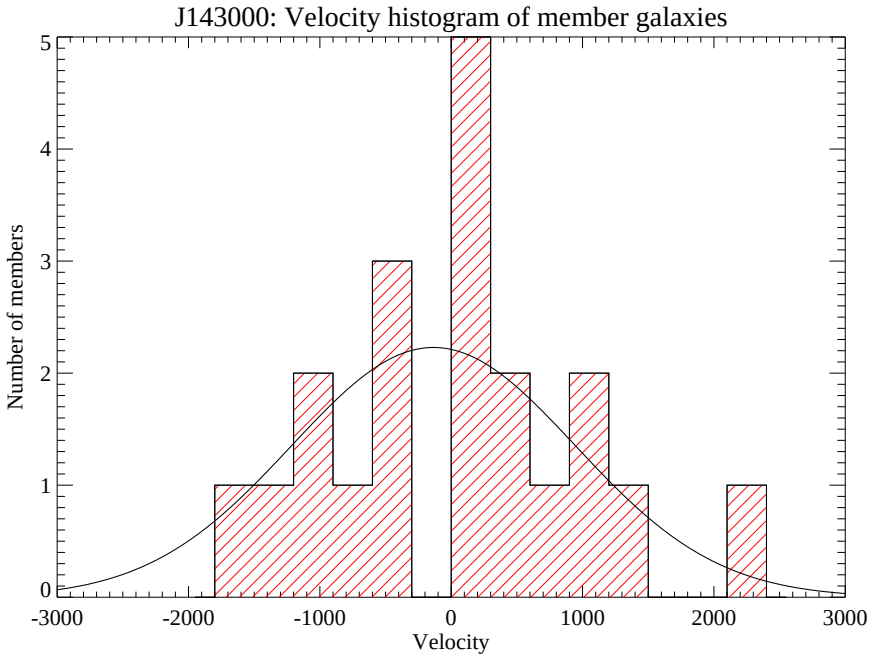

Figure 5.8: Histogram showing the velocity distribution of the member galaxies of SL2SJ143000 about the bi-weight mean redshift of the group. Overplotted is the Gaussian fit to the velocity distribution with parameters estimated by ROSTAT, as described in Section 5.3.4

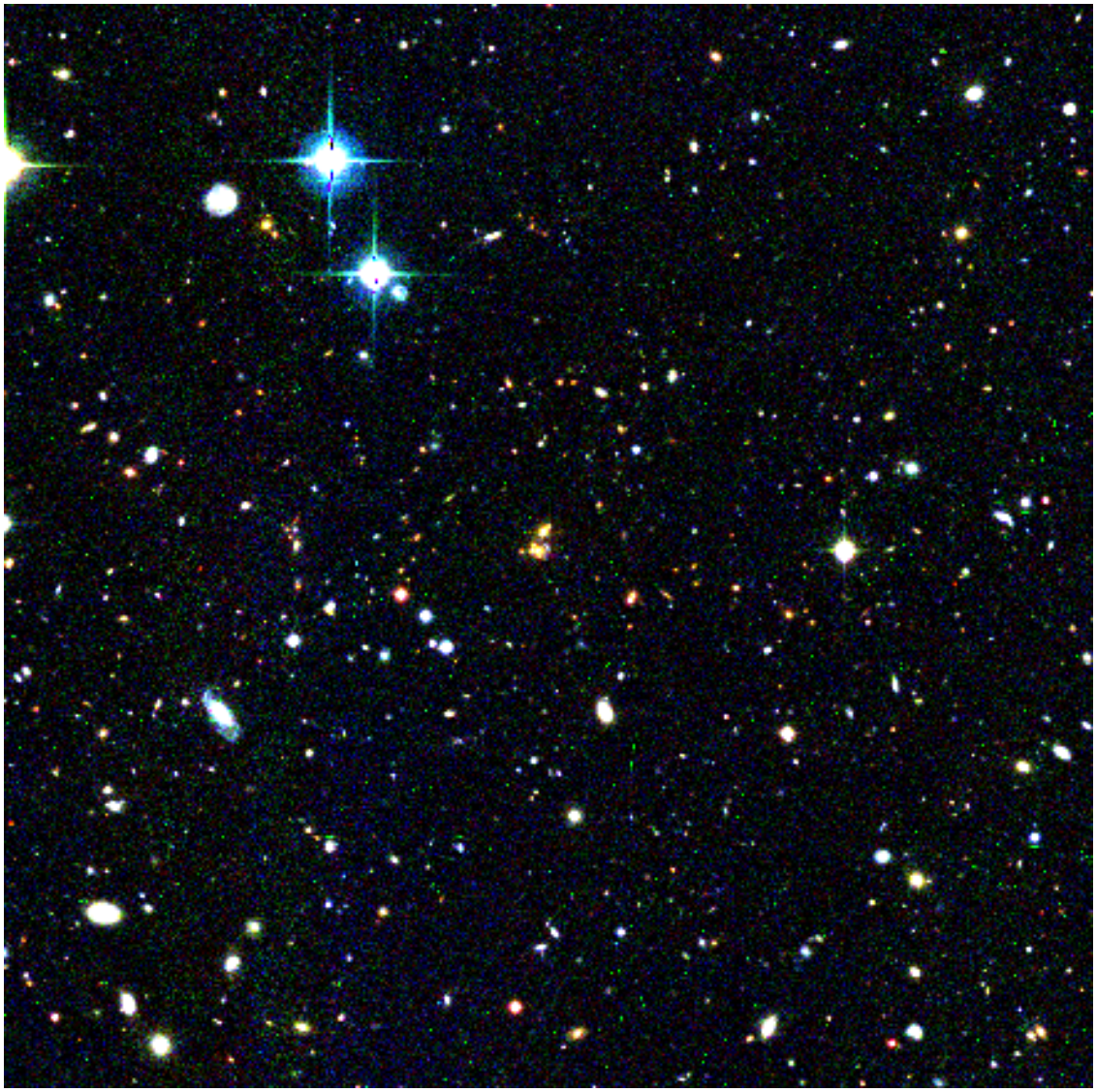

Figure 5.9: RGB color image of a $5'.5 \times 5'.5$ GMOS field of view centered on the lensing cluster SL2SJ143139, observed as part of our observational program, GN-2007A-Q-92. The color image was made from CFHTLS-W g,r,i images of the field

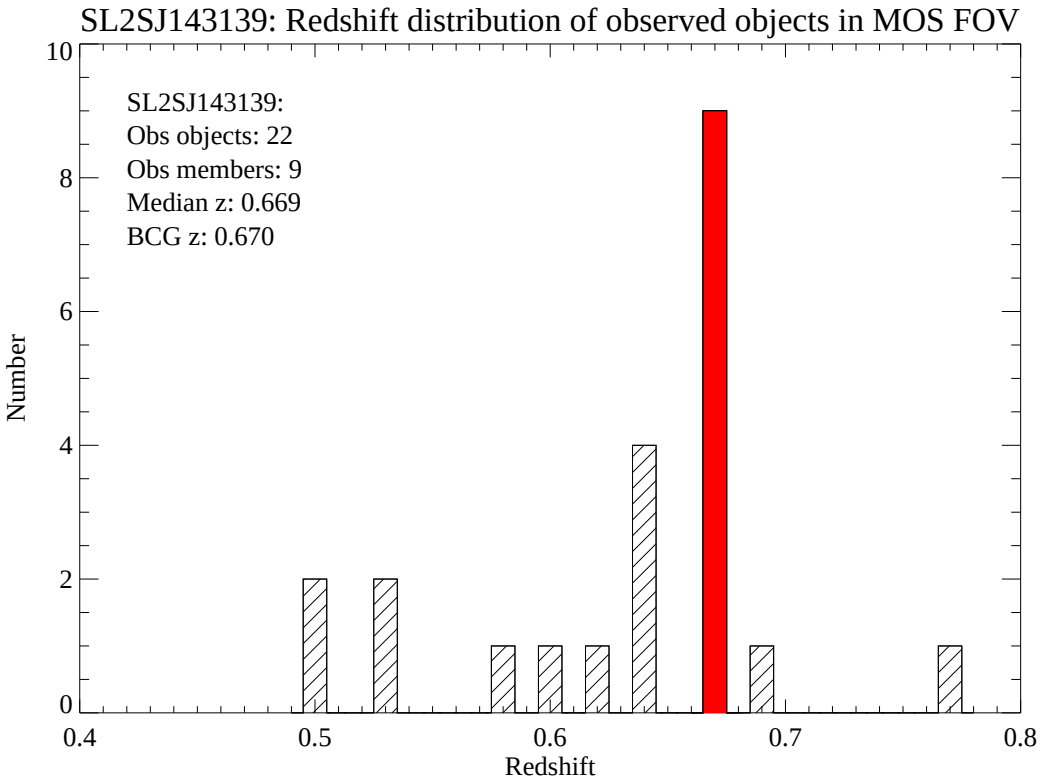

Figure 5.10: Histogram showing the redshifts of the observed galaxies in the SL2SJ143139 MOS field; the bin width used is 0.01. Of these, 9 galaxies (highlighted in red) are consistent with the red shift of the BCG

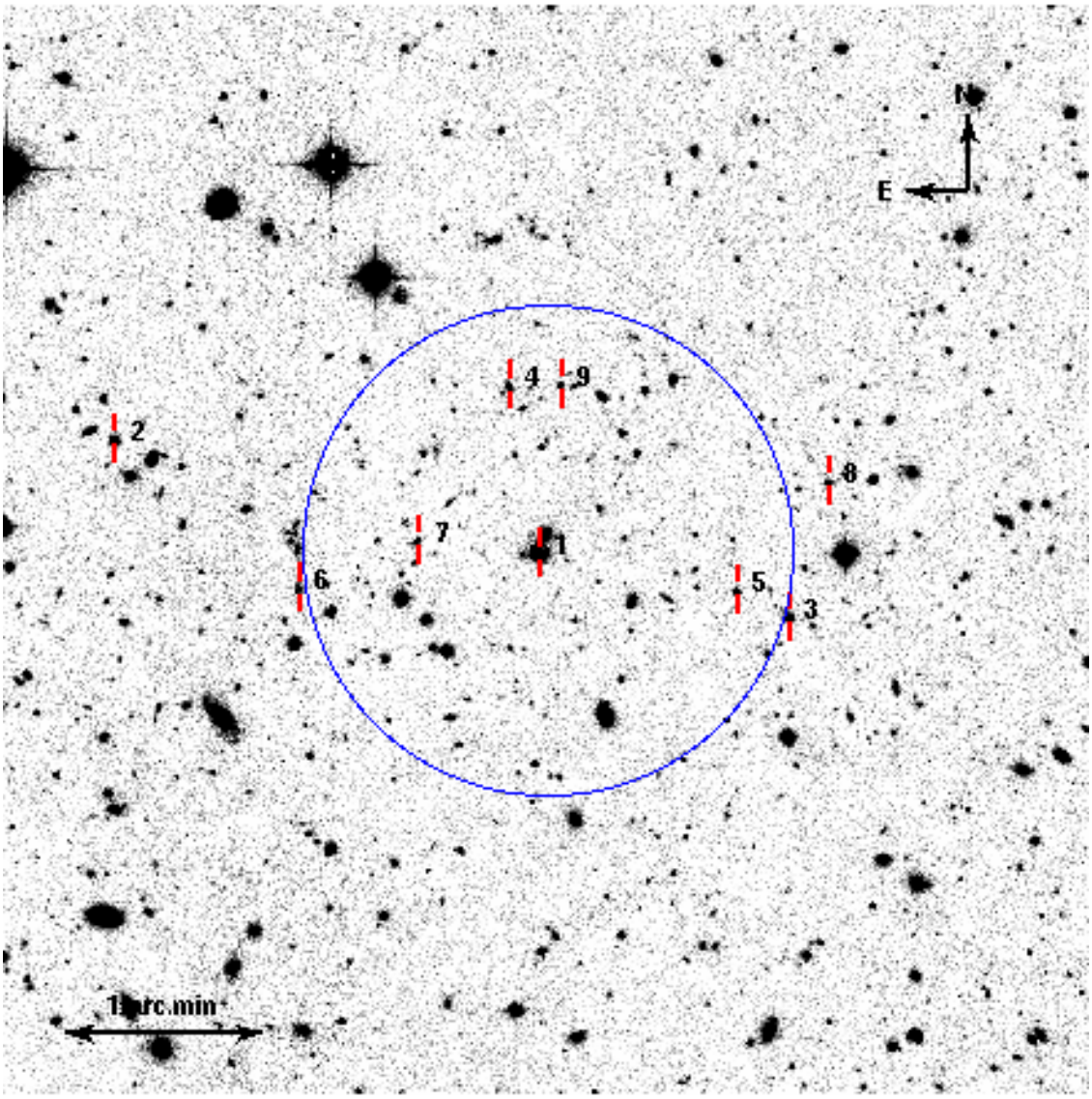

Figure 5.11: A 5′.5 × 5′.5 CFHTLS-W i'-image showing the observed GMOS-MOS field centered on SL2SJ143139 at z=0.6694, with the confirmed cluster members indicated (numbered in descending order of brightness). An aperture corresponding to 0.5Mpc at the redshift of the cluster is shown (blue circle) for reference.

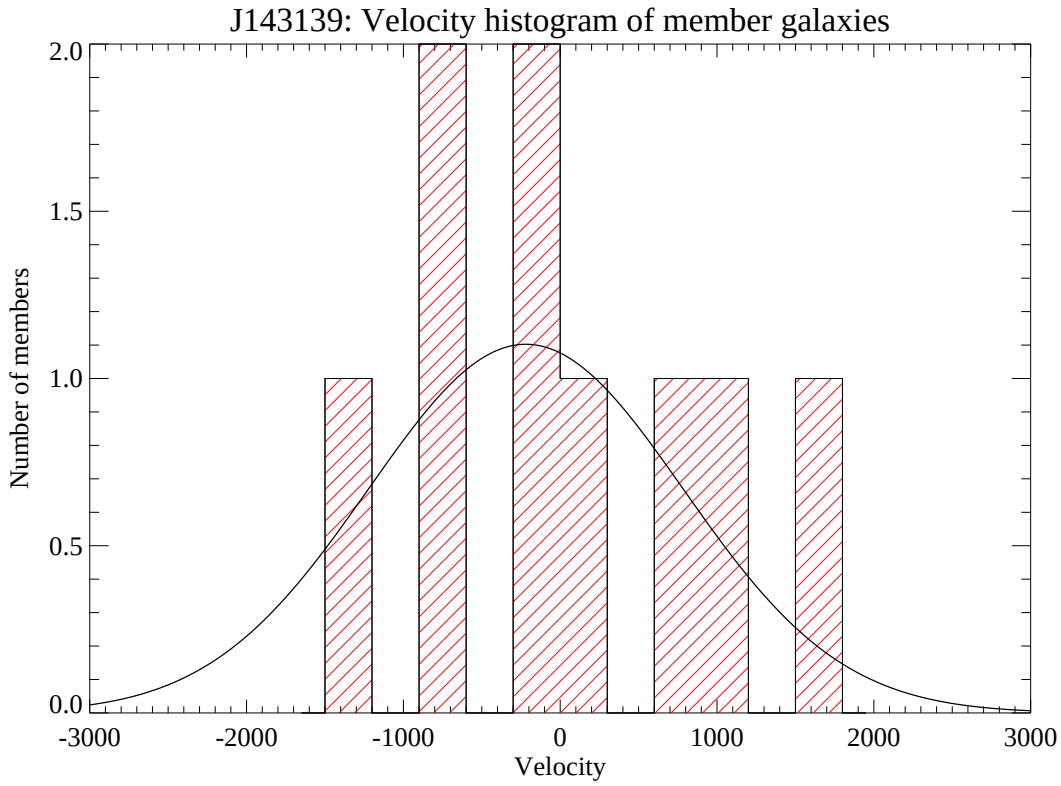

Figure 5.12: Histogram showing the velocity distribution of the member galaxies of SL2SJ143139 about the bi-weight mean redshift of the group. Overplotted is the Gaussian fit to the velocity distribution with parameters estimated by ROSTAT, as described in Section 5.3.4

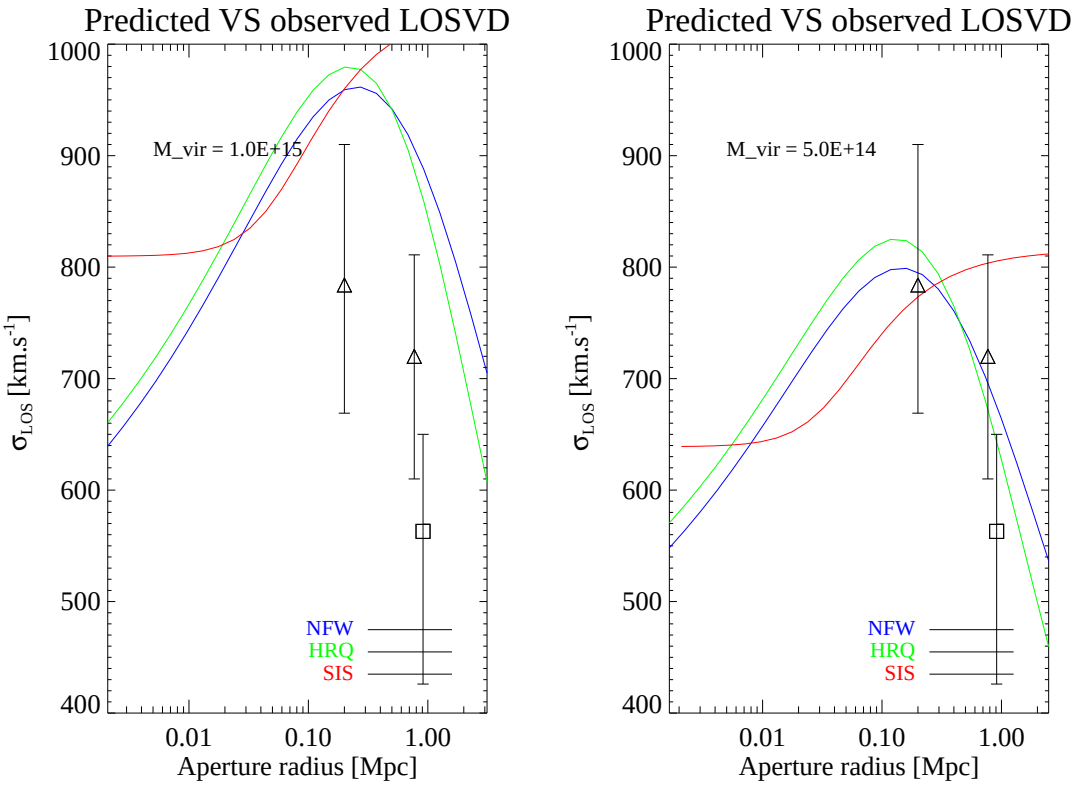

Figure 5.13: Comparison of the measured LOSVD values for the two lensing groups from our GMOS observations against the predicted values for NFW, HRQ and SIS density profiles. The left panel is for a virial mass of $1.E15\,\mathrm{M}_{\odot}$, while the right is for $5.E14\,\mathrm{M}_{\odot}$; observed LOSVD of SL2SJ143000 (triangle) and SL2SJ143139 (square) for the inner and outer apertures with 1σ confidence intervals from ROSTAT are overplotted

Chapter 6

Concluding remarks and future direction

The principal observational goal of this thesis is to develop innovative methods, which harness the magnification boost offered by gravitational lensing with recent technological advances in spectroscopy on 8m class telescopes, as viable probes of the distant universe, succinctly, Gravitational Lens Assisted Spectroscopy, *GLAS*. We have reported the development, application and current results from two such methods in this thesis.

The principal scientific goals motivating the two avenues of research are,

- – to quantify the important, but at present poorly understood, role of baryonic processes in the evolution of star forming galaxies at redshifts ≥ 1, (reported in Chapter 2), and

- – to map the distribution of dark matter in galaxy groups as a key test of the hierarchical structure formation model of the universe (the focus of Chapter 5).

Along with building the necessary data processing and analytical tools, we have also developed and implemented an algorithm for detecting gravitational lenses suitable for these investigations. The current implementation, tuned for two-color photometric data, consists of two steps, detecting mass enhancements in clusters and groups as high likelihood regions for lensing in step 1 (described in Chapter 3), followed by the detection of arcs either by visual examination or by an automated scheme (details provided in Chapter 4). In these concluding remarks, we summarize

the results and contributions of each aspect of our work and discuss the status of the ongoing observational survey as well as plans for future developments.

6.1 GLAS Application I

The baryonic processes referred in our first objective are active star formation and associated processes such as supernovae feedback and their effects, individually as well as collectively, on the evolution of the host galaxies at early cosmic times. Due to the complex and interconnected nature of these processes, their individual effects may only be estimated from observations with sub-galactic scale resolution. At the redshift of interest, $z \geq 1$, observations of these faint ($\mu_i \sim 22\,\mathrm{mag.arc.sec}^{-2}$), compact galaxies (with a length scale, $3kpc \sim 0''.3$ at z=1) are extremely challenging, even from space. Gravitational strong lensing however, 'magnifies' these compact, faint galaxies into giant arc-like images of length $\sim 10''$, while leaving their surface brightness unchanged, and therefore provides a viable avenue to achieve the needed resolution even from ground based observations.

The observational technique we have developed as part of this thesis, utilizes IFU spectroscopy to effectively gather the spatial and the spectral information in these lensed images. The quantities of interest to achieve our science goals and the observables we measure are, the rate of star formation from UV continuum or spectral line (e.g. [OII] 3727Å) indicators, galaxy kinematics and gas outflow velocities from the relative offsets of stellar and nebular line centroids and chemical enrichment from the relative strengths of the spectral lines. In these observations, the grating configuration may be chosen to match the desired velocity resolution; the spatial resolution is determined by the IFU design and the PSF during observation. For example, the optical fibers in the Gemini GMOS-IFU, which we used for our pilot program, have a resolution of $0''.2$ per spatial element while the median seeing was $0''.6$; the PSF was therefore well sampled by the IFU fibers, while the

lensed arc, which we observed, had a minimum of 12 individual spatial elements, adequate for deriving the kinematics. However, it must be emphasized that this latter estimate assumes that every IFU element samples a different region of the lensed galaxy and does not take into account any reflection symmetries that may be present in the lensed image. Such intrinsic image symmetries depend on the lensing mass distribution, the relative alignment of the deflector and the source and their redshifts, and can only be determined from a lens model. The development of the lens model, though not accomplished in this thesis work, is planned as part of the future work discussed below.

As a pilot program, we used available GMOS-IFU observations of a confirmed gravitational lens, CFRS03+1077, described in §2.2. Even though the observations were obtained for deriving the velocity dispersion of the field elliptical galaxy, which is the deflector, and the spectrograph was tuned for this goal, the presence of the lensed image in the FOV permitted us to apply our technique on the 4h of spectroscopic data.

The processing of the data permitted us to characterize the newly commissioned GMOS-IFU and evaluate the performance of the Gemini data reduction pipeline. We identified scattered light within the camera optics of the spectrograph as the principal contributor to the significant *continuum* residuals following sky subtraction; the residuals occur in spectral regions where the flux level is high and, in the worst cases, is $\sim 3\times$ the expected residual level from Poisson statistics alone. To reduce the scattered light contamination, we have implemented a scheme which uses the residuals in the sky blocks to interpolate, with a least squares cubic polynomial fit, and correct for the scattered light in the science blocks. Tests done using a twilight flat field spectrum indicate that the residuals are reduced to within $\sim 10\%$ of the Poisson noise and we assume this to be the case for the science observations as well (where the presence of the object spectrum does not allow a similar test to be carried out). The tests on the twilight flat also indicated that the cubic fit, being

an approximation with just 5 data points, may result in inadequate correction or overcompensation with resulting loss of object flux, as discussed in §2.11.

An alternative approach, therefore, may be to assess the scattered light from IFU fibers in the science field itself, which are exposed to blank sky regions within the observed target field. This simple extension of the method we have used, however depends on how much of the science field falls on blank sky regions; in the case of CFRS03, the light from the central elliptical galaxy and the lensed arc left very few fibers which could be used. A third approach may be to estimate the scattered light level from the CCD rows which form the boundary between the 5 rows for adjacent IFU fibers; due to the low light throughput by the edge of an optic fiber, any measurable flux in these edge rows would provide an estimate of scattered light. This approach would therefore sample the scattered light uniformly across the entire CCD and thus provide a better estimate of the scattered light. However, the estimate *per CCD row* would have low SNR due to the low levels of flux, requiring a robust, non-parametric fitting procedure. We have implemented such a fitting procedure using *B-splines* for flat fielding and sky subtraction of our MOS observations described in Chapter 4. We propose to adapt this B-spline method for estimating the scattered light in the GMOS-IFU as part of future developments.

With the processed observations of CFRS03, we measured the LOSVD of the elliptical galaxy, which is the deflector, as $267.5 \pm 12.7\,\mathrm{km\,s^{-1}}$. The galaxy spectrum was extracted from the processed data cube using a spectral cross correlation technique, which assured adequate S/N (≥ 15) in the spectral regions used for estimating the velocity dispersion. Due to the uncertainty in the level of residual scattered light discussed above, we adopted this cross correlation method instead of the S/N per spectral pixel estimated over the entire spectrum. For the LOSVD measurement, we chose to implement a method which directly fits a set of broadened stellar templates to the observed galaxy spectrum and thus estimates the intrinsic velocity broadening; the advantages of this approach as well as details of our the im-

plementation, which combines a χ^2minimization with a SVD solution scheme, are described in §2.9.1. Tests using 'synthetic' galaxy spectra (artificially broadened stellar spectra), show that the our method effectively estimates the LOSVD with an error $\leq 5\%$ of the true value (in the observed range, 150-300 $\mathrm{km\,s^{-1}}$, of LOSVD in elliptical galaxies). The quoted error applies to spectra with SNR ≥ 15 in the spectral regions used for the velocity measurement; the errors increase to $\sim 10\%$ with a drop of SNR to 8. Comparison of our LOSVD estimates for 25 observed SDSS elliptical galaxy spectra, taken from their public catalogs, against published SDSS velocity dispersion estimates for these galaxies indicated a match of 96% between the two values, the only case of failure being a galaxy with only two spectral lines available for the velocity fitting.

Our estimate of the velocity dispersion of the elliptical galaxy in CFRS03 differs by over 5σ from the value of $380\,\mathrm{km\,s^{-1}}$ determined by Crampton et al. (2002) and is more consistent with the lower value of $\sim 214\,\mathrm{km\,s^{-1}}$, which they argue would be indicative of passive evolution; as further support, our estimate is also consistent with the velocity dispersion based on the lens model put forth by Treu and Koopmans (2004). Taken together, these results argue against the hypothesis of Crampton et al. (2002) that elliptical galaxies may have followed different evolutionary paths. Instead our result lends support to the uniform evolutionary scenario indicated by Fundamental Plane studies, thus successfully achieving the principal objective of these IFU observations.

As an additional positive result, we identified the location of the lensed counter image of the star forming galaxy. The identification was done by cross correlating a coadded arc spectrum against individual elliptical galaxy spectra drawn from the region with a high likelihood of containing the counter image, based on image geometry. A peak in the cross correlation was taken to be indicative of a spectrum similar to that of the lensed galaxy and hence arising from a counter image. The coadded spectrum of the lensed galaxy that was used in the cross correlation con-

tained 12 absorption features in the rest frame UV range from 1380-2100Å. The location of the counter image matches a bright feature seen on the periphery of the elliptical galaxy in the HST image and falls close to the position proposed by Crampton et al. (2002) using their lens model.

The LOSVD of the elliptical galaxy, taken as a proxy for its mass distribution, as well as the location of the counter image place constraints on the geometry of the gravitational lens. With the archival HST F814W image of CFRS03 combined with these additional constraints, we are well poised to build a lens model, which is necessary to interpret any results we may have from the spatially resolved observations of the lensed image. With regard to building the lens model, our inclusion into the SL2S has made the vast experience and the necessary software (Jullo et al. (2007), Suyu et al. (2006) and Kneib et al. (1996)) available to us. We propose to undertake this work in the near future.

Finally, the spatially resolved spectroscopy that we aimed to achieve with this IFU observation of a star forming galaxy at z=2.94, was unsuccessful due to inadequate S/N, ~ 1 per IFU pixel, from 4h of integration even with the improved data reduction procedure we implemented. However, the experience permitted us to establish another key condition needed for successful IFU spectroscopy of gravitational lenses at present, the presence of an emission line to boost the S/N even with modest integration times ($\sim$ 5h, instead of $\sim$ 25h per target needed if using absorption lines). The successful results from similar observations of star forming galaxies at redshift ≤ 1.5 by Swinbank et al. (2007), Swinbank et al. (2006) and Swinbank et al. (2003) using the GMOS-IFU provide adequate proof of concept. The key challenge at present is to increase the sample size of lensed star forming galaxies suitable for these investigations - a challenge we have successfully addressed with our lensing clusters search in the CFHTLS-W fields.

6.2 Search for lensed arcs

As the first step in our search for gravitational lenses in wide field imaging, we have developed and implemented an automated search algorithm that uses the observed clustering in color and position of the population of early type galaxies in the cores of groups and clusters to isolate them from the dominant field galaxy populations. By isolating these regions of mass concentration which have higher likelihood of lensing background galaxies, we effectively reduce the area over which we carry out a dedicated visual search for lenses - without compromising the chances of locating them.

Monte Carlo simulations have established that the completeness of our cluster detector is better than 80% for clusters resembling or richer than Fornax, at all redshifts up to 0.6; poorer clusters are detected with an equivalent completeness up to z=0.3 and the completeness drops to 60% by z=0.6. These completeness results from simulations were borne out in the comparison of our catalog for the CFHTLS-Deep 1 with the confirmed XMM-LSS X-ray selected clusters for the same field - in this blind test, our catalog included all the XMM clusters up to z=0.8; all five XMM clusters not detected by our method lie at higher redshift. At redshift ≥ 0.8, the drop in the number of cluster members above the magnitude threshold we use for detection, and the increase in the photometric color errors are the likely reasons for the decline in the detection efficiency.

It must be emphasized however, that our principal focus at present is on detecting lenses, therefore it is in this context that the completeness results have to interpreted. The lensing cross section (using the Einstein radius as a simple measure) correlates directly with the mass of the deflector. In addition, a significant fraction of the known highly magnified giant arcs -the ideal candidates we seek for the IFU spectroscopy -are found in rich clusters at redshift below 0.6 (Abell 2218, shown in Figure 1.1, is a well known example). Therefore, for a given distribution of background objects, we expect that the current version of the cluster detector

is locating $\sim 80\%$ of lenses *suitable for IFU observations*. We plan to carry out a systematic estimate of the completeness of our lens detections along with the implementation of an automated lens search method, as discussed later in this section.

Our immediate goal hence, is to build the cluster catalogs and complete the search for lenses in all the CFHTLS-Wide fields for which g, r and i photometry is available; at present only the cluster catalogs for the $41 deg^2$ of CFHTLS-W3 fields with g, r and i imaging is complete and visual inspection for lenses in these fields is pending. Along with this work, confirmation of lens candidates with MOS spectroscopy and assessing their suitability for IFU follow-up will be undertaken. SL2SJ143000+554648, the confirmed lensed star forming galaxy at z=1.435, will be our first GMOS-IFU proposal in the forthcoming observing semester. Along with these applications however, there is ample scope to expand the applications of both our cluster as well as lens catalogs to address other cosmological questions and it is toward these that the future developments, discussed in the following paragraphs are directed.

In the observing strategy adopted by the CFHTLS, all the Wide fields were initially observed only in g, r and i filters, with the u and z (along with a re-observation in r filter) planned for and completed during a second pass through all these fields. In keeping with the available imaging, the current version of cluster detector was designed to use only two colors. However, inclusion of additional colors, which are now available for a significant number of fields, in the detection scheme involves only minor modifications along with the selection of magnitude limits and widths of color cuts appropriate for each color. Though this has not been implemented, the advantage for cluster detection that we anticipate, especially from the red (i-z) color, will be the detection of clusters beyond the current completeness limit at z=0.6. The four color photometry would also permit photometric redshift estimates of the cluster candidates, thereby increasing the usefulness of the cluster catalogs, for example for measuring the luminosity function of clusters and test for evolution

with redshift. In this context, Mazure et al. (2007) have reported cluster catalogs for the CFHTLS-Deep fields constructed using an adaptive kernel for detecting structures as density enhancements in measured photometric redshifts. Comparing their catalog with the results from our cluster detector, with both methods relying on color information, will reveal similarities as well as any inherent bias in either scheme. Finally, the blue (u-g) color would enhance the visual detection of the lensed arcs in the RGB color images.

For arc detection, the visual inspection of color images has been a direct and successful approach, resulting in the current tally of 9 lens candidates. However, selection effects and the subjective bias in visual detection are difficult to quantify making comparisons of our lens catalogs with those from other surveys difficult. It is for this reason that we have implemented the automated *Arc_Detector*, assessing its performance by comparing it with the visual detections; the results have been favorable with $\geq 65\%$ of matches between the two methods. The tests have also helped us identify that low surface brightness and proximity to the deflector (separation $\leq 2''$) are two probable reasons for the cases in which *Arc_Detector* failed to identify a visually detected arc. The tests for false detection rates showed that another aspect that requires refinement is the set of rules used to distinguish arcs from other elongated objects, such as edge on spiral galaxies. Our test results have been conveyed to Lenzen et al. (2004), the developers of the algorithm with whose active collaboration we plan to implement these developments. Estimating the selection bias of this method and understanding the completeness of the detections using simulations are planned for the long term work.

6.3 GLAS Application II

The second objective pursued in this thesis is to determine the distribution of dark matter in galaxy groups using a joint analysis of strong lensing plus dynamical

mass measurement from MOS spectroscopy of member galaxies. Due to the complementary use of gravitational lensing along with spectroscopic measurements of galaxy kinematics to estimate the mass distribution in galaxy groups, we classify this project, perhaps debatably, as our second application of GLAS. This work is being carried out as an integral part of a multi-wavelength survey by the SL2S group, which aims to incorporate weak lensing, X-ray and NIR measurements to build a comprehensive picture of the baryonic and dark matter profiles in virialized structures in the mass range $\sim 10^{13}\,M_{\odot}$ and thus understand hierarchical mass assembly in galaxy groups within the framework of the Λ-CDM model. The development of the necessary formalism for our contribution is complete and we have already determined the LOSVD of two lensing groups, as proxies to their dynamical mass, with Gemini MOS observations.The completion of this work requires the estimate of the mass in the core of these objects, which is determined from strong lensing analysis. HST observations (Cycle 16, PI J-P. Kneib) of these targets, which are required for building the lens models, are ongoing as part of a SL2S program. The status of the observations in the other wavelengths are in the preliminary stages. Our plan for the immediate future, therefore is to continue with the MOS observations of confirmed lensing galaxy groups, along with the MOS and IFU observations proposed in §6.2.

The thesis began with a narrow and deep focus on investigating the role of star formation in the evolution of late type galaxies at high redshift ($z \geq 3$) using IFU spectroscopy of lensed galaxies. Based on results from pilot observations, the focus has since been revised to target emission line galaxies at $z \leq 1.5$. At the same time, the scope of the thesis has been expanded to include two other projects, building galaxy cluster and group catalogs from wide field imaging as well as identifying a subset of these objects with associated strong lensing images for follow-up spectroscopy. However, both catalogs provide avenues for several related cosmological investigations. The mapping of dark matter in galaxy groups,

which may be taken to be the fourth component of this thesis, is an example. The necessary data processing and analytical tools for all four aspects of our work have been developed, tested and applied. In addition, our inclusion with the SL2S collaboration provides access to a wealth of relevant experience and additional tools to assist in all aspects of our work. Thus, we are confident that the contributions we have made so far to the general body of knowledge in Physical Cosmology, will continue to increase in the near future.

Basic theory of gravitational lensing

A.1 Introduction

The principal observational focus of this thesis is on developing and applying innovative techniques for cosmological investigations, by harnessing the magnification boost of gravitational lensing with the advances in astronomical instrumentation on the modern 8m class telescopes. In order to supplement or explain the lensing related terms and concepts used in the thesis, this appendix presents pertinent results drawn mainly from three treatises on lensing theory, namely, Kochanek et al. (2004), Mollerach and Roulet (2002) and Schneider et al. (1992). Due to the large overlap in the material amongst the three references, they are not individually referenced, except where specifically warranted.

Gravitational Lensing is a direct manifestation of the curvature of space-time postulated by Einsteins General Theory of Relativity (GR). GR postulates that the geometry of space-time of the Universe is intimately related to the total energy density present where there is non-zero energy density, space-time is curved. This equivalence between geometry and energy density is given by the field equations.

The predominant contribution ($\sim 90\%$) to the lensing mass density is from dark matter. On the spatial scales at which strong lensing occurs (a few kpc, the scale radius of a galaxy cluster), the contribution from dark energy to the total mass (energy) is minimal and therefore its effect on lensing may be neglected.

A.2 Lens equation for a point point mass

The deflection of light in lensing is related to the curvature of space. Light travels along null geodesics, according to GR; the geodesics follow the curvature of space induced by any massive object, e.g., a cluster this resembles the deflection of a

light ray in an ordinary glass lens, hence the name.

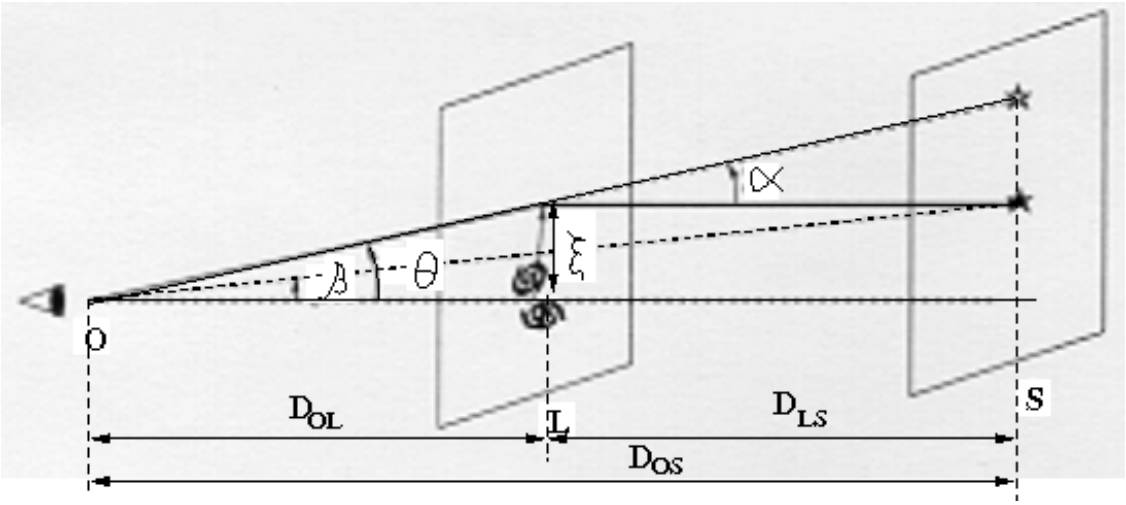

Figure A.1: Schematic to illustrate the geometry of a single, point mass lens. The source, S, is lensed by the mass in the lensing plane, L, and appears as the image, I to the observer at O. β is the angle to the unlensed source and θ is the angle to the lensed image, both angles measured from the optic axis joining the observer and the lensing mass. α is the deflection angle. All distances are cosmological, angular diameter distances.

The deflection angle for a point mass is calculated using a Schwarzschild metric. A light ray incident at a radial distance, ξ (impact parameter) from a point mass, M, will be deflected by an angle, α, given by,

$$\alpha(\xi) = \frac{4GM}{c^2\xi} = \frac{2R_s}{\xi} \tag{A.1}$$

where, G is the gravitational constant, c, the velocity of light and R_s is the Schwarzschild radius of the mass. This result holds only when $\xi >> R_s$, therefore permitting the use of the weak gravitational field approximation. This assumption is fully justified on the scale of cluster lenses since $R_s \sim 0.01$pc for a cluster of mass $\sim 10^{14}$ $M_\odot$, while the typical impact parameter is few hundred Kpc (calculated using a nominal angle of separation, $\sim 10''$, between the cluster center and the lensed arc).

The position of the lensed image may be calculated using geometric optics provided all distances are measured as angular diameter distances to account for the curvature of space-time. In a typical lensing geometry, shown in Figure A.1, a light beam from a distant source, S, is deflected through an angle, α, by a mass located in the plane, L, and reaches the observer, O; the observer therefore sees the lensed image, I. The line connecting the observer and the lens defines the optic axis, OL. The angle to the unlensed source is β and that to the lensed image is θ, both angles measured with respect to OL.

For the simple case of a point mass lens, the lens equation may be obtained by equating distances on the source plane and re-arranging terms,

$$\eta = \frac{D_{OS}}{D_{OL}}\xi - D_{LS}\,\alpha(\xi) \tag{A.2}$$

Substituting for the deflection angle and replacing the impact parameter, $\xi = D_{OL}\,\theta$, yields the lens equation,

$$\beta = \theta - \hat{\alpha}(\theta) \tag{A.3}$$

The scaled deflection angle, $\hat{\alpha}$, is computed in terms of the *Einstein angle*, θ_E, as,

$$\hat{\alpha}(\theta) = \frac{\theta_E^2}{\theta} \tag{A.4}$$

with the Einstein angle defined as,

$$\theta_E^2 = \frac{4GM}{c^2}\,\frac{D_{LS}}{D_{OL}\,D_{OS}} \tag{A.5}$$

Taken with the *Einstein Radius*, $\xi_E = \theta_E\,D_{OL}$, these last three quantities provide scales for comparing different lensing geometries.

A.3 Lens equation for a distributed mass

For light deflection by the distributed mass of a cluster lens, the lens equation for a point mass is extended by linear superposition, permitted in the weak field limit. In

addition, the 3D mass distribution of the cluster lens is projected on the lens plane as a surface mass distribution, Σ. This thin lens approximation holds since the linear dimension of the lensing mass in the direction of the light ray is insignificant in comparison with the distances between lens, source and observer. A suitable point, e.g., the centre of mass, is chosen for the optic axis. This point also forms the origin of a coordinate system in which the impact parameter and all the angles are measured as 2D vectors. Under these conditions, the 2D deflection angle is given by,

$$\vec{\alpha}(\vec{\xi}) = \frac{4G}{c^2} \int_{R^2} \Sigma(\xi') \frac{(\vec{\xi}' - \vec{\xi})}{|\vec{\xi}' - \vec{\xi}|} \, d^2\xi' \tag{A.6}$$

and the corresponding vectorial thin lens equation may be expressed as,

$$\vec{\beta} = \vec{\theta} - \vec{\hat{\alpha}} \tag{A.7}$$

The scaled 2D deflection angle is given in terms of the surface mass distribution as,

$$\vec{\hat{\alpha}}(\vec{\theta}) = \frac{1}{\pi} \int_{R^2} \kappa(\vec{\theta}') \frac{(\vec{\theta}' - \vec{\theta})}{|\vec{\theta}' - \vec{\theta}|} \, d^2\theta' \tag{A.8}$$

where, κ, is the non-dimensional surface mass density. We define a critical surface mass density, Σ_{cr}, for the generalized (distributed) lens, similar to the Einstein radius for a point mass.

$$\kappa(\vec{\theta}) = \frac{\Sigma(D_{OL}\ \vec{\theta})}{\Sigma_{cr}} \tag{A.9}$$

where, the critical mass density is given by,

$$\Sigma_{cr} = \frac{c^2}{4\pi G} \frac{D_{OS}}{D_{OL}\ D_{LS}} \tag{A.10}$$

The non-dimensional surface mass density, κ, is a measure of the strength of the lensing. Strong lensing occurs in regions where $\kappa \geq 1$ this is the area where multiple images and giant arcs occur. By estimating Σ_{cr} for given source and lens redshifts (i.e., for known angular diameter distances), the areas where arcs are likely to occur may be mapped out *for a known or assumed mass distribution.*

A.4 Magnification

In gravitational lensing, the light ray is only deflected; there is neither absorption nor emission (assuming that extinction due to dust is negligible). Therefore, the specific intensity of the light beam remains unaffected, which implies that the surface brightness of the lensed image equals that of the (hypothetical) unlensed image.

However, the areas (= solid angles subtended) of the lensed image and the unlensed source differ due to the lensing e.g., a $0''.3$ galaxy at z=1 is lensed into a giant arc of area ~ 10 square arc.seconds.

Magnification is, therefore, defined as the ratio of the solid angles subtended by the lensed image to that subtended by the unlensed source. Since the lens equation, Equation A.7 is just a coordinate transformation, the ratio of areas is given by the Jacobian determinant, A, of the transformation.

$$A(\vec{\theta}) = \left| \frac{\delta\vec{\beta}}{\delta\vec{\theta}} \right| \tag{A.11}$$

The magnification, μ, is then given by,

$$\mu(\theta) = \frac{1}{A} \tag{A.12}$$

Equation A.12 implies that wherever the Jacobian vanishes, the magnification diverges. For a given lensing mass distribution and for specified source and lens redshift, the locus of points on the lens plane where A vanishes may be computed from the lens equation, A.7 this locus is called the *critical line* of the lens geometry. The lens equation may be inverted and the corresponding points on the source plane may also be computed the locus of these points is the *caustic*.

The critical curve is smooth and has continuous first derivatives. The slope of the caustic, however, may change abruptly due to the non-linear nature of the lens equation. The points on the critical line where the slope is undefined are the *cusps*. A giant arc is formed only when an extended source, such as a galaxy, lies at a cusp.

Though brief, this treatment is intended to summarize some of the principal concepts of gravitational lensing for the sake of completeness. For a more complete treatment, please refer to the cited references.

Acronyms and abbreviations

gr, ri	(g-r) and (r-i) colors
BG	bright galaxy
BCG	bright central galaxy
CFHT	Canada France Hawaii Telescope
CFHTLS	Canada France Hawaii Telescope Legacy Survey
CFRS	Canada France Redshift Survey
CMB	Cosmic Microwave Background
CuAr	Copper-Argon calibration arc lamp
FITS	Flexible Image Transport System
FOV	field of view
FWHM	Full width at half maximum
GMOS	Gemini Multi-Object Spectrograph
HLR	half light radius
HRQ	Hernquist density profile
HST	Hubble Space Telescope
IFU	Integral Field Unit
IGM	intergalactic medium
IMF	initial (stellar) mass function
IRAF	Image Reduction and Analysis Facility
Λ-CDM	Λ (dark energy) - cold dark matter

LBG	Lyman break galaxy
LOSVD	Line of sight velocity dispersion
mag	magnitude
MF	Matched Filter
NFW	Navarro Frenk and White density profile
RGB	red-green-blue pseudo-color images
ROSTAT	Robust Statistics software
SDSS	Sloan Digital Sky Survey
SFR	star formation rate
SIS	Singular Isothermal Sphere density profile
S/N	signal-to-noise
SL2S	Strong Lensing Legacy Survey
SNR	signal to noise ratio
SVD	Singular value decomposition
MOS	Multi-object spectroscopy
UV	Ultraviolet
XMM-LSS	X-ray Multi-Mirror telescope, Large Scale Structure survey

Bibliography

G. O. Abell. The Distribution of Rich Clusters of Galaxies. *ApJSupp*, 3, 1958.

R. G. Abraham, K. Glazebrook, P. J. McCarthy, D. Crampton, R. Murowinski, I. Jørgensen, K. Roth, I. M. Hook, S. Savaglio, H.-W. Chen, R. O. Marzke, and R. G. Carlberg. The Gemini Deep Deep Survey. I. Introduction to the Survey, Catalogs, and Composite Spectra. *AJ*, 127, 2004.

K. L. Adelberger, C. C. Steidel, M. Giavalisco, M. Dickinson, M. Pettini, and M. Kellogg. A Counts-in-Cells Analysis Of Lyman-break Galaxies At Redshift Z = 3. *ApJ*, 505, 1998.

K. L. Adelberger, C. C. Steidel, A. E. Shapley, and M. Pettini. Galaxies and Intergalactic Matter at Redshift $z \sim 3$: Overview. *ApJ*, 584, 2003.

C. Alard. Automated detection of gravitational arcs. *ArXiv Astrophysics e-prints*, 2006.

J. Allington-Smith, G. Murray, R. Content, G. Dodsworth, R. Davies, B. W. Miller, I. Jorgensen, I. Hook, D. Crampton, and R. Murowinski. Integral Field Spectroscopy with the Gemini Multiobject Spectrograph. I. Design, Construction, and Testing. *PASP*, 114, 2002.

M. L. Balogh, I. G. McCarthy, R. G. Bower, and V. R. Eke. Testing cold dark matter with the hierarchical build-up of stellar light. *MNRAS*, 385, 2008.

S. C. Barden. Review of Fiber-Optic Properties for Astronomical Spectroscopy. In S. Arribas, E. Mediavilla, and F. Watson, editors, *Fiber Optics in Astronomy III*, volume 152 of *Astronomical Society of the Pacific Conference Series*, 1998.

C. M. Baugh, S. Cole, C. S. Frenk, and C. G. Lacey. The Epoch of Galaxy Formation. *ApJ*, 498, 1998.

T. C. Beers, K. Flynn, and K. Gebhardt. Measures of location and scale for velocities in clusters of galaxies - A robust approach. *AJ*, 100, 1990.

T. C. Beers, K. Gebhardt, W. Forman, J. P. Huchra, and C. Jones. A dynamical analysis of twelve clusters of galaxies. *AJ*, 102, 1991.

E. F. Bell, C. Wolf, K. Meisenheimer, H.-W. Rix, A. Borch, S. Dye, M. Kleinheinrich, L. Wisotzki, and D. H. McIntosh. Nearly 5000 Distant Early-Type Galaxies in COMBO-17: A Red Sequence and Its Evolution since z = 1. *ApJ*, 608, 2004.

E. F. Bell, X. Z. Zheng, C. Papovich, A. Borch, C. Wolf, and K. Meisenheimer. Star Formation and the Growth of Stellar Mass. *ApJ*, 663, 2007.

R. Bender. Unraveling the kinematics of early-type galaxies - Presentation of a new method and its application to NGC4621. *A&A*, 229, 1990.

E. Bertin and S. Arnouts. SExtractor: Software for source extraction. *A&ApSupp*, 117, 1996.

S. Bertone, G. De Lucia, and P. A. Thomas. The recycling of gas and metals in galaxy formation: predictions of a dynamical feedback model. *MNRAS*, 2007.

C. Bild. Brightest Cluster Galaxies: Optical Properties at Intermediate Redshift. Master's thesis, University of Victoria, 2007.

J. Binney. The radius-dependence of velocity dispersion in elliptical galaxies. *MNRAS*, 190, 1980.

J. Binney and S. Tremaine. *Galactic dynamics*. Princeton, NJ, Princeton University Press, 1987, 1987.

A. Biviano, P. Katgert, T. Thomas, and C. Adami. The ESO Nearby Abell Cluster Survey. XI. Segregation of cluster galaxies and subclustering. *A&A*, 387, 2002.

A. W. Blain, I. Smail, R. J. Ivison, J.-P. Kneib, and D. T. Frayer. Submillimeter galaxies. *PhysRep*, 369, 2002.

J. P. Blakeslee, M. Franx, M. Postman, P. Rosati, B. P. Holden, G. D. Illingworth, H. C. Ford, N. J. G. Cross, C. Gronwall, N. Benítez, R. J. Bouwens, T. J. Broadhurst, M. Clampin, R. Demarco, D. A. Golimowski, G. F. Hartig, L. Infante, A. R. Martel, G. K. Miley, F. Menanteau, G. R. Meurer, M. Sirianni, and R. L. White. Advanced Camera for Surveys Photometry of the Cluster RDCS 1252.9-2927: The Color-Magnitude Relation at z = 1.24. *ApJLett*, 596, 2003.

M. R. Blanton, D. W. Hogg, N. A. Bahcall, J. Brinkmann, M. Britton, A. J. Connolly, I. Csabai, M. Fukugita, J. Loveday, A. Meiksin, J. A. Munn, R. C. Nichol, S. Okamura, T. Quinn, D. P. Schneider, K. Shimasaku, M. A. Strauss, M. Tegmark, M. S. Vogeley, and D. H. Weinberg. The Galaxy Luminosity Function and Luminosity Density at Redshift z = 0.1. *ApJ*, 592, 2003.

M. Bolzonella, J.-M. Miralles, and R. Pelló. Photometric redshifts based on standard SED fitting procedures. *A&A*, 363, 2000.

R. J. Bouwens, R. I. Thompson, G. D. Illingworth, M. Franx, P. G. van Dokkum, X. Fan, M. E. Dickinson, D. J. Eisenstein, and M. J. Rieke. Galaxies at z = 7-8: z 850 -Dropouts in the Hubble Ultra Deep Field. *ApJLett*, 616, 2004.

R. G. Bower, J. R. Lucey, and R. S. Ellis. Precision photometry of early-type galaxies in the Coma and Virgo clusters: A test of the universality of the colour-magnitude relation. I - The data. II. Analysis. *MNRAS*, 254, 1992.

R. G. Bower, A. J. Benson, R. Malbon, J. C. Helly, C. S. Frenk, C. M. Baugh, S. Cole, and C. G. Lacey. Breaking the hierarchy of galaxy formation. *MNRAS*, 370, 2006.

T. G. Brainerd, R. D. Blandford, and I. Smail. Weak Gravitational Lensing by Galaxies. *ApJ*, 466, 1996.

S. Brough, R. Proctor, D. A. Forbes, W. J. Couch, C. A. Collins, D. J. Burke, and R. G. Mann. Spatially resolved kinematics and stellar populations of brightest cluster and group galaxies. *MNRAS*, 378, 2007.

G. Bruzual and S. Charlot. Stellar population synthesis at the resolution of 2003. *MNRAS*, 344, 2003.

H. Butcher and A. Oemler, Jr. The evolution of galaxies in clusters. V - A study of populations since Z approximately equal to 0.5. *ApJ*, 285, 1984.

R. A. Cabanac, C. Alard, M. Dantel-Fort, B. Fort, R. Gavazzi, P. Gomez, J. P. Kneib, O. Le Fèvre, Y. Mellier, R. Pello, G. Soucail, J. F. Sygnet, and D. Valls-Gabaud. The CFHTLS strong lensing legacy survey. I. Survey overview and T0002 release sample. *A&A*, 461, 2007.

M. Cappellari and E. Emsellem. Parametric Recovery of Line-of-Sight Velocity Distributions from Absorption-Line Spectra of Galaxies via Penalized Likelihood. *PASP*, 116, 2004.

A. Cattaneo, J. Blaizot, D. H. Weinberg, D. Kereš, S. Colombi, R. Davé, J. Devriendt, B. Guiderdoni, and N. Katz. Accretion, feedback and galaxy bimodality: a comparison of the GalICS semi-analytic model and cosmological SPH simulations. *MNRAS*, 377, 2007.

J. D. Cohn and M. White. The formation histories of galaxy clusters. *Astroparticle Physics*, 24, 2005.

S. Cole and C. Lacey. The structure of dark matter haloes in hierarchical clustering models. *MNRAS*, 281, 1996.

M. Colless, G. Dalton, S. Maddox, W. Sutherland, P. Norberg, S. Cole, J. Bland-Hawthorn, T. Bridges, R. Cannon, C. Collins, W. Couch, N. Cross, K. Deeley, R. De Propris, S. P. Driver, G. Efstathiou, R. S. Ellis, C. S. Frenk, K. Glazebrook, C. Jackson, O. Lahav, I. Lewis, S. Lumsden, D. Madgwick, J. A. Peacock, B. A. Peterson, I. Price, M. Seaborne, and K. Taylor. The 2dF Galaxy Redshift Survey: spectra and redshifts. *MNRAS*, 328, 2001.

J. M. Comerford and P. Natarajan. The observed concentration-mass relation for galaxy clusters. *MNRAS*, 379, 2007.

L. L. Cowie, A. Songaila, E. M. Hu, and J. G. Cohen. New Insight on Galaxy Formation and Evolution From Keck Spectroscopy of the Hawaii Deep Fields. *AJ*, 112, 1996.

D. Crampton, D. Schade, F. Hammer, A. Matzkin, S. J. Lilly, and O. Le Fèvre. The Gravitational Lens CFRS 03.1077. *ApJ*, 570, 2002.

D. J. Croton, V. Springel, S. D. M. White, G. De Lucia, C. S. Frenk, L. Gao, A. Jenkins, G. Kauffmann, J. F. Navarro, and N. Yoshida. The many lives of active galactic nuclei: cooling flows, black holes and the luminosities and colours of galaxies. *MNRAS*, 365, 2006.

J. C. Cuillandre, B. Fort, J. P. Picat, J. P. Soucail, B. Altieri, F. Beigbeder, J. P. Duplin, T. Pourthie, and G. Ratier. 'Va-et-Vient' spectroscopy: A new mode for faint object CCD spectroscopy with very large telescopes. *A&A*, 281, 1994.

G. De Lucia and J. Blaizot. The hierarchical formation of the brightest cluster galaxies. *MNRAS*, 375, 2007.

G. De Lucia, V. Springel, S. D. M. White, D. Croton, and G. Kauffmann. The formation history of elliptical galaxies. *MNRAS*, 366, 2006.

G. De Lucia, B. M. Poggianti, A. Aragón-Salamanca, S. D. M. White, D. Zaritsky, D. Clowe, C. Halliday, P. Jablonka, A. von der Linden, B. Milvang-Jensen, R. Pelló, G. Rudnick, R. P. Saglia, and L. Simard. The build-up of the colour-magnitude relation in galaxy clusters since z ˜ 0.8. *MNRAS*, 374, 2007.

M. E. de Rossi, P. B. Tissera, and C. Scannapieco. Clues for the origin of the fundamental metallicity relations - I. The hierarchical building up of the structure. *MNRAS*, 374, 2007.

G. de Vaucouleurs. Integrated Colors of Bright Galaxies in the u, b, V System. *ApJSupp*, 5, 1961.

A. Dressler. Galaxy morphology in rich clusters - Implications for the formation and evolution of galaxies. *ApJ*, 236, 1980.

H. Ebeling and G. Wiedenmann. Detecting structure in two dimensions combining Voronoi tessellation and percolation. *PhRvE*, 47, 1993.

O. J. Eggen, D. Lynden-Bell, and A. R. Sandage. Evidence from the motions of old stars that the Galaxy collapsed. *ApJ*, 136, 1962.

R. Ellis, M. R. Santos, J.-P. Kneib, and K. Kuijken. A Faint Star-forming System Viewed through the Lensing Cluster Abell 2218: First Light at z=5.6? *ApJLett*, 560, 2001.

D. K. Erb, A. E. Shapley, M. Pettini, C. C. Steidel, N. A. Reddy, and K. L. Adelberger. The Mass-Metallicity Relation at $z > 2$. *ApJ*, 644, 2006.

J. Estrada, J. Annis, H. T. Diehl, P. B. Hall, T. Las, H. Lin, M. Makler, K. W. Merritt, V. Scarpine, S. Allam, and D. Tucker. A Systematic Search for High

Surface Brightness Giant Arcs in a Sloan Digital Sky Survey Cluster Sample. *ApJ*, 660, 2007.

S. M. Faber, C. N. A. Willmer, C. Wolf, D. C. Koo, B. J. Weiner, J. A. Newman, M. Im, A. L. Coil, C. Conroy, M. C. Cooper, M. Davis, D. P. Finkbeiner, B. F. Gerke, K. Gebhardt, E. J. Groth, P. Guhathakurta, J. Harker, N. Kaiser, S. Kassin, M. Kleinheinrich, N. P. Konidaris, R. G. Kron, L. Lin, G. Luppino, D. S. Madgwick, K. Meisenheimer, K. G. Noeske, A. C. Phillips, V. L. Sarajedini, R. P. Schiavon, L. Simard, A. S. Szalay, N. P. Vogt, and R. Yan. Galaxy Luminosity Functions to $z \sim 1$ from DEEP2 and COMBO-17: Implications for Red Galaxy Formation. *ApJ*, 665, 2007.

G. E. Farin. *Curves and surfaces for computer aided geometric design : a practical guide*. Boston : Academic Press, c1988., 1988.

C. D. Fassnacht, D. D. Kocevski, M. W. Auger, L. M. Lubin, J. L. Neureuther, T. E. Jeltema, J. S. Mulchaey, and J. P. McKean. The X-Ray Properties of Moderate-Redshift Galaxy Groups Selected by Association with Gravitational Lenses. *ApJ*, 681, 2008.

H. C. Ferguson. Galaxy populations in the Fornax and Virgo clusters. *Ap&SS*, 157, 1989.

K. Finlator, Ž. Ivezić, X. Fan, M. A. Strauss, G. R. Knapp, R. H. Lupton, J. E. Gunn, C. M. Rockosi, J. E. Anderson, I. Csabai, G. S. Hennessy, R. B. Hindsley, T. A. McKay, R. C. Nichol, D. P. Schneider, J. A. Smith, D. G. York, and the SDSS Collaboration. Optical and Infrared Colors of Stars Observed by the Two Micron All Sky Survey and the Sloan Digital Sky Survey. *AJ*, 120, 2000.

N. M. Förster Schreiber, R. Genzel, M. D. Lehnert, N. Bouché, A. Verma, D. K. Erb, A. E. Shapley, C. C. Steidel, R. Davies, D. Lutz, N. Nesvadba, L. J. Tacconi, F. Eisenhauer, R. Abuter, A. Gilbert, S. Gillessen, and A. Sternberg. SINFONI

Integral Field Spectroscopy of $z \sim 2$ UV-selected Galaxies: Rotation Curves and Dynamical Evolution. *ApJ*, 645, 2006.

M. Franx and G. D. Illingworth. A counterrotating core in IC 1459. *ApJLett*, 327, 1988.

M. Franx, G. D. Illingworth, D. D. Kelson, P. G. van Dokkum, and K.-V. Tran. A Pair of Lensed Galaxies at z=4.92 in the Field of CL 1358+62. *ApJLett*, 486, 1997.

K. C. Freeman. Dark Halos: An HI Perspective. In J. E. Hibbard, M. Rupen, and J. H. van Gorkom, editors, *Gas and Galaxy Evolution*, volume 240, 2001.

J. W. Fried, B. von Kuhlmann, K. Meisenheimer, H.-W. Rix, C. Wolf, H. H. Hippelein, M. Kümmel, S. Phleps, H. J. Röser, I. Thierring, and C. Maier. The luminosity function of field galaxies and its evolution since z=1. *A&A*, 367, 2001.

R. Gavazzi, B. Fort, Y. Mellier, R. Pelló, and M. Dantel-Fort. A radial mass profile analysis of the lensing cluster MS 2137.3-2353. *A&A*, 403, 2003.

R. Gavazzi, T. Treu, L. V. E. Koopmans, A. S. Bolton, L. A. Moustakas, S. Burles, and P. J. Marshall. The Sloan Lens ACS Survey. VI. Discovery and Analysis of a Double Einstein Ring. *ApJ*, 677, 2008.

K. Gebhardt and T. C. Beers. Bound populations around cD galaxies and cD velocity offsets in clusters of galaxies. *ApJ*, 383, 1991.

K. Gebhardt, D. Richstone, J. Kormendy, T. R. Lauer, E. A. Ajhar, R. Bender, A. Dressler, S. M. Faber, C. Grillmair, J. Magorrian, and S. Tremaine. Axisymmetric, Three-Integral Models of Galaxies: A Massive Black Hole in NGC 3379. *AJ*, 119, 2000.

B. F. Gerke, J. A. Newman, S. M. Faber, M. C. Cooper, D. J. Croton, M. Davis, C. N. A. Willmer, R. Yan, A. L. Coil, P. Guhathakurta, D. C. Koo, and B. J.

Weiner. The DEEP2 galaxy redshift survey: the evolution of the blue fraction in groups and the field. *MNRAS*, 376, 2007.

M. Giavalisco, C. C. Steidel, and F. D. Macchetto. Hubble Space Telescope Imaging of Star-forming Galaxies at Redshifts Z = 3. *ApJ*, 470, 1996.

M. D. Gladders and H. K. C. Yee. A New Method For Galaxy Cluster Detection. I. The Algorithm. *AJ*, 120, 2000.

M. D. Gladders and H. K. C. Yee. The Red-Sequence Cluster Survey. I. The Survey and Cluster Catalogs for Patches RCS 0926+37 and RCS 1327+29. *ApJSupp*, 157, 2005.

M. D. Gladders, H. Hoekstra, H. K. C. Yee, P. B. Hall, and L. F. Barrientos. The Incidence of Strong-Lensing Clusters in the Red-Sequence Cluster Survey. *ApJ*, 593, 2003.

J. D. Goldader, G. Meurer, T. M. Heckman, M. Seibert, D. B. Sanders, D. Calzetti, and C. C. Steidel. Far-Infrared Galaxies in the Far-Ultraviolet. *ApJ*, 568, 2002.

T. Goto, M. Sekiguchi, R. C. Nichol, N. A. Bahcall, R. S. J. Kim, J. Annis, Ž. Ivezić, J. Brinkmann, G. S. Hennessy, G. P. Szokoly, and D. L. Tucker. The Cut-and-Enhance Method: Selecting Clusters of Galaxies from the Sloan Digital Sky Survey Commissioning Data. *AJ*, 123, 2002.

F. Hammer, D. Crampton, O. Le Fevre, and S. J. Lilly. The Canada-France Redshift Survey. IV. Spectroscopic Selection Effects and 0300+00 Field Spectroscopic Data. *ApJ*, 455, 1995.

S. M. Hansen, T. A. McKay, R. H. Wechsler, J. Annis, E. S. Sheldon, and A. Kimball. Measurement of Galaxy Cluster Sizes, Radial Profiles, and Luminosity Functions from SDSS Photometric Data. *ApJ*, 633, 2005.

W. G. Hartley, L. Gazzola, F. R. Pearce, S. T. Kay, and P. A. Thomas. Nature versus nurture: the curved spine of the galaxy cluster X-ray luminosity-temperature relation. *MNRAS*, 386, 2008.

S. F. Helsdon and T. J. Ponman. The intragroup medium in loose groups of galaxies. *MNRAS*, 315, 2000.

S. F. Helsdon and T. J. Ponman. The morphology-density relation in X-ray-bright galaxy groups. *MNRAS*, 339, 2003.

L. Hernquist. An analytical model for spherical galaxies and bulges. *ApJ*, 356, 1990.

P. C. Hewett, S. J. Warren, J. P. Willis, J. Bland-Hawthorn, and G. F. Lewis. High-Redshift Gravitationally Lensed Galaxies and Tunable Filter Imaging. In W. van Breugel and J. Bland-Hawthorn, editors, *Imaging the Universe in Three Dimensions*, volume 195 of *Astronomical Society of the Pacific Conference Series*, 2000.

A. Horesh, E. O. Ofek, D. Maoz, M. Bartelmann, M. Meneghetti, and H.-W. Rix. The Lensed Arc Production Efficiency of Galaxy Clusters: A Comparison of Matched Observed and Simulated Samples. *ApJ*, 633, 2005.

J. P. Huchra and M. J. Geller. Groups of galaxies. I - Nearby groups. *ApJ*, 257, 1982.

I. Jorgensen, M. Franx, and P. Kjaergaard. The Fundamental Plane for cluster E and S0 galaxies. *MNRAS*, 280, 1996.

E. Jullo, J.-P. Kneib, M. Limousin, Á. Elíasdóttir, P. J. Marshall, and T. Verdugo. A Bayesian approach to strong lensing modelling of galaxy clusters. *New Journal of Physics*, 9, 2007.

S. Juneau, K. Glazebrook, D. Crampton, P. J. McCarthy, S. Savaglio, R. Abraham, R. G. Carlberg, H.-W. Chen, D. Le Borgne, R. O. Marzke, K. Roth, I. Jørgensen, I. Hook, and R. Murowinski. Cosmic Star Formation History and Its Dependence on Galaxy Stellar Mass. *ApJLett*, 619, 2005.

G. Kauffmann and S. Charlot. Chemical enrichment and the origin of the colour-magnitude relation of elliptical galaxies in a hierarchical merger model. *MNRAS*, 294, 1998.

D. D. Kelson. Optimal Techniques in Two-dimensional Spectroscopy: Background Subtraction for the 21st Century. *PASP*, 115, 2003.

D. D. Kelson, G. D. Illingworth, P. G. van Dokkum, and M. Franx. The Evolution of Early-Type Galaxies in Distant Clusters. II. Internal Kinematics of 55 Galaxies in the z=0.33 Cluster CL 1358+62. *ApJ*, 531, 2000.

R. C. Kennicutt, Jr. Star Formation in Galaxies Along the Hubble Sequence. *ARA&A*, 36, 1998.

J. Kepner, X. Fan, N. Bahcall, J. Gunn, R. Lupton, and G. Xu. An Automated Cluster Finder: The Adaptive Matched Filter. *ApJ*, 517, 1999.

R. S. J. Kim, J. V. Kepner, M. Postman, M. A. Strauss, N. A. Bahcall, J. E. Gunn, R. H. Lupton, J. Annis, R. C. Nichol, F. J. Castander, J. Brinkmann, R. J. Brunner, A. Connolly, I. Csabai, R. B. Hindsley, Ž. Ivezić, M. S. Vogeley, and D. G. York. Detecting Clusters of Galaxies in the Sloan Digital Sky Survey. I. Monte Carlo Comparison of Cluster Detection Algorithms. *AJ*, 123, 2002.

A. L. Kinney, D. Calzetti, R. C. Bohlin, K. McQuade, T. Storchi-Bergmann, and H. R. Schmitt. Template Ultraviolet to Near-Infrared Spectra of Star-forming Galaxies and Their Application to K-Corrections. *ApJ*, 467, 1996.

J.-P. Kneib, R. S. Ellis, I. Smail, W. J. Couch, and R. M. Sharples. Hubble Space Telescope Observations of the Lensing Cluster Abell 2218. *ApJ*, 471, 1996.

J.-P. Kneib, P. Hudelot, R. S. Ellis, T. Treu, G. P. Smith, P. Marshall, O. Czoske, I. Smail, and P. Natarajan. A Wide-Field Hubble Space Telescope Study of the Cluster Cl 0024+1654 at z=0.4. II. The Cluster Mass Distribution. *ApJ*, 598, 2003.

J.-P. Kneib, R. S. Ellis, M. R. Santos, and J. Richard. A Probable z=7 Galaxy Strongly Lensed by the Rich Cluster A2218: Exploring the Dark Ages. *ApJ*, 607, 2004.

C. S. Kochanek, E. E. Falco, C. D. Impey, J. Lehár, B. A. McLeod, H.-W. Rix, C. R. Keeton, J. A. Muñoz, and C. Y. Peng. The Fundamental Plane of Gravitational Lens Galaxies and The Evolution of Early-Type Galaxies in Low-Density Environments. *ApJ*, 543, 2000.

C. S. Kochanek, P. Schneider, and J. Wambsganss. Part 2 of Gravitational Lensing: Strong, Weak and Micro, Proceedings of the 33rd Saas-Fee Advanced Course. Springer-Verlag: Berlin, 2004.

T. Kodama and R. Bower. The K-band luminosity and stellar mass functions of galaxies in z = 1 clusters. *MNRAS*, 346, 2003.

T. Kodama, N. Arimoto, A. J. Barger, and A. Arag'on-Salamanca. Evolution of the colour-magnitude relation of early-type galaxies in distant clusters. *A&A*, 334, 1998.

T. Kodama, R. G. Bower, and E. F. Bell. The colour-magnitude relation of early-type galaxies in the Hubble Deep Field. *MNRAS*, 306, 1999.

T. Kodama, I. Tanaka, M. Kajisawa, J. Kurk, B. Venemans, C. De Breuck, J. Ver-

net, and C. Lidman. The first appearance of the red sequence of galaxies in proto-clusters. *MNRAS*, 377, 2007.

E. Komatsu, J. Dunkley, M. R. Nolta, C. L. Bennett, B. Gold, G. Hinshaw, N. Jarosik, D. Larson, M. Limon, L. Page, D. N. Spergel, M. Halpern, R. S. Hill, A. Kogut, S. S. Meyer, G. S. Tucker, J. L. Weiland, E. Wollack, and E. L. Wright. Five-Year Wilkinson Microwave Anisotropy Probe (WMAP) Observations: Cosmological Interpretation. *ArXiv e-prints*, 803, 2008.

Y. Komiyama, M. Sekiguchi, N. Kashikawa, M. Yagi, M. Doi, M. Iye, S. Okamura, K. Shimasaku, N. Yasuda, B. Mobasher, D. Carter, T. J. Bridges, and B. M. Poggianti. A Photometric and Spectroscopic Study of Dwarf and Giant Galaxies in the Coma Cluster. I. Wide-Area Photometric Survey: Observation and Data Analysis. *ApJSupp*, 138, 2002.

L. V. E. Koopmans, T. Treu, A. S. Bolton, S. Burles, and L. A. Moustakas. The Sloan Lens ACS Survey. III. The Structure and Formation of Early-Type Galaxies and Their Evolution since z = 1. *ApJ*, 649, 2006.

A. V. Kravtsov, A. A. Klypin, J. S. Bullock, and J. R. Primack. The Cores of Dark Matter-dominated Galaxies: Theory versus Observations. *ApJ*, 502, 1998.

K. Krisciunas. Optical Night-Sky Brightness at Mauna Kea over the Course of a Complete Sunspot Cycle. *PASP*, 109, 1997.

S. J. LaRoque, M. Joy, J. E. Carlstrom, H. Ebeling, M. Bonamente, K. S. Dawson, A. Edge, W. L. Holzapfel, A. D. Miller, D. Nagai, S. K. Patel, and E. D. Reese. Sunyaev-Zeldovich Effect Imaging of MACS Galaxy Clusters at z0.5. *ApJ*, 583, 2003.

D. R. Law, C. C. Steidel, D. K. Erb, J. E. Larkin, M. Pettini, A. E. Shapley, and S. A. Wright. Integral Field Spectroscopy of High-Redshift Star Forming

Galaxies with Laser Guided Adaptive Optics: Evidence for Dispersion-Dominated Kinematics. *ArXiv e-prints*, 707, 2007.

F. Lenzen, S. Schindler, and O. Scherzer. Automatic detection of arcs and arclets formed by gravitational lensing. *A&A*, 416, 2004.

C. E. Lidman and B. A. Peterson. An Optically Based Search for Distant Galaxy Clusters. *AJ*, 112, 1996.

S. J. Lilly, O. Le Fevre, D. Crampton, F. Hammer, and L. Tresse. The Canada-France Redshift Survey. I. Introduction to the Survey, Photometric Catalogs, and Surface Brightness Selection Effects. *ApJ*, 455, 1995.

H. Lin, H. K. C. Yee, R. G. Carlberg, S. L. Morris, M. Sawicki, D. R. Patton, G. Wirth, and C. W. Shepherd. The CNOC2 Field Galaxy Luminosity Function. I. A Description of Luminosity Function Evolution. *ApJ*, 518, 1999.

E. L. Łokas and G. A. Mamon. Properties of spherical galaxies and clusters with an NFW density profile. *MNRAS*, 321, 2001.

M. S. Longair. *Galaxy Formation*. Berlin: Springer, 1998, 1998.

P. Madau, L. Pozzetti, and M. Dickinson. The Star Formation History of Field Galaxies. *ApJ*, 498, 1998.

C. Marinoni and M. J. Hudson. The Mass-to-Light Function of Virialized Systems and the Relationship between Their Optical and X-Ray Properties. *ApJ*, 569, 2002.

M. Markevitch. The L X-T Relation and Temperature Function for Nearby Clusters Revisited. *ApJ*, 504, 1998.

R. Massey, A. Refregier, D. J. Bacon, R. Ellis, and M. L. Brown. An enlarged cosmic shear survey with the William Herschel Telescope. *MNRAS*, 359, 2005.

A. Mazure, C. Adami, M. Pierre, O. Le Fèvre, S. Arnouts, P. A. Duc, O. Ilbert, V. Lebrun, B. Meneux, F. Pacaud, J. Surdej, and I. Valtchanov. Structure detection in the D1 CFHTLS deep field using accurate photometric redshifts: a benchmark. *A&A*, 467, 2007.

K. McQuade, D. Calzetti, and A. L. Kinney. Ultraviolet to optical spectral distributions of northern star-forming galaxies. *ApJSupp*, 97, 1995.

C. J. Miller, R. C. Nichol, D. Reichart, R. H. Wechsler, A. E. Evrard, J. Annis, T. A. McKay, N. A. Bahcall, M. Bernardi, H. Boehringer, A. J. Connolly, T. Goto, A. Kniazev, D. Lamb, M. Postman, D. P. Schneider, R. K. Sheth, and W. Voges. The C4 Clustering Algorithm: Clusters of Galaxies in the Sloan Digital Sky Survey. *AJ*, 130, 2005.

B. Mobasher, T. Dahlen, A. Hopkins, N. Z. Scoville, P. Capak, R. M. Rich, D. B. Sanders, E. Schinnerer, O. Ilbert, M. Salvato, and K. Sheth. Relation Between Stellar Mass and Star Formation Activity in Galaxies. *ArXiv e-prints*, 808, 2008.

S. Mollerach and E. Roulet. *Gravitational lensing and microlensing*. Gravitational lensing and microlensing by Silvia Mollerach, and Esteban Roulet. xi, 191 p. : ill. ; 23 cm. Includes bibliographical references and index. ISBN : 9810248520, 2002.

J. S. Mulchaey. The Intragroup Medium. In J. S. Mulchaey, A. Dressler, and A. Oemler, editors, *Clusters of Galaxies: Probes of Cosmological Structure and Galaxy Evolution*, 2004.

J. F. Navarro, C. S. Frenk, and S. D. M. White. A Universal Density Profile from Hierarchical Clustering. *ApJ*, 490, 1997.

N. P. H. Nesvadba, M. D. Lehnert, R. Genzel, F. Eisenhauer, A. J. Baker, S. Seitz, R. Davies, D. Lutz, L. Tacconi, M. Tecza, R. Bender, and R. Abuter. Intense

Star Formation and Feedback at High Redshift: Spatially Resolved Properties of the z = 2.6 Submillimeter Galaxy SMM J14011+0252. *ApJ*, 657, 2007.

L. F. Olsen, C. Benoist, A. Cappi, S. Maurogordato, A. Mazure, E. Slezak, C. Adami, C. Ferrari, and F. Martel. Galaxy clusters in the CFHTLS. First matched filter candidate catalogue of the Deep fields. *A&A*, 461, 2007.

J. P. F. Osmond and T. J. Ponman. The GEMS project: X-ray analysis and statistical properties of the group sample. *MNRAS*, 350, 2004.

D. E. Osterbrock, J. P. Fulbright, A. R. Martel, M. J. Keane, S. C. Trager, and G. Basri. Night-Sky High-Resolution Spectral Atlas of OH and O2 Emission Lines for Echelle Spectrograph Wavelength Calibration. *PASP*, 108, 1996.

D. E. Osterbrock, J. P. Fulbright, and T. A. Bida. Night-Sky High-Resolution Spectral Atlas of OH Emission Lines for Echelle Spectrograph Wavelength Calibration. II. *PASP*, 109, 1997.

F. Pacaud, M. Pierre, C. Adami, B. Altieri, S. Andreon, L. Chiappetti, A. Detal, P.-A. Duc, G. Galaz, A. Gueguen, J.-P. Le Fèvre, G. Hertling, C. Libbrecht, J.-B. Melin, T. J. Ponman, H. Quintana, A. Refregier, P.-G. Sprimont, J. Surdej, I. Valtchanov, J. P. Willis, D. Alloin, M. Birkinshaw, M. N. Bremer, O. Garcet, C. Jean, L. R. Jones, O. Le Fèvre, D. Maccagni, A. Mazure, D. Proust, H. J. A. Röttgering, and G. Trinchieri. The XMM-LSS survey: the Class 1 cluster sample over the initial 5 deg^2*anditscosmologicalmodelling*. *MNRAS*, 382, 2007.

C. Papovich, M. Dickinson, and H. C. Ferguson. The Stellar Populations and Evolution of Lyman Break Galaxies. *ApJ*, 559, 2001.

W. J. Percival, W. Sutherland, J. A. Peacock, C. M. Baugh, J. Bland-Hawthorn, T. Bridges, R. Cannon, S. Cole, M. Colless, C. Collins, W. Couch, G. Dalton, R. De Propris, S. P. Driver, G. Efstathiou, R. S. Ellis, C. S. Frenk, K. Glazebrook,

C. Jackson, O. Lahav, I. Lewis, S. Lumsden, S. Maddox, S. Moody, P. Norberg, B. A. Peterson, and K. Taylor. Parameter constraints for flat cosmologies from cosmic microwave background and 2dFGRS power spectra. *MNRAS*, 337, 2002.

M. Pettini, C. C. Steidel, K. L. Adelberger, M. Dickinson, and M. Giavalisco. The Ultraviolet Spectrum of MS 1512-CB58: An Insight into Lyman-Break Galaxies. *ApJ*, 528, 2000.

M. Pettini, A. E. Shapley, C. C. Steidel, J.-G. Cuby, M. Dickinson, A. F. M. Moorwood, K. L. Adelberger, and M. Giavalisco. The Rest-Frame Optical Spectra of Lyman Break Galaxies: Star Formation, Extinction, Abundances, and Kinematics. *ApJ*, 554, 2001.

M. Pettini, S. A. Rix, C. C. Steidel, K. L. Adelberger, M. P. Hunt, and A. E. Shapley. New Observations of the Interstellar Medium in the Lyman Break Galaxy MS 1512-cB58. *ApJ*, 569, 2002.

M. Pierre, L. Chiappetti, F. Pacaud, A. Gueguen, C. Libbrecht, B. Altieri, H. Aussel, P. Gandhi, O. Garcet, E. Gosset, L. Paioro, T. J. Ponman, A. M. Read, A. Refregier, J.-L. Starck, J. Surdej, I. Valtchanov, C. Adami, D. Alloin, A. Alshino, S. Andreon, M. Birkinshaw, M. Bremer, A. Detal, P.-A. Duc, G. Galaz, L. Jones, J.-P. Le Fèvre, O. Le Fèvre, D. Maccagni, A. Mazure, H. Quintana, H. J. A. Röttgering, P.-G. Sprimont, C. Tasse, G. Trinchieri, and J. P. Willis. The XMM-Large Scale Structure catalogue: X-ray sources and associated optical data. Version I. *MNRAS*, 382, 2007.

R. Piessens, E. de Doncker-Kapenga, and C. W. Ueberhuber. *Quadpack. A subroutine package for automatic integration.* Springer Series in Computational Mathematics, Berlin: Springer, 1983, 1983.

M. Postman, L. M. Lubin, J. E. Gunn, J. B. Oke, J. G. Hoessel, D. P. Schneider,

and J. A. Christensen. The Palomar Distant Clusters Survey. I. The Cluster Catalog. *AJ*, 111, 1996.

W. H. Press, S. A. Teukolsky, W. T. Vetterling, and B. P. Flannery. *Numerical recipes in C. The art of scientific computing*. Cambridge: University Press, —c1992, 2nd ed., 1992.

J. R. Primack. Summary talk: How serious are the problems faced by CDM: cusps, thin disks, and halo substructure. In S. Ryder, D. Pisano, M. Walker, and K. Freeman, editors, *Dark Matter in Galaxies*, volume 220, 2004.

J. R. Primack. Precision cosmology. *New Astronomy Review*, 49, 2005.

M. Ramella, W. Boschin, D. Fadda, and M. Nonino. Finding galaxy clusters using Voronoi tessellations. *A&A*, 368, 2001.

J. Rasmussen, T. J. Ponman, J. S. Mulchaey, T. A. Miles, and S. Raychaudhury. First results of the XI Groups Project: studying an unbiased sample of galaxy groups. *MNRAS*, 373, 2006.

N. A. Reddy, C. C. Steidel, M. Pettini, K. L. Adelberger, A. E. Shapley, D. K. Erb, and M. Dickinson. Multiwavelength Constraints on the Cosmic Star Formation History from Spectroscopy: the Rest-Frame Ultraviolet, H-alpha, and Infrared Luminosity Functions at Redshifts 1.9 - z - 3.4. *ApJSupp*, 175, 2008.

A. G. Riess, L.-G. Strolger, S. Casertano, H. C. Ferguson, B. Mobasher, B. Gold, P. J. Challis, A. V. Filippenko, S. Jha, W. Li, J. Tonry, R. Foley, R. P. Kirshner, M. Dickinson, E. MacDonald, D. Eisenstein, M. Livio, J. Younger, C. Xu, T. Dahlén, and D. Stern. New Hubble Space Telescope Discoveries of Type Ia Supernovae at z = 1: Narrowing Constraints on the Early Behavior of Dark Energy. *ApJ*, 659, 2007.

K. Rines and A. Diaferio. CIRS: Cluster Infall Regions in the Sloan Digital Sky Survey. I. Infall Patterns and Mass Profiles. *AJ*, 132, 2006.

H.-W. Rix and S. D. M. White. Optimal estimates of line-of-sight velocity distributions from absorption line spectra of galaxies - Nuclear discs in elliptical galaxies. *MNRAS*, 254, 1992.

S. Rucinski. Determination of Broadening Functions Using the Singular-Value Decomposition (SVD) Technique. In J. B. Hearnshaw and C. D. Scarfe, editors, *IAU Colloq. 170: Precise Stellar Radial Velocities*, volume 185, 1999.

S. M. Rucinski. Radial Velocity Studies of Close Binary Stars. VII. Methods and Uncertainties. *AJ*, 124, 2002.

S. M. Rucinski. Spectral-line broadening functions of WUMa-type binaries. I - AW UMa. *AJ*, 104, 1992.

S. M. Rucinski, W.-X. Lu, and J. Shi. Spectral-line broadening functions of W UMa-type binaries. III - W UMa. *AJ*, 106, 1993.

P. Saha and T. B. Williams. Unfolding kinematics from galaxy spectra: A Bayesian method. *AJ*, 107, 1994.

E. E. Salpeter. The Luminosity Function and Stellar Evolution. *ApJ*, 121, 1955.

D. J. Sand, T. Treu, G. P. Smith, and R. S. Ellis. The Dark Matter Distribution in the Central Regions of Galaxy Clusters: Implications for Cold Dark Matter. *ApJ*, 604, 2004.

W. L. W. Sargent, P. L. Schechter, A. Boksenberg, and K. Shortridge. Velocity dispersions for 13 galaxies. *ApJ*, 212, 1977.

S. Savaglio, K. Glazebrook, R. G. Abraham, D. Crampton, H.-W. Chen, P. J. P. McCarthy, I. Jørgensen, K. C. Roth, I. M. Hook, R. O. Marzke, R. G. Murowinski,

and R. G. Carlberg. The Gemini Deep Deep Survey. II. Metals in Star-forming Galaxies at Redshift $1.3 < z < 2$. *ApJ*, 602, 2004.

M. Sawicki and H. K. C. Yee. Optical-Infrared Spectral Energy Distributions of Z 2 Lyman Break Galaxies. *AJ*, 115, 1998.

D. Schade, S. J. Lilly, D. Crampton, F. Hammer, O. Le Fevre, and L. Tresse. Canada-France Redshift Survey: Hubble Space Telescope Imaging of High-Redshift Field Galaxies. *ApJLett*, 451, 1995.

D. Schade, S. J. Lilly, D. Crampton, R. S. Ellis, O. Le Fèvre, F. Hammer, J. Brinchmann, R. Abraham, M. Colless, K. Glazebrook, L. Tresse, and T. Broadhurst. Hubble Space Telescope Imaging of the CFRS and LDSS Redshift Surveys. III. Field Elliptical Galaxies at 0.2 - z - 1.0. *ApJ*, 525, 1999.

P. Schneider, J. Ehlers, and E. E. Falco. *Gravitational Lenses*. Gravitational Lenses, XIV, 560 pp. 112 figs.. Springer-Verlag Berlin Heidelberg New York. Also Astronomy and Astrophysics Library, 1992.

G. Seidel and M. Bartelmann. Arcfinder: an algorithm for the automatic detection of gravitational arcs. *A&A*, 472, 2007.

S. Seitz, R. P. Saglia, R. Bender, U. Hopp, P. Belloni, and B. Ziegler. The z=2.72 galaxy cB58: a gravitational fold arc lensed by the cluster MS1512+36. *MNRAS*, 298, 1998.

A. E. Shapley, C. C. Steidel, M. Pettini, K. L. Adelberger, and D. K. Erb. The Direct Detection of Lyman Continuum Emission from Star-forming Galaxies at $z \sim 3$. *ApJ*, 651, 2006.

J. Silk. Dark Matter and Galaxy Formation: Challenges for the Next Decade. In R. E. Allen, D. V. Nanopoulos, and C. N. Pope, editors, *The New Cosmology: Conference on Strings and Cosmology*, volume 743, Dec. 2004.

S. M. Simkin. Measurements of Velocity Dispersions and Doppler Shifts from Digitized Optical Spectra. *A&A*, 31, 1974.

G. P. Smith, J.-P. Kneib, I. Smail, P. Mazzotta, H. Ebeling, and O. Czoske. A Hubble Space Telescope lensing survey of X-ray luminous galaxy clusters - IV. Mass, structure and thermodynamics of cluster cores at z= 0.2. *MNRAS*, 359, 2005a.

G. P. Smith, T. Treu, R. S. Ellis, S. M. Moran, and A. Dressler. Evolution since z = 1 of the Morphology-Density Relation for Galaxies. *ApJ*, 620, 2005b.

R. S. Somerville, J. R. Primack, and S. M. Faber. The nature of high-redshift galaxies. *MNRAS*, 320, 2001.

D. N. Spergel. The Cosmic Microwave Background as a Cosmological Probe. In C. Lidman and D. Alloin, editors, *The Cool Universe: Observing Cosmic Dawn*, volume 344 of *Astronomical Society of the Pacific Conference Series*, 2005.

D. N. Spergel, L. Verde, H. V. Peiris, E. Komatsu, M. R. Nolta, C. L. Bennett, M. Halpern, G. Hinshaw, N. Jarosik, A. Kogut, M. Limon, S. S. Meyer, L. Page, G. S. Tucker, J. L. Weiland, E. Wollack, and E. L. Wright. First-Year Wilkinson Microwave Anisotropy Probe (WMAP) Observations: Determination of Cosmological Parameters. *ApJSupp*, 148, 2003.

V. Springel, S. D. M. White, A. Jenkins, C. S. Frenk, N. Yoshida, L. Gao, J. Navarro, R. Thacker, D. Croton, J. Helly, J. A. Peacock, S. Cole, P. Thomas, H. Couchman, A. Evrard, J. Colberg, and F. Pearce. Simulations of the formation, evolution and clustering of galaxies and quasars. , 435, 2005.

S. A. Stanford, P. R. Eisenhardt, and M. Dickinson. The Evolution of Early-Type Galaxies in Distant Clusters. *ApJ*, 492, 1998.

T. Statler. Bringing the cross-correlation method up to date. *AJ*, 109, 1995.

C. C. Steidel, M. Giavalisco, M. Pettini, M. Dickinson, and K. L. Adelberger. Spectroscopic Confirmation of a Population of Normal Star-forming Galaxies at Redshifts $z > 3$. *ApJLett*, 462, 1996.

C. C. Steidel, K. L. Adelberger, M. Giavalisco, M. Dickinson, and M. Pettini. Lyman-Break Galaxies and the Evolution of the Ultraviolet Luminosity Density at High Redshift. *ApJ*, 519, 1999.

S. H. Suyu, P. J. Marshall, M. P. Hobson, and R. D. Blandford. A Bayesian analysis of regularized source inversions in gravitational lensing. *MNRAS*, 371, 2006.

A. M. Swinbank, J. Smith, R. G. Bower, A. Bunker, I. Smail, R. S. Ellis, G. P. Smith, J.-P. Kneib, M. Sullivan, and J. Allington-Smith. Galaxies under the Cosmic Microscope: A Gemini Multiobject Spectrograph Study of Lensed Disk Galaxy 289 in A2218. *ApJ*, 598, 2003.

A. M. Swinbank, R. G. Bower, G. P. Smith, I. Smail, J.-P. Kneib, R. S. Ellis, D. P. Stark, and A. J. Bunker. Galaxies under the cosmic microscope: resolved spectroscopy and new constraints on the z = 1 Tully-Fisher relation. *MNRAS*, 368, 2006.

A. M. Swinbank, R. G. Bower, G. P. Smith, R. J. Wilman, I. Smail, R. S. Ellis, S. L. Morris, and J.-P. Kneib. Resolved spectroscopy of a gravitationally lensed L* Lyman-break galaxy at z - 5. *MNRAS*, 376, 2007.

E. Tago, J. Einasto, E. Saar, M. Einasto, I. Suhhonenko, M. Joeveer, J. Vennik, P. Heinamaki, and D. L. Tucker. Clusters and groups of galaxies in 2dF (Tago+, 2006). *VizieR On-line Data Catalog: J/other/AN/327.365. Originally published in: 2006AN....327..365T*, 10, 2006.

E. Tago, J. Einasto, E. Saar, E. Tempel, M. Einasto, J. Vennik, and V. Müller.

Groups of galaxies in the SDSS Data Release 5. A group-finder and a catalogue. *A&A*, 479, 2008.

H. I. Teplitz, I. S. McLean, E. E. Becklin, D. F. Figer, A. M. Gilbert, J. R. Graham, J. E. Larkin, N. A. Levenson, and M. K. Wilcox. The Rest-Frame Optical Spectrum of MS 1512-CB58. *ApJLett*, 533, 2000.

T. Thomas and P. Katgert. The ESO nearby Abell cluster survey. IX. The morphology-radius and morphology-density relations in rich galaxy clusters. *A&A*, 446, 2006.

J. Tonry and M. Davis. A survey of galaxy redshifts. I - Data reduction techniques. *AJ*, 84, 1979.

T. Treu and L. V. E. Koopmans. Massive Dark Matter Halos and Evolution of Early-Type Galaxies to z - 1. *ApJ*, 611, 2004.

R. B. Tully and J. R. Fisher. A new method of determining distances to galaxies. *A&A*, 54, 1977.

R. P. van der Marel, H. W. Rix, D. Carter, M. Franx, S. D. M. White, and T. de Zeeuw. Velocity Profiles of Galaxies with Claimed Black-Holes - Part One - Observations of M31 M32 NGC3115 and NGC4594. *MNRAS*, 268, 1994.

N. Visvanathan and A. Sandage. The color-absolute magnitude relation for E and S0 galaxies. I - Calibration and tests for universality using Virgo and eight other nearby clusters. *ApJ*, 216, 1977.

G. M. Voit. Tracing cosmic evolution with clusters of galaxies. *Reviews of Modern Physics*, 77, 2005.

R. V. Wagoner. Big-Bang Nucleosynthesis Revisited. *ApJ*, 179, 1973.

R. A. White, M. Bliton, S. P. Bhavsar, P. Bornmann, J. O. Burns, M. J. Ledlow, and C. Loken. A Catalog of Nearby Poor Clusters of Galaxies. *AJ*, 118, 1999.

J. A. Willick and N. Padmanabhan. Weak Lensing Constraints on Cluster Structural Parameters. *ArXiv Astrophysics e-prints*, 2000.

J. P. Willis, F. Pacaud, I. Valtchanov, M. Pierre, T. Ponman, A. Read, S. Andreon, B. Altieri, H. Quintana, S. Dos Santos, M. Birkinshaw, M. Bremer, P.-A. Duc, G. Galaz, E. Gosset, L. Jones, and J. Surdej. The XMM Large-Scale Structure survey: an initial sample of galaxy groups and clusters to a redshift z 0.6*. *MNRAS*, 363, 2005.

J. P. Willis, P. C. Hewett, S. J. Warren, S. Dye, and N. Maddox. The OLS-lens survey: the discovery of five new galaxy-galaxy strong lenses from the SDSS. *MNRAS*, 369, 2006.

C. N. A. Willmer, S. M. Faber, D. C. Koo, B. J. Weiner, J. A. Newman, A. L. Coil, A. J. Connolly, C. Conroy, M. C. Cooper, M. Davis, D. P. Finkbeiner, B. F. Gerke, P. Guhathakurta, J. Harker, N. Kaiser, S. Kassin, N. P. Konidaris, L. Lin, G. Luppino, D. S. Madgwick, K. G. Noeske, A. C. Phillips, and R. Yan. The Deep Evolutionary Exploratory Probe 2 Galaxy Redshift Survey: The Galaxy Luminosity Function to $z \sim 1$. *ApJ*, 647, 2006.

S. A. Wright, J. E. Larkin, M. Barczys, D. K. Erb, C. Iserlohe, A. Krabbe, D. R. Law, M. W. McElwain, A. Quirrenbach, C. C. Steidel, and J. Weiss. Integral Field Spectroscopy of a Candidate Disk Galaxy at z - 1.5 Using Laser Guide Star Adaptive Optics. *ApJ*, 658, 2007.

H. K. C. Yee, E. Ellingson, J. Bechtold, R. G. Carlberg, and J.-C. Cuillandre. A Proto-Galaxy Candidate at z=2.7 Discovered by its Young Stellar Population. *AJ*, 111, 1996.

F. Zwicky. On the Masses of Nebulae and of Clusters of Nebulae. *ApJ*, 86, 1937.

F. Zwicky, E. Herzog, and P. Wild. *Catalogue of galaxies and of clusters of galaxies*. Pasadena: California Institute of Technology (CIT), 1961-1968, 1968.